JOURNAL OF APPLIED PHYSICS

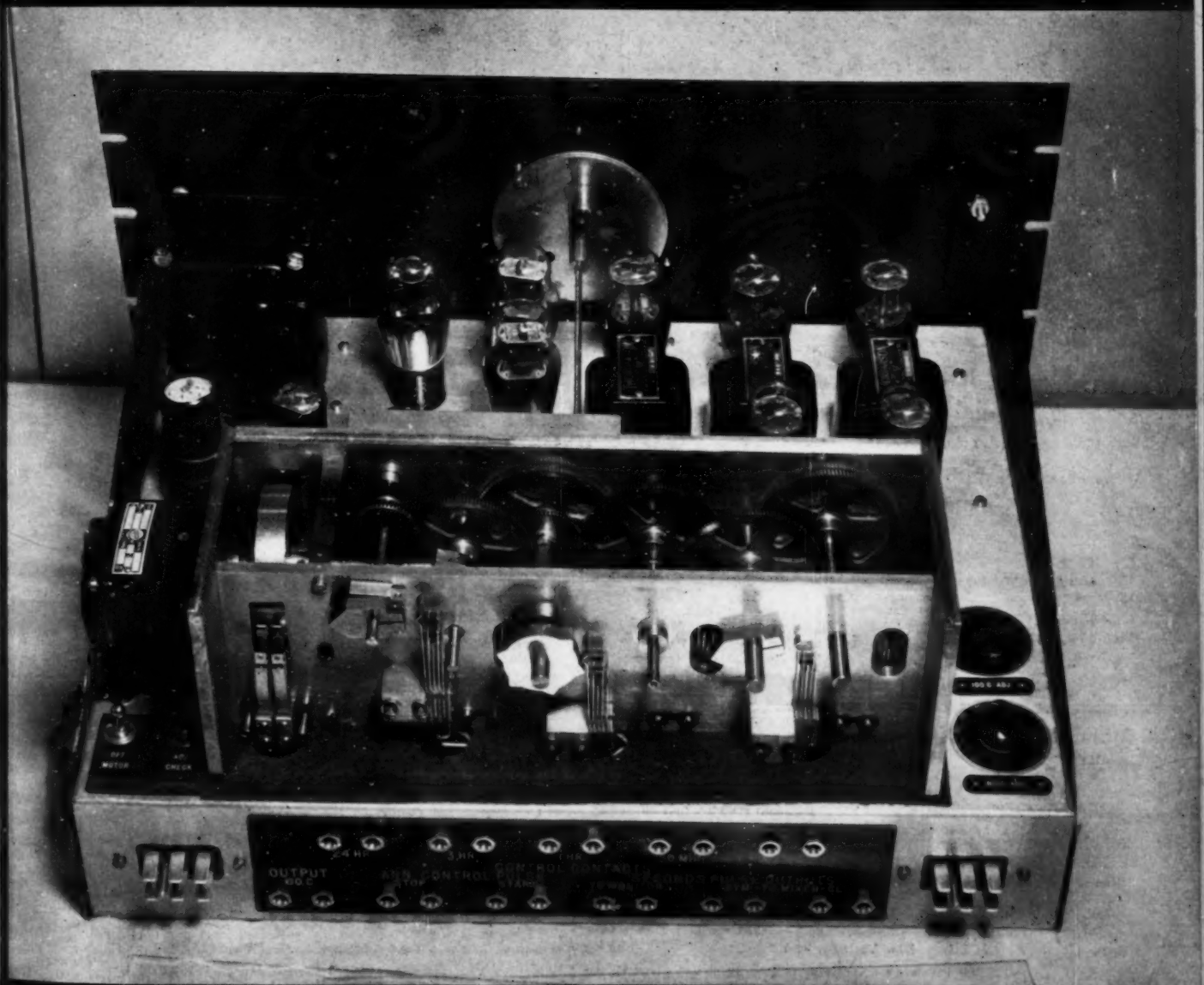

JOURNAL
OF
APPLIED PHYSICS

Vol. 18, No. 6 JUNE, 1947

In This Issue

Page

Crystal Pattern Synthesis by an Approximate Summation of Fourier Series JOSEPH S. LUKESH 493

Single Crystal Electron Diffraction by Micro-Crystalline Materials NORMAN DAVIDSON AND JAMES HILLIER 499

Microsecond Measurement of the Phosphorescence of X-Ray Fluorescent Screens FITZ-HUGH MARSHALL 512

X-Ray Diffraction Studies of Chrome-Steel Slags G. P. CHATTERJEE AND S. S. SIDHU 519

Spherical Aberration of Compound Magnetic Lenses L. MARTON AND K. BOL 522

Physical Properties of Calcium Tungstate X-Ray Screens J. W. COLTMAN, E. G. EBBIGHAUSEN, AND W. ALTAR 530

Pressure and Oil Flow in Oil-Filled Cables at Load Variations HANS LOTTRUP KNUDSEN 545

Electrostatic Field of a Point Charge Inside a Cylinder, in Connection with Wave Guide Theory C. J. BOUWKAMP AND N. G. DE BRUIJN 562

Elastic Constants of Materials Loaded with Non-Rigid Fillers JANE M. DEWEY 578

Heat Transfer between a Fluid and a Porous Solid Generating Heat STUART R. BRINKLEY, JR. 582

Letters to the Editor:

Concerning Estimates of the Minimum Sparking Potential Based upon the Cathode Work Function DONALD H. HALE AND W. S. HUXFORD 586

Measurement of the Dynamic Stretch-Modulus and Hysteresis of Tire Cords W. JAMES LYONS AND IRVEN B. PRETTYMAN 586

On the Analysis of Internal Flow Machinery SABINUS H. CHRISTENSEN 587

Objective Aperture System for the Electron Microscope CECIL E. HALL 588

In Every Issue

New Books 590

New Booklets 591

Here and There 592

Calendar of Meetings 511

Index to Advertisers xxviii

BOARD OF EDITORS

ELMER HUTCHISSON, *Editor*

Associate Editors

R. BOWLING BARNES
OTTO BEECK
W. F. BUSSE
SELIG HECHT
W. JAMES LYONS
PHILIP MORRISON
PAUL E. SABINE
FREDERICK SEITZ
J. R. TOWNSEND
JOHN VON NEUMANN

Publication of the American Institute of Physics

ADMINISTRATIVE STAFF

HENRY A. BARTON, *Director*

MARGARET S. GRIFFIN, *Publications Manager*

THEODORE VORBURGER, *Business Manager*

JOHN T. TATE, *Adviser on Publications*

GOVERNING BOARD

GEORGE R. HARRISON, *Chairman*

WALLACE WATERFALL, *Secretary*

GEORGE B. PEGRAM, *Treasurer*

E. U. CONDON
A. J. DEMPSTER
W. F. FAIR, JR.
FLOYD A. FIRESTONE
HARVEY FLETCHER
R. C. GIBBS
K. S. GIBSON
PAUL E. KLOPSTEG
A. H. PFUND
JOHN T. TATE
M. W. WHITE
A. G. WORTHING

The JOURNAL OF APPLIED PHYSICS, published monthly at Prince and Lemon Sts., Lancaster, Pa., is devoted to physics in its role as the science basic to other natural sciences and to the arts and industries. Previous to 1937 this publication was known as PHYSICS. The JOURNAL OF APPLIED PHYSICS publishes editorials, news of physicists, and reviews, as well as technical papers of applied physics.

Manuscripts should be submitted to Elmer Hutchisson, Editor, Case School of Applied Science, Cleveland 6, Ohio.

Subscriptions and orders for back numbers should be addressed to Prince and Lemon Streets, Lancaster, Pa. or to the American Institute of Physics, 57 East 55 Street, New York 22, N. Y.

Subscription Price

	U.S. AND CANADA	ELSEWHERE
To members and associate members of the American Institute of Physics	$6.00	$7.00
To all others	8.00	9.00

Back Number Prices

Complete set: Vol. 1, July, 1931–Vol. 17, 1946—$124.00

Yearly back number rate: $10.00

Single copies: $1.00 each.

Changes of address and proofs should be addressed to the Publications Manager.

Advertising rates supplied on request. Orders, advertising copy, and cuts should be sent to the American Institute of Physics.

Entered as second class matter January 22, 1937, at the Post Office at Lancaster, Pennsylvania, under the Act of March 3, 1879. Accepted for mailing at the special rate of postage provided for in the Act of February 28, 1925, authorized May 2, 1932.

Copyright 1947, by the American Institute of Physics

Journal of
Applied Physics

Volume 18, Number 6 June, 1947

Crystal Pattern Synthesis by an Approximate Summation of Fourier Series

JOSEPH S. LUKESH
Crystallographic Laboratory, Department of Geology, Massachusetts Institute of Technology, Cambridge, Massachusetts
(Received February 10, 1947)

A faithful representation of the locations of the peaks of electron density maps can be obtained rapidly by determining for each point in the projected unit cell the algebraic sum of the amplitudes of those reflections which are contributing either a maximum or a minimum at each point. Since maxima and minima do not, in general, fall at the specific points of the grid, an approximation must be introduced. Using the semi-polar form of Fourier series, the approximate summation can be accomplished with the use of one hundred and fifty strips. The method was tested by determining the peak locations in the structure of diopside projected on 001. Potential applications of the approximate summation include rapid checking of the validity of assumed crystal structures.

INTRODUCTION

CRYSTAL patterns can be synthesized conveniently by determining the projected electron density through the summation of a Fourier series of the following general type:

$$\rho(x, y) = (1/A)\sum_h \sum_k F_{(hk0)} \cos(2\pi/N)(hx+ky), \quad (1)$$

which gives the projection normal to the c axis. Other axes are treated by appropriate choice of the indices, h, k, or l. Equation (1) is valid only when the projection is centrosymmetrical. The non-centrosymmetrical case will not be considered here; however, it can be treated in a similar manner by applying the same reasoning to the sine terms. The form of the contribution of a given reflection, $hk0$, to the total electron density is invariant, regardless of the actual crystal structure. It consists of a sinusoidal alternation of positive and negative density. Actually it is a cosine surface whose periodicity in each axial direction is given by the appropriate index. The different distributions of electron density in different crystals arise from varying amplitudes of the cosine surfaces and from different arrays of contributing reflections. Obviously, in order that an accumulation of electron density occur at any point in the projected unit cell, the sum of the positive solutions of the terms of Eq. (1) must be greater than the sum of the negative solutions. In order that a high peak occur, not only must a large number of reflections give positive solutions, but also they must be near their maxima. Similarly, in order that there be little or no accumulation of electron density, either most reflections are contributing very little, or those near their maxima are compensated for by others near their minima. This suggests that if one were to list for each point in the unit cell the amplitudes of all reflections that are contributing a maximum and all that are near a minimum, one might obtain a faithful representation of the electron density distribution merely by subtracting the negative terms from the positive. If this hypothesis is valid, the labor of computation is reduced to the listing and totalling of the appropriate amplitudes. Of course, detail will be lost in the regions

of low electron density, but these regions are unimportant in at least the early stages of crystal structure analysis. In many cases, location of the strongest peaks will be of material aid in the solution of a crystal structure.

THEORY

In an earlier paper the writer[1] developed a semi-polar form of the series of Eq. (1). This concept, while not essential to the approximate method to be discussed, offers a number of advantages in computational simplicity and will be followed in this report. If the point, x, y, is specified by the coordinate, x, and the slope, c, of the line from the origin to the point, Eq. (1) may be written:

$$\rho(x, c) = (1/A)\sum_h \sum_k F_{(hk0)} \cos(2\pi/N)x(h+ck). \quad (2)$$

The half-unit cell for which the summation is to be made is divided into four segments, and the form of the cosine term varies for each. For a given plane and a given radial line, Eq. (2) reduces to

$$\rho(x, c) = (1/A)\sum_h \sum_k F_{(hk0)} \cos(2\pi/N)Cx, \quad (3)$$

where C is a constant and x is an integer. In the article cited[1] it was pointed out that the conventional rectilinear grid is inconvenient, since the slopes of the lines from the origin to the various points are not suited for easy calculation. Furthermore, only a few points occur along any one line. For these reasons, a semi-polar grid was described in which the points at which Eq. (3) is to be evaluated are defined by the intersections of radial lines and either the x or y coordinates. If the axes are divided into thirty points (a sufficient number since the projection is only an approximation), the number, N, in Eq. (3) is thirty. For this spacing of points, it is convenient to choose radii whose slopes are .1, .2, .3, etc., and the constant, C, can be determined from the indices of a plane merely by inspection. Thus, for the reflection, 320, the constant along the radius whose slope is .4 is equal to 3 plus .4(2), or 3.8.

If Eq. (3) is plotted as a function of x for a given amplitude, F, and a given constant, C, a cosine curve results. This is the form of the density contribution of a reflection, $hk0$, along a radial line of slope, c. The amplitude is determined by F and the periodicity by C. It is obvious that maxima and minima occur at various points along the radius. Since the positions of the maxima and minima depend only on the indices of the reflection and on the slope of the radius, they can be determined in advance and tabulated for use in all structure determinations. Because, as was pointed out in the article previously cited,[1] there are only one hundred and fifty independent values of C for the grid chosen, the table will not be extensive.

In general, the maxima and minima will not occur at integral values of the coordinate, x. This necessitates the introduction of an approximation, since it is at the integral values of x that the summation is being made. For the purposes of this report, it has been assumed, quite arbitrarily, that a plane contributes to the electron density only at those points where its amplitude times the appropriate value of the cosine is fifty or more percent of the maximum. Similarly, a plane subtracts from the density only when the product is fifty or more percent of the minimum. In other words, a reflection is assumed to be ineffectual when the product of its amplitude times the cosine is between zero and either plus or minus one-half of F. Furthermore, it is assumed that a plane contributes or subtracts the entire value of F when it is effective. This latter assumption eliminates all calculation, and the summation consists of tabulation of the amplitudes of the effective planes at each point and their summation.

EXAMPLE OF THE APPROXIMATION

In order to test the hypothesis developed above, computations have been made of the electron density of diopside projected on (001). Data for the amplitudes of the various reflections and a map of the conventional summation have been reported by Bragg.[2] Because of the high symmetry of diopside in this projection, only one-eighth of the cell need be considered. However, in order to test the approximation, computations were made for one-quarter of the cell.

[1] Joseph S. Lukesh, J. App. Phys. **18**, 321 (1947).

[2] W. L. Bragg, Zeits. f. Krist. **70**, 475 (1929).

TABLE I. Coordinates, x, for which the function: $\cos(\pi/15)Cx$ has maxima and minima.

C	Maxima	Minima	C
0.0	0–15	None	30.0
0.1	0–15	None	29.9
0.2	0–15	None	29.8
0.3	0–15	None	29.7
0.4	0–12	None	29.6
0.5	0–10	None	29.5
0.6	0–8	None	29.4
0.7	0–7	15	29.3
0.8	0–6	13–15	29.2
0.9	0–5	12–15	29.1
1.0	0–5	10–15	29.0
1.1	0–4	10–15	28.9
1.2	0–4	9–15	28.8
1.3	0–3	8–15	28.7
1.4	0–3	8–14	28.6
1.5	0–3	7–13	28.5
1.6	0–3	7–12	28.4
1.7	0–2, 15	6–11	28.3
1.8	0–2, 14, 15	6–11	28.2
1.9	0–2, 14, 15	6–10	28.1
2.0	0–2, 13–15	5–10	28.0
2.1	0–2, 12–15	5–9	27.9
2.2	0–2, 12–15	5–9	27.8
2.3	0–2, 11–15	5–8	27.7
2.4	0–2, 11–14	5–8	27.6
2.5	0–2, 10–14	4–8	27.5
2.6	0, 1, 10–13	4–7	27.4
2.7	0, 1, 10–12	4–7, 15	27.3
2.8	0, 1, 9–12	4–7, 15	27.2
2.9	0, 1, 9–12	4–6, 14, 15	27.1
3.0	0, 1, 9–11	4–6, 14, 15	27.0
3.1	0, 1, 9–11	4–6, 13–15	26.9
3.2	0, 1, 8–10	4–6, 13–15	26.8
3.3	0, 1, 8–10	4–6, 13–15	26.7
3.4	0, 1, 8–10	3–5, 12–14	26.6
3.5	0, 1, 8–10	3–5, 12–14	26.5
3.6	0, 1, 7–9	3–5, 12, 13	26.4
3.7	0, 1, 7–9, 15	3–5, 11–13	26.3
3.8	0, 1, 7–9, 15	3–5, 11–13	26.2
3.9	0, 1, 7, 8, 15	3–5, 11, 12	26.1
4.0	0, 1, 7, 8, 14, 15	3–5, 10–12	26.0
4.1	0, 1, 7, 8, 14, 15	3, 4, 10–12	25.9
4.2	0, 1, 6–8, 14, 15	3, 4, 10, 11	25.8
4.3	0, 1, 6–8, 13–15	3, 4, 10, 11	25.7
4.4	0, 1, 6, 7, 13, 14	3, 4, 10, 11	25.6
4.5	0, 1, 6, 7, 13, 14	3, 4, 9–11	25.5
4.6	0, 1, 6, 7, 12–14	3, 4, 9, 10	25.4
4.7	0, 1, 6, 7, 12, 13	3, 4, 9, 10, 15	25.3
4.8	0, 1, 6, 7, 12, 13	3, 4, 9, 10, 15	25.2
4.9	0, 1, 6, 7, 12, 13	3, 4, 9, 10, 15	25.1
5.0	0, 1, 5–7, 11–13	2–4, 8–10, 14, 15	25.0
5.1	0, 5, 6, 11, 12	2, 3, 8, 9, 14, 15	25.9
5.2	0, 5, 6, 11, 12	2, 3, 8, 9, 14, 15	24.8
5.3	0, 5, 6, 11, 12	2, 3, 8, 9, 14, 15	24.7
5.4	0, 5, 6, 11, 12	2, 3, 8, 9, 13, 14	24.6
5.5	0, 5, 6, 10, 11	2, 3, 8, 9, 13, 14	24.5
5.6	0, 5, 6, 10, 11	2, 3, 8, 13, 14	24.4
5.7	0, 5, 6, 10, 11, 15	2, 3, 8, 13, 14	24.3
5.8	0, 5, 6, 10, 11, 15	2, 3, 7, 8, 13	24.2
5.9	0, 5, 10, 11, 15	2, 3, 7, 8, 12, 13	24.1
6.0	0, 5, 10, 15	2, 3, 7, 8, 12, 13	24.0
6.1	0, 5, 10, 14, 15	2, 3, 7, 8, 12, 13	23.9
6.2	0, 5, 9, 10, 14, 15	2, 3, 7, 8, 12	23.8
6.3	0, 4, 5, 9, 10, 14, 15	2, 3, 7, 12	23.7
6.4	0, 4, 5, 9, 10, 14	2, 3, 7, 11, 12	23.6
6.5	0, 4, 5, 9, 10, 14	2, 3, 7, 11, 12	23.5
6.6	0, 4, 5, 9, 13, 14	2, 3, 7, 11, 12	23.4
6.7	0, 4, 5, 9, 13, 14	2, 6, 7, 11, 15	23.3
6.8	0, 4, 5, 9, 13	2, 6, 7, 11, 15	23.2
6.9	0, 4, 5, 8, 9, 13	2, 6, 7, 11, 15	23.1
7.0	0, 4, 5, 8, 9, 13	2, 6, 7, 10, 11, 15	23.0
7.1	0, 4, 8, 9, 12, 13	2, 6, 7, 10, 11, 15	22.9
7.2	0, 4, 8, 9, 12, 13	2, 6, 10, 11, 14, 15	22.8
7.3	0, 4, 8, 12, 13	2, 6, 10, 14, 15	22.7
7.4	0, 4, 8, 12	2, 6, 10, 14	22.6
7.5	0, 4, 8, 12	2, 6, 10, 14	22.5
7.6	0, 4, 8, 12	2, 6, 10, 14	22.4
7.7	0, 4, 8, 12, 15	2, 6, 10, 13, 14	22.3
7.8	0, 4, 8, 11, 12, 15	2, 6, 9, 10, 13, 14	22.2
7.9	0, 4, 7, 8, 11, 12, 15	2, 6, 9, 10, 13	22.1
8.0	0, 4, 7, 8, 11, 15	2, 5, 6, 9, 10, 13	22.0
8.1	0, 4, 7, 8, 11, 15	2, 5, 6, 9, 13	21.9
8.2	0, 4, 7, 11, 15	2, 5, 6, 9, 13	21.8
8.3	0, 4, 7, 11, 14, 15	2, 5, 6, 9, 13	21.7
8.4	0, 3, 4, 7, 11, 14	2, 5, 9, 12, 13	21.6
8.5	0, 3, 4, 7, 10, 11, 14	2, 5, 9, 12	21.5
8.6	0, 3, 4, 7, 10, 11, 14	2, 5, 9, 12	21.4
8.7	0, 3, 4, 7, 10, 14	2, 5, 9, 12, 15	21.3
8.8	0, 3, 7, 10, 14	2, 5, 8, 9, 12, 15	21.2
8.9	0, 3, 7, 10, 13, 14	2, 5, 8, 12, 15	21.1
9.0	0, 3, 7, 10, 13	2, 5, 8, 12, 15	21.0
9.1	0, 3, 7, 10, 13	2, 5, 8, 11, 12, 15	20.9
9.2	0, 3, 6, 7, 10, 13	2, 5, 8, 11, 15	20.8
9.3	0, 3, 6, 10, 13	2, 5, 8, 11, 14, 15	20.7
9.4	0, 3, 6, 10, 13	2, 5, 8, 11, 14	20.6
9.5	0, 3, 6, 9, 10, 13	2, 5, 8, 11, 14	20.5
9.6	0, 3, 6, 9, 12, 13	2, 5, 8, 11, 14	20.4
9.7	0, 3, 6, 9, 12, 15	2, 5, 8, 11, 14	20.3
9.8	0, 3, 6, 9, 12, 15	2, 5, 8, 11, 14	20.2
9.9	0, 3, 6, 9, 12, 15	2, 5, 8, 11, 14	20.1
10.0	0, 3, 6, 9, 12, 15	1, 2, 4, 5, 7, 8, 10, 11, 13, 14	20.0
10.1	0, 3, 6, 9, 12, 15	1, 4, 7, 10, 13	19.9
10.2	0, 3, 6, 9, 12, 15	1, 4, 7, 10, 13	19.8
10.3	0, 3, 6, 9, 12, 15	1, 4, 7, 10, 13	19.7
10.4	0, 3, 6, 9, 12, 14	1, 4, 7, 10, 13	19.6
10.5	0, 3, 6, 9, 11, 14	1, 4, 7, 10, 13	19.5
10.6	0, 3, 6, 11, 14	1, 4, 7, 10, 13	19.4
10.7	0, 3, 6, 8, 11, 14	1, 4, 7, 10, 13, 15	19.3
10.8	0, 3, 6, 8, 11, 14	1, 4, 7, 10, 15	19.2
10.9	0, 3, 8, 11, 14	1, 4, 7, 10, 12, 15	19.1
11.0	0, 3, 5, 8, 11, 14	1, 4, 7, 10, 12, 15	19.0
11.1	0, 3, 5, 8, 11	1, 4, 7, 12, 15	18.9
11.2	0, 3, 5, 8, 11, 13	1, 4, 7, 9, 12, 15	18.8
11.3	0, 3, 5, 8, 11, 13	1, 4, 7, 9, 12, 15	18.7
11.4	0, 3, 5, 8, 13	1, 4, 7, 9, 12	18.6
11.5	0, 3, 5, 8, 10, 13	1, 4, 9, 12, 14	18.5
11.6	0, 3, 5, 8, 10, 13	1, 4, 9, 12, 14	18.4
11.7	0, 5, 8, 10, 13, 15	1, 4, 6, 9, 14	18.3
11.8	0, 5, 8, 10, 13, 15	1, 4, 6, 9, 14	18.2
11.9	0, 5, 10, 13, 15	1, 4, 6, 9, 11, 14	18.1
12.0	0, 5, 10, 15	1, 4, 6, 9, 11, 14	18.0
12.1	0, 5, 10, 12, 15	1, 4, 6, 9, 11, 14	17.9
12.2	0, 5, 7, 10, 12, 15	1, 4, 6, 9, 11	17.8
12.3	0, 5, 7, 10, 12, 15	1, 4, 6, 11	17.7
12.4	0, 5, 7, 10, 12	1, 4, 6, 11, 13	17.6
12.5	0, 2, 5, 7, 10, 12, 14	1, 4, 6, 8, 11, 13	17.5
12.6	0, 2, 5, 7, 12, 14	1, 6, 8, 11, 13	17.4
12.7	0, 2, 5, 7, 12, 14	1, 6, 8, 11, 13, 15	17.3
12.8	0, 2, 5, 7, 9, 12, 14	1, 6, 8, 13, 15	17.2
12.9	0, 2, 5, 7, 9, 12, 14	1, 6, 8, 13, 15	17.1
13.0	0, 2, 5, 7, 9, 14	1, 6, 8, 10, 13, 15	17.0
13.1	0, 2, 7, 9, 14	1, 6, 8, 10, 15	16.9
13.2	0, 2, 7, 9, 11, 14	1, 6, 8, 10, 15	16.8
13.3	0, 2, 7, 9, 11	1, 6, 8, 10, 15	16.7
13.4	0, 2, 7, 9, 11	1, 3, 8, 10, 12	16.6
13.5	0, 2, 7, 9, 11, 13	1, 3, 8, 10, 12	16.5
13.6	0, 2, 9, 11, 13	1, 3, 8, 10, 12, 14	16.4
13.7	0, 2, 9, 11, 13, 15	1, 3, 8, 10, 12, 14	16.3
13.8	0, 2, 4, 9, 11, 13, 15	1, 3, 10, 12, 14	16.2
13.9	0, 2, 4, 11, 13, 15	1, 3, 10, 12, 14	16.1
14.0	0, 2, 4, 11, 13, 15	1, 3, 5, 10, 12, 14	16.0
14.1	0, 2, 4, 13, 15	1, 3, 5, 12, 14	15.9
14.2	0, 2, 4, 6, 13, 15	1, 3, 5, 14	15.8
14.3	0, 2, 4, 6, 15	1, 3, 5, 7	15.7
14.4	0, 2, 4, 6, 8	1, 3, 5, 7	15.6
14.5	0, 2, 4, 6, 8, 10	1, 3, 5, 7, 9	15.5
14.6	0, 2, 4, 6, 8, 10, 12	1, 3, 5, 7, 9, 11	15.4
14.7	0, 2, 4, 6, 8, 10, 12, 14	1, 3, 5, 7, 9, 11, 13, 15	15.3
14.8	0, 2, 4, 6, 8, 10, 12, 14	1, 3, 5, 7, 9, 11, 13, 15	15.2
14.9	0, 2, 4, 6, 8, 10, 12, 14	1, 3, 5, 7, 9, 11, 13, 15	15.1
15.0	0, 2, 4, 6, 8, 10, 12, 14	1, 3, 5, 7, 9, 11, 13, 15	15.0

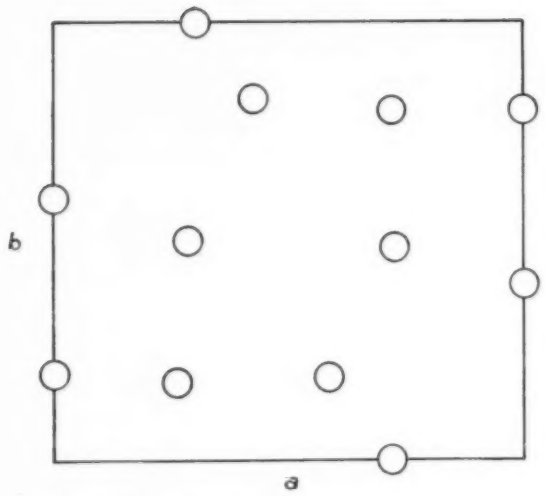

FIG. 1. Peak locations in the 001 projection of diopside determined by the approximate summation, Case I (equal amplitudes).

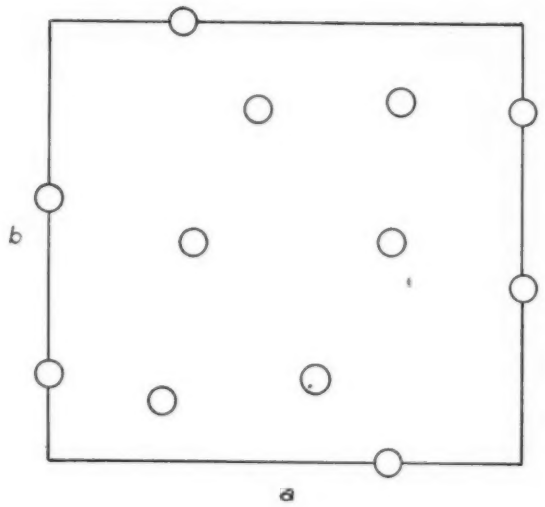

FIG. 2. Peak locations in the 001 projection of diopside determined by the approximate summation, Case II (estimated amplitudes).

Since the quarter-cell is in itself centrosymmetrical, the amount the major peaks depart from centrosymmetry will be a test of the value of the approximation. Three electron density maps have been computed. In the first, only the signs of the amplitudes have been used, all magnitudes being considered equal. In the second, estimated magnitudes have been introduced; and in the third, the actual measured values were used.

In Table I are listed the one hundred and fifty values of the constant, C, of Eq. (3) and the corresponding values of x for which maxima and minima, as defined previously, occur. To compute the summation it is only necessary to list for each radial line the amplitudes of the reflections which are maximum and minimum at each point. As a typical example, the maxima and minima of the plane 570 along the radial line whose slope, c, is .4, will be determined. The constant, C, is equal to 5 plus .4(7), or 7.8. From Table I, opposite 7.8 it is found that maxima and minima occur at the following points:

Maxima—0, 4, 8, 11, 12, 15
Minima— 2, 6, 9, 10, 13, 14

If the amplitude of the reflection, 570, is plus forty, the number forty is recorded in the columns of the worksheet corresponding to the coordinates, x, for which the contribution is a maximum. Similarly, minus forty is recorded in the columns corresponding to the minima. When the amplitude is negative, one must, of course, make appropriate sign changes.

Case I—Equal Amplitudes

This example, which represents an exploration of the possibility of determining atomic locations from knowledge of the array of reciprocal lattice points, but not their relative weights, is of little

TABLE II. F values of the reflections of the type $hk0$.*

$hk0$	F	$hk0$	F
200	0	040	0
400	15	240	16
600	100	440	−50
800	76	640	29
110	0	150	−84
310	76	350	−55
510	−63	550	0
710	41	750	−96
020	19	060	−94
220	−51	260	31
420	−23	460	0
620	−19	170	0
820	−17	370	0
130	13	570	40
330	50	080	0
530	37	280	−32

* After W. L. Bragg, Zeits. f. Krist. **70**, 475 (1929).
Note: Because of symmetry, reflections of the types $\bar{h}k0$, $h\bar{k}0$, and $\bar{h}\bar{k}0$ have the same F values as those of the type $hk0$.

practical importance, since one can always estimate the relative weights from a photographic film. It is included here because the results are rather striking.

The data used in this and succeeding cases were taken from Bragg[2] and are listed in Table II. The peaks of the "electron density" map drawn from the computations are represented in Fig. 1 by circles. (The actual map is, of course, distorted. In the interests of clarity, only the peak positions are shown.) Figure 1 should be compared with Fig. 4, which shows the peak locations taken from the conventional summation of Bragg.[2] It is important to note that the major peaks, representing heavy atoms or two or more atoms superimposed, are correctly positioned; small peaks are slightly displaced.

Case II—Estimated Amplitudes

In this example, the amplitudes listed in Table II have been assigned weights of from one to five. Those from one to twenty-five, for instance, have been given the weight of one; those from twenty-six to fifty, two, etc. This was done in an attempt to simulate amplitudes that might be calculated from intensities estimated from an x-ray film. Figure 2 shows the locations of the peaks in the summation. Improvement is noted in the positions of the smaller peaks.

Case III—Measured Amplitudes

In Fig. 3 are shown the peaks, with their relative heights indicated by contours, resulting from the approximate summation in which measured amplitudes were used. There is no appreciable change in the positions found in the previous case.

DISCUSSION

The parameters of the peaks shown in Figs. 1 through 4 are listed in Table III. In all cases, the values obtained from the approximate summations are within .02 of those from the conventional summation. (The values for the conventional summation may or may not be in agreement with the actual parameters of diopside. Those listed were measured from the electron density map in order to present a fair comparison with those derived in the same manner from the approximate summations.) On the basis of this one test, it would appear that the electron density peaks can, indeed, be located with reasonable accuracy by considering only the maximum and minimum contributions at each point in the cell. One would, however, hesitate to recommend the approximate method until independent checks have been made. The choice of diopside may have been a fortuitous one.

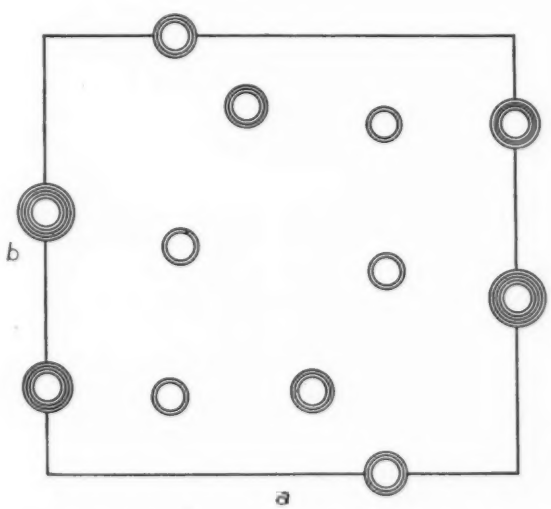

FIG. 3. Peak locations in the 001 projection of diopside determined by the approximate summation, Case III (measured amplitudes).

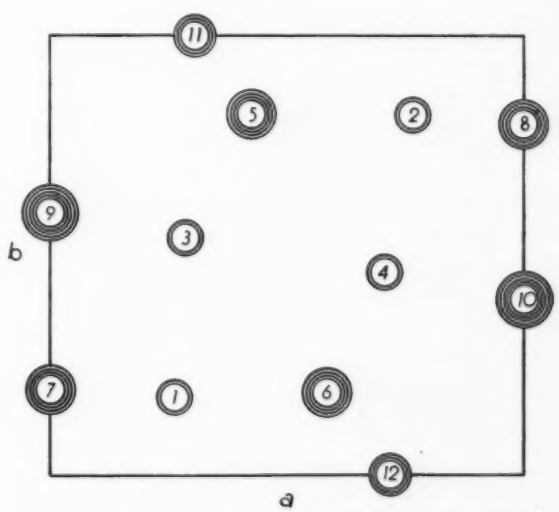

FIG. 4. Peak locations in the 001 projection of diopside determined by the conventional summation (after Bragg).

TABLE III. Parameters measured from Figs. 1 through 4.

Peak number		Case I (no amplitudes)	Case II (estimated amplitudes)	Case III (measured amplitudes)	Complete summation (after Bragg)
1	*a*	.12	.13	.13	.13
	b	.07	.09	.09	.09
2	*a*	.37	.36	.36	.38
	b	.41	.40	.40	.41
3	*a*	.15	.14	.14	.14
	b	.25	.25	.26	.27
4	*a*	.36	.36	.36	.35
	b	.25	.24	.23	.23
5	*a*	.22	.21	.21	.21
	b	.40	.41	.42	.41
6	*a*	.28	.29	.28	.29
	b	.09	.09	.09	.09
7	*a*	0	0	0	0
	b	.10	.10	.10	.10
8	*a*	.50	.50	.50	.50
	b	.40	.40	.40	.40
9	*a*	0	0	0	0
	b	.30	.30	.30	.30
10	*a*	.50	.50	.50	.50
	b	.20	.20	.20	.20
11	*a*	.14	.15	.14	.15
	b	.50	.50	.50	.50
12	*a*	.35	.35	.35	.35
	b	0	0	0	0

One of the potential uses of the approximate method is in the checking of an assumed structure. If a logical structure can be deduced from crystal chemical knowledge, the phases of the strong reflections can be computed. An approximate summation, using only those reflections, might suffice to demonstrate whether or not the assumed structure is consistent.

COMPUTATION BY MEANS OF STRIPS

Although the labor of computation is reduced in the approximate method to the addition of columns of numbers, it is still necessary to look up data in a table and to record them. This effort can be eliminated by preparing a series of strips, one for each value of the constant, C. Each strip has a space for each value of the coordinate, x, and those spaces where the function is a maximum are colored blue. Minima are indicated by red. The labor of summation involves only the selection of the strips, their arrangement on a suitable board, and the addition of the coefficients.

In checking an assumed structure, it is not necessary to perform the entire summation. Only those regions which should be high in density need be treated. Using the approximate method, the summation can be done in a very short time.

Single Crystal Electron Diffraction by Micro-Crystalline Materials*

NORMAN DAVIDSON** AND JAMES HILLIER
RCA Laboratories, Princeton, New Jersey

(Received March 11, 1947)

It is shown that the double lens probe-type electron diffraction camera described earlier is capable of producing useful electron diffraction patterns of single microscopic crystals in the size range 200–2000A; the formation of an opaque carbonaceous deposit, which occurs when an electron probe is focused on a specimen, is prevented in the diffraction camera by previously exposing the specimen chamber to an electron spray. A number of examples of two-dimensional grating patterns and Kikuchi-line patterns obtained from such crystals are shown. From either type of pattern it is possible to obtain accurate values for some of the lattice spacings, while from the Kikuchi-line patterns it is possible to deduce accurately the orientation of the crystals relative to the electron beam. The results are shown to agree reasonably well with the predictions of the dynamical theory as presented by MacGillavry. It is concluded that a two-dimensional grating pattern is to be expected from a crystal oriented with an important lattice vector approximately parallel to the electron beam independent of slight disorders or warping of the crystal. Kikuchi-line patterns are to be expected for most other crystals which are not excessively thick or disordered. The theory also shows that both types of patterns may be obtained simultaneously.

I. INTRODUCTION

THE study of the diffraction of fast electrons by single crystals has been pursued in several different ways up to date. Because of the limited penetration of the electron beam, work with macroscopic crystals which are readily manipulated and oriented is restricted either to reflection diffraction by a surface or, for transmission electron diffraction, to the relatively rare case of materials, such as mica, which can be obtained as thin sheets.

There would be many useful applications of an effective technique for obtaining single crystal electron diffraction patterns and thus determining the lattice constants of crystals of dimensions less than a micron—that is, crystals of dimensions appropriate to electron diffraction and electron microscopy. Some of these applications are:

(a) Identification of a material which has a complex powder pattern or which is present as a minor constituent of a mixture of crystals.

(b) The determination of crystal structure when single crystals of sufficient size for x-ray diffraction are not available.

(c) Further study of the fundamental phenomena of electron diffraction by crystals.

Various methods of observing the electron diffraction patterns from single micro-crystals have been reported in the literature. The observations of crystalline reflections in electron micrographs[1,2] have been used to confirm the dynamical theory of electron diffraction, to study the warping of crystals, and in general to provide information about strong reflections by properly oriented crystals. The method is limited to strong reflections.

Boersch has obtained electron diffraction patterns in which the collimated electron beam was restricted by an aperture to have a cross section of 0.005 mm at the specimen.[3] The spot patterns obtained for the various films examined were such that only one or a few crystals were responsible for the diffraction, but no correlation was possible between the morphology of the irradiated portion of the specimen and its diffraction pattern.

The same author has suggested a scheme in which a fine aperture moves in the image plane of an electron microscope.[4] When the aperture

* Presented before the American Society for X-Ray and Electron Diffraction, June 10, 1946, at Silver Bay, New York.

** Present Address: Gates and Crellin Laboratories of Chemistry, California Institute of Technology, Pasadena, California.

[1] R. D. Heidenreich and L. Sturkey, J. App. Phys. **16**, 97 (1945).

[2] J. Hillier and R. F. Baker, Phys. Rev. **61**, 722 (1942). References 1 and 2 refer to other papers on this topic.

[3] H. Boersch, Zeits. f. Physik **116**, 469 (1940).

[4] H. Boersch, Ann. d. Physik **27**, 78 (1936).

is placed on the image of a particular crystal, the angular distribution of the transmitted rays provides information about the diffraction pattern of the particular crystal. Boersch used this technique to obtain diffraction patterns of 0.08-mm portions of gold foil. This method would be difficult to develop into a practical method for true micro-crystals because of the effects of spherical aberration on the diffracted rays, and of the decrease, caused by magnification, in angular aperture of an imaging pencil.

Ardenne has suggested several schemes for modifying the electron optical system of an electron microscope so as to obtain diffraction patterns from fields 1–10 microns in diameter.[5, 6]

The purpose of the present article is to report the phenomena observed using a mode of operation of the electron diffraction camera described by Hillier and Baker[7] wherein a beam of electrons reduced to a probe of *ca.* 200A cross section, and of maximum angular aperture *ca.* 7.5×10^{-3} radian is diffracted by single micro-crystals. It is believed that this method offers a practical approach to the problem of obtaining electron diffraction patterns from single micro-crystals, and of correlating the morphology and orientation of a particular crystal with its diffraction pattern.

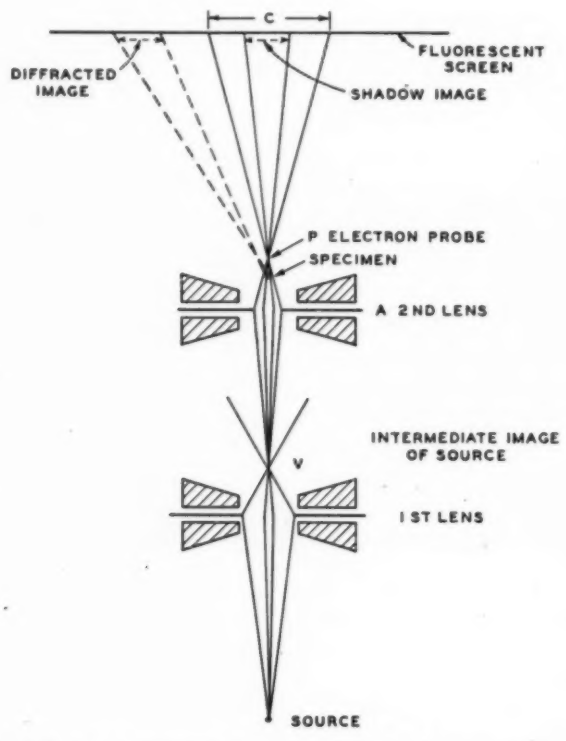

FIG. 1. Schematic diagram of lens system and ray paths in the electron diffraction camera as used for shadow microscopy and single crystal diffraction.

II. EXPERIMENTAL TECHNIQUES

The double lens system of the electron diffraction camera can be used in the two following ways (Fig. 1):

(a) Using the first lens as a strong lens to form a reduced image, V, of the electron source, and the second lens to re-focus the image on the photographic plate or fluorescent screen, a focused electron diffraction pattern is obtained of an area of specimen determined by the size of the limiting aperture, A, of the second lens.

(b) When the focal length of the second lens is reduced, the image V of the source is re-focused to an electron probe P, somewhere between A and the image screen. A bright field shadow image of the specimen is formed on the image screen within the central cone of illumination, C. The rays diffracted out of C by crystalline material in the irradiated field are the subject matter of this article.

From the point of view of obtaining a conventional powder diffraction pattern, one is producing, in this mode of operation, a "defocused" electron diffraction pattern. The degree of defocusing may be expressed by the numerical value of the angular aperture of the convergent beam of electrons passing through crystalline material in the field of irradiation. It will be seen, however, that under some circumstances it is possible to obtain precise values of interplanar spacings and lattice constants from defocused patterns.

For the sake of clarity, some of the well-known facts about the operation of a shadow microscope[8, 9] should be mentioned before describing

[5] M. von Ardenne, Zeits. f. Physik **117**, 515 (1941).
[6] M. von Ardenne, E. Schiebold and F. Gunther, Zeits. f. Physik **119**, 352 (1942).
[7] J. Hillier and R. F. Baker, J. App. Phys. **17**, 12 (1946).

[8] These factors are discussed in some detail and other references given in reference 7.
[9] V. K. Zworykin, G. A. Morton, E. G. Ramberg, J. Hillier, and A. W. Vance, *Electron Optics and the Electron Microscope* (John Wiley and Sons, New York, 1945), Chapters III and XIX.

FIG. 2. Two-dimensional grating pattern from graphite, *kho*, reproduced from Hillier and Baker, reference 7, Fig. 15 (c). The bright field shadow image of the crystal has been printed on from a negative given a shorter exposure. Note the variation of reflecting power of different areas of the crystal for different reflections.

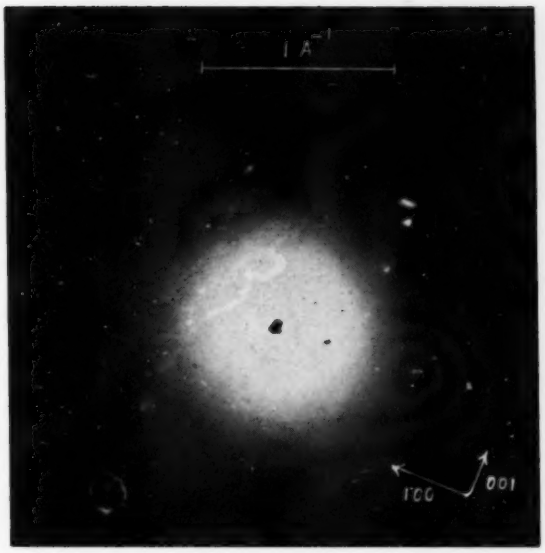

FIG. 3. Two-dimensional grating pattern, BeO (hexagonal), *hol*, $d_{100}=2.33$A, $d_{001}=4.38\pm0.02$A. (ASTM, 2.34A, 4.38A, respectively.) The bright field shadow image of the crystal has been printed on from a negative given shorter exposure. The $10\bar{4}$ reflection is relatively much brighter than for the x-ray case; the $\bar{3}01$ and $\bar{3}03$ are evident, although the calculated structure factor for these reflections is zero.

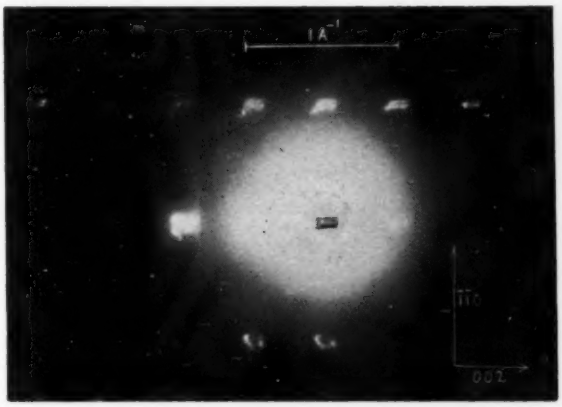

FIG. 4. BeO, *hhl*, $d_{110}=1.33_8\pm0.01$A, $d_{002}=2.20_8\pm0.01$A. (ASTM, 1.350A, 2.19A.) Note the intensity of the *hh*4 and *hh*$\bar{4}$ reflections. The central image of the crystal has been printed on from a shorter exposure.

the diffraction results. The magnification and the resolving power of a shadow microscope are dependent on the probe position with respect to specimen and electron-recording screen and the probe size. To obtain a small probe, the focal length of the lens should be as short as possible. To obtain high magnification the probe should be reasonably close to the specimen. In practice a probe of minimum cross section of *ca.* 100–200A is obtainable with lenses of 2–3 mm focal length. While no precise tests of the resolving power of the present instrument have been made, resolutions less than 1000A and probably somewhat more than 200A have been obtained with magnifications of from 4×10^3 to 10^4. With the pole piece configuration employed the focal point of the second lens for a probe of *ca.* 200A cross section was beyond the lens opening; it was, therefore, easy to mount the specimen close to the probe position. Under these conditions and with a 25-μ aperture for A, the maximum angular aperture of irradiation of the specimen was *ca.* 7.5×10^{-3} radian. The angular aperture decreases rapidly as the separation of the probe and specimen is increased, and was 10^{-3} for most of the work described below.

When the probe is focused directly on the specimen, the magnification is infinite and no specimen image is observed, but rather a projection of the limiting aperture, A, provided the specimen is partially transparent. Actually, be-

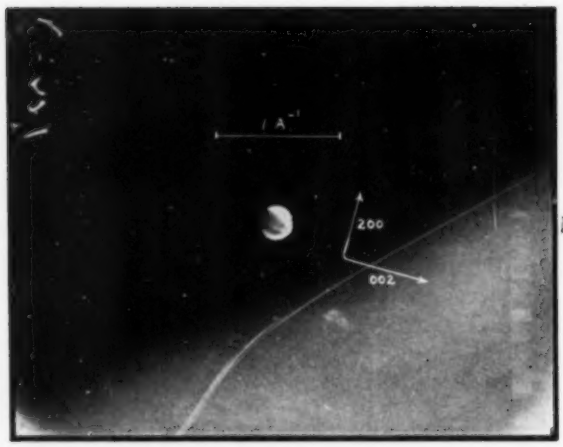

(a)

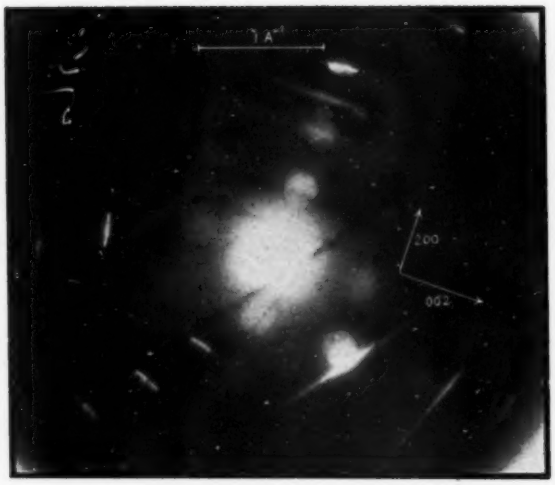

(c)

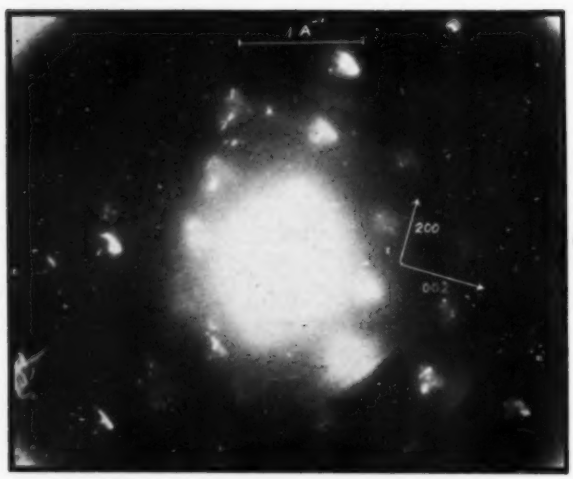

(b)

FIG. 5. Tip of $\alpha Al_2O_3 \cdot H_2O$ crystal (böhmite) (orthorhombic) $2h02l$, $d_{100}=1.86\pm0.01$A, $d_{002}=1.42\pm0.01$A. (ASTM, 1.86A, 1.43A.) (a) Short exposure showing image of crystal and one strong diffracted image, $\bar{2}02$. (b) Longer exposure showing full two-dimensional pattern and some $2h+1$, ?, $2l+1$ reflections. (c) Probe focused on specimen; each diffraction spot is an image of the defining aperture, some containing the striations discussed in the text. The Kikuchi-line pattern shows that the strongly diffracting $\bar{2}02$ plane is oriented at its Bragg angle with respect to the incident beam.

cause of asymmetries in the lens,[10] the image will first go to infinity in one direction, and then in another perpendicular to the first as the focal power is varied. Images observed at near infinite magnification were somewhat distorted because of this asymmetry.

The correlation of diffraction pattern with morphology and orientation of the crystal can be made on the basis of the electron shadow micrograph. Alternately, the shadow micrograph may be used for control purposes. With a little practice, the same crystal can be located in the field of view of a conventional magnetic electron microscope, which provides a higher resolution image of the crystal. One difficulty with the electron shadow microscope as used here is that the magnification, which varies with the exciting current of the magnetic electron lens, the position of the pole-piece material on its hysteresis loop, and the specimen-lens distance, was unknown for any particular photograph. It is estimated that most of the crystals shown here for which conventional micrographs are not shown were *ca.* 2000A–5000A in dimensions. The $\alpha Al_2O_3H_2O$ crystals are usually 5–10 microns long.

III. EXPERIMENTAL RESULTS

The diffraction results are very similar to those observed by Kossel and Möllenstedt for the diffraction of a convergent beam of electrons by thin sheets of mica.[11] The present work is an extension of their results to single crystal analyses of *arbitrary* micro-crystals.

Two principal types of diffraction patterns were observed under the experimental conditions described above: (a) two-dimensional grating patterns and (b) Kikuchi-line patterns. Figures 2–7 are illustrations of two-dimensional grating

[10] J. Hillier, J. App. Phys. **17**, 307 (1946).

[11] W. Kossel and G. Möllenstedt, Ann. d. Physik **36**, 113 (1939).

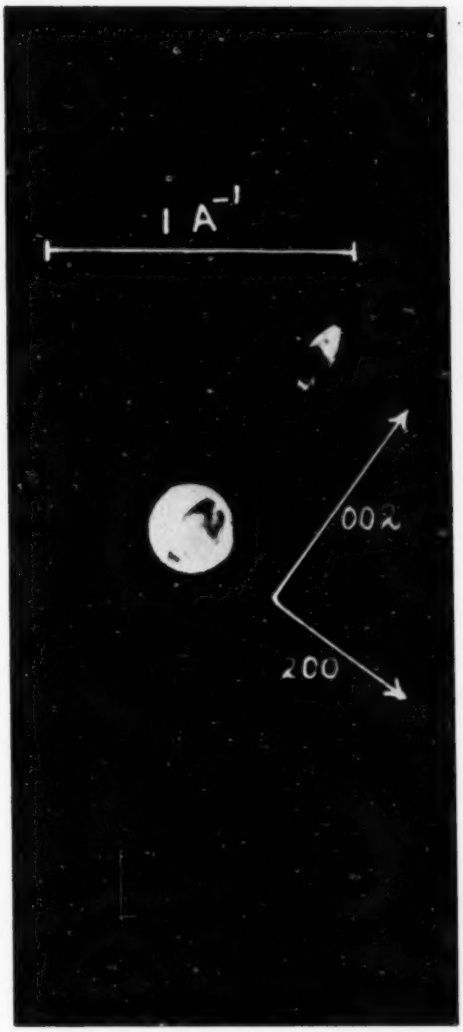

(a)

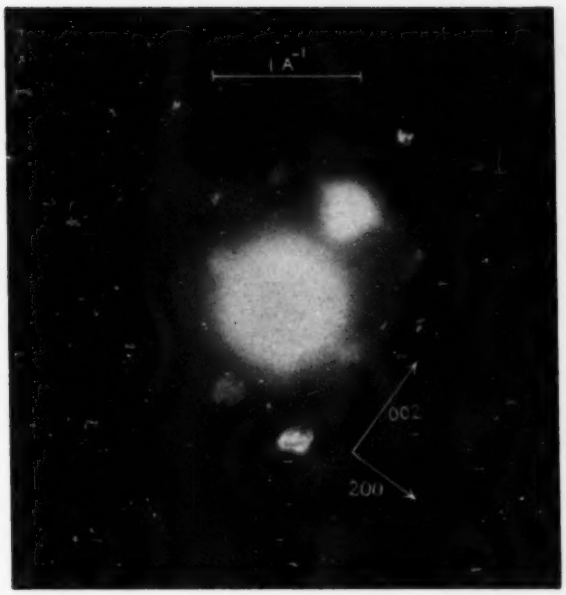

(b)

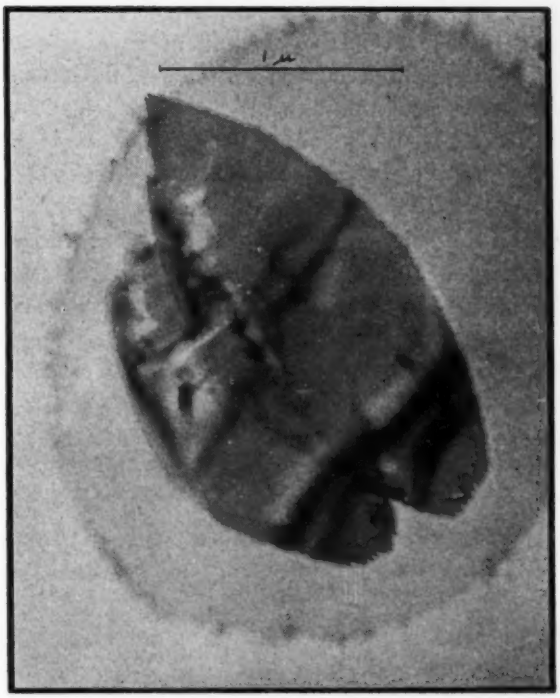

(c)

FIG. 6. Diffraction pattern from a pair of $Al_2O_3 \cdot H_2O$ crystals. In the short exposure (a), there is one strong diffracted image (002) from one of the crystals. One portion of this crystal diffracts much more strongly than the other. It is evident from the position of the Kikuchi line in the longer exposure (b) that the strongly diffracting region of the crystal makes the Bragg angle with the incident beam. A two-dimensional grating pattern is developing in (b) and became much more evident in longer exposures not shown here. Because the two crystals are not exactly parallel, the diffracted images are separated. Note the variation in reflecting power of neighboring parts of the crystal for a particular reflection, especially in the 002 and $20\bar{2}$ reflections. This was noted in the other images on longer exposure. An electron micrograph of the same pair of crystals is shown, for comparison, in (c). Because of the large field of view required to include both crystals, the shadow micrograph in (a) was not obtained with the highest usable magnification and the smallest probe size, and is not intended to illustrate the ultimate in performance of the shadow microscope.

patterns. In these cases, the probe was focused between the specimen and the electron-recording screen, so that a bright field shadow image of the crystal is formed in the central cone of illumination.

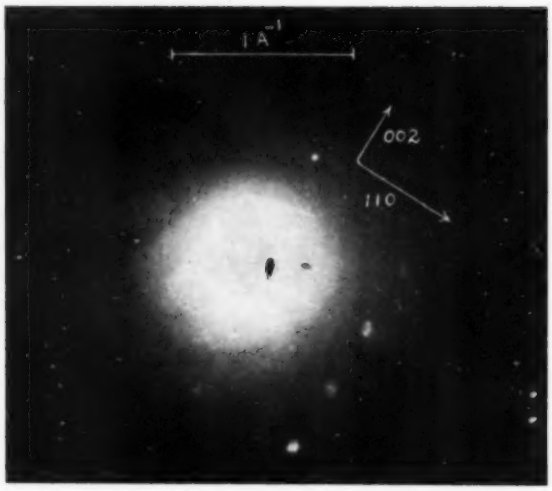

FIG. 7. ZnO (hexagonal), $hh2$, $d_{110}=1.62\pm0.01$A, $d_{002}=2.61\pm0.02$A. (ASTM, 1.61A, 2.61A.)

The field of view was adjusted so that only one crystal was present. Through any one point of the crystal passes a pencil of rays of very small angular aperture (*ca.* 10^{-4} radian, depending on the probe size and the specimen to probe separation). If only the rays passing through one portion of the crystal were diffracted, there would be an uncertainty in the diffraction angle proportional to the dimensions of the shadow image. Actually it is frequently observed in the two-dimensional grating patterns that each diffracted spot is a dark field shadow image of the diffracting crystal. Furthermore, the distances between corresponding points of a diffracted image and the central image correspond precisely to the angles of scattering deduced from the interplanar spacings of the crystal; the azimuthal directions of scattering are those of the normals to the corresponding planes of the crystal. The two-dimensional grating patterns may be considered as being formed by linear combinations (with integer coefficients) of two vectors, $\bar{b}_{hkl}$ and $\bar{b}_{h'k'l'}$, of the reciprocal lattice of the crystal. The total deviation of any ray that is diffracted must be twice the Bragg angle for a particular reflection.

When such two-dimensional grating (cross-grating) patterns are obtained, there is an apparent breakdown of the Bragg law for the diffraction of electrons by the crystal. Although the total deviation of a ray is invariably twice the Bragg angle for a particular reflection, the beam need not be incident on a crystal at precisely the Bragg angle with respect to the reflecting plane. It is sufficient that the ray be approximately parallel to the reflecting plane.

It is evident that in order for a cross-grating pattern to be possible, two of the shorter vectors of the reciprocal lattice must be approximately perpendicular to the electron beam; an equivalent statement is that an important lattice vector must be approximately parallel to the electron beam.

The method of specimen dispersion generally used[12]—spreading a drop of an amyl acetate solution of collodion containing a fraction of a milligram of the powdered specimen between two microscope slides by sliding them against each other—favors orientation of the crystals with well developed faces parallel to the collodion film. For the crystals used, this condition is equivalent to having an important lattice vector approximately parallel to the electron beam.

It should be emphasized that the intensity diffracted onto most of the spots observed in the cross-grating patterns is quite low—from 0.1 percent to 3 percent of the incident intensity. Sometimes one or two of the reflections are very strong containing practically all of the scattered intensity. The crystal is presumably oriented so that the beam makes an angle close to the Bragg angle with the plane responsible for these reflections. Figures 5 and 6 provide examples of this phenomenon.

As will be discussed in more detail later on, calculations based on the dynamical theory of electron diffraction indicate that diffracted intensities of the order of magnitude of from 0.1 percent to 3 percent are to be expected for each of a set of spots of a two-dimensional grating pattern when an electron beam is incident approximately parallel to an important lattice vector of a perfect crystal. In addition, any disorder or warping of the crystal will contribute to the development of a two-dimensional grating

[12] This technique was used in all the examples cited in this article except for the case of $\alpha Al_2O_3 \cdot H_2O$. An aqueous suspension of this material dries down on a collodion film with most of the crystals lying flat on the film.

pattern, a factor which is probably important for most of the patterns exhibited here.

Qualitatively, it is observed that the relative intensities of the various diffraction spots of a two-dimensional grating pattern are not the same as the x-ray diffraction intensities for the given material. In particular, reflections which are very weak for the x-ray case may have a much greater relative intensity for electron diffraction. Of course, these anomalous intensities have been observed frequently before in electron diffraction patterns.[13] A reflection which would be weak or vanishing by the structure-factor criterion, but which can be formed by the vector sum of two strong reflections will have appreciable intensity because it will be formed by the process of multiple scattering. This is possible for electron diffraction because a beam need not be incident at the Bragg angle with a plane to be strongly diffracted by that plane.

The most striking examples of this phenomenon of anomalous intensities among the samples studied occurred for BeO. The $h04$ reflections of Figs. 3 and 4 are as strong as the other reflections, although the $hk4$ reflections of BeO are extremely weak in the case of x-ray diffraction.[14] The 301 and 303 reflections are weak but evident (Fig. 3) although the structure factor for these reflections is zero. The 301 reflection, for example, may be considered as resulting from the combination of 200 and 101, or 300 and 001, etc., all of which are allowed and strong. However, in Fig. 4 there are only $hh\,2l$ reflections, and no $hh\,2l+1$. In this case there is no way of combining two allowed reflections to obtain a forbidden reflection.

It should be recalled at this point that Bethe in his fundamental paper on the dynamical theory of electron diffraction[15] suggested the possibility of these "anomalous" reflections, resulting from the combination of two strong reflections.[16]

In the x-ray diffraction patterns from $\alpha Al_2O_3 \cdot H_2O$, the symmetry of the orthorhombic crystal prohibits all but the $2h\ 0\ 2l$ reflections of the $h0\,l$ series.[17] However, in longer exposures images appear in the middle of the rectangles that form the orthorhombic pattern. The lattice constants of $\alpha Al_2O_3 \cdot H_2O$ are $a = 3.72$A, $b = 12.5$A, $c = 2.83$A. Because of the large value of b, the $h1l$ reflections occur through nearly the same angle, and at approximately the same angle of incidence as the hol reflections. Therefore, the indices of the "anomalous" spots are probably $2h+1,\ 1,\ 2l+1$.

The second general class of phenomena observed are the production of Kikuchi-line patterns. In general, three requirements must be fulfilled in order for the Kikuchi-line phenomena to occur:

(a) The crystal must be sufficiently thick so that the primary process of incoherent scattering—to produce a cone of rays of much larger angular aperture than the incident cone of illumination—take place with sufficient probability to produce a general blackening of the entire photographic plate. In order that all the background scattering should contribute to the patterns, the electron probe is focused on the crystal in these experiments.

(b) The Bragg law must be satisfied for the diffraction of electrons by the crystal; that is, electrons incident upon a reflecting plane at the Bragg angle must be diffracted with much greater intensity than electrons incident at another angle.

(c) Some planes must be oriented approximately parallel to the axis of the electron beam. This requirement will usually be fulfilled because of the great number of reflecting planes in a crystal.

The distance from a "depleted" line to the corresponding "enhanced" line of a Kikuchi pattern corresponds to an angle of scattering of twice the Bragg angle. The positions of the various lines of a Kikuchi-diffraction pattern allow one to infer not only some of the interplanar spacings of the crystal, but also the precise orientation of the crystal with respect to the electron beam. Where a "depleted" line runs through the central area of irradiation, some of the rays of the incident radiation must make an angle equal to the Bragg angle with this particular plane, and the entire cone of illumination makes an angle quite close to the Bragg angle. There will then be a weak diffracted image of the defining aperture containing the strongly dif-

[13] e.g., L. H. Germer, Phys. Rev. **61**, 309 (1942).
[14] W. H. Zachariasen, Zeits. f. Physik **40**, 637 (1927), lists as the relative intensities of the 002 and 004 reflections for BeO, 2.5 and 0–0.5.
[15] H. Bethe, Ann. d. Physik **87**, 55 (1928).
[16] *Ibid.*, pp. 97–99.
[17] S. Goldstaub, Bull. Soc. Franc. Mineral. **59**, 348 (1936). See also C. Gottfried, Strukturbericht, **4**, 129 (1936).

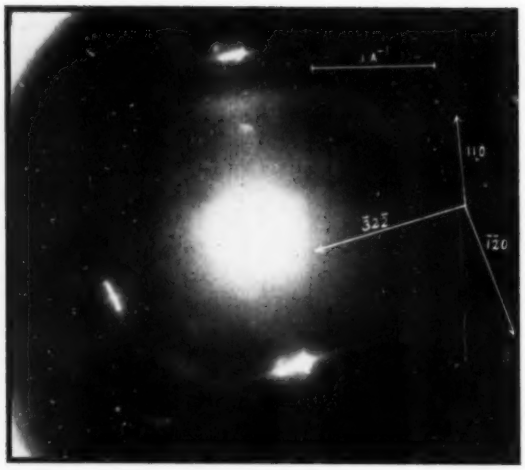

(a)

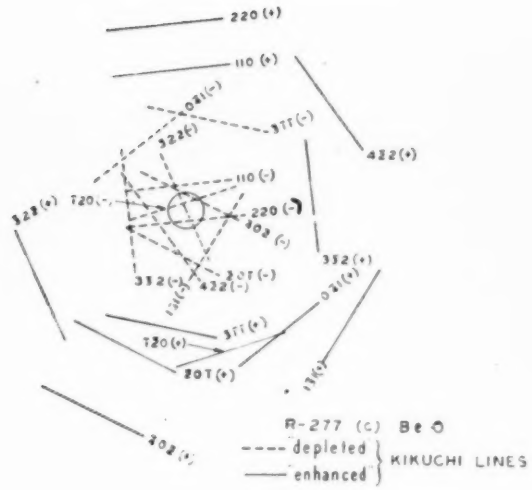

(c)

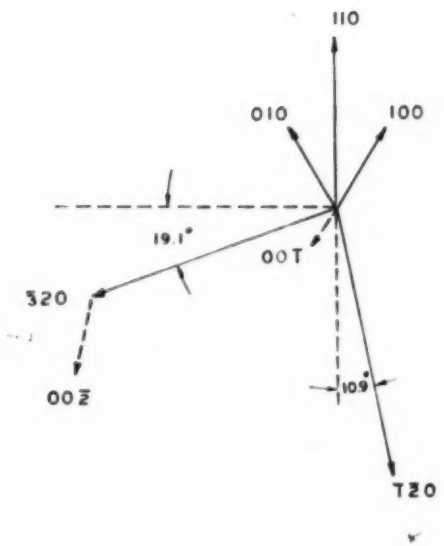

$$\bar{b}_{100} = 3.89\,\hat{x} - 2.67\,\hat{y} - 1.00\,\hat{z}$$

$$\bar{b}_{010} = 4.42\,\hat{x} + 1.82\,\hat{y} + 0.68\,\hat{z}$$

$$\bar{b}_{001} = \quad -0.90\,\hat{y} + 2.41\,\hat{z}$$

$$11.24\text{mm} = 1\,\text{A}^{-1}$$

R-277 (c) Be O

(b)

(d)

FIG. 8. (a) Kikuchi-line pattern from a BeO crystal, with diffracted images of aperture of illumination. Note that there is a 110-diffracted image and a broad 110-Kikuchi line that does not go through this image. (b) Deduced orientation of the reciprocal vectors of the BeO lattice with respect to axes in space. The electron beam is moving in the direction of the $+z$-axis. (c) Calculated Kikuchi-line pattern from the transformation equation. All the calculated lines are present in the photograph except in cases (such as $\bar{3}\ \bar{1}\ \bar{1}$ or $0\ \bar{4}\ 1$) where the + and − lines are almost symmetrically disposed with respect to the central unscattered beam. (d) An electron micrograph of the crystal responsible for this pattern. It seems likely that the crystal is oriented with the hexagonal axis perpendicular to the collodion film; because of proximity to the supporting mesh, the film is not perpendicular to the electron beam direction.

fracted beam caused by the rays that were incident at the Bragg angle. In the circular images, there may be a set of striations perpendicular to the direction from the central image to the diffracted image. (These parallel striations will be bent and otherwise perturbed when another Kikuchi line runs through them.) This

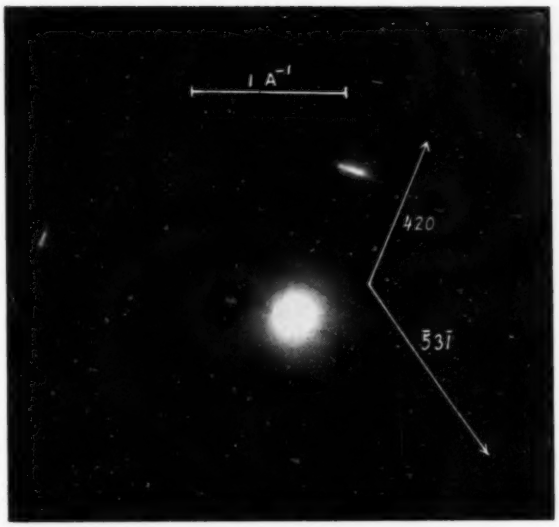

(a)

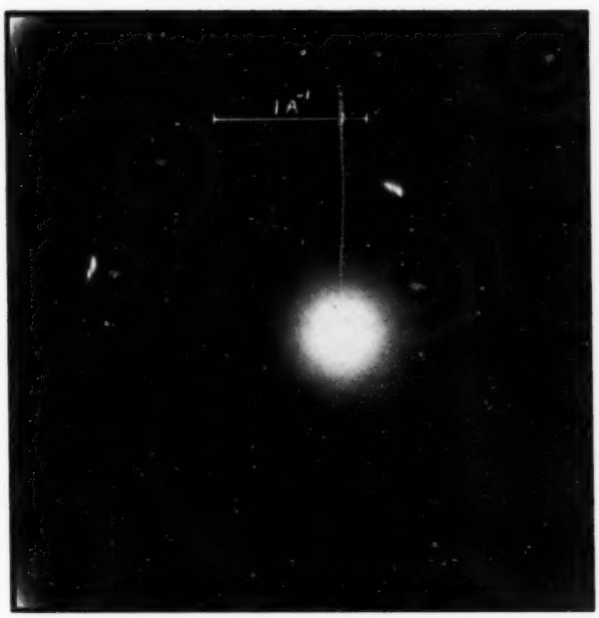

(b)

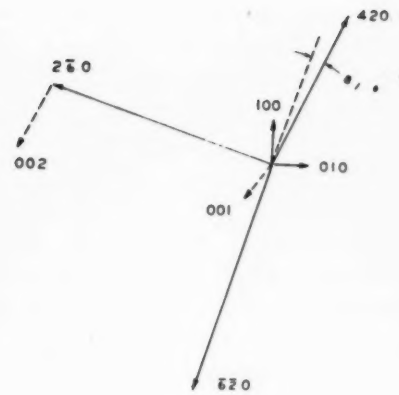

$$\hat{u}_{100} = 0.894\,\hat{x} + 0.434\,\hat{y} + 0.086\,\hat{z}$$
$$\hat{u}_{010} = 0.446\,\hat{x} - 0.865\,\hat{y} - 0.238\,\hat{z}$$
$$\hat{u}_{001} = -0.028\,\hat{x} + 0.252\,\hat{y} - 0.968\,\hat{z}$$

R-274 (c) MgO

(c)

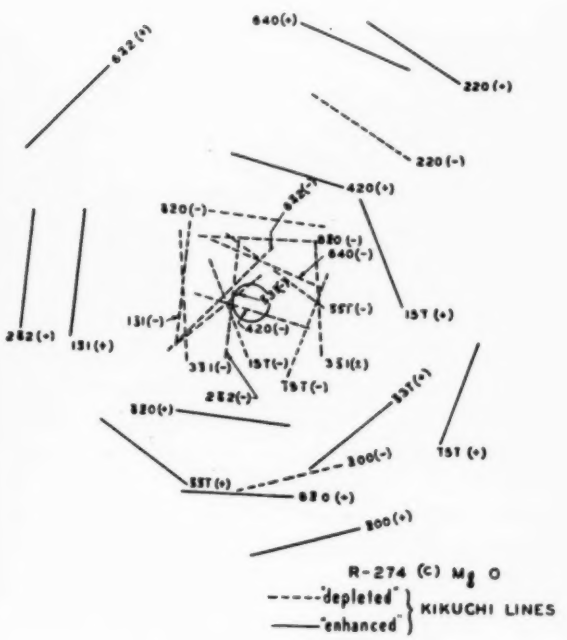

(d)

FIG. 9. (a) and (b) show the Kikuchi-line pattern from an MgO micro-crystal. The deduced orientation is exhibited in (c) and (d). In this case, the unit vectors perpendicular to the faces, rather than the reciprocal vectors, are used in the transformation equations. The specimen was prepared by dispersing MgO smoke in collodion; this procedure promoted the isolation of single MgO crystals.

Note the difference in the (420) striation patterns of (a) and (b), two different exposures, indicating a very slight change in orientation between exposures. The calculated and observed Kikuchi patterns are in agreement except that the reflections with odd indices are absent except for the case of $(\bar{5}\ 3\ \bar{1})$, where the plane is at its Bragg angle with respect to the incident beam.

phenomenon was observed for mica by Kossel and Möllenstedt, and interpreted by MacGillavry[18] in terms of the dynamical theory of electron diffraction. The spacings of these striations permit a determination of the thickness of the crystal (assuming that it is of uniform thickness in the direction of the electron beam), and

[18] C. H. MacGillavry, Physica **7**, 329 (1940).

in favorable cases, of the structure factor for the particular reflection.

Figures 8, 9 and 5c are examples of the Kikuchi lines produced when the electron probe is concentrated on a micro-crystal. Calculated patterns and the inferred orientation of the crystal are also illustrated for Figs. 8 and 9. The orientations were deduced by requiring that two of the planes whose negative Kikuchi lines run through the central cone of illumination make an angle equal to their respective Bragg angles with the z-axis (the direction of the electron beam in Figs. 8b and 9c). The predicted patterns are calculated by finding by inspection all the linear combinations (with integer coefficients) of the unit reciprocal vectors that have small negative components along the z-axis. In all cases, the measured spacings and angles between Kikuchi lines were correct within experimental errors (± 0.2–5 percent for the spacings, depending on the sharpness of line; $\pm ca.$ 1°–2° for the angles, depending on the length and sharpness of the lines).

In the early stages of the present work, when the electron probe was focused on a specimen or a membrane, a contamination "spot" formed rapidly on the irradiated area. Figure 6 (c) is a conventional electron micrograph of a pair of $Al_2O_3 \cdot H_2O$ crystals that had been exposed to an electron beam of rather large area for several minutes in the diffraction unit; the contamination spot, defining the area of irradiation, approximately 2.5 microns in diameter, is clearly visible. In practice, the area irradiated with a concentrated probe would become completely opaque to electrons after 30–60 seconds of bombardment. It was not possible, therefore, to study systematically the production of Kikuchi lines by micro-crystals until a method of preventing contamination was developed.

This difficulty in "probe" analysis was previously encountered in the electron microanalyzer.[19] The carbonaceous nature of the deposit is demonstrated in this instrument; the inelastic scattering spectra of thin films of silver or silica[20] showed no peak caused by the K-level of carbon when first exposed to a probe of *ca.* 2000A diameter. In later exposures the carbon K-line developed, and by the time the specimen was opaque only the carbon line was observed.

It has been discovered that, in the diffraction unit or in the electron microanalyzer, contamination can be avoided if the specimen chamber of the unit is exposed to an electron spray (60ma at 800v) for a few minutes before concentrating the probe on the specimen. Contamination will be entirely negligible for 10 minutes or so, and not serious for several days after this treatment. It should be mentioned that this technique is not effective in preventing contamination of electron microscope specimens. Here contamination appears to be a somewhat more complicated phenomenon.

In early stages of the work, before the method of avoiding contamination was discovered, patterns of a few spots were frequently obtained when the probe was focused behind or in front of the specimen. If the diffracted spot does not form a complete image of the crystal, and if a complete two-dimensional array is not obtained, it is difficult to interpret the pattern. One reason for this is that the particular portion of the crystal that is diffracting the beam is unknown, so that a precise measurement of the angle of scattering is not feasible. It is believed, however, that most of such crystals would give useful Kikuchi patterns which provide precise information about the inter-planar spacings and angles.

In concluding the description of the experimental work, it should be pointed out that the work to date has been confined to the study of the patterns produced by crystals of known structure. It is evident in the Kikuchi patterns of Figs. 8 and 9 that even a highly symmetrical and simple crystal can give rise to a quite complicated electron diffraction pattern. The application of the method to the identification of unknown crystals or the determination of their lattice constants, would be greatly facilitated by the development of a stage which allows precise adjustment of the orientation of the crystal with respect to the electron beam without moving it from the field of view.

IV. THEORETICAL INTERPRETATION

The spacings of the striations in the 420 reflection of MgO in Fig. 9(a) were compared with the predictions based on the dynamical

[19] J. Hillier and R. F. Baker, J. App. Phys. **15**, 671 (1944).
[20] Silica experiment by R. F. Baker.

TABLE I. Observed and calculated displacements between maxima of striations of Fig. 9a.

Maxima involved	$\bar{1}$–0	0–1	1–2	2–3	3–4	4–5
Observed displacement ($\times 10^4$)	13.0	13.4$_5$	7.3	7.8	6.9	5.9
Calculated displacement	13.1	13.1	7.9	7.4	7.0	7.0

theory of electron diffraction. The formula given by MacGillavry[18] for the angular variation of diffracted intensity is:

$$\frac{I(\Delta)}{I_0}=\frac{\sin^2\left\{\frac{1}{2}\frac{Dv_{hkl}}{K}\left(1+\frac{4\pi^2\Delta^2K^2}{d_{hkl}^2v_{hkl}^2}\right)^{\frac{1}{2}}\right\}}{1+\frac{4\pi^2\Delta^2K^2}{d_{hkl}^2v_{hkl}^2}}, \quad (1)$$

where Δ = deviation of angle of incidence from Bragg angle, in radians

$K=2\pi/\lambda$ = wave vector of electron beam,

D = thickness of crystal,

d_{hkl} = inter-planar spacing,

$$v_{hkl}=\frac{8\pi^2me}{h^2}\frac{d^2e}{\pi R}\sum_j(z_j-f_j)\exp\{2\pi i(\bar{b}_{hkl}\cdot\bar{r}_j)\}.$$

In this last relation, R is the volume of the unit cell, and $\sum_j$ the electronic structure factor for the hkl reflection. The total deviation of the rays in this treatment is always $2\theta_B$.

The formula (1) is applicable to a crystal slab of uniform thickness in the direction of the electron beam. It is assumed that only one strong reflection occurs. There are clearly two strong reflections in Fig. 9. In Fig. 9(a), the striations are sensibly parallel and perpendicular to the direction of scattering so that this pattern was chosen for analysis. It is interesting that in the next exposure (a minute or so later) (Fig. 9(b)) the 420 pattern was highly perturbed by interaction with the $2\bar{6}2$ reflection; evidently a very slight change in the orientation of the crystal took place. The next exposure showed parallel striations again. If in formula (1) we set $\Delta_l=d/D$,

$$\frac{I(\Delta)}{I_0}=\frac{\sin^2\left\{\pi\left(\frac{\Delta^2}{\Delta_l^2}+\frac{d_{hkl}^2v_{hkl}^2}{4\pi^2\Delta_l^2K^2}\right)^{\frac{1}{2}}\right\}}{1+\frac{4\pi^2\Delta^2K^2}{d_{hkl}^2v_{hkl}^2}}. \quad (2)$$

The quantity Δ_l is evidently the limiting value of the angular displacement in radians between the intensity maxima of the striations as Δ increases. Table I lists the measured values of the displacements (in radians) between maxima. Taking $\Delta_l=6.7\pm0.5\times10^{-4}$, and $\Delta_0-\Delta_1=13.2\pm0.2\times10^{-4}$, one calculates that $D=1400\pm100$A and $v_{420}=7.7\pm2.0\times10^{15}$ cm^{-2}. The value calculated from the definition of v_{hkl} is 7.85×10^{15} cm^{-2}. Using this value and the value 1400A for the thickness of the crystal, the calculated displacements between maxima of Table I are obtained. Evidently the greatest distance is between the central maximum and the next one; all the other distances are rather close to the limiting value. For a strong reflection the method provides a reasonably accurate determination of the structure factor for a reflection; for a weak reflection the percentage accuracy would be very low.

In the particular example cited here, no electron micrograph was obtained to substantiate the assumption of uniform thickness of the crystal. The agreement of the results with theory, however, supports this assumption.

We may now consider why in some cases cross-grating patterns, in which the Bragg law of incidence is apparently not obeyed, were observed and in other cases, Kikuchi-line patterns, which depend on those electrons incident at or very close to the Bragg angle being much more strongly diffracted than those incident at other angles. We first note that there is no logical contradiction between the occurrence of a strong reflection of rays incident at the Bragg angle, and weak reflections of rays incident at other angles for a particular crystal. Figure 5 is an example of a two-dimensional grating pattern and a Kikuchi-line pattern obtained from the same böhmite crystal; from the pattern of Fig. 8 for BeO we see that there is a 110 reflection of the entire aperture of illumination and displaced from that a broad Kikuchi line because of electrons inelastically scattered onto a direction making the Bragg angle with the 110 plane.

It is beyond the scope of the present paper to attempt to assess exactly the effect of disorder in a crystal on its diffraction pattern. In general the effect of such disorder will be to increase the intensity of diffraction of rays not incident at the Bragg angle.

TABLE II. "Rocking crystal" curve for MgO, 200 reflection.

Δ	0	10^{-3}	$\frac{5}{\times 10^{-3}}$	10^{-2}	$\frac{1.285}{\times 10^{-2}}$	$\frac{5}{\times 10^{-2}}$
I/I_0	1/2	0.485	0.29	0.127	0.085	0.068
D_0 (period of $\sin^2$ term, A)	360	354	274	254	181	149

The dynamic theory of electron diffraction, however, does indicate that even for perfect crystals the kinds of diffraction pattern reported in this paper are to be expected. MacGillavry's formula (1) for the intensity of a reflection gives for the half-width of incidence of a reflection (neglecting the $\sin^2$ term)

$$\Delta_{\frac{1}{2}} \sim v_{hkl} d_{hkl},$$

$$\Delta_{\frac{1}{2}} \sim (\textstyle\sum_j)_{hkl} d_{hkl}{}^3,$$

so that wide angle reflections give the best Kikuchi lines, whereas the inner reflections give broad Kikuchi lines and readily contribute to cross-grating patterns. This relation is evident in the 110 and 220 Kikuchi lines of BeO in Fig. 8.

As an example of the intensity of diffraction for angles of incidence that are considerably different from the Bragg angle, it is of interest to apply MacGillavry's formula to calculate a "rocking curve" for the 200 reflection of MgO, using $\lambda = 5.4 \times 10^{-10}$ cm. In this calculation (Table II), the average value of the $\sin^2$ term is taken as $\frac{1}{2}$.

Even at normal incidence ($\Delta = \theta_B$) the diffracted intensity is great enough to give noticeable reflection. One similarly computes for the intensities of the 220 and 400 reflections at $\Delta = \theta_{220}$ and $\Delta = \theta_{400}$ the values 0.011 and 0.0013, respectively.

Miss MacGillavry's formula (1) considers only the interaction between one diffracted ray and the incident ray, the treatment of the general case of the interaction of all the diffracted rays being very complicated. It is of interest, however, to present calculations for the symmetrical case of normal incidence on a cube face of MgO considering the interaction of all four of the 200 reflections and all four of the 220 reflections. This is a simple computation and serves to indicate if formula (1) is seriously wrong or if it gives results of the same order of magnitude as those obtained by more elaborate calculations. Only an outline of the methods of calculation and the results need be presented.[21]

Bethe's dynamical equations for this case are:

$$(K^2 - k_{000}{}^2)\psi_{000} + 4v_{200}\psi_{200} + 4v_{220}\psi_{220} = 0,$$

$$v_{200}\psi_{000} + \left(K^2 - k_{000}{}^2 - \frac{4\pi^2}{d_{200}{}^2} + v_{400} + 2v_{220}\right)\psi_{200} + (2v_{200} + 2v_{420})\psi_{220} = 0,$$

$$v_{220}\psi_{000} + (2v_{200} + 2v_{420})\psi_{200} + \left(K^2 - k_{000}{}^2 - \frac{4\pi}{d_{220}{}^2} + 2v_{400} + v_{440}\right)\psi_{220} = 0.$$

In these relations, k_{000} is the magnitude of the wave vector of the undiffracted wave in the crystal; its three possible values are determined by equating the determinant of the linear equations to zero. The ψ's are the amplitudes of the various waves in the crystal. With numerical coefficients inserted, the cubic characteristic equation is solved, and the relative amplitudes of the internal waves determined for each solution. The customary boundary conditions for the Laue case lead to the intensity formulae: (D in Angstrom units)

$$I_{000} = 1 - 0.904 \sin^2(\pi D/146) - 0.032 \sin^2(\pi D/125) - 0.060 \sin^2(\pi D/67.4),$$

$$I_{200} = 0.192 \sin^2(\pi D/146) + 0.0088 \sin^2(\pi D/125) - 0.0083 \sin^2(\pi D/67.4),$$

$$I_{220} = 0.037 \sin^2(\pi D/146) - 0.0077 \sin^2(\pi D/125) + 0.0098 \sin^2(\pi D/67.4).$$

The average value for the intensity of the diffracted waves is $\bar{I}_{200} \cong 0.10$, $\bar{I}_{220} \cong 0.02$.

The precise numerical values obtained are of no great significance because of the very special case treated; what is important is that these values are of the same order of magnitude as those obtained from formula (1) so that this formula may be used to indicate reliably the extent of a cross-grating pattern for a perfect crystal.

An outstanding deficiency of the dynamic theory as presented is that it neglects the effect of incoherent scattering on the propagation of a

[21] See references 15 and 18 for a complete discussion.

wave system in a crystal. The energy of the electron beam in the crystal is pictured as oscillating back and forth between the incident and the diffracted beams without damping. The effect of incoherent scattering will be to increase the general background, to tend to destroy the diffracted rays—particularly for rays not incident at the Bragg angle,—and to cause the development of Kikuchi lines.

V. CONCLUSIONS

One can conclude then that two-dimensional grating patterns are to be expected for crystals oriented with an important lattice vector approximately parallel to the electron beam, provided the crystals are not too thick and independent of whether or not the crystals are slightly disordered or warped. Kikuchi-line patterns are to be expected for most other crystals that are not excessively thick or disordered; the wide angle reflections will give the sharpest and best Kikuchi lines. Because of the shape of the "rocking crystal" reflection curves, crystals which give rise to two-dimensional grating patterns may also give rise to Kikuchi-line patterns.

ACKNOWLEDGMENTS

The authors wish to thank E. G. Ramberg for reading the manuscript and checking some of the calculations.

Calendar of Meetings

June

1–6 American Society of X-Ray Technicians, Buffalo, New York
1–6 Society of Automotive Engineers, French Lick, Indiana
8–10 American Society of Refrigerating Engineers, Los Angeles, California
9–14 Symposium on Molecular Structure and Microscopy, Ohio State University, Columbus, Ohio
12–14 Canadian Association of Professional Physicists, University of Western Ontario, London, Ontario, Canada
12–14 National Organic Chemistry Symposium, Boston, Massachusetts
16–19 American Society of Mechanical Engineers, Chicago, Illinois
16–20 American Society for Testing Materials, Atlantic City, New Jersey
16–20 American Association for the Advancement of Science (Pacific Division), San Diego, California
18–20 American Association of Physics Teachers, Regional Meeting, University of Minnesota, Minneapolis, Minnesota
18–21 American Society for Engineering Education, Minneapolis, Minnesota
19–21 American Physical Society, Montreal, Quebec, Canada
23–25 American Society for X-Ray and Electron Diffraction, Montreal, Quebec, Canada
23–25 American Chemical Society (Mid-West Regional Meeting), Kansas City, Missouri

July

11–12 American Physical Society, Stanford University, California
16–19 American Society of Civil Engineers, Duluth, Minnesota

August

21–23 Society of Automotive Engineers (Transportation and Maintenance Meeting), Los Angeles, California
26–29 American Institute of Electrical Engineers, San Diego, California

September

1–2 Mathematical Association of America, New Haven, Connecticut
1–4 American Society of Mechanical Engineers, Salt Lake City, Utah
8–12 Instrument Society of America, Chicago, Illinois
15–19 American Chemical Society, New York, New York
15–19 Illuminating Engineering Society, New Orleans, Louisiana
17–18 Society of Automotive Engineers, Milwaukee, Wisconsin

October

2–4 Society of Automotive Engineers, Los Angeles, California
15–18 American Society of Civil Engineers, New Orleans, Louisiana
20–24 American Society for Metals, Chicago, Illinois
21–25 American Chemical Society, San Francisco, California
23–25 Optical Society of America, Cincinnati, Ohio

Microsecond Measurement of the Phosphorescence of X-Ray Fluorescent Screens*

FITZ-HUGH MARSHALL
Westinghouse Research Laboratory, East Pittsburgh, Pennsylvania
(Received February 4, 1947)

Microsecond square-wave x-ray pulses, repeated a thousand times a second, were obtained by operating an x-ray tube directly from a radar pulser. The phosphorescent build-up and decay of light emitted by fluorescent materials when irradiated by the x-ray pulses was observed with a multiplier phototube connected to an oscilloscope. Oscillograms of $CaWO_4$ (radiographic intensifying screen) and $BaSO_4$ indicate simple exponential response, with decay to 1/*e*th intensity in 6 and 0.8 microseconds, respectively. $MgWO_4$ and Patterson B (fluoroscopic) and D (photofluorographic) screens were found to complete their main response to microsecond excitation in 10 to 100 microseconds, but their decay is not exponential.

A SUSTAINED interest in the subject of phosphorescence during the last decade has led to extensive experimental work, though rarely with x-ray excitation, and to various theoretical proposals to account for the many cases in which the observed decay does not follow a simple exponential law as would be expected for a simple monomolecular process.[1–4] Attempts have been made to interpret these more complicated cases as composites of superimposed exponential curves, as hyperbolic decay associated with a bimolecular mechanism, or as due to emission delays by electron traps. The present experiment is not sufficiently comprehensive to test the validity of these theories, for it had as its immediate purpose only the determination of the speed of response of standard types of commercial fluorescent x-ray screens. But the experimental method employed has proved so simple and effective that others may wish to develop it for a more detailed treatment, either for the study of x-ray screens as such or for a more fundamental investigation of phosphorescence. The microsecond timing technique used, instead of the more common millisecond timing, is clearly necessary to resolve rapid phosphorescence effects, which should not be disregarded in a general study. The use of x-rays, instead of the more usual ultraviolet or cathode-ray excitation, not only provides new test conditions but also simplifies absorption corrections when they are necessary, as in hyperbolic decay: in general the x-ray correction is less, can be determined accurately and easily, and does not involve taking into account a large change of intensity within individual crystals.

The equipment used in this study of the short persistence phosphorescence of x-ray fluorescent screens is illustrated in the block diagram of Fig. 1. An x-ray tube was operated directly from a radar pulser. The pulser provided microsecond square-wave potential pulses at 10 to 30 kv, repeated a thousand times a second. The x-ray tube current during the pulse was as high as 500 ma, but the corresponding average current was well within the rating of the air-cooled fluoroscopic tube used. With a water- or oil-

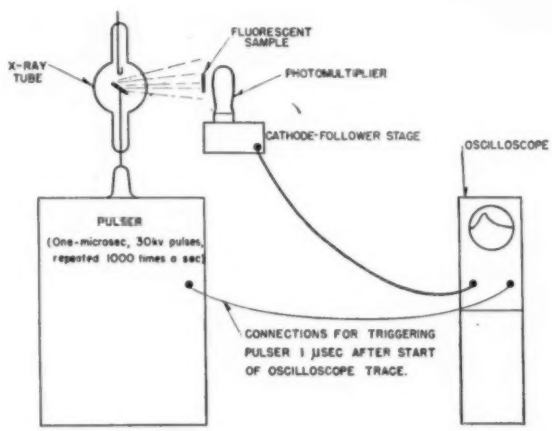

FIG. 1. Equipment for microsecond measurement of the phosphorescence of x-ray fluorescent screen materials.

* Reported at the Chicago meeting of the Am. Phys. Soc., June 22, 1946 (Phys. Rev. **70**, 114 (1946)).

[1] J. T. Randall, M. H. F. Wilkens, and G. F. J. Garlick, Proc. Roy. Soc. **A184**, 347–433 (1945).

[2] J. W. Strange and S. T. Henderson, Proc. Phys. Soc. London **58**, 369–401 (1946).

[3] R. T. Ellickson and W. L. Parker, Phys. Rev. **70**, 290–299 (1946).

[4] W. B. Nottingham, R. B. Nelson, and R. P. Johnson, J. App. Phys. **10**, 335–342 (1939).

cooled tube, much larger currents could have been obtained if needed, though probably with some reduction in the filament life because of operation at abnormally high temperatures. The x-rays irradiated the fluorescent sample, which for simplicity was taped directly against the R.C.A. multiplier phototube used to measure the light emitted, the phototube then being wrapped in black paper to exclude room light. The distance from the x-ray target to the fluorescent sample was about 15 cm. Stray high-frequency pickup from the pulser was practically eliminated by (1) covering the phototube with a grounded hood of aluminum foil to complete the system of standard grounded circuit shields, (2) introducing a cathode-follower stage mounted in pre-amplifier position directly under the phototube, and (3) grounding various extra points of the equipment for optimum results as determined by trial and error. The phototube and cathode-follower stage were mounted on top of the pulser along with the x-ray tube and its filament isolation transformer. The multiplier phototube was operated at about 90 v per stage from a d.c. supply, which was well filtered and well regulated.

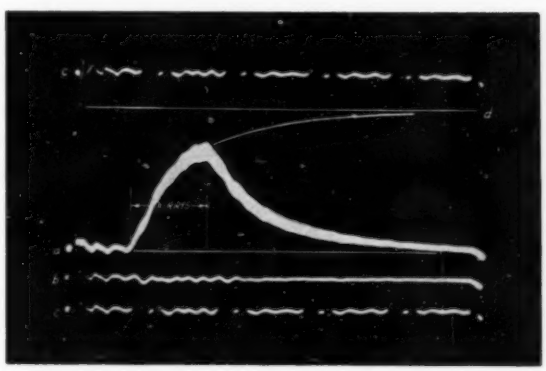

FIG. 2. Oscillogram of the growth and decay of the phosphorescent response of barium sulphate. The total time of the trace is 5 microseconds.

The cathode-follower stage was connected directly to the amplifier input of a DuMont 248 oscilloscope, no additional amplification being required. This oscilloscope, which has a number of special auxiliary circuit features, was used as a synchroscope to trigger the pulser a microsecond after the beginning of the rapid sweep of the cathode-ray beam. The sweep time could be varied and accurate time-marker intervals superimposed on the trace. From the phototube through the oscilloscope the response of the circuit was checked to be nearly flat to about 5 megacycles per second. The response of the phototube itself is good to about 100 megacycles per second.

The phosphorescent response of the fluorescent sample during and after the microsecond of irradiation by x-rays thus registered on the oscilloscope screen and was photographed. Additional exposures on the same film were used to introduce reference traces. Figure 2 is an oscillogram obtained in this way for barium sulphate, the fastest fluorescent material studied. The time represented by the complete curve is 5 microseconds. Trace *a* is the main response curve, trace *b* is a base line recorded with x-rays off and displaced downward to prevent confusion from overlapping of the small initial irregularities caused by stray pick-up, and traces *c* are similar lines above and below upon which microsecond time markers have been introduced for accurate time measurement.

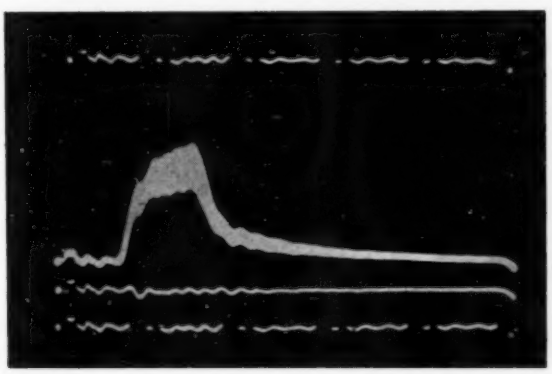

FIG. 3. Response to direct x-rays.

As will be shown, the response for barium sulphate is exponential. Following through the succession of events recorded in Fig. 2, we see that during the first microsecond there are no x-rays. Then the x-ray pulse starts, and the phosphorescent response begins to rise as the material is irradiated at constant intensity for a microsecond. During excitation active phosphorescent centers are created at a constant rate. But as the number of active centers increases,

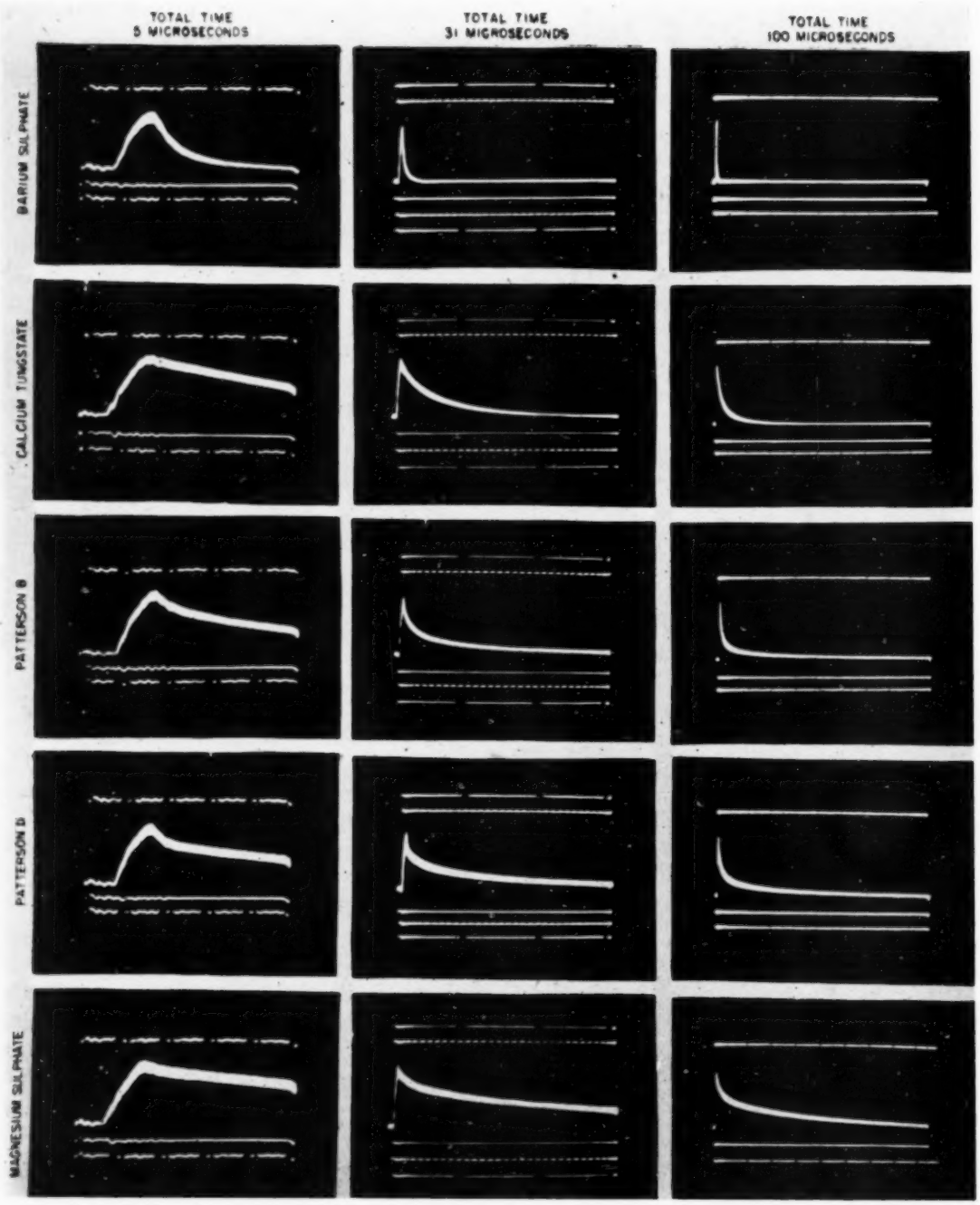

FIG. 4. Comparative oscillograms of the phosphorescent response of various fluorescent materials to a microsecond x-ray pulse.

so does the rate at which they disappear with the emission of light, this rate being always proportional to the number remaining. If the excitation were to continue indefinitely, the response would exponentially approach that equilibrium level d at which the active centers disappear as fast as they are created. But in this case the x-rays are turned off after a microsecond of irradiation, and the light intensity decays exponentially toward zero as the active

centers disappear. For barium sulphate the phosphorescent period (time for decay to $1/e$th intensity) is only 0.8 microsecond.

A direct test of the resolution and general effectiveness of the equipment is provided by Fig. 3. It so happens that the phototube responds weakly to direct x-rays with no intervening fluorescent screen. The oscillogram of Fig. 3 is for direct x-rays of extremely high intensity. The curve differs from a square wave because of the presence within the phototube of a weakly fluorescent material which phosphoresces exponentially with a period of 1.2 microseconds. When this superimposed response, similar to the one in Fig. 2, is subtracted, a reasonably square wave remains, resolved to about 0.2 microsecond.

The broadening of the main trace in all oscillograms recorded has been studied carefully and found to be due to noise of the statistical fluctuations in the number of x-ray quanta that are effective in producing phototube response.[5] The noise is exceptionally high in Fig. 3 for the following reason: although very few x-ray quanta are absorbed at the photosurface, each quantum which is absorbed produces a shower of photoelectrons.

In Fig. 4 is presented a complete set of oscillograms for the various fluorescent materials studied. The first, at the upper left, is a repetition of the 5-microsecond curve for barium sulphate shown in Fig. 2. On the 31-microsecond oscillograms, 10-microsecond time markers have been introduced in addition to the 1-microsecond markers. On the 100-microsecond oscillograms only 10-microsecond markers are included. This set of oscillograms covers the fastest and slowest materials studied and the three most commonly used types of x-ray screens. The x-ray intensity has been adjusted to bring the maximum response to approximately the same value for all curves.

The barium sulphate (which included 5 percent of lead sulphate) and the magnesium tungstate were selected from an assortment of available experimental powders which had been prepared for an unrelated purpose in another laboratory; the fluorescent intensity of each of these powders was very low in comparison with that of commercial x-ray screens. The calcium tungstate, which fluoresces blue, was a standard commercial radiographic intensifying screen; the shape of the response curve appeared to be the same for the several brands, grades, and thicknesses of screens tested, though this has not been checked by careful measurement. The Patterson B screen fluoresces with the familiar yellow-green of fluoroscopic screens, of which it is a standard example; it may be classed as a zinc-cadmium sulphide screen. The Patterson D screen, which fluoresces blue, is one which has been developed recently for photofluorography; it may be broadly classed as a zinc sulphide screen.

The simplest kind of phosphorescent response is an exponential one, the equations for the intensity, I_g during excitation or growth and I_d

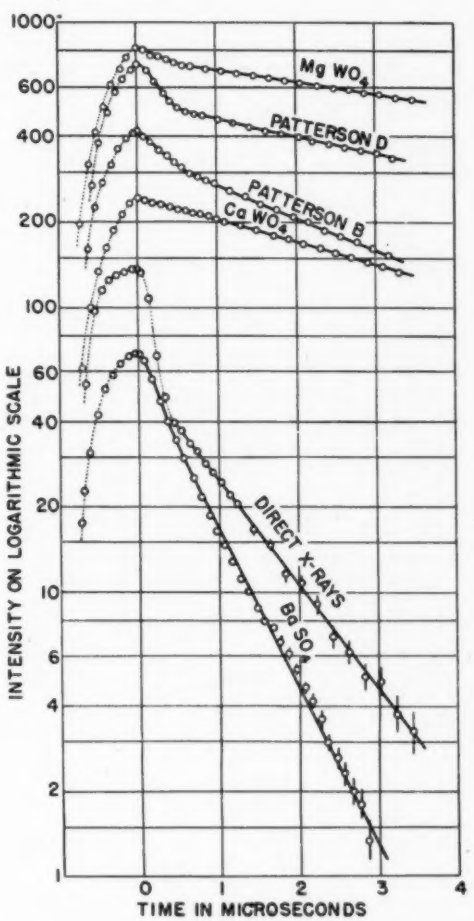

FIG. 5. Response curves plotted from measurement of 5-microsecond oscillograms.

[5] Fitz-Hugh Marshall, J. W. Coltman, and L. P. Hunter, Rev. Sci. Inst. tentatively scheduled for publication in July, 1947 issue.

during decay, being of the form

$$I_g = A(1-e^{-t/T}) \quad \text{and} \quad I_d = Be^{-t/T},$$

where t is time, T is the phosphorescent period, and A and B are constants. While there is no particular reason for expecting exponential response, it is a simple matter to check whether a response is exponential from either the growth or the decay portions of the curve. In this experiment the decay portion yielded much greater accuracy than the steep, poorly resolved growth portion.

In Figs. 5 and 6 the decay curves for the various materials studied are plotted on semi-logarithmic paper, on which a simple exponential decay would appear as a straight line. The data are taken from careful measurement of the oscillograms. Intensities have been multiplied by arbitrary factors to separate the curves conveniently. An attempt has been made to adjust the time scale so that the decay is shown starting at zero time. In Fig. 5 portions of the earlier growth curves are included as dotted lines for reference; the initial drop-off of the curve for direct x-rays is also dotted, for it represents the poorly resolved response of the circuit to the cut-off of the square wave rather than a phosphorescent decay. The spread shown for lower points on some of the curves indicates error due to uncertainty in measurement of small ordinates on the oscillograms; the deviation shown is about a thirtieth of the width of the recorded trace. Somewhat larger errors may very well be present from non-linearity in registration of the cathode ray tube.

Within the limits of experimental error, the response appears to be exponential for calcium tungstate, barium sulphate, and the fluorescence of the phototube under direct x-rays, the phosphorescent periods being 6, 0.8, and 1.2 microseconds, respectively. The several small but clearly discernible deviations from linearity in the curves for those materials can be explained qualitatively in the following way. A slight bend for barium sulphate during the first microsecond of decay is attributable to a small component of direct x-ray action on the phototube. A bend in the calcium tungstate curve at 5 microseconds must be ascribed to an overswing in the amplifying circuit, for at the corresponding time a dip through a minimum is clearly observed on the 31- and 100-microsecond oscillograms for barium sulphate and also on the oscillograms in Fig. 7. As for the deviation of the points from a straight line at the lower end of the calcium tungstate curve, other experiments[1,4] indicate that calcium tungstate is so rapid in its decay that it would be uncalled for to suspect a progressive upswing in the curve on the basis of these few points of large experimental error; however, Strange has reported two approximately exponential cathodoluminescent periods for calcium tungstate.[2]

A detailed analysis has not been attempted for the magnesium tungstate and sulphide screens. Their decays are obviously not exponential. The comparatively sharp bends near the start of these curves are evidently real, and they suggest the presence of superimposed decay curves. The later portions of these curves fit simple hyperbolic decay a little better than exponential decay, but the difference is not considered significant in the absence of additional supporting evidence and a more complete knowledge of the composition of the commercial screens involved. No change in the shape of the curves was noticed on the oscilloscope with variation of x-ray potential or intensity, as might be expected for hyperbolic decay. If a more detailed experiment is undertaken by others, this point should be checked more carefully, along with temperature dependence. Other studies which might be of interest include the response as a function of wave-length

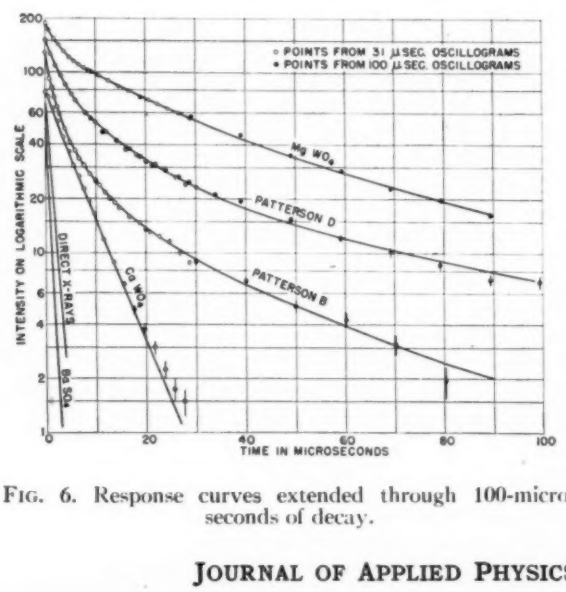

FIG. 6. Response curves extended through 100-microseconds of decay.

of light emitted by the screen and the effect of infra-red stimulation of the screen.[3]

In interpreting the oscillograms and curves in this paper, it is important to note that the unusual technique of microsecond excitation has altered the shape of all curves which are not simple exponential responses in such a way as to accentuate rapid phosphorescence effects and to suppress slow persistence effects. Thus the results may not immediately appear to be consistent with observations made under more conventional conditions. This was forcibly brought out during the experiment by an attempt to observe the phosphorescence of willemite, a screen with a persistence comparable to the flicker time of the eye. Although the willemite could be seen to glow brightly when irradiated with x-rays, an oscillogram obtained according to the normal procedure of this experiment (i.e., one made with x-ray intensity adjusted to bring the peak response to the usual amplitude) revealed only the response of the phototube to direct x-rays and was indistinguishable from an oscillogram for direct x-rays without the intervening willemite. A difference was finally obtained, as illustrated in Fig. 7, by greatly increasing the x-ray intensity (and the amplification), past the point of overloading the amplifier at the peak. In the second part of Fig. 7, the main evidence of the luminescence of the willemite is the broadening of the curve by the high noise level of the light, which is intense but which does not decrease appreciably during the short interval between pulses.

Let us assume for simplicity that the reciprocity law holds perfectly for each of the components involved in the oscillogram at the right in Fig. 7, that is, that the total area under the curve (extended to infinite time) associated with each component is independent of the time of x-ray excitation so long as the total quantity of x-rays remains unchanged. It is evident that if the same quantity of x-rays had been introduced during a pulse time of 10 microseconds, instead of one microsecond, the willemite portion of the response would not have been appreciably altered, but the direct x-ray portion of the response would have been spread over approximately ten times as much time and would therefore have risen only a tenth as high above the willemite response. With a pulse time of a thousandth of a second, such as might ordinarily be used for studying willemite, it is doubtful that any direct x-ray component could be detected, even with the x-ray intensity increased further to bring the peak response to the usual level.

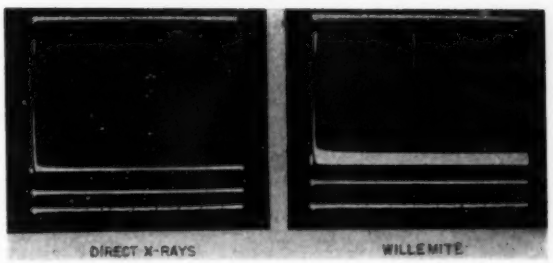

FIG. 7. Comparative 100-microsecond oscillograms for direct x-rays and willemite. The amplifier gain and the x-ray intensity have been so greatly increased as to cause overloading at the peaks.

This dependence of the shape of the response curve upon the length of time of excitation might provide the basis of a method for isolating component decays in composite curves. A pulser with variable pulse time would permit observation of the change of shape of the response curve with pulse time. A further useful innovation might be that of Strange of balancing out the main part of the response with counter exponential condenser discharge curves and measuring only the difference.[2] It should be noted that hyperbolic decay curves would behave differently from composite exponential curves, there being an actual energy shift from long-persistence effects to short-persistence effects as the pulse length is shortened.

It should be mentioned that in the present experiment all persistence after a thousandth of a second is rendered completely indistinguishable by the beginning of the next sweep cycle and the advent of a new x-ray pulse; the zero ordinate point seen at the beginning of each oscillogram trace is merely the response level at the end of the previous millisecond cycle.

Let us finally consider the practical importance of the results of this experiment with respect to the speed of response of commercial x-ray screens. It is necessary to introduce supplementary information from other sources, inasmuch as long-persistence effects of relatively high energy might be present without detection by the present experiment.

Under ordinary conditions calcium tungstate does not show any detectible persistence. When a calcium tungstate screen is whirled as a disk before a narrow beam of x-rays, there is no noticeable blurring of the edge of the primary spot on the screen covered by the x-ray beam. We may therefore conclude that the curves for calcium tungstate recorded in this experiment include all of the response which is of practical importance and that the response is almost complete in 10^{-5} second.

In contrast, the sulphide screens, especially Patterson D, are commonly known to have long-persistence effects which are visible for some seconds or minutes after exposure to intense x-rays. Since these are not detected in the present experiment, it is necessary to consider whether a large fraction of the total light emitted by the screen is associated with the long-persistence effects. The case for Patterson D is of greatest practical importance, for it is usually found to be the brightest screen as measured photographically or photoelectrically. A rotating-disk test shows the primary spot on the screen to be bright and sharply delineated from the phosphorescent trail. On the basis of this and other tests, it appears safe to say that the main useful part of the response (perhaps three-fourths for Patterson D, more for Patterson B) is included in the oscillograms of this experiment and is complete in 20 microseconds or so. Thus the amount of long-persistence light is too small to be especially important from the standpoint of efficiency; on the other hand, it is large enough to be a disturbing factor in fast response applications for which it is essential that there be no detectible residual from earlier x-ray events.

As a practical case in point, we may consider x-ray motion pictures. These are now generally obtained by photographing the fluorescent screen. When Patterson D is used with conventional x-ray and camera equipment, noticeable blurring or multiple-image effects occur, especially at the leading edge of a dark area moving into a bright area. This blurring does not occur when calcium tungstate screen is used, but the effective intensity is less.

These conclusions also apply to the photomultiplier x-ray detector.[5] This detector consists of a fluorescent screen wrapped around a multiplier phototube and is therefore equivalent to the x-ray detector used in this experiment. Speed of response is important in the analysis of fast x-ray phenomena. Here again the rapid response and high intensity of Patterson D make it very suitable for many applications. However, the long-persistence effects of this screen cannot always be disregarded. For example, when the detector is used as an integrating exposure meter to terminate a radiographic exposure after the incidence of a given quantity of x-rays, the long-persistence effects result in an objectionable dependency upon exposure time and upon recent exposure history.

X-Ray Diffraction Studies of Chrome-Steel Slags[1]

G. P. Chatterjee and S. S. Sidhu
University of Pittsburgh, Pittsburgh, Pennsylvania

(Received March 21, 1947)

X-ray diffraction studies of the crystalline constituents in the acid open hearth chrome-steel samples showed that chromium exists in these samples as a chrome-iron spinel of the form, $FeO \cdot Cr_2O_3$. Its density was 5.109 g/cc and its melting 2160°C. It crystallized in the face-centered cubic structure with $a_0 = 8.348$A and $Z = 8$.

I. INTRODUCTION

THE essential major elements in most of the common alloy steels are chromium (Cr), nickel (Ni), and manganese (Mn). Nickel is not oxidized during steel making. Of the other two elements, Cr is more costly, and its loss in slag through oxidation or any other combination increases the cost of steel to a greater extent than an equivalent loss of Mn. The nature of control methods, which may lead to decreased losses of Cr, depends on the knowledge of the different phases in which Cr is present in the slag. The object of this investigation was to study by x-ray diffraction methods if Cr exists in the acid open hearth chrome-steel slag as (a) free Cr_2O_3 or CrO, (b) solute in FeO solvent, (c) silicates of chromium, and/or (d) spinels of the type $FeO \cdot Cr_2O_3$ or $CrO \cdot Fe_2O_3$.

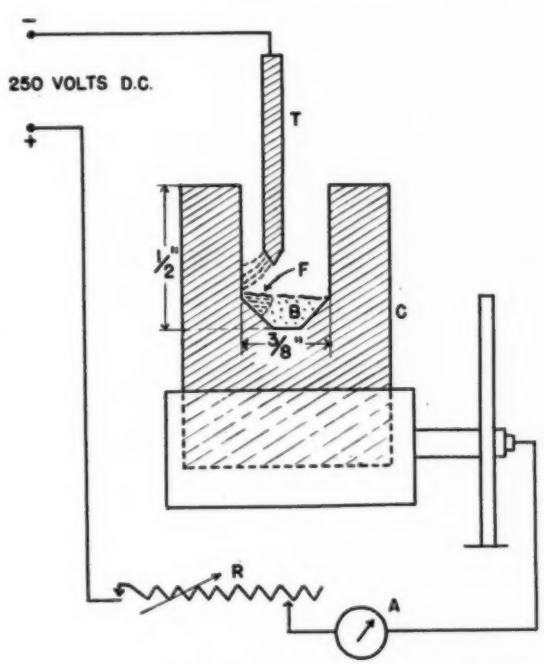

FIG. 1. The schemetic diagram of the small indirect arc furnace for preparing synthetic spinel. T = top electrode; C = rotating crucible; F = fused charge; B = unfused charge; R = variable resistance; and A = ammeter.

II. EXPERIMENTAL PROCEDURE

Acid open hearth chrome-steel slag samples were obtained from regular heats of steel and poured into Fluidimeter.[2] The slag solidified and cooled rapidly inside the mould to preserve nearly the original conditions in which the different constituents existed in the molten slag. From the chemical analyses of these samples, samples of synthetic slag were prepared. A mixture of pure FeO and Cr_2O_3 (mole proportion by weight) was put in graphite crucible C of a small 250-volt d.c. arc furnace as shown in Fig. 1. A small amount of borax was added to facilitate rapid melting. The top electrode T was placed slightly eccentric with respect to the bore of the crucible. An indirect arc was struck on the side of the crucible while the crucible was rotated. In one complete rotation of the crucible, the entire mixture was melted beneath the arc. The time of rotation was 20 seconds and the current through the electrodes was 10 amperes. During the arcing the electrode T was kept negative and the crucible positive. It was found by optical pyrometer that the positive electrode was always at higher temperature than the negative electrode.

[1] The paper was presented, in part, at the joint meeting of the American Society for X-Ray and Electron Diffraction and the Electron Microscope Society of America, Pittsburgh, Pennsylvania (Dec. 1946).

[2] Fluidimeter designed by the Acid Open Hearth Research Association under the direction of Dr. G. R. Fitterer, University of Pittsburgh, Pittsburgh, Pennsylvania.

To remove borates and other contaminants formed during melting, the synthetic samples were powdered and boiled in 1:2 HCl solution for a few minutes in a test tube. The solution with the residue was filtered and washed several times with hot water until the filtrate was free from iron salts and chlorides. The residue was dried in a muffle furnace at 120°C for one hour.

X-ray diffraction patterns of both the natural and synthetic slag samples were made by the usual powder method with filtered Mo$K\alpha$ radiation and a cylindrical camera of 171.9 mm effective diameter.

TABLE I. Powder diffraction data.

d = interplanar spacing in A units, I/I_0 = estimated relative intensity. V = very; S = strong; M = medium; W = weak.

Chrome steel slag I/I_0	Chrome steel slag d	Synthetic slag I/I_0	Synthetic slag d	Faylite I/I_0	Faylite d
M	4.82	M	4.83	—	—
M	3.70	—	—	S	3.71
—	—	—	—	M	3.53
S(broad)	2.93	M	2.95	S	2.85
V.S.	2.54	V.S.	2.51	M	2.55
M	—	—		M	2.29
M(broad)	2.08	M	2.08	W	2.06
S	1.91	S	1.91	V.W.	1.91
M	1.72	W	1.71	S	1.76
S	1.61	S	1.61	M	1.61
W	1.54	—	—	M	1.51
S	1.492	S	1.488	—	—
W	1.442	—	—	M	1.42
W	1.352	V.W.	1.328	W	1.33
M	1.281	M	1.279	V.W.	1.277
W	1.216	W	1.210	—	—
—	—	—		V.W.	1.197
W	1.176	V.W.	1.170	V.W.	1.176
M	1.111	V.W.	1.115	—	—
W	1.079	M	1.083	—	—
—	—	W	1.045	—	—
M	0.968	M	0.965	—	—
—	—	W	0.933	—	—
W	0.878	W	0.878	—	—
M	0.858	M	0.854	—	—

III. DISCUSSION OF RESULTS

The x-ray diffraction data obtained from the powder patterns are given in Table I. It is apparent from the data that the chrome-steel slag contains the same compound or compounds that are present in the synthetic slag and also small amounts of faylite, $(FeO)_2SiO_2$. The analysis of the diffraction data of the synthetic slag sample shows that it contains no free FeO, Cr_2O_3, nor a solid solution of FeO and Cr_2O_3, but a compound formed from the two oxides. That this compound is a spinel similar to chromite ($FeO \cdot Cr_2O_3$), one of the natural spinels reported by Dana[3] may be shown from its crystal structure as determined below:

For cubic crystal system

$$d_{hkl} = a_0/(h^2+k^2+l^2)^{\frac{1}{2}},$$

or

$$(h^2+k^2+l^2) = a_0^2 \times \frac{1}{d_{hkl}^2}, \qquad (1)$$

where d_{hkl} = interplanar spacing corresponding to plane hkl and a_0 = side of the unit cubic cell. For face-centered cubic crystal, the Miller indices of the planes that given reflections and the sum of the squares of the Miller indices are given in Table II. By plotting $(h^2+k^2+l^2)$ as function of $1/d^2$, one gets a straight line as shown in Fig. 2. The slope of this line as given in Eq. (1) is a_0^2. An accurate value of a_0 thus determined is 8.348A.

The density of the synthetic slag sample determined by the usual picnometer method was 5.109 g/cc. The molecular weight of the compound $FeO \cdot Cr_2O_3$ is 223.87 g/mole. Therefore the number of molecules per unit cell of the compound is

TABLE II. Interplanar spacings and the corresponding Miller indices of the first eight lines of the synthetic spinel.

I/I_0	d in A	$1/d^2$ in A^{-2}	Miller indices hkl	$(h^2+k^2+l^2)$
M	4.83	.043	111	3
M	2.95	.115	110(2)	8
V.S.	2.51	.158	113	11
M	2.08	.231	100(4)	16
S	1.91	.274	133	19
W	1.71	.342	112(2)	24
S	1.61	.386	111(3), 115	27
S	1.48	.457	110(4)	32

$$Z = \frac{5.109 \text{ g/cc} \times (8.348)^3 \times 10^{-24} \text{ cc} \times 6.023 \times 10^{23}/\text{mole}}{223.87 \text{ g/mole}} = 8.00.$$

[3] E. S. Dana, *A Text-Book of Mineralogy* (John Wiley and Sons, New York), p. 418.

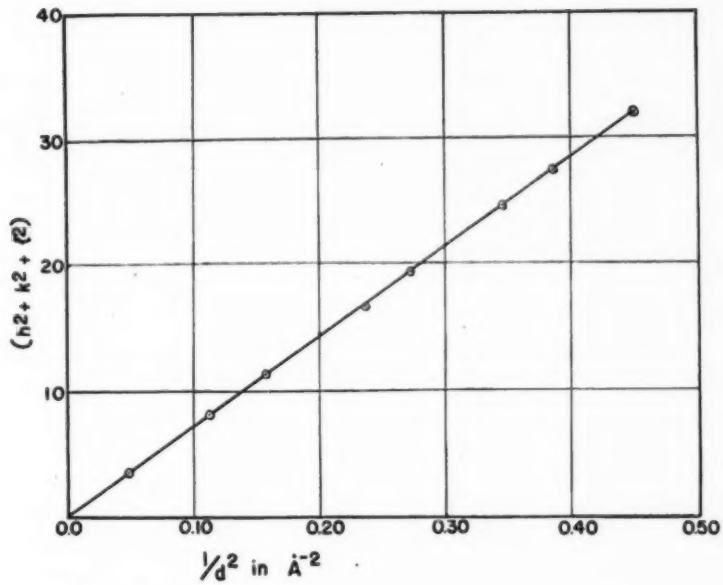

FIG. 2. $(h^2+k^2+l^2)$ as a function of $1/d^2$ for $FeO \cdot Cr_2O_3$.

If, on the other hand, it is assumed that the compound formed is $CrO \cdot Fe_2O_3$ whose molecular weight is 227.71 g/mole the number of molecules per unit cell is

$$Z = \frac{5.109 \text{ g/cc} \times (8.348)^3 \times 10^{-24} \text{ cc} \times 6.023 \times 10^{23}/\text{mole}}{227.71 \text{ g/mole}} = 7.86.$$

Since for a compound the number of molecules per unit cell must necessarily be whole number, it is evident that the chemical formula of the compound formed is $FeO \cdot Cr_2O_3$ with Fe^{++} as the divalent element and Cr^{+++} as the trivalent element.

IV. CONCLUSIONS

1. The crystalline constituents in the acid open hearth chrome-steel slag samples are (a) chrome-iron spinel of the type $FeO \cdot Cr_2O_3$[4] and (b) small amounts of $(FeO)_2SiO_2$.

2. The density of the spinel as determined by the picnometer method is 5.109 g/cc and its melting point about 2160°C.

3. The spinel crystallizes in the face-centered cubic system with lattice constant a_0 as 8.348A and the number of molecules per unit cell is 8.

ACKNOWLEDGMENT

The authors express their thanks to G. R. Fitterer for his very valuable suggestions and his assistance in supplying some of the necessary materials for this investigation.

[4] More exactly $(FeO, MnO) \cdot Cr_2O_3$, since the acid open hearth slag sample contains some amount of MnO which is usually present as $(MnO)_2SiO_2$ dissolved in $(FeO)_2SiO_2$. It is not unlikely, however, that some MnO may replace FeO in the spinel $FeO \cdot Cr_2O_3$. The atomic weight of Mn differs only by 0.92 from that of Fe and the atomic scattering factor of Mn does not differ much from that of Fe, the effects of replacing FeO to a small extent by MnO is therefore hardly detectable.

Spherical Aberration of Compound Magnetic Lenses

L. MARTON* AND K. BOL
Stanford University, Stanford University, California
(Received January 15, 1947)

A reduction of the spherical aberration of strong electron lenses can be achieved by a strong lens as a virtual image former and by a transformation of the image in a real one by means of one or more weak lenses. Calculations are carried out for bell-shaped magnetic fields of the axial field distribution

$$H(z)=\frac{H_0}{1+(z/a)^2},$$

and numerical values of the achieved reduction of the aberration are given for different lens strength, magnification, and image distance of the compound system.

EARLY in the development of electron optics, it was recognized that spherical aberration is one of the most serious limiting factors in the performance of electron lenses. From the beginning, efforts have been directed toward a reduction of this defect. One of the earliest attempts was that of Scherzer[1] who demonstrated that for a thin and weak electrostatic lens an axial field distribution of the form $\phi(z)=\phi_0 e^{-Bz^2}$ gives the minimum spherical aberration. The first similar calculation for a magnetic lens was carried out by Glaser.[2] Later Recknagel[3] and Plass[4] contributed to the same subject. All these calculations deal with very weak lenses; the only practical lenses with somewhat reduced aberration were designed by Gray[5] and Law.[6]

Scherzer demonstrated in another paper[7] that the spherical aberration of electron lenses can never be reduced to zero. Rebsch and Schneider[8] showed furthermore that no combination of electric and/or magnetic lenses can have less aberration than any of the components alone would have. Already at that time, however, Rebsch[9] demonstrated that, theoretically, the aperture defect may be reduced below any prescribed limit if in a compound lens the physical size of the component lenses is reduced proportionately. For obvious reasons this method is not very practical.

A somewhat different approach to the problem of reduction of the spherical aberration of short focus, thick electron lenses was briefly reported eight years ago by one of us.[10] It consists of combining a strong lens, forming a virtual image, with one or more weak lenses which convert the virtual image into a real image. This procedure is universally adopted for the construction of light microscope objectives and other light optical systems, and a more thorough investigation of its application to electron optical systems seems desirable. In what follows, a quantitative evaluation of the reduction of the spherical aberration of strong magnetic lenses is given. For this purpose the theory of strong magnetic lenses, developed by Glaser,[11] must be somewhat extended. Since this discussion is limited to the reduction of spherical aberration, the reduction of other aberrations by the use of compound lenses, which was recently reported,[12] will be completely omitted.

Glaser has shown[11] that for practical fields both the spherical and chromatic aberrations have minima when the object is near the center of the lens, for which position the image is virtual for practically all lenses.

---

* Now at the National Bureau of Standards, Washington 25, D. C.

[1] O. Scherzer, Zeits. f. Physik **101**, 23 (1936).
[2] W. Glaser, Zeits. f. Physik **109**, 700 (1938); **116**, 19 (1940).
[3] A. Recknagel, Zeits. f. Physik **117**, 67 (1940).
[4] G. N. Plass, J. App. Phys. **13**, 49 (1942); **13**, 542 (1942).
[5] F. Gray, Bell Sys. Tech. J. **18**, 1 (1939).
[6] R. R. Law, Proc. I.R.E. **25**, 954 (1937).
[7] O. Scherzer, Zeits. f. Physik **101**, 593 (1936).
[8] R. Rebsch, and W. Schneider, Zeits. f. Physik **107**, 138 (1937).
[9] R. Rebsch, Ann. d. Physik **31**, 551 (1938).
[10] L. Marton, Phys. Rev. **55**, 672 (1939). (Abstract: more detail is given in U. S. Patent No. 2,233,264.)
[11] W. Glaser, Zeits. f. Physik **117**, 285 (1941).
[12] J. Hillier, J. App. Phys. **17**, 411 (1946).

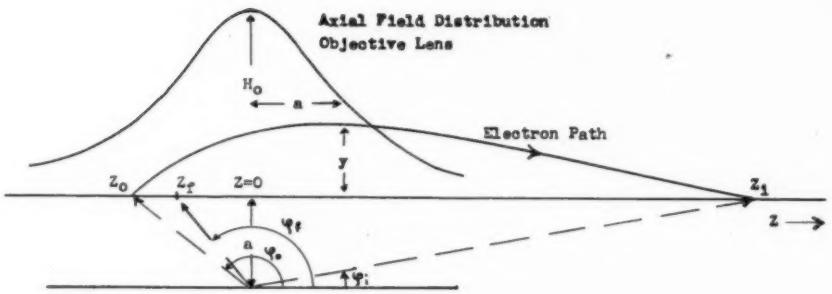

FIG. 1. Representation of symbols and coordinates used in Case I, a single objective lens.

Our problem, then, is to determine how small is the additional aberration introduced by the weak lenses. If it is sufficiently less than the decrease achieved by the formation of a virtual image by the first lens, our purpose is accomplished.

BASIC THEORY FOR FIELDS OF FORM $H_0/[1+(z/a)^2]$

It was first shown by Glaser[1] that the spherical aberration produced by a magnetic lens with field distribution H along the z-axis is given by:

$$\frac{\Delta r}{M}=\alpha^3\frac{e}{96mV}\int_{z_0}^{z_i}\left(\frac{2e}{mV}H^4+5H'^2-HH''\right)y_1^4dz. \tag{1}$$

Here y_1 represents the path equation of an electron satisfying the initial condition:

$$y_1(z_0)=0, \quad y_1'(z_0)=1. \tag{2}$$

As for the other symbols: Δr is the divergence in the image plane, z_i, of a beam of aperture α at z_0, M is the magnification, V the electron energy in terms of the accelerating voltage, and e/m the ratio of charge to mass of the electron. If H is given by

$$H=H_0/[1+(z/a)^2], \tag{3}$$

then the path equation is

$$y=a(1+(z/a)^2)^{\frac{1}{2}}\{D_1\sin[(1+k^2)^{\frac{1}{2}}\operatorname{arccot}z/a] +D_2\cos[(1+k^2)^{\frac{1}{2}}\operatorname{arccot}z/a]\}, \tag{4}$$

D_1 and D_2 being arbitrary, while $k^2=eH_0^2a^2/8mV$. a is the so-called half-width of the magnetic field. k^2 is a measure of the refracting power. The equation is put in a more palatable form if one sets $z/a=\cot\varphi$ (see Fig. 1) and $(1+k^2)^{\frac{1}{2}}=\omega$. One then obtains

$$y=aC_1\frac{\sin\omega(\varphi-\varphi_0)}{\sin\varphi}, \tag{5}$$

one constant having been chosen so that $y(z_0)=0$. For convenience we quote a few more formulas from Glaser:

$$z_{F_0}=a\cot(n\pi/\omega), \quad z_{F_i}=-a\cot(n\pi/\omega), \tag{6a}$$

$$f_0=\frac{a}{\sin(n\pi/\omega)}, \quad f_i=\frac{-a}{\sin(n\pi/\omega)}, \tag{6b}$$

$$N<\omega<N+1, \tag{6c}$$

N being the number of focal positions. Here f is the focal length and z_F is the location of the focal point.

The aberration for a single lens of this type has been thoroughly studied, whence we give just a resumé of some of Glaser's work.

Our problem, to be sure, is to study the aberration produced by a compound objective. This, however, we can immediately do by extending Eq. (1) over the whole system, as long as we obey the restriction that the radial distance of a paraxial ray be zero at the endpoints of the path of integration.

Case I. Single lens. The equation for the spherical aberration is obtained by integrating Eq. (1). From it follows that:

$$\frac{\Delta r}{M}=\alpha^3\frac{a_1k_1^2}{6\omega_1^4}\frac{1}{\sin^4\varphi_0}K_1, \tag{7}$$

where K_1 is given by

$$K_1=\int_{\varphi_0}^{\varphi_i}[2(4k_1^2-3)\sin^2\varphi+7]\sin^4\omega_1(\varphi-\varphi_0)d\varphi. \tag{8}$$

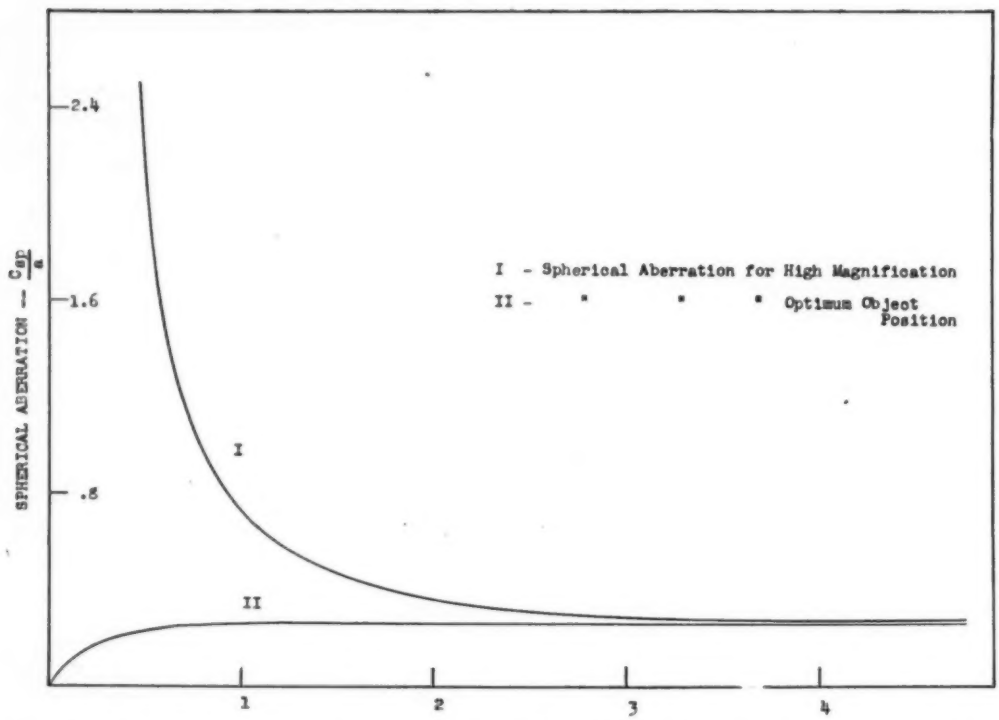

FIG. 2. Spherical aberration *vs.* lens strength for high magnification and optimum object position. (From Glaser.)

Since we need other upper limits later on, we leave it variable and obtain for the complete expression:

$$K_1(\varphi_0, \varphi) = \tfrac{3}{2}\omega_1^2(\varphi-\varphi_0) - \omega_1 \sin 2\omega_1(\varphi-\varphi_0) + \tfrac{1}{8}\omega_1 \sin 4\omega_1(\varphi-\varphi_0) - \frac{3(4k_1^2-3)}{16}\sin 2\varphi$$
$$+\frac{3}{4}\frac{\omega_1^4}{k_1^2}\frac{4k_1^2-3}{4k_1^2+3}\sin 2\varphi_0 + \frac{4k_1^2-3}{4k_1^2}\omega_1 \sin 2\omega_1(\varphi-\varphi_0)\cos 2\varphi - \frac{4k_1^2-3}{4k_1^2}\cos 2\omega_1(\varphi-\varphi_0)\sin 2\varphi$$
$$-\frac{1}{8}\frac{4k_1^2-3}{4k_1^2+3}\omega_1 \sin 2\omega_1(\varphi-\varphi_0)\cos 2\varphi + \frac{1}{16}\frac{4k_1^2-3}{4k_1^2+3}\cos 4\omega_1(\varphi-\varphi_0)\sin 2\varphi. \quad (9)$$

For high magnification, however, $\varphi_0 \cong \varphi_F$ while $\varphi_i \sim 0$, and from the lens equation (6) $\omega\varphi_F = \pi$, so that the expression is much simplified. The aberration for $\varphi_0 = \varphi_F$ as a function of k^2 is given by Fig. 2.

The aberration is, to be sure, not a minimum for $\varphi_0 = \varphi_F$. The presence of the factor $\sin^{-4}\varphi_0$ suggests immediately that the object should be close to the center, or $\varphi_0 \sim \pi/2$, as was mentioned in the introduction. Indeed, Glaser also plots the aberration for the optimum object position, which we give in Fig. 2.

For high k^2 the aberration is not appreciably altered by picking the optimum position; for the lower k^2 that are actually used in practice ($1 < k^2 < 2$), however, improvement is possible.

There are two objections to having the object right at the optimum position: the magnification is almost unity for practical values of k, and the image is virtual.

In order to accomplish anything we must therefore sacrifice some improvement in the aberration to gain magnification, and we must put in at least a second lens to attain a real image. We must, therefore, invesigate next the aberration introduced by the second lens.

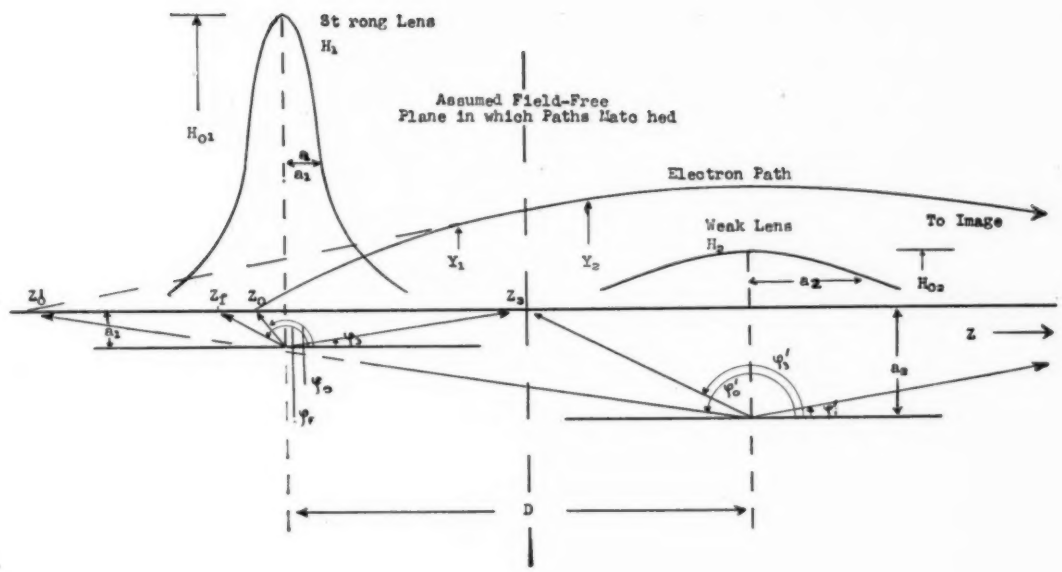

FIG 3. Representation of symbols and coordinates used in Case II, for a doubly compound objective lens.

Case II. Two lenses. We first define our axial field H as follows:

$$H=\begin{cases}H_1=H_{01}/[1+(z/a_1)^2] \text{ for } -\infty<z<z_3,\\ H_2=H_{02}/\{1+[(z-D)/a_2]^2\} \text{ for } z_3<z<\infty.\end{cases} \tag{10}$$

D is the distance between lens centers.

Quite arbitrarily we choose z_3 so that

$$H_1(z_3)\cong H_2(z_3).$$

We also assume that the two fields do not interact to an appreciable extent. This is done so that we can use the path equations of the previous section for each field, the constants of the second being adjusted to match the first at z_3. Only in the absence of such interaction are the calculations strictly valid.[11,12]

Equation (1) then becomes

$$\frac{\Delta r}{M}=\alpha^3\frac{e}{96mV}\left[\int_{z_0}^{z_3}f(H_1)y_1{}^4dz+\int_{z_3}^{z_i}f(H_2)y_2{}^4dz\right]. \tag{11}$$

The integrals can be transformed into that of Eq. (8) by adopting a new coordinate system for the second lens. We take $z'=z-D$ and $z'/a_2=\cot\varphi'$ (Fig. 3). Applying furthermore the initial condition (2) to Eq. (5), we obtain for y_1 and y_2

$$\left.\begin{aligned}y_1&=\frac{a_1}{\omega_1\sin\varphi_0}\frac{\sin\omega_1(\varphi_0-\varphi)}{\sin\varphi},\\ \text{and}\qquad y_2&=a_2C_2\frac{\sin\omega_2(\varphi'-\varphi_i')}{\sin\varphi'},\end{aligned}\right\} \tag{12}$$

where φ_i' is chosen in accordance with Newton's image equations, which hold for this type lens, and where C_2 is to satisfy the matching condition.

Slightly modifying Glaser's results we then obtain

$$\begin{aligned}\frac{\Delta r}{M}&=\alpha^3\left[\frac{a_1k_1{}^2}{6\omega_1{}^4}\frac{1}{\sin^4\varphi_0}K_1+\frac{a_2k_2{}^2}{6}C_2{}^4K_2\right]\\ &=\alpha^3C_{sp}.\end{aligned} \tag{13}$$

For K_1 and K_2 we write (see Eq. (8))

$$\left.\begin{aligned}K_1&=\int_{\varphi_0}^{\varphi_3}f(k_1,\varphi,\varphi_0)d\varphi,\\ K_2&=-\int_{\varphi_i'}^{\varphi_3'}f(k_2,\varphi',\varphi_i')d\varphi'.\end{aligned}\right\} \tag{14}$$

As we have already seen, (Eq. (9)), the exact expressions for K_1 and K_2 are exceedingly cumbersome; but fortunately they may be approxi-

mated—for the values we use—to within a few percent by the following equations:

$$K_1 = \tfrac{3}{2}\omega_1^2(\varphi_3-\varphi_0)+\frac{3\omega_1^4}{4k_1^2}\frac{4k_1^2-3}{4k_1^2+3}\sin 2\varphi_0,$$
$$K_2 = -\left[\tfrac{3}{2}\omega_2^2(\varphi_3'-\varphi_i')+\frac{4k_2^2-3}{4k_2^2}\omega_2 \sin 2\omega_2(\varphi_3'-\varphi_i')\cos 2\varphi_3'-\frac{4k_2^2-3}{4k_2^2}\cos 2\omega_2(\varphi_3'-\varphi_i')\sin 2\varphi_3'\right]. \tag{15}$$

Now we but need an evaluation of C_2 to have an analytic expression for the aberration constant, C_{sp}. To do this it is convenient to write y_2 as

$$y_2 = a_2 C_2 \frac{\sin\omega_2(\varphi'-\varphi_0')}{\sin\varphi'}, \tag{16}$$

φ_0' being the position of the virtual image formed by the first lens as seen by the second, and again being determined by the Newtonian image relations.

Although we must match both y_1 and y_2 and their slopes, it is obvious, φ_0' having been determined, that if C_2 satisfies either condition it will automatically satisfy the other. We thus pick as most convenient the condition that the path distances (see Eq. (12)) be equal. We have then:

$$a_2 C_2 \frac{\sin\omega_2(\varphi_3'-\varphi_0')}{\sin\varphi_3'} = \frac{a_1}{\omega_1 \sin\varphi_0}\frac{\sin\omega_1(\varphi_0-\varphi_3)}{\sin\varphi_3}. \tag{17}$$

Fortunately, the arguments are such that we can approximate as follows:

$$a_2 C_2 \frac{\omega_2(\varphi_3'-\varphi_0')}{\pi-\varphi_3'} = \frac{a_1}{\omega_1 \sin\varphi_0}\frac{\pi-\omega_1(\varphi_0-\varphi_3)}{\varphi_3}. \tag{18}$$

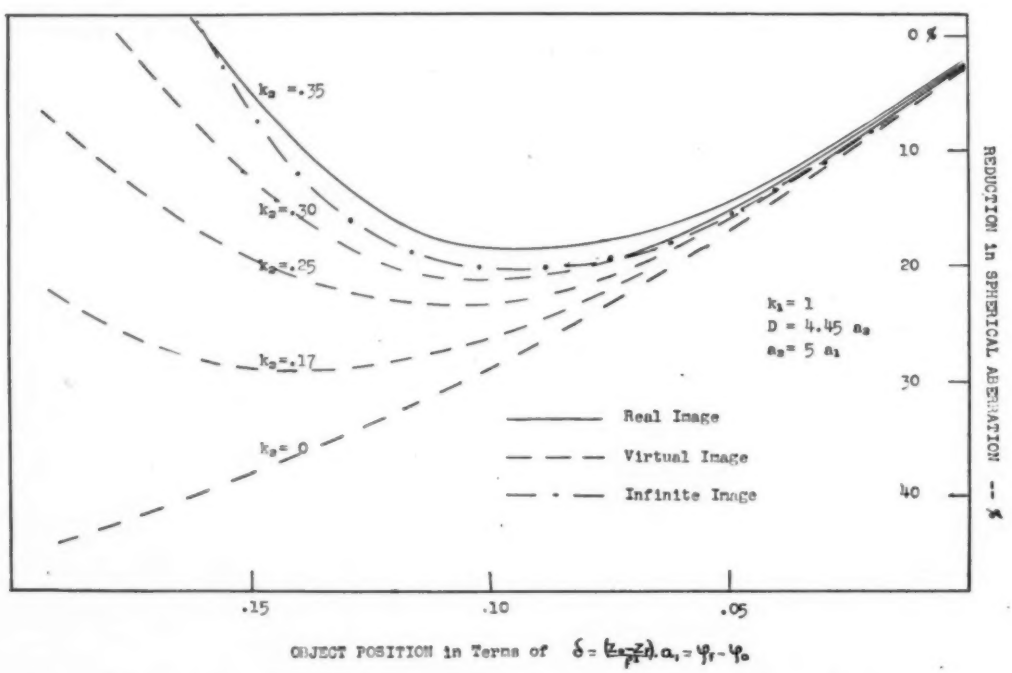

FIG. 4. Spherical aberration *vs.* objective position in first lens, for a second lens of varying strength, but fixed half-width. An infinite image is formed when the first lens forms a virtual image on the focal position of the second lens. Above this boundary, the system forms a real final image, below, a virtual one.

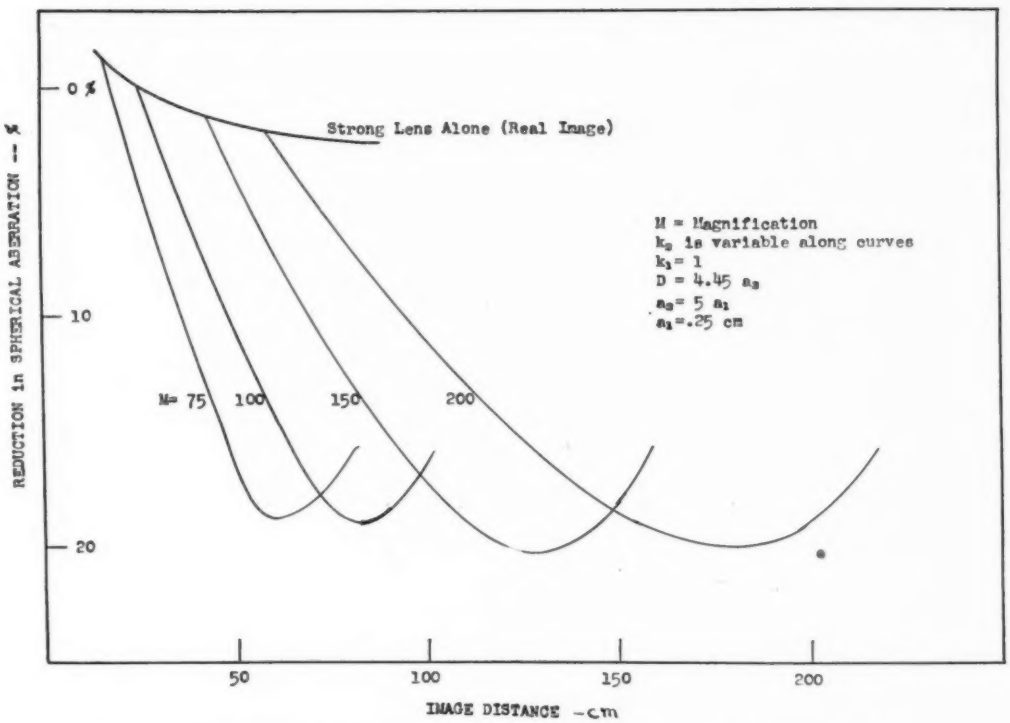

FIG. 5. Spherical aberration *vs.* the final image distance for a typical set of conditions.

Now setting $\varphi_0=\varphi_F-\delta$, and applying the fact that $\omega\varphi_F=\pi$ (Eq. (6)), φ_F being the focal position, we obtain:

$$C_2=\frac{a_1}{a_2}\frac{1}{\sin\varphi_0}\frac{1+\delta/\varphi_3}{\omega_2}\frac{\pi-\varphi_3'}{\varphi_3'-\varphi_0'}. \tag{19}$$

Thus we have obtained for the aberration constant of a two-component compound lens:

$$\frac{C_{sp}}{a_1}=\frac{1}{6\sin^4\varphi_0}\left[\frac{k_1^2}{\omega_1^4}K_1+\left(\frac{a_1}{a_2}\right)^3K_2\frac{k_2^2}{\omega_2^4}(1+\delta/\varphi_3)^4\left(\frac{\pi-\varphi_3'}{\varphi_0'-\varphi_3'}\right)^4\right]. \tag{20}$$

DISCUSSION

We have already seen that φ_0 should be close to $\pi/2$. The question remains how the second term varies with φ_0. As the beam leaving the first lens is converged less, or $\varphi_0\rightarrow\pi/2$, one can expect it to increase rapidly, since the aberration increases with the cube of the aperture. The behavior with φ_0 for different k_2 is shown in Fig. 4.

For the same reason the two lenses should be close together. It is unfortunate that we have not succeeded so far in treating the case of interacting fields, so that we could find the exact behavior when D becomes small. It is certain, however, that practical compound lenses will need to be close enough together to make field interaction inevitable.

One reason for the need is the final image distance involved. Figure 5 gives an idea of the increase in image distance for only a 20 percent reduction in the aberration. Decreasing D is the only way of decreasing the aberration and keeping a reasonable image distance.

Another way of decreasing C_{sp} is by increasing the ratio of the half-width of the second lens to that of the first. (See Fig. 6.) But here again we increase the final image distance, as is also indicated on the graph, in a manner approximately proportional to a_2/a_1.

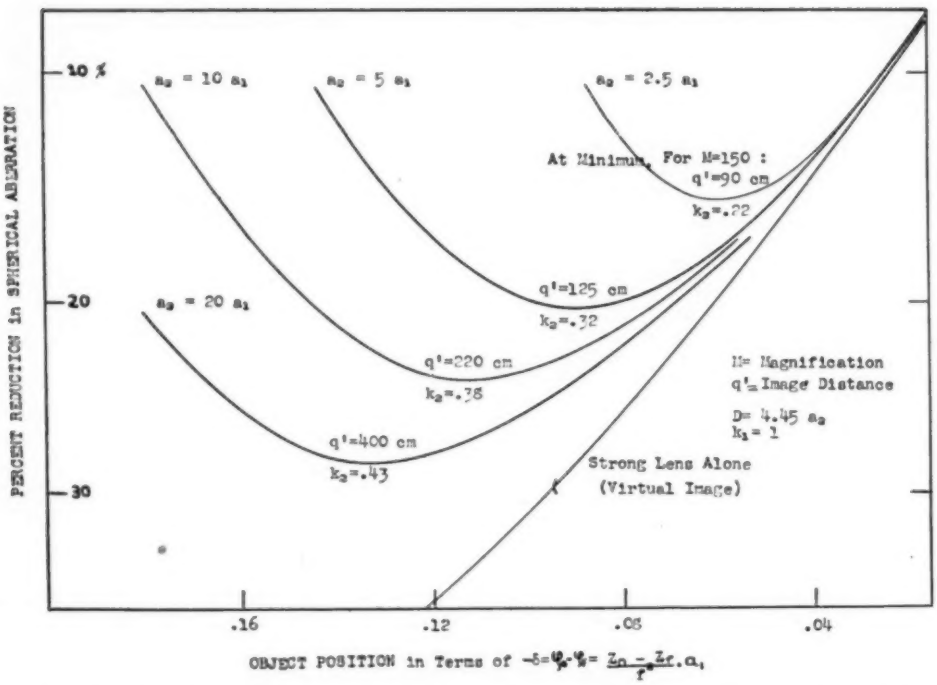

FIG. 6. Spherical aberration *vs.* object position, for a second lens of varying half-width. The total magnification along the curves is infinite, but to gain an idea as to how the image distance q' varied, we took the lens strength indicated by the aberration minimum and calculated q' for a magnification of 150.

Thirdly, the contribution of the second lens is almost proportional to $k_2^2(k_2^2 \ll 1)$, shown in Fig. 4. There again, however, another consideration enters. The focal length of the second lens is inversely proportional to k_2^2. The greater this focal length, the higher must be the magnification by the first lens in order to produce a virtual image outside the second focal point and thus secure a real final image.

But for high magnification by the first lens one achieves almost no reduction in the aberration. The result is that there is an optimum value for k_2, as is shown in Fig. 7 (which is merely Fig. 4 plotted against total magnification).

This optimum value, we note, is not necessarily the best from the point of view of image distance. Referring once more to Fig. 5, it is seen that especially for high magnification the aberration minimum is very flat. One can thus gain a considerably shortened image distance, without appreciably increasing the aberration, by taking a value of k_2^2 somewhat less than the optimum value.

We saw from Fig. 4 that some decrease in the aberration is possible using only two lenses, but that even greater decreases come with the formation of a virtual image by a very weak second lens. The question then arises whether one cannot use three lenses to good advantage.

Our next problem is to decide therefore whether the contribution of the third lens can be made sufficiently small to make its addition worth while.

Case III. Three lenses. Again proceeding as in the previous section we easily obtain for the aberration:

$$\frac{C_{sp}}{a_1}=\frac{1}{6\sin^4\varphi_0}\left\{\frac{k_1^2}{\omega_1^4}K_1+\left[\left(\frac{a_1}{a_2}\right)^3\left(1+\frac{\delta}{\varphi_3}\right)^4 K_2\frac{k_2^2}{\omega_2^4}\left(\frac{\pi-\varphi_3'}{\varphi_3'-\varphi_3'}\right)^4\right]\right.$$
$$\left.\times\left[1+\left(\frac{a_2}{a_3}\right)^3\frac{K_3}{K_2}\cdot\frac{k_3^2}{k_2^2}\frac{\sin^4\omega_2(\varphi_4'-\varphi_0')}{\sin^4\omega_3(\varphi_4''-\varphi_4'')}\frac{\sin^4\varphi_4''}{\sin^4\varphi_4'}\right]\right\}. \quad (21)$$

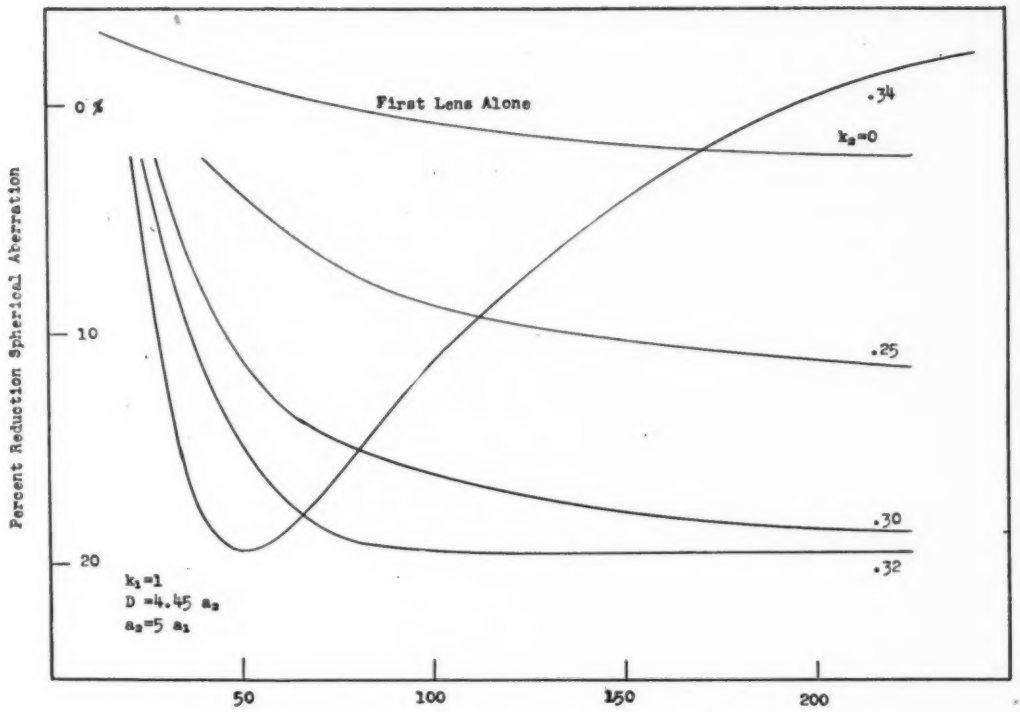

FIG. 7. Aberration *vs.* total magnification. This is a plot of graph II *vs.* magnification instead of object position.

The symbolism is exactly analogous to that for Case II except that the subscript 4 refers to the field-free plane between the second and third lenses. All double primes refer to the coordinate system of the third lens.

Equation (21) leads us to the following qualitative conclusions:

(1) By making a_2/a_3 small enough (say $\frac{1}{5}$) we can obtain $C_{sp_{3\text{ lenses real image}}} = C_{sp_{2\text{ lenses virtual image}}}$. In other words, the last term in Eq. (21) must be $\ll 1$.

(2) The image distance, q, depends almost entirely on the spacing between the last two lenses. If we wish to satisfy the condition of no interaction between the lenses, q will be greater than for the two lens combination.

Both aberration and image distance, for the combination of two or three lenses, show a considerable improvement only for conditions exceeding the limits imposed by our method of derivation. It is hoped that a more rigorous derivation and/or experiments will enable us in the near future to substantiate and to extend the results of this preliminary calculation.

CONCLUSION

By combining two lenses one can approach the lower limit to the aberration set by the first lens, used as a virtual image former. For such lens separation for which the interaction of the lens fields is negligible, the image distance is considerably greater than that of the first lens used as a real image former.

How closely one can approach this lower limit cannot be answered without a study of the aberration for very close, interacting fields.

Certainly it seems desirable to have the lenses close together.

In addition it has been found that there is an optimum value for the strength of the second lens in a two-lens system, and that the half-width of the second field should be several times greater than that of the first.

Three lenses may be used to improve the aberration, but only at a cost of a great image distance.

Physical Properties of Calcium Tungstate X-Ray Screens

J. W. Coltman, E. G. Ebbighausen,* and W. Altar
Westinghouse Research Laboratories, Pittsburgh, Pennsylvania
(Received January 6, 1947)

The absolute energy of the light from a fluorescent calcium tungstate x-ray screen, its spectral distribution, and the efficiency of conversion from x-rays to light have been determined. The absolute energy and its spectral distribution were obtained spectrographically by comparison with a standard tungsten filament lamp. Equations are given for determining the distribution of light in the diffusing screen material, and calculation of the light losses are made for varying screen thickness and x-ray absorption. The data for energy distribution of the ingoing x-rays were taken from measurements obtained in this laboratory by a new method to be published elsewhere. Allowance for scattering and secondary *x*-radiation was made and a conversion efficiency of 5.0 percent was obtained for this calcium tungstate phosphor.

INTRODUCTION

THE primary purpose of this research was to obtain experimentally the absolute efficiency of the transformation of x-ray energy into light energy by calcium tungstate. Of the various fluorescent materials which might have been examined, calcium tungstate appeared to be the one whose investigation would be most fruitful, first, because of its wide utilization in radiography, and second, because the fluorescence of this phosphor is not due to the presence of a foreign material serving as an activator. Thus calcium tungstate phosphors produced by different manufacturers should have the same spectral distribution, and probably will not vary greatly in their efficiency. As a basis for theoretical studies of fluorescence, knowledge of the behavior of calcium tungstate is probably of more value than that for the sulphide phosphors which are very sensitive to minute quantities of impurities.

The problem of determining the conversion efficiency divides itself into three main parts. First, the absolute energy and spectral distribution of the light emitted from the screen must be determined. Second, the light losses in the screen must be determined in order that the total light generated may be calculated. Third, the energy of x-rays absorbed in the screen must be measured. The resultant efficiency will be a characteristic of the calcium tungstate itself and of the wave-length of the exciting x-rays. With this information and a knowledge of the functional dependence of the light losses on the structure of the screen as presented herein, the behavior of any calcium tungstate screen may be predicted. The method of analysis developed to obtain the light losses are applicable to the transmission of light in diffuse media in general and, in particular, to phosphors other than calcium tungstate.

* Now at University of Oregon, Eugene, Oregon.

Ia. LIGHT ENERGY AND ITS SPECTRAL DISTRIBUTION

The spectrographic part of the problem consisted of the determination of the spectral energy distribution of the $CaWO_4$ screen when excited by 80 kv x-rays, filtered by one half millimeter of Cu and one millimeter of Al, and with a tube current of 20 milliamperes. The procedure involved a photographic comparison between the known spectral energy distribution of a temperature-calibrated tungsten ribbon filament lamp and that of the $CaWO_4$ screen.

The Experimental Apparatus

The standard source was a lamp with a tungsten ribbon filament and quartz window loaned by the National Bureau of Standards. The ribbon filament is about $1\frac{1}{2}$ inches long and $\frac{1}{8}$ inch wide and is supported in the bulb by heavy nickel leads.

The temperature calibration of the lamp was made by Mr. M. S. Van Dusen, Acting Chief of the Pyrometry Section, who gave the value of the brightness temperature outside of the quartz

window as 2614°K at a current of 39.20 amperes and for a point about midway along the filament. The position is marked by a small nick on one edge of the filament itself. Values of the spectral transmission of the quartz window were also supplied by Mr. Van Dusen.

In order to compute the spectral distribution of the radiation from the filament, it was necessary to obtain the true temperature of the filament inside the bulb and to have a knowledge of the spectral emissivity of tungsten over the intended working range of wave-length (3000A–7000A). A compilation of spectral emissivities was furnished by Dr. W. W. Coblentz, retired head of the Radiation Laboratory of the National Bureau of Standards. The conversion from the brightness temperature to the true temperature is accomplished by the following formula, derived from Planck's radiation formula:

$$\frac{1}{T_t}=\frac{1}{T_{BO}}+\frac{\lambda}{.4343C_2}\log_{10}(t_\lambda\cdot\epsilon_\lambda), \qquad (1.1)$$

where

T_t = true temperature of the filament
T_{BO} = brightness temperature of the filament outside the window as determined by the N.B.S. optical pyrometer
λ = mean effective wave-length in cm of the filter used in the N.B.S. optical pyrometer
C_2 = the second constant in Planck's radiation formula
t_λ = transmission of the quartz window at the above-mentioned wave-length
ϵ_λ = the spectral emissivity of tungsten at λ.

With $T_{BO}=2614°K$, $\lambda=6650\times10^{-8}$ cm, $C_2=1.435$, $t_\lambda=0.927$, $\epsilon_\lambda=0.426$, the true temperature of the filament is 2947°K.

The spectral energy distribution outside the lamp was obtained by substitution of the above value of the true temperature in Planck's radiation formula, and correction of the result for the spectral emissivities of tungsten and for the spectral transmission of the quartz window.

When the image of the central portion of the filament was focussed on the slit of the spectrograph, the resulting spectrum was a continuous band with a narrower and darker band running down its length. This latter band was caused by the region of the filament at the nick where the filament was narrower, and its resistance and hence its temperature higher, than regions of the filament above and below the nick. This narrow band was not wide enough to measure in the microphotometer, so it was necessary to use some other portion of the filament where the temperature variation with length was small. Measurements of temperature with an optical pyrometer were made covering the $\frac{1}{2}''$ range from a point $\frac{1}{8}$ inch above the nick to within $\frac{1}{8}$ inch of the top of the filament. The true temperature fell only about seven degrees over this range, and at its center was 41° lower than that at the nick. The portion of this region used for projection onto the length of the slit (2 mm) of the spectrograph was about $\frac{3}{8}$ inch. Hence the true temperature variation over this range was of the order of about 4°. From Planck's radiation law one derives the percentage change in energy at a given wave-length for a change in true temperature to be

$$(dE_\lambda/E_\lambda)\text{ percent}=100(C_2/\lambda T^2)dT. \qquad (1.2)$$

For a true temperature of 2906°K the percentage change of E_λ per degree is about 0.57 percent at 3000A and 0.28 percent at 6000A. One may take 0.4 percent as a mean. Hence, a change of 4° (true) corresponds to less than a 2 percent change in E_λ. Furthermore, since the quartz lens used to focus the filament on the slit of the spectrograph does not give a perfectly sharp image, the effect is to smooth out variations in E_λ and produce a spectrum of uniform density across its width. Instead of recomputing the energy distribution for the adopted temperature of 2906°K, the one for 2947°K was used with the correction factor

$$C=\exp(C_2/\lambda)(T_1-T_2/T_1T_2)$$
$$=\exp(C_2/\lambda)(\Delta T/T^2), \qquad (1.3)$$

where $\Delta T=41°$ and T is the mean of 2947°K and 2906°K. It appears that the combined error from all sources in the computed energy varies from about 6 percent at 3000A to about 3.0 percent at 6500A with an average for the middle of the spectrum of about 4.5 percent.

One of the most difficult problems was the reduction of the filament brightness to a value closely approximating that of the fluorescent screen. This was necessary because of reciprocity failure of the photographic emulsion which demands that the exposure times on the standard lamp and the fluorescent screen be of quite the

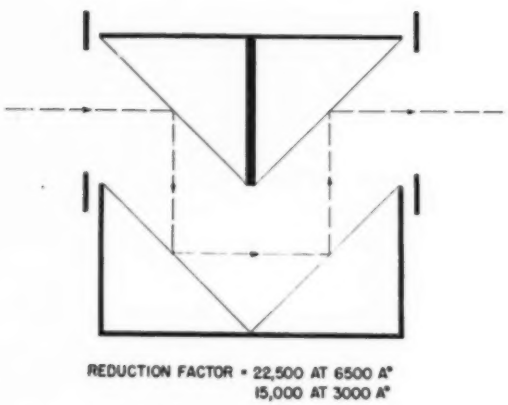

FIG. 1. Schematic arrangement of reflection-type attenuator.

same order of magnitude. A rough computation on the basis of available data indicated that the lamp might be brighter by a factor of the order of one million. Only by the combined use of three methods could the filament brightness be reduced to the point where the exposure times became nearly equal. Reduction by transmission filters had to be rejected as impractical, because transmission coefficients were not known with sufficient accuracy at the various wave-lengths. Of the following three methods used, one will be discussed in detail now and the second and third in later sections:

1. The method of successive reflections.
2. Rotating sectors.
3. Stops in the collimator of the spectrograph.

In the first method the brightness was reduced by successive reflections from four air-glass surfaces. The apparatus designed and constructed for this purpose was called the "attenuator." The attenuator consisted of four borosilicate crown glass prisms arranged as in Fig. 1. The arrows indicate the path of the light through the system. The system was enclosed in a brass box, and the prisms were carefully aligned so that parallelism and perpendicularity of the faces was assured. The angle of incidence of the central ray of the beam closely approximated 45° at all of the four surfaces of reflection. At each surface a small fraction of the light was reflected, and the remainder was transmitted into the prism. In order that as little as possible of this light should be returned to the beam by internal reflections, all prism surfaces except the ones used for reflection were coated with a solution of propyl methacrylate mixed with lampblack, and the prisms were baked in an oven at 120°F for two hours. The result was a non-reflecting and absorbing coating which served to remove to a very high degree all light transmitted into the prism.

According to Fresnel's formulas the amplitude ratios of the reflected light are:

$$\frac{\sin(I-I')}{\sin(I+I')} \quad \text{and} \quad \frac{\tan(I-I')}{\tan(I+I')}$$

for light polarized in, and, respectively, at right angles to, the plane of incidence. The intensity of the parallel component after four successive reflections becomes:

$$R(I_{11})=\left[.707\left(\frac{\sin(I-I')}{\sin(I+I')}\right)^4\right]^2 =\frac{1}{2}\left(\frac{\sin(I-I')}{\sin(I+I')}\right)^8, \quad (1.4)$$

and similarly for the perpendicular component:

$$R(I_1)=\frac{1}{2}\left(\frac{\tan(I-I')}{\tan(I+I')}\right)^8. \quad (1.5)$$

Computation shows that for the range of spectrum to be studied, I_1 is about 9000 times fainter than I_{11} and hence the light may be said to be completely polarized.

With I fixed at 45°, I' depends upon n (Snell's Law) and since n varies with the wave-length, R itself is a function of the wave-length.

In order to determine the variation of n with wave-length, one of the prisms was mounted on a spectrometer and n was determined for each of the three mercury lines of wave-length 5460.7A, 4358.3A, and 4046.6A. The resulting indices were, respectively, 1.5260, 1.5349, and 1.5389. Each determination had a standard deviation of unity in the fourth place of $n-1$. With these three values of the wave-length and their respective indices, the constants of the Hartmann formula were obtained:

$$n=1.5041+\frac{83.416}{\lambda-1648.0}. \quad (1.6)$$

For several wave-lengths between 3000A and 6500A, n was determined from (1.6), then I' from Snell's Law and finally the reduction factors from (1.4). The curve of reduction factor *vs.* wave-length is given in Fig. 2. These factors were applied to the spectral energy distribution curve of the filament outside the lamp and result in the distribution curve of the light as it leaves the attenuator.

Attention must be given to the fact that the light from the attenuator is practically completely polarized, while the light from the fluorescent screen is unpolarized. Thus the loss in the spectrograph may not be the same for both sources. In order to test this, two spectrograms of equal exposure times were taken of the lamp through the attenuator. For the first exposure, the plane of the normals to the reflecting surfaces was held perpendicular to the length of the slit and parallel for the second exposure. From the resulting densities of the spectra it appeared that the effective exposure was only about half as great in the first case as in the second. In order to avoid the difficulty the attenuator was mounted so that the plane of the normals made an angle of 45° with the slit and, therefore, as far as the spectrograph was concerned, it was receiving isotropic light.

The errors in the computed reduction factors are evaluated as follows:

1. As already stated n has been determined with a standard deviation of one part in the fourth place of $n-1$. For the middle of the spectral range, this value results in an error of about 0.1 percent in the value of $R-$ a negligible quantity.

2. Since n was determined for only three wave-lengths, interpolation had to be used for shorter and longer wave-lengths using formula (1.6). The error in R to be expected, particularly in the short wave-length region where n is changing rapidly, is estimated to be of the order of 0.3 percent in the neighborhood of 3200A and of 0.1 percent for wave-lengths longer than 4000A.

3. The beam through the attenuator, as defined by the lens which focusses the filament on the slit and by the angular size of the collimator, has an angular diameter of about two degrees, of which only the central ray will strike the reflecting surfaces at an angle of incidence of 45°. The limiting values at the first surface will be 44° and 46°. However, it will be seen that (by design) if I is 46° at the first surface, it will have the same value at the second, 44° at the third, and 44° at the last surface. Calculation shows that the error made in R by assuming $I=45°$ for the whole beam is about 0.2 percent and thus is negligible.

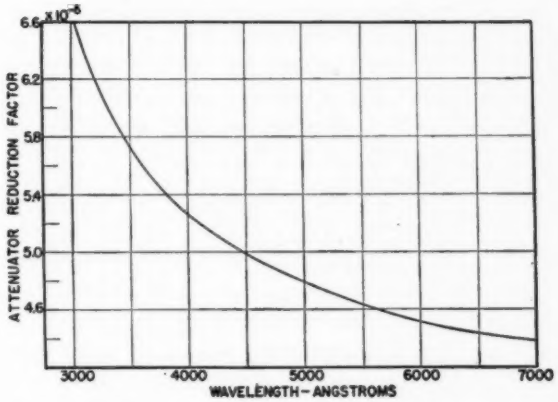

FIG. 2. Reduction factor of attenuator as a function of wave-length.

4. Particular care was used in the alignment of the attenuator so that the resulting error in R is probably less than 0.4 percent.

The total error is probably not in excess of 1 percent.

The spectrograph was an all quartz optics, low dispersion instrument. The arrangement was such that the plate holder could be moved at right angles to the spectrum, and thus several spectra could be obtained on one plate. The length of spectrum from 3000A to 6500A was about $\frac{3}{4}$ inch. The spectrograph was mounted on a turntable which permitted the slit to be turned to either the standard lamp, the mercury lamp (for a comparison spectrum), or the fluorescent screen. By means of lead sheets, the whole instrument was very well shielded from the direct or scattered radiation of the x-ray tube. On the turntable was mounted a motor to turn cardboard sectors, used to reduce the lamp brightness by a given amount, and also a mount for the quartz lens to focus the lamp filament on the slit. Inside the prism case was an arrangement to hold stops for the further control of the lamp brightness. The length of the slit was 2 mm and the width 0.2 mm.

The fluorescent material, a sample of Eastman Ultra Speed back screen, consisted of a layer of $CaWO_4$ covered by a film of lacquer and mounted on a sheet of white cardboard four inches square. It was centered over a two inch square hole in a sheet of $\frac{1}{8}$ inch lead and the whole unit was mounted over the open end of the protective cone of the x-ray tube.

The Experimental Procedure

Generally speaking, our procedure was a comparison, at a number of wave-lengths, between the brightness of the screen and the standard lamp filament as seen through the attenuator. Given the magnitude of the latter and its spectral distribution, it was possible to compute the light output of the screen on an absolute scale.

One of the most difficult problems, the reduction of the brightness of the standard lamp to a level comparable to that of the fluorescent screen, was accomplished by the use of the attenuator (already described), rotating sectors, and collimator stops. This permitted the use of equal exposure times for the lamp and the fluorescent screen and thereby avoided the danger of reciprocity failure. In order to provide a calibration on each plate, five exposures were made using five cardboard sector disks, eight inches in diameter; the first, *A*, providing a reduction factor 12.5 and the others, *B*, *C*, *D*, and *E* approximately 25, 50, 100, and 200. When using these disks, one must avoid the intermittency effect because of which the photographic density is a measure of the total light impinging only under certain conditions. A continuous exposure and an intermittent one of the same total energy will produce the same density on the photographic plate, provided the total time of exposure is the same in both cases, and the frequency of interruption is above a certain critical rate. The Eastman Kodak Company's publication, "Photographic Plates for use in Spectroscopy and Astronomy," states that this critical rate varies from about 100 flashes per second for a one-second exposure to a few flashes per second for a one hour exposure. The motor used to drive the sectors operated at 2850 r.p.m. and since no exposure was less than twenty minutes, no error caused by the intermittency effect was incurred.

The final adjustment of lamp brightness was obtained by placing one of several stops between the prism and the collimator lens at a position close to the latter. The first stop defined the beam leaving the collimator lens to the extent that all of the beam entered the prism and passed through the camera lens to the photographic plate. This stop was used when photographing the spectrum of the fluorescent screen, and its reduction factor was designated as unity. Six more stops were made with reduction factors varying from 2 to 37. With this last stop, the total reduction of the lamp brightness, including the average of that of the attenuator and that of sector *A*, reached a factor of nine million. This much was needed when working in the region around 6000A where the screen fluorescence is weak, and the lamp output high.

All photographic plates used were coated with Eastman 103-F emulsion. On each plate eight exposures were made; one from the fluorescent screen, five from the standard lamp using sector disks *A* to *E*, and two exposures from a mercury lamp to obtain wave-length scales at the top and bottom of a plate.

The densities of the spectra were compared in an Arl Dietert microphotometer. At each position the density was determined for the fluorescent spectrum and for each of the five comparison spectra.

Since different portions of the spectrum required widely varying exposure times to give densities on the linear portion of the emulsions, it was necessary to use several plates to cover the complete spectrum. For each wave-length the transparencies of the five comparison spectra were plotted on semi-logarithmic paper against the reduction factors of the sectors, taking that for sector *A* as unity. From this curve was determined the factor by which the fluorescent spectrum was fainter than the spectrum belonging to sector *A*.

This factor was combined with reduction factors for the collimator stop, the factor 12.5 for the sector disk *A* and the factor for the attenuator, to give a total reduction ratio between intensities at corresponding wave-lengths from the standard lamp and from the $CaWO_4$ screen. A total of seven plates were measured.

Experimental Results

Near the end of the investigation it was found that the portion of the $CaWO_4$ screen which had been exposed to x-rays was somewhat fainter, showing that it had suffered a certain degree of "fatigue." Measurements indicated that the exposed portion of the screen was about 8 percent

fainter than the outer portion that had been protected from x-radiation by the lead.

In order to deduce from the measurements on a fatigued screen the spectrum of a fresh screen, measurements on each plate were corrected by an amount proportional to the total x-ray exposure time of the screen up to the time when the plate in question was taken.

The total time of exposure of the screen to x-rays was about six and one-half hours. This includes exposure times for test plates and several others that for one reason or another were not used. The results from the individual plates are given collectively in Fig. 3. The ordinates are 10^{-5} ergs/cm² sec. A unit. The assumption is made that both the lamp filament and fluorescent screen radiate according to Lambert's cosine law, and a correction for departures will be added later.

The curve given in Fig. 3 is not final, but must be corrected for slit broadening. The effect is to pull in both ends of the curve to a certain extent without changing the total area. Integration of this curve yields the result that the total energy output of the screen was 2.54 ergs/cm²/sec.

A correction factor of 0.92 must be applied to this value to correct for the departure from Lambert's law in the angular distribution of the light from the screen. The experimental determination of this factor is described in Section Ib. The total energy thus reduces to 2.34 ergs/square centimeter per second, for a measured x-ray intensity of 0.149 r-units per second incident on the screen. The final corrected spectral curve, Fig. 4, is given in terms of light energy generated in the screen per r-unit absorbed. The method for measuring the light losses is given in Section 2.

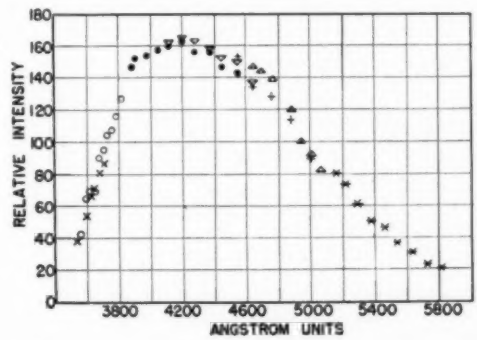

FIG. 3. Spectrum of $CaWO_4$ as obtained from seven plates (uncorrected).

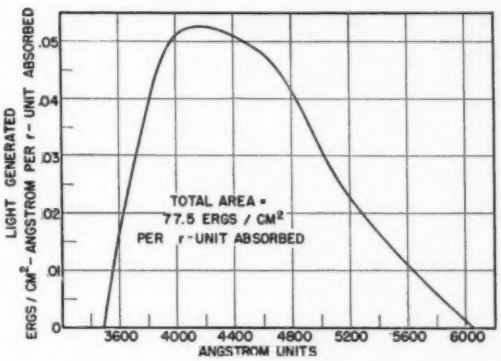

FIG. 4. Fluorescent spectrum of $CaWO_4$ excited by 80 Kv constant potential x-rays. Filter used was ½ mm copper+1 mm aluminum. Screen contained .109 gm/cm² of $CaWO_4$.

An estimate of the accuracy of this determination involves a consideration of such sources of error as the temperature of the lamp, the spectral emissivities of tungsten, the brightness reduction factors, and errors of the photographic emulsion. It appears that the final total energy has been determined to within an accuracy of about 12 percent.

Ib. ANGULAR DISTRIBUTION OF THE LIGHT

In order to calculate the total light emitted from the screen from the measured brightness in a specific direction, it is necessary to know the angular distribution of the emission from the screen. In the case of the filament, this factor was taken care of by using the normal emissivity of tungsten for calculation. For the screen, measurement of the angular distribution was made by means of a photo-multiplier cell illuminated through a collimator consisting of a simple lens and a small diaphragm stop at its focal point. The whole assembly was capable of rotation about an axis lying in the plane of the fluorescent screen.

If the emission of light followed a Lambertian (cosine) distribution, the light received by the photocell would be independent of angle. Actually a falling-off at large angles was observed as shown in Fig. 5. Integration of this curve combined with suitable angular variables yields a constant which relates the total light emitted from the screen to that which would have been emitted from a Lambertian source with the same normal intensity. This factor varies slightly with

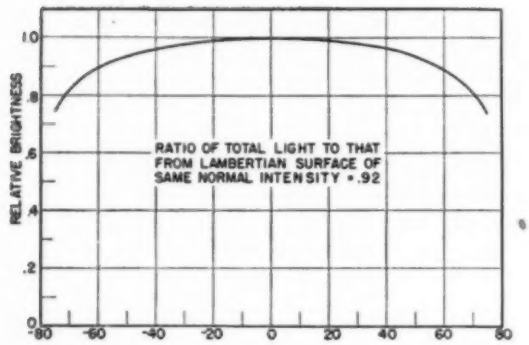

FIG. 5. Angular distribution of light from $CaWO_4$ screen relative to a Lambertian surface.

the wave-length of the exciting x-rays, since the latter affects the distribution of light-generating centers within the screen. Under the conditions of the spectroscopic experiment the $CaWO_4$ screen had a factor of 0.920.

II. TRANSMISSION OF LIGHT IN DIFFUSE SCREENS

The light produced by the x-rays in the interior of the fluorescent layer is eventually transmitted out of the screen by means of a series of reflections and refractions from individual crystals. Part of the light is lost by absorption in the crystals and in the binder, and part finds its way out of the back surface of the layer. Some of the latter may be recovered by means of a reflecting backing, a white mounting card being commonly used.

Since the particles involved are small compared to the area of interest, and the lateral dimensions of the screen are large compared to the thickness, the problem can be treated as if the material were homogeneous and as if the light were traveling in one dimension only, i.e., perpendicular to the screen.

In the following discussion the words "light forward" and "light backward" refer to directions in the same sense as that of the x-rays. Thus with the screen located between the x-ray tube and the observer, the light forward is that seen by the observer and comes from what will be termed the front of the screen; the light backward from the back of the screen is directed toward the x-ray tube.

The first step in the analysis is to derive the reflection and transmission coefficients of a diffuse layer as a function of its thickness. A layer of thickness x (Fig. 6) has by definition a reflection coefficient $R(x)$. If a layer of thickness dx is added to this, a new reflection coefficient will result. The reflection coefficient of the elementary layer itself will to the first order be proportional to its thickness. Let this reflection coefficient be kdx. Similarly, the amount *not* transmitted will be proportional to the thickness to the first order; let this coefficient be αdx. It will be evident that $\alpha \geq k$, being equal to k if there is no true absorption of light in the layer. (In Fig. 6 the layer dx is shown separated from the layer x for convenience in tracing the course of the light. It is to be understood that in this and later derivations the layers are actually continuous.) Light is incident on the combination from the left. A fraction kdx will be reflected from the first layer, a portion $1-\alpha dx$ will be transmitted to the second layer. The amount reflected from the second layer is $(1-\alpha dx)R$, of which a quantity $(1-\alpha dx)^2R$ is transmitted out to the right and adds to the initially reflected light. The portion $kdx(1-\alpha dx)R$ which is returned undergoes an exactly similar set of steps. Summing up the infinite series of rapidly diminishing contributions:

$$kdx+R(1-\alpha dx)^2(1+Rkdx+R^2(kdx)^2+\cdots)$$
$$=kdx+\frac{R(1-\alpha dx)^2}{1-Rkdx}=R(x+dx), \qquad (2.1)$$

the new reflection coefficient $R(x+dx)$ is obtained. Subtracting R from both sides, and

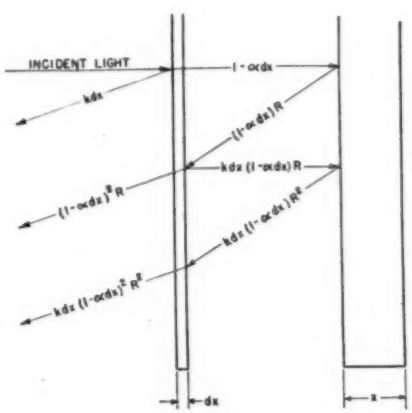

FIG. 6. Schematic representation of light flow for derivation of reflection coefficient formula.

neglecting differentials of higher order than one, we obtain

$$R(x+dx)-R(x)=k(1-2(\alpha/k)R+R^2)dx$$

or

$$\frac{dR}{dx}=k(1-2(\alpha/k)R+R^2).$$

Thus:

$$kx=\int \frac{dR}{[1-2(\alpha/k)R+R^2]},$$

$$kx=-\frac{1}{[(\alpha/k)^2-1]^{\frac{1}{2}}}\tanh^{-1}\frac{R-\alpha/k}{[(\alpha/k)^2-1]^{\frac{1}{2}}}+\text{const.},$$

$$R=\frac{\alpha}{k}+[(\alpha/k)^2-1]^{\frac{1}{2}}\tanh((\alpha^2-k^2)^{\frac{1}{2}}x+\text{const.}). \tag{2.2}$$

The constant is determined by setting $R=0$ when $x=0$, and by further reduction we obtain

$$R=\frac{(k/p)\sinh px}{\cosh px+(\alpha/p)\sinh px}, \tag{2.3}$$

where

$$p\equiv(\alpha^2-k^2)^{\frac{1}{2}}.$$

By similar consideration of the multiple reflections in the transmission case, and by use of formula 2.3, the expression for the transmission coefficient is found to be

$$T=\frac{1}{\cosh px+(\alpha/p)\sinh px} \tag{2.4}$$

where p has the same meaning as before.

The constant p is an important characteristic of the material and represents the degree of absorption. For very large x, 2.4 reduces to

$$T=\text{constant } e^{-px}$$

the usual exponential function, and p plays the role of a linear absorption coefficient. At large x, R approaches a constant, and only after this condition is reached will T be exponential. The physical reason for this is clear; if a thin layer is placed behind another layer, the *incident* light on the new layer is enhanced by the multiple reflections between the two, and only if the original layer is so thick as to have attained the limiting reflection coefficient will the transmission be exponential. The form of these functions is shown in Fig. 7 for values of k and α typical of $CaWo_4$. The values of k and p (or k and α) suffice to describe completely the light yield from the front and back of the screen, as well as the light absorbed, if the thickness and distribution of light sources within the screen are given. These coefficients may be experimentally determined by measuring R and T.

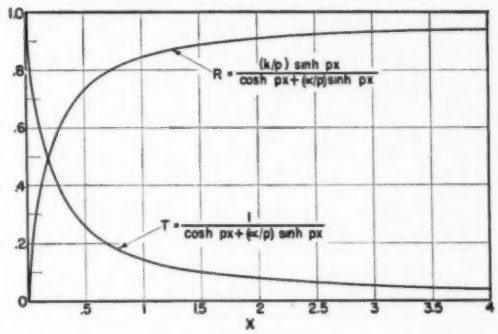

FIG. 7. Reflection and transmission coefficients as a function of thickness (x) of diffusing material.

Determination of the Optical Constants

Values for p, k and α could be obtained in principle by measuring T or R as a function of thickness, by virtue of Eqs. (2.3) and (2.4). In carrying out such an experiment one must make sure, however, that the amount of light from the source and the action of the detector for the light are not affected by introduction of the sample. For example, a ground-glass diffuser is not a suitable source because it is itself reflecting; introduction of the sample will enhance the incident light intensity to a value higher than that measured without the sample. For the same reason the detector must be non-reflecting; a photographic plate, for instance, is not sufficiently absorbing to avoid errors due to multiple reflections.

Since the procurement of such ideal light sources and detectors constitutes a serious experimental difficulty, it seemed preferable to eliminate the error altogether by means of a method which does not require measurement of light intensity in the absence of the sample. A tungsten bulb, suitably housed, was used to illuminate one side of the layer; the brightnesses of the two sides were measured by means of a Macbeth Illuminometer and the ratio of the

brightnesses was taken to be R/T. This was repeated with samples of varying thickness.

By definition, R and T are the results of a scattering process which does not alter the angular distribution of the light. Therefore, Eqs. (2.3) and (2.4) must not be applied indiscriminately to the present case where a nearly parallel light beam is incident on the front of the sample and, upon entering, is gradually scattered in all directions, approaching an equilibrium distribution in direction only as a limiting case. The angular distribution of the light thus varies with depth of penetration, whereas Eqs. (2.3) and (2.4) were derived from an assumed stationary equilibrium for the angular distribution; so the latter is presumed to remain unaffected by further scattering and not to vary with depth.

While this poses a very serious difficulty, generally speaking, for the measurement of arbitrary samples, the calcium tungstate screen has the fortunate quality that its scattering power outweighs its absorbing power by an order of magnitude; consequently determination is possible by examining sufficiently thick samples. If the conversion from parallel light to light with completely random orientation takes place in a relatively thin front layer, further re-distribution will proceed in accordance with the underlying assumptions of Eqs. (2.3) and (2.4).

An empirical criterion of this condition is afforded by inspection of the spatial distribution of the light emerging from the front and back of the screen. For a very thin layer it is clear that while the reflected light has a nearly random distribution, the transmitted light will contain large portions of unscattered light; thus a difference in the angular distribution of the light from the front and the back indicates that equilibrium has not yet been reached. In the thinnest sample used a rough check of the angular distributions showed they were alike and nearly Lambertian. Furthermore, the reflectivity of the thinnest sample was calculated to be 85 percent. Thus addition of further layers can change the reflected light by 10 percent at most and the brightness of the front side is always a good measure of the incident light quantity. For this reason, even though the values of k and α may be somewhat in error due to our use of a parallel beam, this does not apply to the value for p, which can be computed from the logarithmic derivative $d \log T/dx$ for large thicknesses x.

Samples were prepared by soaking an Eastman Ultra-Speed front screen in alcohol and thus removing its fluorescent layer. This layer contained 0.0445 gm/cm² of $CaWO_4$ per cm². It is self-supporting because the internal binder is not soluble in alcohol, whereas the cement used to mount it on the card is soluble. One-inch squares were cut from the layer while still wet, and were superimposed to make up samples of 1, 2, and 4 layers. These were cemented over holes in metal sheets and allowed to dry.

It might be supposed that the protective coating on the layers (a film of cellulose plastic) would violate the assumption of homogeneity of the material. However, consideration of the multiple reflections between the crystalline material boundary and film-air interface show that for the index of refraction of this film the effect is completely negligible for the thicknesses used.

Four points on the R/T curve were determined, at zero, 1, 2, and 4 layers. Values of R/T are shown in Table I. From Eqs. (2.3) and (2.4) we see R/T should be of the form $k/p \sinh px$. Values of k and p were chosen to fit the experimental points, namely, $k=5.55$/layer and $p=0.30$/layer. The third column gives the calculated points for comparison. Since $\alpha^2=k^2+p^2$, α is also 5.55/layer within the experimental error, with the understanding of course that

$$(\alpha^2-k^2)^{\frac{1}{2}}=0.30/\text{layer}.$$

From the fit obtained, the values of k, α, and p are estimated to have probable errors of less than 3 percent. In the following treatment these values have been used, and the thickness x is always measured in terms of one layer as the dimensional unit.

TABLE I.

x (layers)	R/T (exp.)	18.5 sinh.30x
0	0	0
1	5.43±.05	5.63
2	11.8 ±.13	11.8
4	27.6 ±.4	27.9

After these measurements had been evaluated and the results had been used to compute the conversion efficiency and the curves of light yields, it was decided to repeat the measurements of the optical constants of the screen using a diffuse source for the incident light. The sample was mounted over an aperture in an Ulbricht photometric sphere arranged so that the brightness of both sides of the sample could be observed with a Macbeth Illuminometer. These measurements gave a good fit for the ratio $R/T=k/p\sinh px$, using $k=6.0$ and $p=0.33$. Adoption of these new values would change the curves of light yields which are presented below. Since these are meant to be illustrative, and quantitative only pending measurement of the optical constants of an individual sample, it did not seem worth while to recompute them. However, the new constants were used for computation of conversion efficiency.

The Light Distribution in the Screen

Having derived expressions for transmission and reflection of a diffuse layer, one is in a position to compute, for a given distribution of light generation throughout the screen, the fractional amounts emerging from the screen in both the forward and backward directions.

Since the x-ray intensity decreases exponentially with depth of penetration, light production also follows an exponential law, being highest at the back where the x-rays are incident. Consider the element of thickness dx located at a distance x from the back of the screen whose thickness is ϵ (Fig. 8). This element is between two layers, of finite thickness x (layer 1) and $\epsilon-x$ (layer 2), respectively. Of the light dL generated in the element, $\frac{1}{2}$ starts out toward layer 2, while $\frac{1}{2}$ starts toward layer 1. These are subject to multiple reflections as shown in Fig. 8, the lower half being concerned with the light starting toward 2 and the upper with that starting toward 1. The fraction f out the front due to dL is given by the sum of the contributions as before, and

$$f=\frac{1}{2}\frac{T_2(1+R_1)}{1-R_1R_2}. \tag{2.5}$$

The coefficients R_1, R_2 and T_2 are, of course, functions of x and $\epsilon-x$ as in formulas (2.3) and

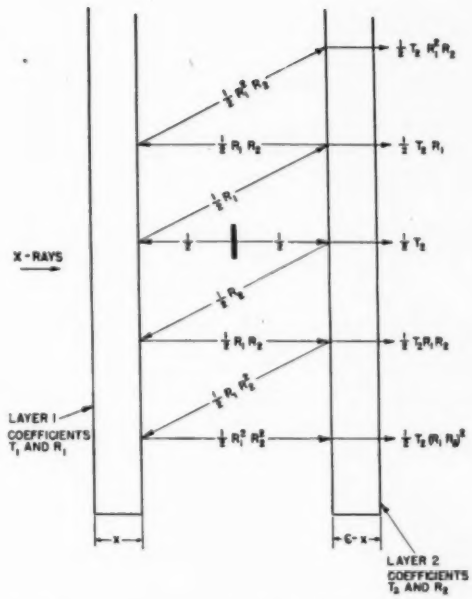

FIG. 8. Schematic representation of light flow from a luminous element within the screen.

(2.4). It is now necessary to multiply f by the light produced in the element dx and integrate over x from 0 to ϵ to obtain the total light out.

If the absorption coefficient of the x-rays is μ, we have by definition that the x-rays absorbed in a layer $dx=I\mu dx$ where I is the intensity of x-rays at the point x. Let $\rho=$conversion efficiency of x-rays into light; the light produced in dx is then $\rho I\mu dx$. But $I=I_0e^{-\mu x}$, where I_0 is the incident x-ray intensity, and $dL=\rho\mu I_0e^{-\mu x}dx$ (2.6)

The forward light yield is then:

$$L=\frac{\rho\mu I_0}{2}\int_0^{\epsilon}e^{-\mu x}\frac{T_{(\epsilon-x)}(1+R_{(x)})}{(1-R_{(x)}R_{(\epsilon-x)})}dx. \tag{2.7}$$

Before performing this integration we shall find it very convenient to derive a relation between the transmission coefficient of the screen as a whole (T_ϵ) and the coefficients of its parts. In Fig. 9 is shown the schematic diagram from which we find:

$$\begin{aligned}&T_\epsilon=T_1T_2(1+R_1R_2+(R_1R_2)^2+\cdots),\\&T_\epsilon=T_1T_2/(1-R_1R_2).\end{aligned} \tag{2.8}$$

Substituting in formula (2.5) we get

$$f=\frac{T_\epsilon}{2}\left(\frac{1}{T_1}+\frac{R_1}{T_1}\right). \tag{2.9}$$

T_ϵ is a constant independent of x, and from 2.3 and 2.4 we have $1/T_1=\cosh px+(\alpha/p)\sinh px$, $R_1/T_1=(k/p)\sinh px$. Formula 2.7 then becomes:

$$L=\frac{\rho\mu I_0 T_\epsilon}{2}\int_0^\epsilon e^{-\mu x}\times\left(\cosh px+\frac{\alpha+k}{p}\sinh px\right)dx. \quad (2.10)$$

In preference to an expression for light out itself, we shall divide L by the total light generated to obtain the fraction F_F which is transmitted out the front of the screen. The total light produced is:

$$\rho I_0(1-e^{-\mu\epsilon})$$

and

$$F_F=\frac{\mu}{(1-e^{-\mu\epsilon})[\cosh p\epsilon+(\alpha/p)\sinh p\epsilon]}\times\int_0^\epsilon e^{-\mu x}\left(\cosh px+\frac{\alpha+k}{p}\sinh px\right)dx. \quad (2.11)$$

Carrying out the integration we obtain the final expression:

$$F_F=\frac{\mu\{(\mu+\alpha+k)-e^{-\mu\epsilon}[(\mu+\alpha+k)\cosh p\epsilon+([\mu(\alpha+k)/p]+p)\sinh p\epsilon]\}}{2(1-e^{-\mu\epsilon})(\mu^2-p^2)(\cosh p\epsilon+(\alpha/p)\sinh p\epsilon)}. \quad (2.12)$$

In an exactly similar manner the formula for the fraction out the back of the screen is found;

$$F_B=\frac{\mu\{(\mu-\alpha-k)(\cosh p\epsilon-e^{-\mu\epsilon})+([\mu(\alpha+k)/p]-p)\sinh p\epsilon\}}{2(1-e^{-\mu\epsilon})(\mu^2-p^2)(\cosh p\epsilon+(\alpha/p)\sinh p\epsilon)}. \quad (2.13)$$

Graphs of these functions are given in Figs. 10 and 11 for various values of μ and ϵ, using $k=5.55$/layer and $p=0.30$/layer. Values of the thickness ϵ are in terms of one-layer units, and μ, the x-ray absorption coefficient is per layer. It is apparent that for zero thickness of screen half of the light is transmitted in each direction regardless of μ. At the limit $\mu\to 0$ light is produced uniformly throughout the screen, and for thicker screens equal amounts of somewhat less than 50 percent are emitted in each direction, the remainder being absorbed in the screen. For thick screens and high μ, the fraction emitted toward the back is much more than 50 percent, while the light forward is much less. For $\mu=\infty$, all of the light is produced in a layer of zero thickness at the back. Half of the light is immediately emitted backwards and a fraction $R(\epsilon)$ of the remaining half is reflected in addition. The fraction out the front is the transmission coefficient times the half originally directed toward the screen. Thus all the curves of Figs. 10 and 11 approach different limits as $\mu\to\infty$.

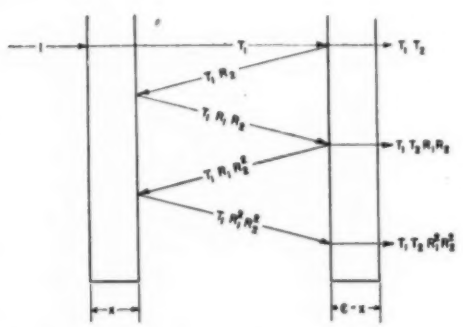

FIG. 9. Light flow diagram for derivation of formula relating partial and total transmission coefficients.

While these curves show wide variations in yields, actually the ranges of μ and ϵ usually encountered in practice are such that the fractions forward and back are fairly close to 50 percent. At 80 kv constant potential, μ is approximately 0.25 per layer; for a screen of $\epsilon=1$ (Eastman Ultra-Speed front) the fraction forward is 47.6 percent, the fraction back 51.2 percent. At higher voltages little error is introduced by assuming 50 percent each way unless the screen is abnormally thick. At the lower voltages, μ rises rapidly, attaining a value of 2.2 at 20 kv and 3 at 17.4 kv. Here the fractions out the front and back are markedly affected by the operating voltage.

Effect of Mounting Card

In practice a screen is never used without a backing of some sort. Usually this is made white, with the intent of recovering the light emitted

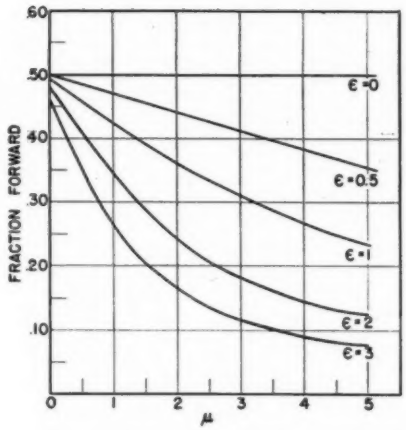

FIG. 10. Fraction of light generated which escapes from the front of the screen as a function of screen thickness (ϵ) and x-ray absorption coefficient (μ).

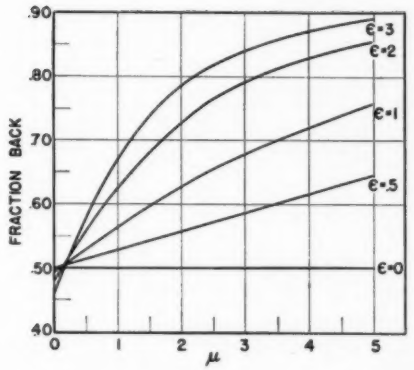

FIG. 11. Fraction of light generated which escapes from the back of the screen as a function of screen thickness (ϵ) and x-ray absorption coefficient (μ).

in the backward direction. The efficacy of this procedure will now be examined. Figure 12 shows schematically a layer of fluorescent material backed by a card of reflection coefficient R_0.

The ratio of the light returned to the light emitted backward from the screen is defined as E.

$$E=R_0T(1+RR_0+(RR_0)^2+\cdots, \qquad (2.14)$$

$$E=\frac{R_0T}{1-RR_0}.$$

By way of example, if a screen of thickness $\epsilon=1$, $R=0.844$ and $T=0.15$, is backed by a card of reflection coefficient $R_0=0.80$, one finds $E=0.37$, so of all light which was previously lost out the back of the screen, only 37 percent is recovered by using a backing card of 80 percent reflectivity. This is the result of the "whiteness" of the calcium tungstate; if the card is not of superior reflecting power, it is of small value. Some of this loss is in the layer itself, but the major portion goes into the card. The card upon which the Eastman screen was mounted had a diffuse reflection coefficient of 0.84. Table II illustrates the role played by this mounting card in the light losses. These data were computed for 80 kv, using the constants $k=6.0$ and $p=0.33$. At higher voltages very little change takes place in the light distribution, and the tabulated values will remain essentially constant. At lower voltages the losses will increase considerably, reaching a limit at $\mu=0$ of 52 percent for the thin screen and 74 percent for the thick screen.

The increase in light to be expected from the use of a card has been plotted in Fig. 13. At first glance these numbers may seem quite high; however, it must be remembered that in the vast majority of cases μ is 0.5 or smaller, so that the increase will seldom exceed 40 percent.

Two experimental checks of the above formulas were made. In the first the light from a fluorescent screen was measured with and without a backing card. In the second, two screens of different thickness were measured and the expected relative light output calculated on the basis of the above formulas. Both tests checked calculated values within 3 percent.

So far we have not discussed the variation with thickness of the amount of x-rays absorbed. This, of course, is the most important factor in determining light output for thin screens. With increasing screen thickness the x-rays are more and more nearly completely absorbed; in addi-

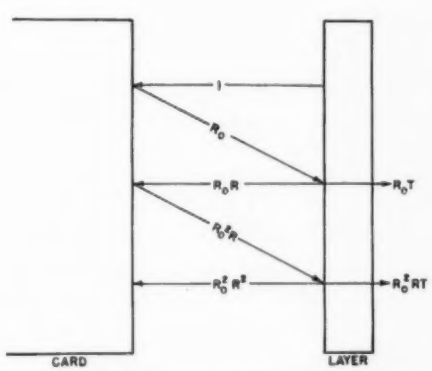

FIG. 12. Light flow diagram for derivation of effect of reflecting card.

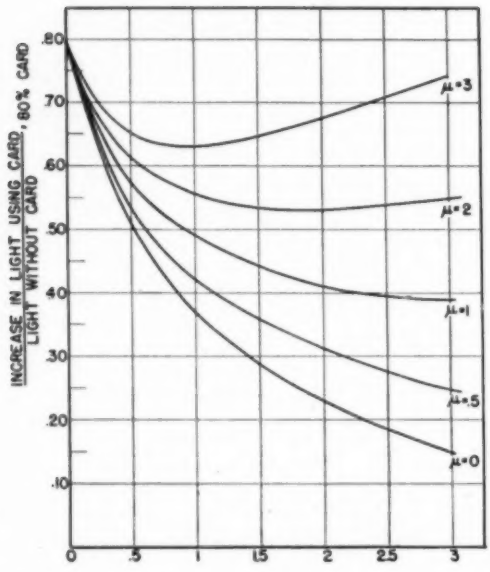

FIG. 13. Increase in light to be gained by using a backing card with 80 percent reflectance, as a function of screen thickness (ϵ) and x-ray absorption coefficient (μ).

tion, the effectiveness of the card backing decreases and losses in the phosphor and binder begin to gain importance. Thus the light output reaches a maximum at a thickness which will depend upon the absorption coefficient (or voltage) of the x-rays. In Figs. 14 and 15 is shown the utilization factor U, defined as the ratio of the light obtained from the front of the screen to the total light which would have been generated had all the x-rays been absorbed. The curves of Fig. 14 were calculated for a screen without mounting card, those of Fig. 15 with a mounting card having 100 percent reflection. It will be seen that in practical cases the utilization is seldom over 30 percent.

In the case of a "back" screen one is interested in the light out the back, i.e., toward the x-ray tube. This quantity increases with the screen thickness, but the gain is very slight beyond a certain point. A thick layer of $CaWO_4$ is much whiter than any available cardboard; for a simple example we can just set the thickness of the back screen at infinity and inquire how the utilization factor varies with μ. If ϵ is infinite, F_B in formula 2.13 is the utilization factor, since all the x-rays are absorbed. The formula reduces to:

$$U_B=[(p+\alpha+k)/2(p+\alpha)](\mu/\mu+p). \quad (2.14)$$

The factor is plotted in Fig. 16 using values of p and α for $CaWO_4$ as before. It is seen that even with an infinitely thick screen the utilization is not very high for μ less than 0.3, i.e., for x-ray voltages above 80 kv.

In the design of screens for radiographic purposes an all-important consideration is the resolving power of the screen-film combination. In general, the thickness of the screen is largely determined by the stringency of this requirement. No treatment of resolving power is attempted here, because the primary purpose of the investigation is to measure the true efficiency of the $CaWO_4$ screen. The curves in the preceding portion show accurately the light produced as the screen thickness and x-ray absorption coefficient vary, but they form a basis for selection of screen thickness only on the assumption that resolving power is to be ignored. For this reason it is of little value to extend the treatment to

TABLE II. Light losses in two typical x-ray intensifying screens.

	Thin screen (1 layer) .045 gm/cm² $CaWO_4$	Thick screen 2.45 layer .109 gm/cm² $CaWO_4$
Light lost in phosphor and binder	2.2%	9.6%
Light lost in mounting card	28.7%	36.0%
Light yield (total)	69.1%	54.4%

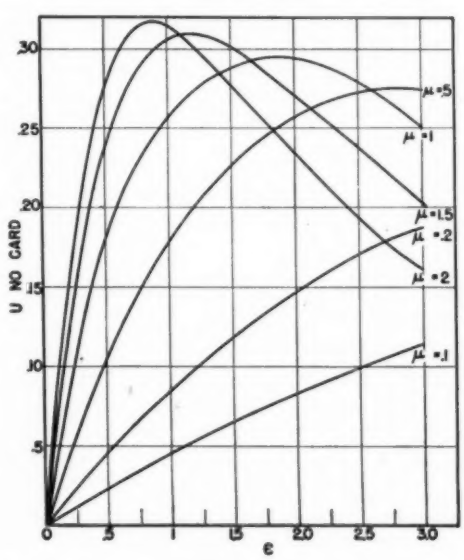

FIG. 14. X-ray utilization factors for a screen with a non-reflecting backing.

other cases, such as a front and back screen combination. The information presented here is sufficient to calculate the light yield of any such combination, given the absorption coefficient, thicknesses, and mounting card reflectances of the screens used.

It should be pointed out here that if the film used with a screen is itself reflecting, all of the light will not be absorbed in the film. Measured white-light reflectances of x-ray screen film are high enough to cause errors of 8 percent with an Ultra-Speed front screen; however, it is quite possible that the reflectance is different for the blue and ultraviolet light of the screens.

III. EFFICIENCY OF FLUORESCENCE

To obtain the x-ray energy absorbed in the screen, it is necessary to have a knowledge of the energy spectrum of the incident radiation and of the absorption of energy from this spectrum by the screen.

Information as to the exact continuous spectrum of x-ray radiation from a thick target is not available in the literature. Curves originally published by Ulrey[1] have been reprinted in all the texts for 25 years in spite of the fact that

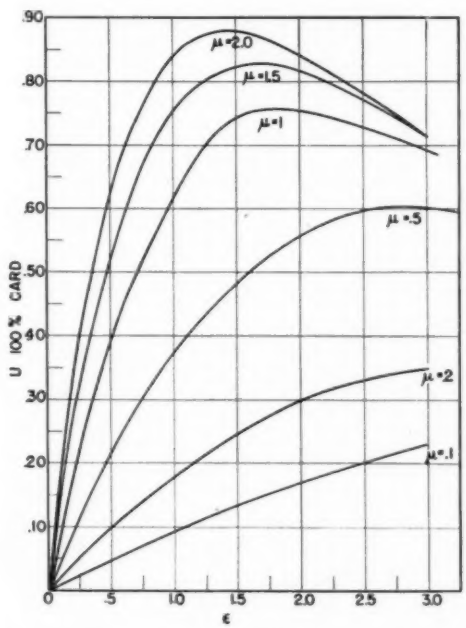

FIG. 15. X-ray utilization factors for a screen with a perfectly reflecting back.

[1] C. T. Ulrey, Phys. Rev. **11**, 401 (1918).

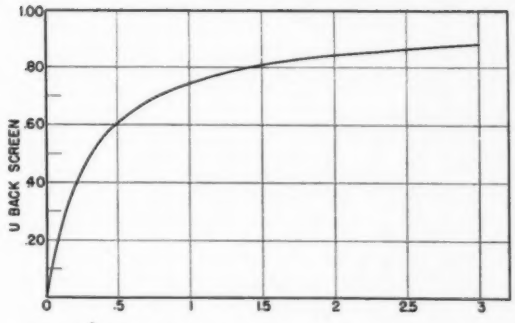

FIG. 16. X-ray utilization factor for a very thick screen used as a back screen, plotted against μ.

they were known to be in serious error at the time of publication. Our use of these curves in combination with the known absorption coefficients of $CaWO_4$ led to obvious and large discrepancies with the measured absorption of the screen, and an independent determination of the x-ray spectrum seemed desirable. Figure 17 shows the energy distribution from the x-ray tube used by us, as determined by Mr. R. L. Longini with a method to be published by him at a later date. This spectrum applies to the tube run at 80 kvc with $\frac{1}{2}$ mm copper and 1 mm aluminum filter. On the same figure is given the curve of energy absorbed by the screen, calculated from the known total absorption coefficients. The integrated areas under these curves, when converted to ionizing power, agreed with our measured absorption value.

All x-radiation which leaves the screen is considered not to be part of the input for the purpose of our computation of conversion efficiency. Our measurement of the undeflected x-ray beam leaving the screen fails to include the scattered and fluorescent x-radiation which leaves under large angles. The former can be shown to be negligible at the voltages used; the latter is important only for energies above the K-absorption edge of tungsten. Of the 299 ergs absorbed in the region to the left of the K-edge in Fig. 17, absorption by K-electron ejection includes 190 ergs which will be re-emitted as K-radiation. Of this, about 5 percent is converted into Auger electrons and 26.5 percent of the remainder is reabsorbed in our particular thickness of screen, so that 133 ergs escaped as x-rays. Thus the total x-ray input must be reduced from 714 ergs to 581 ergs.

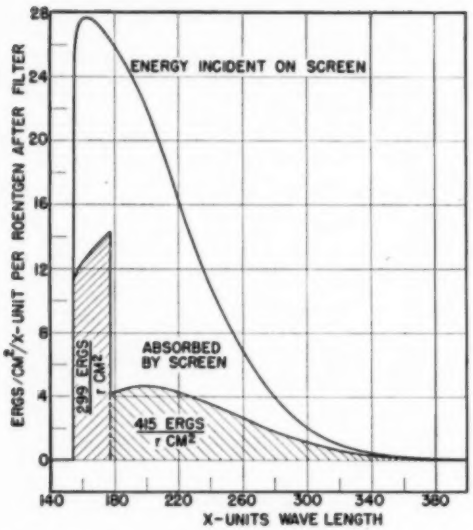

FIG. 17. Spectral energy distributions of x-rays incident on the screen and x-rays absorbed by the screen.

We are now in a position to calculate the efficiency of calcium tungstate. From Part I we have the light out of one side as 2.34 ergs/cm²/sec with an incident radiation of 8.92 r/min. At 581 ergs/cm² r we have then 86.2 ergs/cm²/sec absorbed in the screen. Thus the "gross" efficiency is 2.72 percent. From Part II, however, we find that the screen emits only 54.5 percent of the light generated, and the intrinsic efficiency of the calcium tungstate is finally found to be 5.0 percent.

This efficiency may be expected to vary only slightly with the wave-length of the x-radiation involved, since one electron ejected by an x-photon excites many fluorescent centers and dissipates its energy gradually.

It is of interest to compute the number of fluorescent centers activated by a single absorbed x-photon. Taking the average wave-length of the absorbed x-rays as 0.22 angstroms, and the average wave-length of the light produced as 4400 angstroms, we see that energetically it would be possible to get 20,000 light quanta from one x-photon. Since the material is only 5 percent efficient, however, on the average each x-photon absorbed produces 1000 light quanta.

Pressure and Oil Flow in Oil-filled Cables at Load Variations

HANS LOTTRUP KNUDSEN
Holstebro, Denmark

(Received September 23, 1946)

This paper presents a method for calculating pressure and oil flow in a section of an oil-filled cable at load variations with due regard to both the hydraulic resistance of the oil canals and the elasticity of the sheath and the pressure armor, if any, and the compressibility of the oil. The present article restricts itself to cable sections terminated with oil reservoirs in which the pressure is constant; in a forthcoming paper this restriction will be dropped. Formulas are given for pressure, oil current, and amount of oil which flows through a cross section of the cable for an arbitrarily prescribed oil expansion per unit length. These formulas are applied to the following oil expansion functions: $S_0 \cdot 1$, $d/dt(N_0 \cdot 1)$, $e^{-t/T} \cdot 1$, and $1/\sqrt{t} \cdot 1$, which represent the oil expansion or terms occurring in the series giving the oil expansion in some important cases. Generalized functions are plotted for the pressure at the midpoint, the oil current at the endpoints, and the amount of oil which passes the endpoints for the above mentioned oil expansion functions. Using these generalized functions, the calculation of pressure and oil flow, with the simplifying assumptions made here, is reduced to elementary operations. Numerical examples illustrate the use of the given formulas and curves.

LIST OF SYMBOLS

a	cm^2	Area of oil canal.
A	cm^2	Oil volume per unit length.
c	$kg^{-1}\ cm^4$	Capacitance per unit length.
c_1	$kg^{-1}\ cm^4$	Capacitance per unit length corresponding to the elasticity of sheath and pressure armor.
c_2	$kg^{-1}\ cm^4$	Capacitance per unit length corresponding to the compressibility of oil.
C	$kg^{-1}\ cm^5$	Capacitance of the entire cable.
d	cm	Diameter of oil canal in single-core cable.
D	cm	Diameter of cable under sheath.
E	$kg\ cm^{-2}$	Modulus of elasticity for the sheath material.
f	cm	Perimeter of the conductors in which short-circuit current flows.
$F(x)$	1	Function defined in (54).
$I(x, t)$	$cm^3\ sec.^{-1}$	Current of oil.
k	$kg^{-1}\ cm^2$	Specific compressibility of oil.
K_0	$cm^2\ sec.^{-1}$	Constant factor in an expression for the oil expansion.
l	cm	Arbitrarily defined length in cable cross section.
L	cm	Length of cable.
$M(x, t)$	cm^3	Amount of oil which flows through a cross section of the cable.
N_0	cm^2	Instantaneous oil expansion per unit length.
p	°C cm W^{-1}	Specific thermal resistance for insulation.
$P(t)$	$cm^{-1}\ W$	Effect transferred from conductors to insulation per unit length.
q	$°C^{-1}\ cm^{-3}\ W\ sec.$	Specific heat of insulation.
r	$kg\ cm^{-6}\ sec.$	Hydraulic resistance in cable per unit length.
R	$kg\ cm^{-5}\ sec.$	Hydraulic resistance of entire cable.
$S(t)$	$cm^2\ sec.^{-1}$	Oil expansion per unit time per unit length.
S_0	$cm^2\ sec.^{-1}$	Constant factor in expression for oil expansion.
t	sec.	Time.
T	sec.	Time constant occurring in the expression for oil expansion.
$V(x, t)$	$kg\ cm^{-2}$	Pressure.
β	$°C^{-1}$	Volumetric expansion coefficient of oil.
β'	$°C^{-1}$	Volumetric expansion coefficient of insulation.
γ	$g\ cm^{-3}$	Density of oil.
δ	cm	Sheath thickness.
$\vartheta(x, t)$	°C	Temperature in insulation.
ϑ_0	°C	Temperature of conductors after short circuit.
ν	centistokes	Viscosity of oil.

PRESSURE AND FLOW QUALITATIVELY REGARDED

IN the calculation of oil-filled cable systems it is important to have a method for computing the variations of the pressure for a certain system under the most severe load variations to which

it can be subjected in service. These commonly consist of (1) switching off the load and (2) short circuiting. In the first case the oil in the cable is cooled and consequently the pressure decreases below the normal value until an amount of oil equaling the contraction of the oil has flowed into the cable. In consequence of the diminished pressure the electrical strength of the cable may decrease so much that breakdown occurs. On the other hand, in the case of a short circuit the oil expands rapidly because of the rise in temperature, and the pressure in the cable will for some time increase and later decrease as the surplus of the oil flows towards the oil reservoirs of the system. In the case of a short circuit the pressure in the cable may increase so much that there is a risk of the sheath and the pressure armor being destroyed.

All calculations of the pressure must be based upon the variations of the temperature in the cable with the given load variations. Several methods of computing the variations of the temperature and the oil expansion at load variations in cables placed under different circumstances have been described in the literature. Some of these methods will be mentioned later.

When the oil expansion has been calculated, the variations of the pressure and the oil flow will be investigated. The dependence of the temperature on load variations has been treated thoroughly in the literature. That is not the case with the pressure and the oil flow.

In many cases the increase or decrease in pressure for the greatest expansion of oil per unit time at load variations has been calculated under the assumption of stationary oil flow in the cable. For oil cable systems with different types of oil reservoirs, Emanueli[1] has developed a theory for the calculation of pressure and oil flow, in which the pressure drop along the cable is calculated as if the oil flow were stationary. Shanklin and Buller[2] make the same assumption in their calculations of the pressure drop.

H. Spanne, chief engineer at Sieverts Kabelverk, Sundbyberg, Sweden, however, demonstrated about ten years ago in a factory bulletin, that the elasticity of the sheath and of the pressure armor, if any, and the compressibility of the oil in an oil-filled cable greatly limit the pressure variations occurring at load changes. Spanne has also made an estimate of the pressure variations.

In the present article a method has been developed for calculating the variations of pressure and the oil flow in an oil-filled cable with reservoirs at both ends, for an oil expansion given as a function of the time, with due regard to the flow resistance in the cable as well as to the elasticity of the sheath and the pressure armor, if any, and to the compressibility of the oil. Only those cases in which the expansion of oil per unit time and per unit length is the same at every point of the cable have been treated here.

SIMPLIFYING ASSUMPTIONS

The following assumptions are the most important of those made in this paper:

1. All deformations in the cable are purely elastic.
2. No force is needed to accelerate the oil in the canals.
3. The viscosity of the oil in the oil canals is constant.
4. The pressure in the oil reservoirs is constant.

Assumptions 1 and 2 are approximately satisfied in most practical oil-filled cables. As the viscosity of the oil varies much with the temperature, 3, however, is not well satisfied. The difficulties involved in solving the problem are, however, greatly increased if assumption 3 is not made. Assumption 4 is well satisfied for cable systems with oil reservoirs consisting of oil tanks with atmospheric pressure at the surface of the oil. However, assumption 4 is often rather well satisfied in other types of oil reservoirs, too, as the oil expansion in the cable for a load variation often is small compared with the oil expansion corresponding to the total temperature variation for which the system has been constructed. (The total temperature includes, for instance, the seasonal change of temperature.) This statement applies especially in the case of a short circuit in which the temperature of the conductors may certainly be rather high, but in which the total developed heat energy, and consequently also the oil expansion, often are small.

An article is being prepared, in which assumption 4 is not made, due regard on the contrary being given to the characteristics of different oil reservoirs.

[1] L. Emanueli, Trans. A.I.E.E. **47**, 186 (1928).
[2] G. B. Shanklin and F. H. Buller, Trans. A.I.E.E. **50**, 1411 (1931).

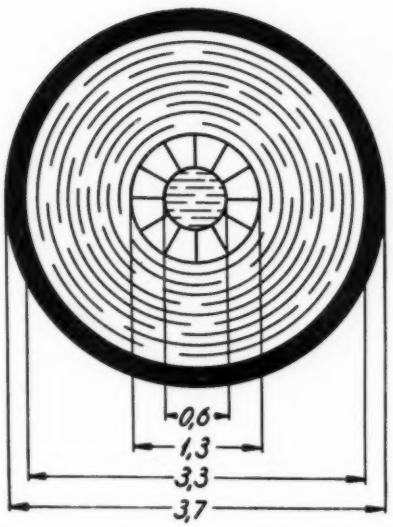

FIG. 1. Single core oil-filled cable, $77/\sqrt{3}kV$, 1×95 mm.[2]

MATHEMATICAL FORMULATION

The mathematical expressions for the flow in an oil-filled cable depend on how the flowing medium is defined. This, for example, can be defined as the mass of the oil, or as the volume of the oil. Here we shall base the calculations on a third and more convenient definition, defining the flowing medium as the volume of the oil reduced to constant pressure.

The amount of medium per unit length at a certain point of the cable will then increase proportionally to the pressure because of the elasticity of the sheath and of the pressure armor, if any, as well as of the compressibility of the oil. We define the capacitance per unit length, c, as the ratio of the increase in amount of medium per unit length to the increase of pressure. The capacitance c is then composed of two parts, one part c_1, arising from the elasticity of the sheath and the pressure armor, and another part c_2, arising from the compressibility of the oil.

When no pressure armor is present, the capacitance c_1 for a cable with a sheath of thickness δ, diameter D, and modulus of elasticity E is

$$c_1=\frac{\pi D^3}{4\delta E}. \tag{1}$$

It is a trivial matter to develop the corresponding formula for cables with a pressure armor.

c_2 is calculated from the compressibility of the oil, k, and the amount of oil per unit length, A.

$$c_2=kA. \tag{2}$$

c is thus

$$c=c_1+c_2. \tag{3}$$

The current of the medium is defined as the amount of oil which passes a section of the cable per unit time. The resistance per unit length is defined as the ratio of the pressure drop per unit length to the current.

The flow at the moderate currents in question will be laminar, and r can consequently be expressed as follows,[3]

$$r=B\frac{\gamma\nu}{l^4}, \tag{4}$$

where γ is the density, ν the kinematic viscosity of the oil, l a length which increases proportional to the linear dimensions of the section of the oil canal, and B a constant which merely depends on the shape of the oil canal and the way in which l has been defined. If l stands for the inner diameter of oil canals with a circular section one gets

$$B=\frac{128}{9.81\cdot\pi}\cdot10^{-7}=4.15\cdot10^{-7}.$$

For a cable with a length L the total capacitance is $C=Lc$ and the total resistance $R=Lr$. The time constant RC for the oil flow in the cable is a measure of the rate at which disturbances in the state of equilibrium of the cable are smoothed. In order to give an idea of the order of magnitude of the time constant it has been computed below in a practical case for two different temperatures.

Example 1

The time constant at the temperatures 20°C and 40°C shall be calculated for an oil-filled cable $77\sqrt{3}kV$, 1×95 mm², without pressure armor and with the principal dimensions as shown in Fig. 1.

$D=3.3$ cm,

$d=0.6$ cm,

[3] *Handbuch der Physik* (1927), Vol. 7, p. 103.

$\delta = 0.2$ cm,

$A = 3.3$ cm^2,

$L = 10^5$ cm,

$E = 1.7 \cdot 10^5$ kg cm^{-2},

$k = 8 \cdot 10^{-5}$ kg cm^2,

$$\gamma_\nu = \begin{cases} 44.8 \text{ centipoise for } 20°\text{C} \\ 16.4 \text{ centipoise for } 40°\text{C}, \end{cases}$$

$$c_1 = \frac{\pi \cdot 3.3^3}{4 \cdot 0.2 \cdot 1.7 \cdot 10^5} = 8.3 \cdot 10^{-4} \text{ kg}^{-1} \text{ cm}^4,$$

$$c_2 = 8 \cdot 10^{-5} \cdot 3.3 = 2.6 \cdot 10^{-4} \text{ kg}^{-1} \text{ cm}^4,$$

$$c = 1.09 \cdot 10^{-3} \text{ kg}^{-1} \text{ cm}^4,$$

$$r = \frac{128}{9.81 \cdot \pi} \cdot 10^{-7} \cdot \frac{\gamma_\nu}{0.6^4} = 3.2 \cdot 10^{-6} \cdot \gamma_\nu$$

$$= \begin{cases} 1.43 \cdot 10^{-4} \text{ kg cm}^{-6} \text{ sec. for } 20°\text{C} \\ 5.3 \cdot 10^{-5} \text{ kg cm}^{-6} \text{ sec. for } 40°\text{C}, \end{cases}$$

$$RC = rcL^2 = \begin{cases} (1.43 \cdot 10^{-4}) \cdot (1.09 \cdot 10^{-3}) \cdot 10^{10} \\ \qquad = 1560 \text{ sec. for } 20°\text{C}, \\ (5.3 \cdot 10^{-5}) \cdot (1.09 \cdot 10^{-3}) \cdot 10^{10} \\ \qquad = 580 \text{ sec. for } 40°\text{C}. \end{cases}$$

This example shows that the time constant for the oil flow is not negligible compared to the intervals of time commonly necessary for smoothing the temperature in a cable under load variations. This means that the elasticity of the sheath and the compressibility of the oil will limit the pressure variations in the cable with changes in load.

The differential equations and the boundary conditions for the oil flow will now be given. Because we have assumed that the cable has constant parameters, without making the treatment of the problem less general we can suppose that the static pressure in the cable and consequently also the pressure at the endpoints of the cable are zero at any moment. Over the dynamic pressure distribution, calculated according to this assumption, we can thus superimpose the static pressure distribution in the cable. In this paper only the dynamic pressure distribution is considered. For a given oil expansion per unit length of the cable per unit time, $S(t)$, we shall

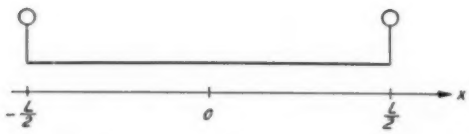

FIG. 2. Coordinate system along a cable section terminated with oil reservoirs.

calculate as functions of time and position the pressure V, the current I, and the amount of oil which flows through a cross section of the cable, M.

A coordinate axis is placed along the cable with the origin at the midpoint (see Fig. 2). V and I then satisfy the following partial differential equations.

$$c\frac{\partial V}{\partial t} = -\frac{1}{r}\frac{\partial^2 V}{\partial x^2} + S, \tag{5}$$

$$I = -\frac{1}{r}\frac{\partial V}{\partial x}, \tag{6}$$

$$V = 0 \text{ for } x = \begin{cases} -L/2 \\ L/2 \end{cases} \quad 0 < t < \infty, \tag{7}$$

$$V = 0 \text{ for } t < 0, \quad -L/2 < x < L/2. \tag{8}$$

Equations formally identical with the equations given above are obtained for several problems within other domains of physics. Suppose we have a metallic wire, isolated against heat, the length being L, with the heat conduction resistance per unit length r, the heat capacitance per unit length c, and with the endpoints at the temperature zero. If an electrical current producing the effect per unit length $S(t)$ is flowing in the wire, the temperature V and the heat current I satisfy Eqs. (5)–(8).

There also exists an electrical analogy to the problem in question. If current sources of the strength per unit length $S(t)$ are supposed homogeneously distributed along a telegraph cable of length L, without inductance and leakage but with resistance per unit length r, capacitance per unit length c (Thomson cable), and with the ends short-circuited, the potential V and the current I will satisfy Eqs. (5)–(8).

In the oil-flow problem the mass of the oil corresponds to the inductance of the cable in the electrical analogy. The mass of the oil has no corresponding meaning in the problem of heat conduction.

It is convenient to solve first the problem given by Eqs. (5)–(8) for $S(t)=S_0\cdot\mathbf{1}$, where S_0 is a constant.

PRESSURE AND FLOW WITH CONSTANT OIL EXPANSION $S_0\cdot 1$

The thermal analogy to this problem has been treated by Straneo,[4] Schaufelberger,[5] and Weinreich[6] for use in measuring the electrical and thermal constants of metallic wires. The authors mentioned above solve the problem by use of eigenfunctions following classical methods.

The problem, however, is very conveniently solved by Heaviside's operational calculus. The appropriate method has been described e.g., by Dahr[7] in his treatment of the telegraphist's equation for transmission lines in which electromotive forces are induced. (See also Jeffrey's treatment of related problems.[8]) For convenient reference the application of the method on the present problem is briefly outlined below.

Introducing the operators

$$\mathfrak{L}V(x,t)=v(x,p), \tag{9}$$

$$\mathfrak{L}I(x,t)=i(x,p), \tag{10}$$

Eqs. (5)–(8) are transformed into the following equations:

$$cpv=-\frac{1}{r}\frac{d^2v}{dx^2}+S_0, \tag{11}$$

$$i=-\frac{1}{r}\frac{dv}{dx}, \tag{12}$$

$$v=0 \text{ for } x=\begin{cases}-L/2\\ L/2.\end{cases} \tag{13}$$

First the more simple problem of a point source 1 acting at the point $x=\xi$ is solved. For the pressure and the current in this problem the differential equations that are obtained from (11) and (12) by setting $S_0=0$ are valid, while to the boundary condition (13) are added the conditions

$$v(\xi-0)=v(\xi+0), \tag{14}$$

$$i(\xi-0)+1=i(\xi+0). \tag{15}$$

As the solution of this problem one gets the following expression for the pressure, which in this special case will be called $w(x,\xi)$,

$$w(x,\xi)=\begin{cases}-rL\dfrac{\sinh\left(-\frac{1}{2}+\frac{\xi}{L}\right)(pRC)^{\frac{1}{2}}\sinh\left(\frac{1}{2}+\frac{x}{L}\right)(pRC)^{\frac{1}{2}}}{(pRC)^{\frac{1}{2}}\sinh(pRC)^{\frac{1}{2}}}=w_1(x,\xi) \text{ for } -\dfrac{L}{2}<x<\xi\\[2ex] -rL\dfrac{\sinh\left(\frac{1}{2}+\frac{\xi}{L}\right)(pRC)^{\frac{1}{2}}\sinh\left(-\frac{1}{2}+\frac{x}{L}\right)(pRC)^{\frac{1}{2}}}{(pRC)^{\frac{1}{2}}\sinh(pRC)^{\frac{1}{2}}}=w_2(x,\xi) \text{ for } \xi<x<\dfrac{L}{2}.\end{cases} \tag{16}$$

The expression for v, in the case of a constant, homogenously distributed source, is now obtained by integration of S_0w over the entire length of the cable

$$v(x,p)=S_0\int_{-L/2}^{L/2}w(x,\xi)d\xi=S_0\left[\int_{-L/2}^{x}w_2(x,\xi)d\xi+\int_{x}^{L/2}w_1(x,\xi)d\xi\right]$$

$$=S_0rL^2\left[\frac{1}{pRC}-\frac{\sinh\left(\frac{1}{2}+\frac{x}{L}\right)(pRC)^{\frac{1}{2}}-\sinh\left(-\frac{1}{2}+\frac{x}{L}\right)(pRC)^{\frac{1}{2}}}{pRC\sinh(pRC)^{\frac{1}{2}}}\right]. \tag{17}$$

[4] P. Straneo, Roma. Rend. Acc. dei Lincei (Ser. 5) **7**, 206 (1898).
[5] W. Schaufelberger, Ann. d. Physik **7**, 589 (1902).
[6] W. Weinreich, Zs. Math. (Leipzig) **63**, 1 (1914).
[7] K. Dahr, *A Course of Integrational and Operational Calculus* (V. Pettersons Bokindustriaktiebolag, Stockholm, 1935), p. 44.
[8] H. Jeffreys, "Operational Methods in Mathematical Physics," Cambridge Tracts in Math. and Math. Ph. **23**, 49 (1931).

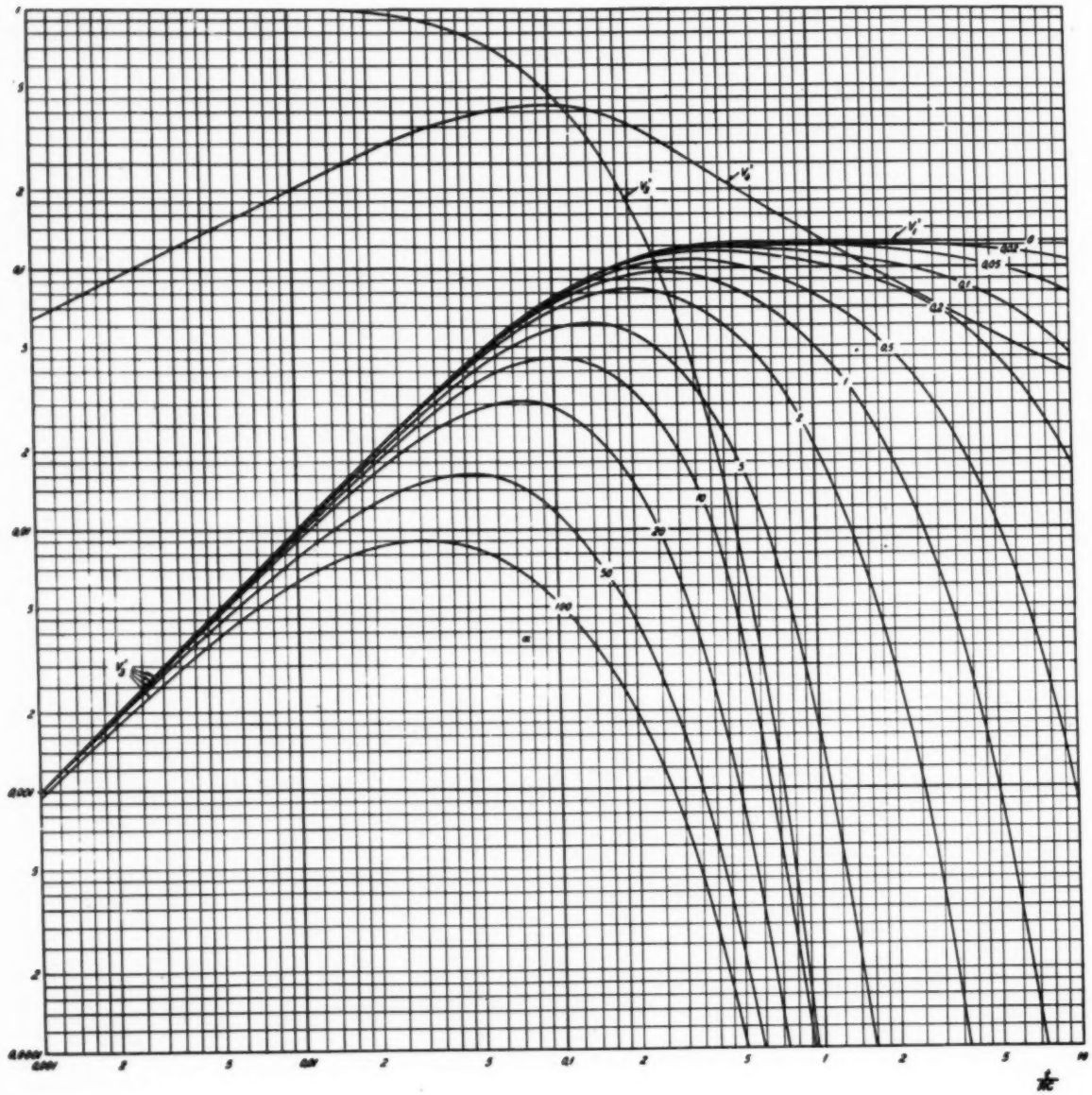

FIG. 3. Generalized functions used in the calculation of the pressure at the midpoint of a cable section with a time constant for the oil flow RC.

$V_1'(t/RC)$ applies in the case of an oil expansion $S(t) = 1 \cdot 1$.
$V_2'(t/RC)$ applies in the case of an oil expansion $S(t) = (d/dt)(1 \cdot 1)$.
$V_3'(t/RC)$ applies in the case of an oil expansion $S(t) = e^{-\alpha t/RC} \cdot 1$.
$V_4'(t/RC)$ applies in the case of an oil expansion $S(t) = 1/(t)^{\frac{1}{2}} \cdot 1$.

The time function for operators of this type can be obtained either by expanding the operator in an infinite series of terms containing exponential functions and transforming this series, term by term, or by applying Heaviside's expansion theorem. The first method corresponds to expressing the solution in reflected waves as demonstrated e.g., by Wagner,[9] whereas by the last method the solution is expressed in eigenfunctions. Here we shall use the last method.

According to Heaviside's expansion theorem the time function $H(t)$ that corresponds to an

[9] K. W. Wagner, Operatorenrechnung (Johann Ambrosius Barth Verlag, Leipzig, 1940), p. 196.

operator $f(p)/g(p)$, where $f(p)$ and $g(p)$ are functions of p, which satisfy certain conditions, and where $g(p)=0$ has the simple roots p_n, $n=1, 2, 3, \cdots$, is

$$H(t)=\mathfrak{L}^{-1}\frac{f(p)}{g(p)}=\frac{f(0)}{g(0)}+\sum\frac{f(p_n)e^{p_nt}}{p_ng'(p_n)}. \quad (18)$$

If we write the operator v (17) as follows

$$v=\frac{f(p)}{g(p)}, \quad (19)$$

where

$$f(p)=S_0rL^2\frac{1}{(pRC)^{\frac{1}{2}}}\left[\sinh(pRC)^{\frac{1}{2}}-\sinh\left(\frac{1}{2}+\frac{x}{L}\right)(pRC)^{\frac{1}{2}}+\sinh\left(-\frac{1}{2}+\frac{x}{L}\right)(pRC)^{\frac{1}{2}}\right], \quad (20)$$

$$g(p)=(pRC)^{\frac{1}{2}}\sinh(pRC)^{\frac{1}{2}}, \quad (21)$$

$v=f(p)/g(p)$ satisfies the conditions for the use of the formula (18). The roots of the equation

$$g(p)=(pRC)^{\frac{1}{2}}\sinh(pRC)^{\frac{1}{2}}=0, \quad (22)$$

different from zero are

$$(p_nRC)^{\frac{1}{2}}=\pm jn\pi, \quad n=1, 2, 3, \cdots, \quad (23)$$

or

$$p_n=-\frac{n^2\pi^2}{RC}, \quad n=1, 2, 3, \cdots. \quad (24)$$

The time function $V=\mathfrak{L}^{-1}v$ is then

$$V(x, t)=S_0rL^2\left\{\frac{1}{8}-\frac{1}{2}\left(\frac{x}{L}\right)^2-\frac{4}{\pi^3}\sum_{n=0}^{\infty}\frac{(-1)^n}{(2n+1)^3}\cos\frac{x}{L}(2n+1)\pi\times\exp\left[-\frac{(2n+1)^2\pi^2t}{RC}\right]\right\}. \quad (25)$$

For $t=0$ the term containing the sign of summation expresses the Fourier series of $\frac{1}{8}-\frac{1}{2}(x/L)^2$ in the interval $-L/2<x<L/2$. V can thus be expressed in the following way

$$V(x, t)=S_0rL^2\frac{4}{\pi^3}\sum_{n=0}^{\infty}\frac{(-1)^n}{(2n+1)^3}\cos\frac{x}{L}(2n+1)\pi\times\left\{1-\exp\left[-\frac{(2n+1)^2\pi^2t}{RC}\right]\right\}. \quad (26)$$

For $x=0$ this leads to

$$V(0, t)=S_0rL^2\frac{4}{\pi^3}\sum_{n=0}^{\infty}\frac{(-1)^n}{(2n+1)^3}\times\left\{1-\exp\left[-\frac{(2n+1)^2\pi^2t}{RC}\right]\right\}. \quad (27)$$

$[V(0, t)/S_0rL^2]=V_1'$ has been plotted as a function of t/RC in Fig. 3.

I is calculated from (6) and (26)

$$I(x, t)=S_0L\frac{4}{\pi^2}\sum_{n=0}^{\infty}\frac{(-1)^n}{(2n+1)^2}\sin\frac{x}{L}(2n+1)\pi\times\left\{1-\exp\left[-\frac{(2n+1)^2\pi^2t}{RC}\right]\right\}. \quad (28)$$

For $x=\pm L/2$ this leads to

$$I\left(\pm\frac{L}{2}, t\right)=\pm S_0L\frac{4}{\pi^2}\sum_{n=0}^{\infty}\frac{1}{(2n+1)^2}\times\left\{1-\exp\left[-\frac{(2n+1)^2\pi^2t}{RC}\right]\right\}. \quad (29)$$

$[I(\pm(L/2), t)/\pm S_0L]=I_1'$ has been plotted as a function of t/RC in Fig. 4.

The amount of oil which flows through a cross section of the cable, M, is calculated by integrating the expression for I, given above.

$$M(x, t)=\int_0^t I(x, \lambda)d\lambda=S_0rcL^3\left\{\frac{x}{L}\frac{t}{RC}-\frac{4}{\pi^4}\sum_{n=0}^{\infty}\frac{(-1)^n}{(2n+1)^4}\sin\frac{x}{L}(2n+1)\pi\times\left[1-\exp\left[-\frac{(2n+1)^2\pi^2t}{RC}\right]\right]\right\}. \quad (30)$$

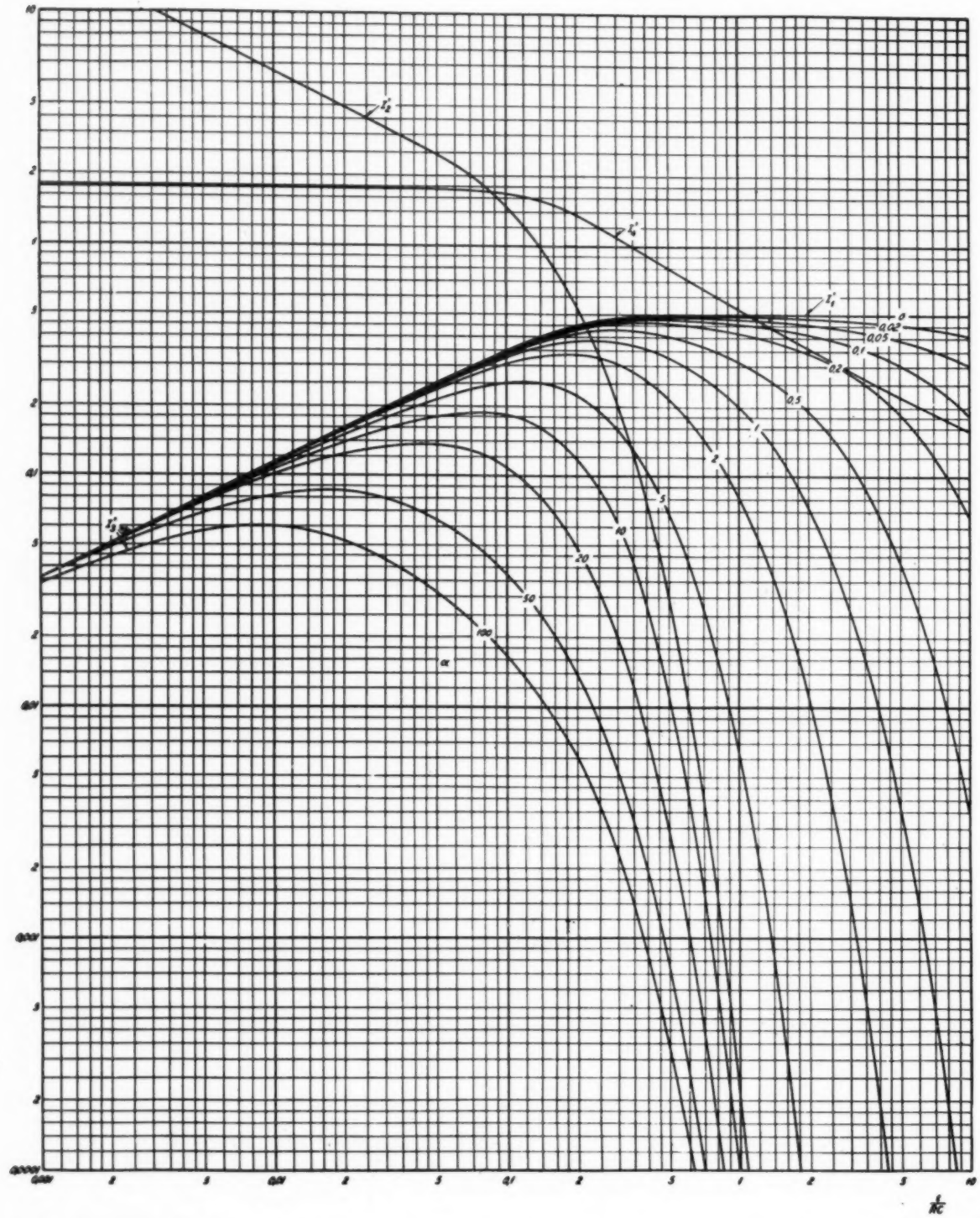

FIG. 4. Generalized functions used in the calculation of the oil current at the endpoints of a cable section with a time constant for the oil flow RC.

$I_1'(t/RC)$ applies in the case of an oil expansion $S(t) = 1 \cdot 1$.
$I_2'(t/RC)$ applies in the case of an oil expansion $S(t) = (d/dt)(1 \cdot 1)$.
$I_3'(t/RC)$ applies in the case of an oil expansion $S(t) = e^{-\alpha t/RC} \cdot 1$.
$I_4'(t/RC)$ applies in the case of an oil expansion $S(t) = 1/(t)^{\frac{1}{2}} \cdot 1$.

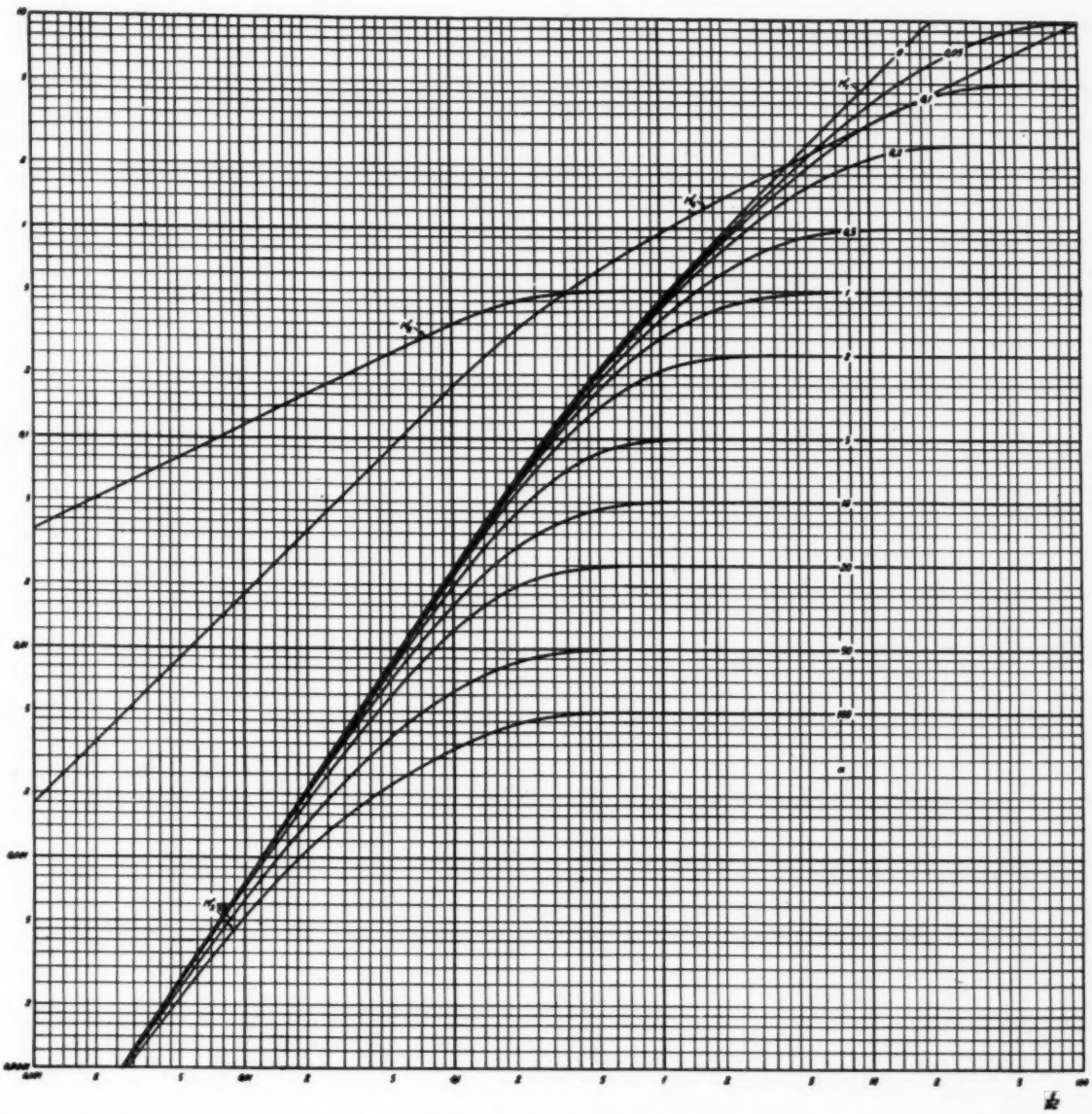

FIG. 5. Generalized functions used in the calculation of the amount of oil which passes the endpoints of a cable section with a time constant for the oil flow RC.

$M_1'(t/RC)$ applies in the case of an oil expansion $S(t)=1\cdot 1$.
$M_2'(t/RC)$ applies in the case of an oil expansion $S(t)=(d/dt)(1\cdot 1)$.
$M_3'(t/RC)$ applies in the case of an oil expansion $S(t)=e^{-\alpha t/RC}\cdot 1$.
$M_4'(t/RC)$ applies in the case of an oil expansion $S(t)=1/(t)^{\frac{1}{2}}\cdot 1$.

For $x=\pm L/2$ this leads to

$$M\left(\pm\frac{L}{2},t\right)=\pm S_0 rcL^3\left\{\frac{t}{2RC}-\frac{4}{\pi^4}\sum_{n=0}^{\infty}\frac{1}{(2n+1)^4}\times\left[1-\exp\left[-\frac{(2n+1)^2\pi^2 t}{RC}\right]\right]\right\}. \quad (31)$$

$[M(\pm(L/2),t)/\pm S_0 rcL^3]=M_1'$ has been plotted as a function of t/RC in Fig. 5.

In consequence of the linearity of the partial differential equations for the flow, the pressure, current and amount of oil which flows through a cross section of the cable for an arbitrary oil expansion $S(t)\cdot 1$ can be calculated from the corresponding solutions, given above, valid for an oil expansion of the form $S_0\cdot 1$. The linearity of the differential equations also causes the action (the pressure, the current, or the amount

of oil) of an oil expansion given as a sum of time functions, to be obtained as the sum of the actions of the individual terms of which the oil expansion consists.

First it is necessary to mention some methods described in the literature for calculating the oil expansion in oil-filled cables for different types of load variations. Then the pressure, current, and amount of oil which flows through a cross section of the cable will be calculated for some important time functions of the oil expansion.

OIL EXPANSION FOR DIFFERENT TYPES OF LOAD VARIATIONS

During the last fifty years a great many papers dealing with temperature variations in cables subjected to load variations have been published. For the purpose of calculating the oil expansion in cables subjected to ordinary load variations the methods suggested by Shanklin and Buller[10] and Miller and Wollaston[11] seem to be very useful. Using either of these methods the oil expansion is obtained as a sum of exponential terms $S_0 e^{-t/T} \cdot 1$. From what has previously been mentioned, pressure, current, and amount of oil which flows through a cross section of the cable are calculated by summing the quantities corresponding to the individual exponential terms. In a later part of this paper, therefore, the pressure, current, and amount of oil for an oil expansion $S_0 e^{-t/T} \cdot 1$ will be calculated.

The above mentioned methods for calculating the variations of temperature and oil expansion in oil-filled cables at load variations are rather inconvenient when the load variation in question is a short circuit. The temperature function in the case of short circuit is better computed on the basis of other simplifying assumptions, as the interesting part of the temperature variation in the case of a short circuit occurs in a relatively thin layer of the insulation near the conductor, in which the short-circuit current is flowing. Herlitz[12] has worked out a theory for temperature during and after a short circuit in conductors in contact with paper-oil insulation, whereby consideration has been given to the heat capacitance of the conductors and to the temperature coefficient of the conductor resistance. The oil-expansion computed on the basis of this theory is expressed by a function involving exponential functions and error integrals.

For use in the present paper we shall develop a very approximate and very simple expression for the oil expansion in an oil-filled cable in the case of short circuit in conductors in contact with paper-oil insulation. We hereby make the simplifying assumptions (1) that the conductors, in which the short-circuit current flows, have a plane surface, (2) that the insulation can be regarded as semi-infinite, (3) that the short circuit is instantaneous, and (4) that the temperature in the conductors remains constant after the short circuit has occurred. The surface of the conductors per unit length of the cable is called f, the specific heat-conduction resistance of the insulation, p, the specific heat of the insulation with respect to a unit volume, q, and the temperature, which the conductors attain at the short circuit, ϑ_0. If x denotes the distance from the surface of a conductor to a point of the insulation, the temperature field ϑ in the insulation is expressed by

$$\vartheta(x, t) = \vartheta_0 \left[1 - \phi\left(\frac{x(pq)^{\frac{1}{2}}}{2(t)^{\frac{1}{2}}} \right) \right] \cdot 1. \quad [13] \qquad (32)$$

The heat effect per unit length of the cable, P, transferred from the conductors to the insulation is then

$$P(t) = -\frac{f}{p}\left(\frac{\partial \vartheta}{\partial t} \right)_{x=0} = \frac{1}{(\pi)^{\frac{1}{2}}} f \vartheta_0 \left(\frac{q}{p} \right)^{\frac{1}{2}} \frac{1}{(t)^{\frac{1}{2}}} \cdot 1. \qquad (33)$$

If we denote the effective volumetric expansion coefficient of the insulation by β', the oil expansion per unit time per unit length of the cable, S, is

$$S(t) = \frac{\beta' P(t)}{q} = \frac{K_0}{(t)^{\frac{1}{2}}} \cdot 1 \qquad (34)$$

where

$$K_0 = \frac{1}{(\pi)^{\frac{1}{2}}} \frac{\beta' f \vartheta_0}{(pq)^{\frac{1}{2}}}. \qquad (35)$$

[10] G. B. Shanklin and F. H. Buller, Gen. Elec. Rev. **34**, 523 (1931).
[11] K. W. Miller and F. O. Wollaston, Trans. A.I.E.E. **52**, 98 (1933).
[12] I. Herlitz, Teknisk Tidskrift, Elektroteknik **71**, 204 (1941).
[13] H. S. Carslaw, *Introduction to the Mathematical Theory of the Conduction of Heat in Solids* (Dover Publications, New York, 1945), second ed., p. 35.

Pressure, current, and amount of oil which flows through a cross section of the cable for an oil expansion according to the very approximate method of computation set forth here will be calculated in a following paragraph. The pressure so obtained will be larger than the actual pressure, especially in cables with small conductor areas, since the temperature of the conductor actually decreases after the short circuit instead of being constant as here supposed.

In a future paper, the pressure, current and amount of oil for the case of a short-circuit current flowing in conductors in contact with paper-oil insulation will be worked out for an oil expansion calculated by a more exact method of computation resembling that given by Herlitz.

The expansion of oil in canals, if any, in the conductors is difficult to calculate, since the heat transfer from the conductors to the oil in the canals takes place both by conduction and by convection. One is safe in assuming that the oil in a canal of any conductor has at any moment the same temperature as the conductor. In the case of an instantaneous short circuit the oil in a conductor canal will then be subjected to a sudden temperature rise resulting in a sudden expansion of the oil. If, as above, ϑ_0 denotes the temperature rise of the conductors because of an instantaneous short circuit, and if a denotes the volume of the conductor canal per unit length, and β the volumetric expansion coefficient of the oil, the oil expansion per unit length per unit time, S, for the oil in the conductor canal in question is, using the terminology of the operational calculus, expressed as follows

$$S(t)=\frac{d}{dt}(N_0\cdot 1), \tag{36}$$

where

$$N_0=a\vartheta_0\beta. \tag{37}$$

Pressure, current, and amount of oil will be computed for an expansion of oil of this kind in the following paragraph. The quantities so obtained turn out to be more convenient for calculating pressure, current, and amount of oil for an arbitrary expansion of oil than the expressions obtained above for an oil expansion $S_0\cdot 1$.

PRESSURE AND FLOW FOR AN INSTANTANEOUS OIL EXPANSION $(d/dt)(N_0\cdot 1)$

Pressure, current, and amount of oil are calculated by the expressions earlier obtained for an oil expansion $S_0\cdot 1$ by differentiating these with respect to time, and writing N_0 instead of S_0. In this way one obtains

$$V(x,t)=\frac{N_0}{c}\frac{4}{\pi}\sum_{n=0}^{\infty}\frac{(-1)^n}{2n+1}\cos\frac{x}{L}(2n+1)\pi\exp\left[-\frac{(2n+1)^2\pi^2 t}{RC}\right]. \tag{38}$$

For $x=0$ this leads to

$$V(0,t)=\frac{N_0}{c}\frac{4}{\pi}\sum_{n=0}^{\infty}\frac{(-1)^n}{2n+1}\exp\left[-\frac{(2n+1)^2\pi^2 t}{RC}\right]. \tag{39}$$

$[cV(0,t)/N_0]=V_2'$ has been plotted as a function of t/RC in Fig. 3.

$$I(x,t)=\frac{N_0}{rcL}4\sum_{n=0}^{\infty}(-1)^n\sin\frac{x}{L}(2n+1)\pi\exp\left[-\frac{(2n+1)^2\pi^2 t}{RC}\right]. \tag{40}$$

For $x=\pm L/2$ this leads to

$$I\left(\pm\frac{L}{2},t\right)=\pm\frac{N_0}{rcL}4\sum_{n=0}^{\infty}\exp\left[-\frac{(2n+1)^2\pi^2 t}{RC}\right]. \tag{41}$$

$[rcLI(\pm(L/2), t)/\pm N_0] = I_2'$ has been plotted as a function of t/RC in Fig. 4.

$$M(x, t) = N_0 L\left\{\frac{x}{L} - \frac{4}{\pi^2}\sum_{n=0}^{\infty}\frac{(-1)^n}{(2n+1)^2}\sin\frac{x}{L}(2n+1)\pi\exp\left[-\frac{(2n+1)^2\pi^2 t}{RC}\right]\right\}$$

$$= N_0 L\frac{4}{\pi^2}\sum_{n=0}^{\infty}\frac{(-1)^n}{(2n+1)^2}\sin\frac{x}{L}(2n+1)\pi\left\{1-\exp\left[-\frac{(2n+1)^2\pi^2 t}{RC}\right]\right\}. \quad (42)$$

For $x = \pm L/2$ this leads to

$$M\left(\pm\frac{L}{2}, t\right) = \pm N_0 L\frac{4}{\pi^2}\sum_{n=0}^{\infty}\frac{1}{(2n+1)^2}\left\{1-\exp\left[-\frac{(2n+1)^2\pi^2 t}{RC}\right]\right\}. \quad (43)$$

$[M(\pm(L/2), t)/\pm N_0 L] = M_2'$ has been plotted as a function of t/RC in Fig. 5.

PRESSURE AND FLOW FOR AN ARBITRARY OIL EXPANSION $S(t)\cdot 1$

If any action (pressure, current, or amount of oil) of an oil expansion $(d/dt)(1\cdot 1)$ is $A(t)$, then because of the linearity of the partial differential equations, valid for the oil flow, the action $G(t)$ of an oil expansion $S(t)$ is expressed by Duhamel's integral

$$G(t) = \int_0^t S(\lambda)A(t-\lambda)d\lambda. \quad (44)$$

Using this equation in connection with the above obtained expressions for pressure, current, and amount of oil for an oil expansion $(d/dt)(N\cdot 1)$, (38), (40), and (42), one obtains

$$V(x, t) = -\frac{1}{c}\frac{4}{\pi}\sum_{n=0}^{\infty}\frac{(-1)^n}{2n+1}\cos\frac{x}{L}(2n+1)\pi\exp\left[-\frac{(2n+1)^2\pi^2 t}{RC}\right]\int_0^t S(\lambda)\exp\left[\frac{(2n+1)^2\pi^2\lambda}{RC}\right]d\lambda, \quad (45)$$

$$I(x, t) = \frac{1}{rcL}4\sum_{n=0}^{\infty}(-1)^n\sin\frac{x}{L}(2n+1)\pi\exp\left[-\frac{(2n+1)^2\pi^2 t}{RC}\right]\int_0^t S(\lambda)\exp\left[\frac{(2n+1)^2\pi^2\lambda}{RC}\right]d\lambda, \quad (46)$$

$$M(x, t) = L\frac{4}{\pi^2}\sum_{n=0}^{\infty}\frac{(-1)^n}{(2n+1)^2}\sin\frac{x}{L}(2n+1)\pi$$

$$\times\left\{\int_0^t S(\lambda)d\lambda - \exp\left[-\frac{(2n+1)^2\pi^2 t}{RC}\right]\int_0^t S(\lambda)\exp\left[\frac{(2n+1)^2\pi^2\lambda}{RC}\right]d\lambda\right\}. \quad (47)$$

PRESSURE AND FLOW FOR AN EXPONENTIALLY DECREASING OIL EXPANSION $S_0e^{-t/T}\cdot 1$

Pressure, current, and amount of oil for the oil expansion $S_0e^{-t/T}\cdot 1$ is calculated by substituting $S(t) = S_0e^{-t/T}$ in Eqs. (45), (46), and (47).

$$V(x, t) = S_0 rL^2\frac{4}{\pi}\sum_{n=0}^{\infty}\frac{(-1)^n}{(2n+1)((2n+1)^2\pi^2 - (RC/T))}\cos\frac{x}{L}(2n+1)\pi$$

$$\times\left\{\exp\left(-\frac{RC}{T}\frac{t}{RC}\right) - \exp\left[-\frac{(2n+1)^2\pi^2 t}{RC}\right]\right\}. \quad (48)$$

For $x = 0$ this leads to

$$V(0, t) = S_0 rL^2\frac{4}{\pi}\sum_{n=0}^{\infty}\frac{(-1)^n}{(2n+1)((2n+1)^2\pi^2 - (RC/T))}\left\{\exp\left(-\frac{RC}{T}\frac{t}{RC}\right) - \exp\left[-\frac{(2n+1)^2\pi^2 t}{RC}\right]\right\}. \quad (49)$$

$[V(0,t)/S_0rL^2]=V_3'$ has been plotted in Fig. 3 as a function of t/RC for $\alpha=RC/T=0.02$, 0.05, 0.1, 0.2, 0.5, 1, 2, 5, 10, 20, 50, and 100.

$$I(x,t)=S_0L4\sum_{n=0}^{\infty}\frac{(-1)^n}{(2n+1)^2\pi^2-(RC/T)}\sin\frac{x}{L}(2n+1)\pi\left\{\exp\left(-\frac{RC}{T}\frac{t}{RC}\right)-\exp\left[-\frac{(2n+1)^2\pi^2t}{RC}\right]\right\}. \quad (50)$$

For $x=\pm L/2$ this leads to

$$I\left(\pm\frac{L}{2},t\right)=\pm S_0L4\sum_{n=0}^{\infty}\frac{1}{(2n+1)^2\pi^2-(RC/T)}\left\{\exp\left(-\frac{RC}{T}\frac{t}{RC}\right)-\exp\left[-\frac{(2n+1)^2\pi^2t}{RC}\right]\right\}. \quad (51)$$

$[I(\pm(L/2),t)/\pm S_0L]=I_3'$ has been plotted in Fig. 4 as a function of t/RC for the same values of $\alpha=RC/T$ as given above.

$$M(x,t)=S_0rcL^3\left\{\frac{x}{L}\frac{T}{RC}\left[1-\exp\left(-\frac{RC}{T}\frac{t}{RC}\right)\right]-\frac{4}{\pi^2}\sum_{n=0}^{\infty}\frac{(-1)^n}{(2n+1)^2((2n+1)^2\pi^2-(RC/T))}\right.$$
$$\left.\times\sin\frac{x}{L}(2n+1)\pi\left[\exp\left(-\frac{RC}{T}\frac{t}{RC}\right)-\exp\left[-\frac{(2n+1)^2\pi^2t}{RC}\right]\right]\right\}. \quad (52)$$

For $x=\pm L/2$ this leads to

$$M\left(\pm\frac{L}{2},t\right)=\pm S_0rcL^3\left\{\frac{T}{2RC}\left[1-\exp\left(-\frac{RC}{T}\frac{t}{RC}\right)\right]-\frac{4}{\pi^2}\sum_{n=0}^{\infty}\frac{1}{(2n+1)^2((2n+1)^2\pi^2-(RC/T))}\right.$$
$$\left.\times\left[\exp\left(-\frac{RC}{T}\frac{t}{RC}\right)-\exp\left[-\frac{(2n+1)^2\pi^2t}{RC}\right]\right]\right\}. \quad (53)$$

$[M(\pm(L/2),t)/\pm S_0rcL^3]=M_3'$ has been plotted in Fig. 5 as a function of t/RC for the same values of $\alpha=RC/T$ as given earlier.

A practical example will demonstrate the use of the curves.

Example 2

For a certain cable the oil expansion per unit length per unit time for a sudden switching on the load is

$$S(t)=S_1[e^{-(t/4000)}-0.6e^{-(t/400)}-0.2e^{-(t/100)}]$$

where S_1 is a constant. It is desired to calculate the variation of pressure at the midpoint of the cable, partly for switching on the load at the time $t=0$, after which the load remains switched on an infinite time, partly for switching on the load at the time $t=0$ and switching off the load at the time $t=200$ sec. The computation of the pressure will be carried out for a time constant of the cable $RC=0$, 1000, and 4000 sec.

For $RC=0$ the pressure V in switching on the load is

$$(V(t))_{RC=0}=\tfrac{1}{8}S_1rL^2[e^{-(t/4000)}-0.6e^{-(t/400)}-0.2e^{-(t/100)}].$$

$[(V(t))_{RC=0}/\tfrac{1}{8}S_1rL^2]$ has been plotted in Fig. 6.

For the case where the load is switched off after 200 sec., the pressure W is

$$(W(t))_{RC=0}=\begin{cases}(V(t))_{RC=0} & \text{for } t<200 \text{ sec.}\\ (V(t))_{RC=0}-(V(t-200))_{RC=0} & \text{for } t>200 \text{ sec.}\end{cases}$$

$[(W(t))_{RC=0}/\tfrac{1}{8}S_1rL^2]$ has been plotted in Fig. 7.

For $RC=1000$ sec. one obtains for the ex-

ponential terms in the expression for S

$$\frac{RC}{T_1}=\frac{1000}{4000}=0.25,$$

$$\frac{RC}{T_2}=\frac{1000}{400}=2.5,$$

$$\frac{RC}{T_3}=\frac{1000}{100}=10.$$

The pressure V in switching on the load is, accordingly,

$$(V(t))_{RC=1000\text{ sec.}}=S_1rL^2\left[\left(V_3'\left(\frac{t}{1000}\right)\right)_{\alpha=0.25}-0.6\left(V_3'\left(\frac{t}{1000}\right)\right)_{\alpha=2.5}-0.2\left(V_3'\left(\frac{t}{1000}\right)\right)_{\alpha=10}\right].$$

The functions V_3' are taken from Fig. 3. $[(V(t))_{RC=1000\text{ sec.}}/\frac{1}{8}S_1rL^2]$ has been plotted in Fig. 6.

The pressure W for the load remaining switched on 200 sec. is calculated in the same way as in the case $RC=0$ treated above.

$[(W(t))_{RC=1000\text{ sec.}}/\frac{1}{8}S_1rL^2]$ has been plotted in Fig. 7.

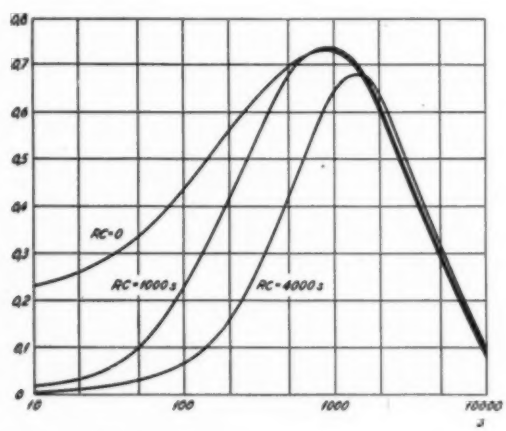

FIG. 6. Relative pressure at the midpoint of a cable in switching on a load giving an oil expansion $S(t)=S_1[e^{-t/4000}-0.6e^{-t/400}-0.2e^{-t/100}]$ for different time constants of the oil flow.

For $RC=4000$ sec. one obtains in a similar way

$$(V(t))_{RC=4000\text{ sec.}}=S_1rL^2\left[\left(V_3'\left(\frac{t}{4000}\right)\right)_{\alpha=1}-0.6\left(V_3'\left(\frac{t}{4000}\right)\right)_{\alpha=10}-0.2\left(V_3'\left(\frac{t}{4000}\right)\right)_{\alpha=40}\right].$$

$[(V(t))_{RC=4000\text{ sec.}}/\frac{1}{8}S_1rL^2]$ has been plotted in Fig. 6 and $[(W(t))_{RC=4000\text{ sec.}}/\frac{1}{8}S_1rL^2]$ in Fig. 7.

Figure 6 shows that in the present case the variation in the computed pressure, resulting from taking into account the elasticity and the compressibility of the cable, is but little even with a time constant for the oil flow so large as 4000 sec. If all the terms in the expression for S had the same sign, the variation in the calculated maximum pressure, however, would have been considerable, with the time constants for the oil flow occurring in the present case. Mostly, however, S is composed of exponential terms with different signs in such a way that S at the time $t=0$ assumes a small value, thereafter increases to a maximum, and then decreases to zero in resemblance to the case occurring in the example. With the values of the time constant for the oil flow, and the time constant in the first exponential term in the expression for the oil expansion occurring in practical cases, the maximum pressure in switching on a constant load calculated for $RC=0$ seldom diverges any

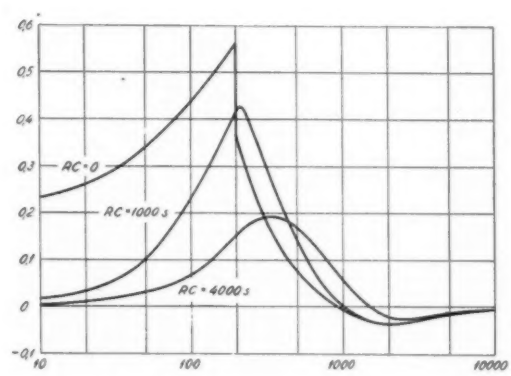

FIG. 7. Relative pressure at the midpoint of a cable in switching on for 200 sec. the same load as occurring in Fig. 6 for different time constants of the oil flow.

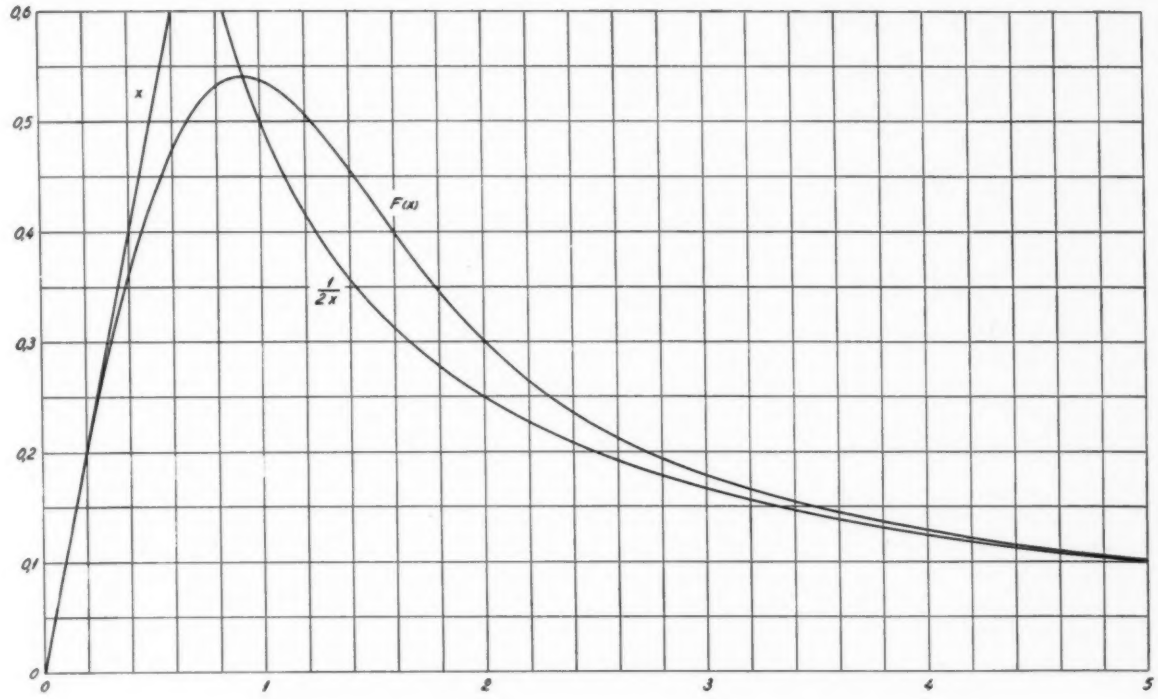

FIG. 8. $F(x)=e^{-x^2}\int_0^x e^{\xi^2}d\xi$ together with the approximations $F(x)\doteq x$ and $F(x)\doteq 1/2x$ valid for small, respectively for large values of x.

considerable amount from the pressure calculated for the actual value of RC.

This is not the case in the calculation of the maximum increase of pressure and the following maximum decrease of pressure occurring in switching on a constant load for a time interval that is small relative to the time constant for the oil flow in the cable. Figure 7 shows thus that the maximum pressure for the load in question with $RC=1000$ sec. comes to 76 percent, and with $RC=4000$ sec. only 34 percent of the maximum pressure with $RC=0$.

The following decrease of pressure is reduced too by the elasticity and the compressibility of the cable.

PRESSURE AND FLOW FOR THE OIL EXPANSION $K_0/(t)^{\frac{1}{2}}\cdot 1$

Pressure, current, and amount of oil for the oil expansion $K_0/(t)^{\frac{1}{2}}\cdot 1$ is calculated by substituting $S(t)=K_0/(t)^{\frac{1}{2}}$ in Eqs. (45), (46), and (47).

The results in the present paragraph are most simply expressed by the function $F(x)$, defined in the following way:

$$F(x)=e^{-x^2}\int_0^x e^{\xi^2}d\xi. \tag{54}$$

This function has been tabulated by Miller and Gordon.[14] $F(x)$ has been plotted in Fig. 8 for $0<x<5$ together with the functions $y=2x$ and $y=1/2x$, which approximate the function $F(x)$ for small respectively large values of the argument x. The advantage in using the function $F(x)$ instead of the function

$$f(x)=\int_0^x e^{\xi^2}d\xi,$$

as used e.g., by Dawson,[15] is that $F(x)$ is limited and more convenient for interpolation than $f(x)$.[14]

Pressure, current, and amount of oil can now

[14] W. L. Miller and A. R. Gordon, J. Phys. Chem. **35**, 2785 (1931).
[15] H. G. Dawson, Proc. Lond. Math. Soc. **29**, 519 (1897–98).

be expressed in the following way:

$$V(x,t)=K_0\left(\frac{r}{c}\right)^{\frac{1}{2}}L\frac{8}{\pi^2}\sum_{n=0}^{\infty}\frac{(-1)^n}{(2n+1)^2}$$
$$\times\cos\frac{x}{L}(2n+1)\pi F\left((2n+1)\pi\left(\frac{t}{RC}\right)^{\frac{1}{2}}\right). \quad (55)$$

For $x=0$ this leads to

$$V(0,t)=K_0\left(\frac{r}{c}\right)^{\frac{1}{2}}L\frac{8}{\pi^2}\sum_{n=0}^{\infty}\frac{1}{(2n+1)^2}$$
$$\times F\left((2n+1)\pi\left(\frac{t}{RC}\right)^{\frac{1}{2}}\right). \quad (56)$$

$[V(0,t)/K_0(r/c)^{\frac{1}{2}}L]=V_4'$ has been plotted as a function of t/RC in Fig. 3.

$$I(x,t)=\frac{K_0}{(rc)^{\frac{1}{2}}}\frac{8}{\pi}\sum_{n=0}^{\infty}\frac{(-1)^n}{2n+1}$$
$$\times\sin\frac{x}{L}(2n+1)\pi F\left((2n+1)\pi\left(\frac{t}{RC}\right)^{\frac{1}{2}}\right). \quad (57)$$

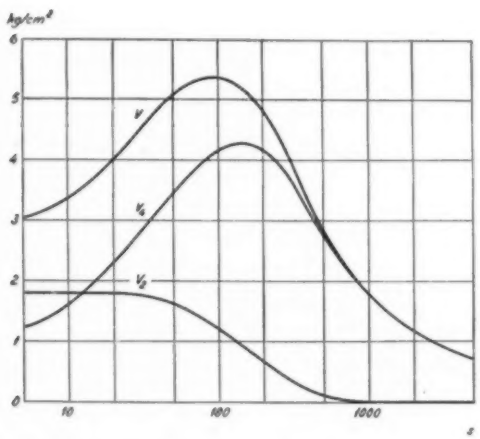

FIG. 9. Pressure V at the midpoint of a cable, occurring at a short circuit in the cable as specified in the text, for 20°C temperature of the oil in the oil canal. $V=V_2+V_4$, where V_2 corresponds to the expansion of the oil in the canal, V_4 to the expansion of the oil in the insulation.

For $x=\pm L/2$ this leads to

$$I\left(\pm\frac{L}{2},t\right)=\pm\frac{K_0}{(rc)^{\frac{1}{2}}}\frac{8}{\pi}\sum_{n=0}^{\infty}\frac{1}{2n+1}$$
$$\times F\left((2n+1)\pi\left(\frac{t}{RC}\right)^{\frac{1}{2}}\right). \quad (58)$$

$[I(\pm(L/2),\ t)/\pm(K_0/(rc)^{\frac{1}{2}})]=I_4'$ has been plotted as a function of t/RC in Fig. 4.

$$M(x,t)=K_0(rc)^{\frac{1}{2}}L^2\left[2\frac{x}{L}\left(\frac{t}{RC}\right)^{\frac{1}{2}}-\frac{8}{\pi^3}\sum_{n=0}^{\infty}\frac{(-1)^n}{(2n+1)^3}\right.$$
$$\left.\times\sin\frac{x}{L}(2n+1)\pi F\left((2n+1)\pi\left(\frac{t}{RC}\right)^{\frac{1}{2}}\right)\right]. \quad (59)$$

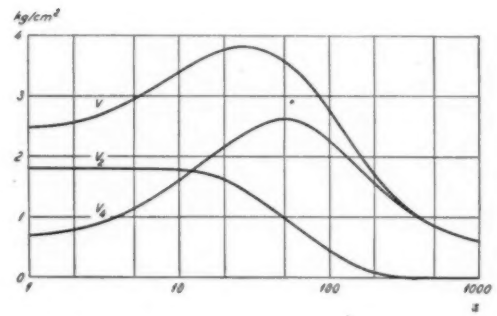

FIG. 10. Pressure V at the midpoint of the same cable and for the same short circuit current in this cable as in Fig. 9 for 40°C temperature of the oil in the oil canal. $V=V_2+V_4$, where V_2 corresponds to the expansion of the oil in the canal, V_4 to the expansion of the oil in the insulation.

For $x=\pm L/2$ this leads to

$$M\left(\pm\frac{L}{2},t\right)=\pm K_0(rc)^{\frac{1}{2}}L^2\left[\left(\frac{t}{RC}\right)^{\frac{1}{2}}\right.$$
$$\left.-\frac{8}{\pi^3}\sum_{n=0}^{\infty}\frac{1}{(2n+1)^3}F\left((2n+1)\pi\left(\frac{t}{RC}\right)^{\frac{1}{2}}\right)\right]. \quad (60)$$

$[M(\pm(L/2),\ t)/\pm K_0(rc)^{\frac{1}{2}}L]=M_4'$ has been plotted as a function of t/RC in Fig. 5.

The use of the formulas worked out in this paragraph is explained by the following example.

Example 3

It is desired to calculate the maximal pressure rise in the single-core cable described in Ex. 1 for a cable length of 1 km in the case of a short circuit of 1 sec. duration, during which the conductor and the oil in the conductor canal are heated 10°C. It is supposed that the heat effect of the secondary current in the sheath is negligible. The pressure will be calculated for the temperature of the oil in the canal 20°C and 40°C.

Besides the data for the cable given in Ex. 1

the following data are needed:

$$p = 550°\text{C cm } W^{-1}, \quad q = 2°\text{C}^{-1}\text{ cm}^{-3}\ W\text{ sec.},$$
$$\beta = 0.0007°\text{C}^{-1}, \quad \beta' = 0.0004°\text{C}^{-1}.$$

From the data given in Ex. 1 are further calculated

$$f = \pi \cdot 1.3 = 4.1 \text{ cm},$$
$$a = (\pi/4) \cdot 0.6^2 = 0.28 \text{ cm}^2.$$

The increase in pressure at the midpoint of the cable $V_2(0, t)$ caused by the expansion of the oil in the canal is according to (37) and (39)

$$V_2(0, t) = a\vartheta_0\beta\frac{1}{c}V_2'\left(\frac{t}{RC}\right)$$

$$= 0.28 \cdot 10 \cdot 0.0007 \cdot \frac{1}{1.09 \cdot 10^{-3}} V_2'\left(\frac{t}{RC}\right)$$

$$= 1.8\, V_2'\left(\frac{t}{RC}\right) \text{ kg cm}^{-2}$$

where $V_2'(t/RC)$ is taken from Fig. 3.

The increase in pressure at the midpoint of the cable $V_4(0, t)$ caused by the heat transferred from the conductor to the insulation is according to (35) and (56)

$$V_4(0, t) = \frac{\beta' f \vartheta_0 L(r)^{\frac{1}{2}}}{(\pi pqc)^{\frac{1}{2}}} V_4'\left(\frac{t}{RC}\right)$$

$$= \frac{0.0004 \cdot 4.1 \cdot 10 \cdot 10^5 V_4'(t/RC)}{(\pi \cdot 550 \cdot 2 \cdot 1.09 \cdot 10^{-3})^{\frac{1}{2}}}$$

$$\cdot \begin{cases} (1.43 \cdot 10^{-4})^{\frac{1}{2}} \\ (5.3 \cdot 10^{-4})^{\frac{1}{2}} \end{cases}$$

$$= 10.1\, V_4'\left(\frac{t}{RC}\right) \text{ at } 20°\text{C}$$

$$= 6.2\, V_4'\left(\frac{t}{RC}\right) \text{ at } 40°\text{C}$$

where $V_4'(t/RC)$ is taken from Fig. 3.

V_2, V_4, and $V = V_2 + V_4$ for 20°C temperature of the oil in the oil canal have been plotted in Fig. 9, and V_2, V_4, and $V = V_2 + V_4$ for 40°C oil temperature in Fig. 10.

From Fig. 9 and Fig. 10 is read the maximum pressure

$$V_{\max} = \begin{cases} 5.4 \text{ kg cm}^{-2} \text{ for } t = 95 \text{ sec. with } 20°\text{C} \\ 3.8 \text{ kg cm}^{-2} \text{ for } t = 30 \text{ sec. with } 40°\text{C}, \end{cases}$$

In working out the theory for the oil expansion after a short circuit we made the simplifying assumption that the temperature of the conductors remained constant after the short circuit. It is interesting to make an estimate in the present case of how much the conductor temperature has decreased from the moment of short circuit to the moment of occurrence of maximum pressure.

With the idealizing assumption mentioned above, namely, that the conductor temperature remains constant, the effect per unit length of the cable, P, transferred to the insulation was given in (33). The amount of heat per unit length, Q, transferred to the insulation from the moment of short circuit to the time t is then

$$Q(t) = \int_0^t P(\lambda)d\lambda = \frac{2}{(\pi)^{\frac{1}{2}}} f\vartheta_0 \left(\frac{q}{p}\right)^{\frac{1}{2}} (t)^{\frac{1}{2}}.$$

Hereby we calculate the amount of heat per unit length in the present case transferred to the insulation from the moment of short circuit to the moment t_1, when the maximum pressure occurs

$$Q(t_1) = \frac{2}{(\pi)^{\frac{1}{2}}} \cdot 4.1 \cdot 10 \cdot \left(\frac{2}{550}\right)^{\frac{1}{2}}$$

$$\cdot \begin{cases} (95)^{\frac{1}{2}} = 26 \text{ W sec. cm}^{-1} \text{ for } 20°\text{C}. \\ (30)^{\frac{1}{2}} = 15 \text{ W sec. cm}^{-1} \text{ for } 40°\text{C}. \end{cases}$$

These transferred amounts of heat have to be compared with the amount of heat per unit length, Q_1, accumulated in the conductor and in the oil canal. The specific heat for copper in respect to a unit volume is $3.4°\text{C}^{-1}\text{ cm}^{-3}$ W sec. Neglecting the amount of heat accumulated in the oil canal we get

$$Q_1 = 0.95 \cdot 3.4 \cdot 10 = 32 \text{ W sec. cm}^{-1}.$$

The amount of heat transferred from the conductor to the insulation from the moment of short circuit to the moment, when the maximal pressure, calculated according to the simplifying

assumption mentioned above, occurs, is consequently not negligible compared with the total amount of heat accumulated in the conductor. The preparation of a more exact theory, as mentioned above, seems to be justified.

The work here presented has been carried out at Sieverts Kabelverk, Sundbyberg, Sweden. I thank Sieverts Kabelverk and especially Mr. H. Spanne, chief engineer at Sieverts Kabelverk, for permission to publish this paper.

The Electrostatic Field of a Point Charge Inside a Cylinder, in Connection with Wave Guide Theory

C. J. Bouwkamp and N. G. de Bruijn
Natuurkundig Laboratorium der N. V. Philips' Gloeilampenfabrieken, Eindhoven, Netherlands
(Received February 21, 1947)

In this paper the field of a point charge inside a hollow, infinitely long circular cylinder is studied. The case of an axial point charge is treated in detail. Three different methods are developed. The first method shows how to calculate the induced charges at the surface of the cylinder without explicit knowledge of the potential itself. The surface charge-density function is obtained as the solution of a Fourier-type integral equation. Then the potential caused by these charges is calculated. The second method works in the opposite direction. Here the potential is obtained as solution of a boundary value problem, followed by the calculation of the corresponding charges at the surface of the cylinder.

The integral, obtained for the surface charge density, is transformed by contour integration. Although the resulting series is very useful for numerical purposes, a stronger method is necessary, in order to calculate the charge density just opposite the point source. Figure 1 shows the calculated values of the induced surface charge density. Several approximations for the charge-density function are considered, in connection with recent work of Weber (cf. Table I).

The same is done for the field inside the cylinder. Various formulas are given which allow of numerical calculations. In Table II some calculated values of the potential are shown.

The third method is based on the theory of Fourier-Bessel-Dini series. The potential is developed in terms of discrete normal solutions of the potential equation in cylindrical coordinates. The coefficients in this development can be derived from the behavior of the potential in the immediate neighborhood of the primary source.

Furthermore, it is emphasized that the study of the above potential problem can serve as a guide in questions of wave propagation in hollow circular cylinders. In this connection the third method is shown to be extremely useful, as it enables us to calculate directly the fields in the far zone from that in the immediate neighborhood of the exciting source. This new method is demonstrated in case of acoustic waves inside a cylinder, caused by a harmonically vibrating point source.

1. INTRODUCTION

PREVIOUS works of Schelkunoff,[1] Weyrich,[2] Buchholz,[3] and Oberhettinger,[4] among others, already contain complete information with regard to fields in circular pipes, as produced by Hertzian dipoles. Therefore, the generation of special types of wave patterns, caused by given current and charge distributions on the exiting antennas, can be dealt with quantitatively. The calculations in this domain of electromagnetics, however, are far from elementary, such that a non-mathematically minded engineer might hardly recognize the usefulness of those theoretical treatments. Hence, every attempt to diminish the necessary amount of mathematics, may be worth while to consider. Until now a considerable amount of complex function theory is required. We believe, however, that this can be greatly avoided if one bases oneself on the theory of Fourier-Bessel-Dini series. This method is undoubtedly within reach of every engineer,

[1] S. A. Schelkunoff, "Modified Sommerfeld's integral and its applications," Proc. I.R.E. **24**, 1388 (1936); and "Transmission theory of plane electromagnetic waves," *ibid.* **25**, 1457 (1937); with bibliography.
[2] R. Weyrich, "Ueber einige Randwertprobleme, insbesondere der Elektrodynamik," J. reine angew. Math. **172**, 133 (1934).
[3] H. Buchholz, "Gekoppelte Strahlungsfelder im kreiszylindrischen Hohlleiter," Ann. d. Physik **39**, 81 (1941).
[4] F. Oberhettinger, "Ueber ein Randwertproblem der Wellengleichung in Zylinderkoordinaten," Ann. d. Physik **43**, 136 (1943).

because the analogous conventional theory of the ordinary Fourier series is common knowledge nowadays.

In this paper we will not consider the vector wave propagation as occurring in electromagnetic theory. Those topics will be treated elsewhere. The new method will be demonstrated in the case of scalar wave propagation only.

The major part of the present article, however, will be devoted to the study of the electrostatic field of a point charge inside the cylinder. Consequently, only a minor part of the mathematics developed here is claimed to be useful in wave guide theory.

Beginning with the simplest problem, we confine ourselves to the case of a point charge situated on the axis of the cylinder. Later on we will briefly indicate how to extend the theory to excentric point charges.

2. STATEMENT OF THE SIMPLEST PROBLEM. CALCULATION OF THE CHARGES INDUCED ON THE SURFACE OF THE CYLINDER

Let a be the radius of the cylinder, and let the point charge have a value $+1$. Furthermore, let z, ρ, φ denote the right-handed cylindrical coordinates of a field point P. Henceforth the origin may coincide with the given point charge, and the z-axis be taken along the axis of the cylinder.

The electric force $\mathbf{E}$ can be derived from a potential V according to $\mathbf{E}=-\operatorname{grad} V$. It is evident that the z-axis is an axis of symmetry, so that V depends only on z and ρ. In addition, V is even in z.

To calculate $\mathbf{E}$ and V, we first follow a rather unconventional method, by calculation of the *charges*, induced on the wall of the cylinder, without explicit knowledge of the potential itself. Afterwards the field is readily found from the original point charge and these induced charges. The surface density of the induced charges will be denoted by $\eta(z)$.

We may remark that V is the so-called Green function of the first kind. It is a regular solution of the potential equation, except for a singularity in the origin, so that the function $V(P)-1/r$ remains finite for $r\to 0$; furthermore, $V=0$ on the boundary, and both V and $\operatorname{grad} V$ tend to zero, if P tends to infinity inside the cylinder.

As is well known, there is one, and only one, function $V(z, \rho)$ fulfilling all these conditions simultaneously. Once this function is obtained, the charges on the boundary of the cylinder can be computed from

$$\eta(z)=\frac{1}{4\pi}\frac{\partial V}{\partial \rho}, \quad (\rho=a). \tag{1}$$

Let us now show how $\eta(z)$ can be found without explicit knowledge of the potential V. Be $g(z, \rho)$ a given regular solution of the potential equation inside the cylinder, and suppose g and $\partial g/\partial z$ to be bounded in that domain. By Green's theorem, we at once express the value of g in the origin as a surface integral over its boundary values, namely

$$g(0, 0)=-\frac{1}{4\pi}\int g\frac{\partial V}{\partial \rho}d\sigma=-\int g(z, a)\eta(z)d\sigma. \tag{2}$$

In this $d\sigma$ means the surface element of the boundary of the cylinder; the integration in (2) extends over this boundary.

Omitting the left-hand integral in (2), the remaining equality can be interpreted as an integral equation for $\eta(z)$, which may be readily solved, if a convenient choice is made for the rather arbitrary function g. We take

$$g(z, \rho)=e^{-i\lambda z}I_0(\lambda\rho) \tag{3}$$

where I_0 is the Bessel function of purely imaginary argument and zeroth order. The function (3) is a regular potential, with g and $\partial g/\partial z$ bounded inside the cylinder, if the constant λ is restricted to *real* values.

Substitution of (3) in (2) leads to

$$1=-\int_0^{2\pi} ad\varphi\int_{-\infty}^{\infty} e^{-i\lambda z}I_0(\lambda a)\eta(z)dz,$$

whence it follows

$$\int_{-\infty}^{\infty} e^{-i\lambda z}\eta(z)dz=-\frac{1}{2\pi a I_0(\lambda a)}, \quad (-\infty<\lambda<\infty). \tag{4}$$

Thus the integral equation (2) is reduced to one of the common Fourier type (4). Its solution can be written down immediately. By inversion of

(4), one obtains for the required charge density

$$\eta(z) = -\frac{1}{4\pi^2 a}\int_{-\infty}^{\infty} e^{i\lambda z}\frac{d\lambda}{I_0(\lambda a)}$$

$$= -\frac{1}{2\pi^2 a^2}\int_0^{\infty}\frac{\cos(z/a)t}{I_0(t)}dt. \qquad (5)$$

Starting from this integral expression, we can develop solutions more useful for numerical purposes. For non-vanishing z we may transform the above integral into a series by means of the conventional contour integration. In the cut plane $z=0$, however, stronger methods must be used, as will be seen below.

Consider the following integral in the complex t-plane:

$$\frac{1}{2\pi i}\int_W \frac{e^{izt/a}}{I_0(t)}dt,$$

the path of integration W leading from $-R$ to R along the real axis, and back from R to $-R$ along a semi-circle of radius R and center 0. Avoiding values of R for which the semi-circle passes through a zero of $I_0(t)$, we can prove that for positive values of z, the contribution of the semi-circle tends to zero, when R tends to infinity. Let $k_1, k_2, \cdots$ denote, in ascending order, the positive zeros of the Bessel function $J_0(k)$. Then ik_n are the simple poles of the integrand in the upper half of the t-plane. The residue theorem now gives

$$\frac{1}{2\pi i}\int_{-\infty}^{\infty}\frac{e^{izt/a}}{I_0(t)}dt = \sum_{n=1}^{\infty}\frac{e^{-k_n z/a}}{I_0'(ik_n)}.$$

We have $I_0'(ik_n) = iJ_1(k_n)$, and so for the charge density

$$\eta(z) = -\frac{1}{2\pi a^2}\sum_{n=1}^{\infty}\frac{e^{-k_n z/a}}{J_1(k_n)}, \quad (z \geqslant 0). \qquad (6)$$

Only for $z=0$ does this series not converge in the ordinary sense. Unless z is very small, it is very useful for numerical computation. A small number of terms are already sufficient in the range $z \geqslant a$.

The total charge, induced on the cylinder between $z \geqslant 0$ and ∞, can be found by integration:

$$2\pi a\int_z^{\infty}\eta(\zeta)d\zeta = -\sum_{n=1}^{\infty}\frac{e^{-k_n z/a}}{k_n J_1(k_n)}, \quad (z \geqslant 0).$$

The latter series does converge at $z=0$. The total amount of induced charge on the upper half of the cylinder should be $-\frac{1}{2}$; we have thus an opportunity to verify a well-known formula in Bessel-function theory, originally credited to Nielsen:

$$\sum_{n=1}^{\infty}\frac{1}{k_n J_1(k_n)} = \tfrac{1}{2}.$$

For small values of z the convergence of the series (6) is too slow for practical evaluation. Hence we have to develop other expressions for $\eta(z)$, which do allow of numerical computation near the "cut plane" $z=0$. This can be accomplished by Watson's method for an analogous problem.[5]

Therefore we consider the following integral

$$\frac{1}{2\pi i}\int\frac{\cos\lambda w}{(w-t)I_0(w)\cos(\pi w/\beta)}dw$$

wherein λ, β, t are real parameters; $\beta>0$, $\cos(\pi t/\beta)\neq 0$. The path of integration is a circle of radius $R>t$, and center 0, not passing through any zero of the denominator of the integrand. When one adds the condition $\beta|\lambda|<\pi$, the integral tends to zero, if R increases to infinite values. Thus the sum of the residues of the integrand is zero also. The poles of the integrand are all simple; they lie at

$$w = t, \qquad (a)$$

$$w = \pm ik_n, \quad (n=1, 2, \cdots), \qquad (b)$$

$$w = \pm(\nu+\tfrac{1}{2})\beta, \quad (\nu=0, 1, 2, \cdots). \qquad (c)$$

The corresponding residues are easily found to be

$$\frac{\cos\lambda t}{I_0(t)\cos(\pi t/\beta)}, \qquad (a')$$

$$-\frac{\cosh\lambda k_n}{J_1(k_n)\cosh(\pi k_n/\beta)[k_n \pm it]}, \qquad (b')$$

$$-\frac{\beta}{\pi}\frac{(-1)^{\nu}\cos(\lambda\beta\nu+\lambda\beta/2)}{I_0(\beta\nu+\beta/2)[(\nu+\frac{1}{2})\beta \mp t]}. \qquad (c')$$

[5] G. N. Watson, "The use of series of Bessel functions in problems connected with cylindrical wind-tunnels," Proc. Roy. Soc. **130**, 29 (1930/31).

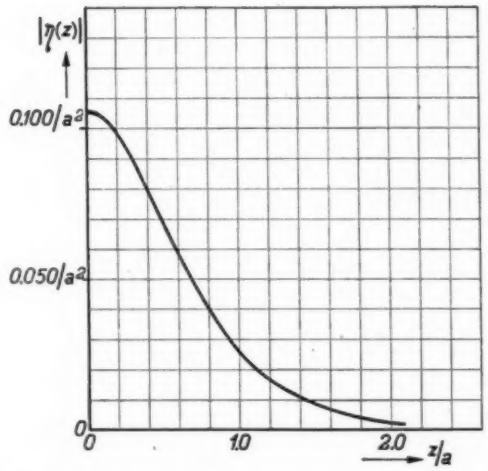

FIG. 1. Curve showing the surface charge density $|\eta|$ on the wall of the grounded cylinder, induced by a unit-point charge situated in the axis at $z=0$; z denotes the distance along the cylinder, measured from the source containing plane; a is the radius of the cylinder.

The sum of all residues together being zero, one has

$$\frac{\cos\lambda t}{I_0(t)\cos(\pi t/\beta)}=\sum_{n=1}^{\infty}\frac{2k_n\cosh\lambda k_n}{J_1(k_n)\cosh(\pi k_n/\beta)}\frac{1}{k_n^2+t^2}$$
$$+\frac{\beta}{\pi}\sum_{\nu=0}^{\infty}\frac{(-1)^\nu\cos(\lambda\beta\nu+\lambda\beta/2)}{I_0(\beta\nu+\beta/2)}\frac{(2\nu+1)\beta}{(\beta\nu+\beta/2)^2-t^2}. \quad (7)$$

Evidently, the right-hand side of (7) is nothing else but the expansion in rational fractions of the left-hand side.

We now multiply both sides of (7) by $\cos(\pi t/\beta)$, thus neutralizing the poles in (c), and integrating from $t=-\infty$ to $t=\infty$. Using the following formulas[5]

$$\int_{-\infty}^{\infty}\frac{\cos(\pi t/\beta)}{k_n^2+t^2}dt=\frac{\pi}{k_n}e^{-\pi k_n/\beta},$$
$$\int_{-\infty}^{\infty}\frac{\cos(\pi t/\beta)}{(\beta\nu+\beta/2)^2-t^2}dt=\frac{(-1)^\nu 2\pi}{(2\nu+1)\beta}, \quad (8)$$

we easily obtain

$$\int_0^{\infty}\frac{\cos\lambda t}{I_0(t)}dt=\beta\sum_{\nu=0}^{\infty}\frac{\cos\lambda\beta(\nu+\frac{1}{2})}{I_0(\beta\nu+\beta/2)}$$
$$+2\pi\sum_{n=1}^{\infty}\frac{\cosh\lambda k_n}{J_1(k_n)[1+e^{2\pi k_n/\beta}]}. \quad (9)$$

Hence, for the induced charge density

$$-a^2\eta(z)=\frac{\beta}{2\pi^2}\sum_{\nu=0}^{\infty}\frac{\cos(\beta\nu+\beta/2)z/a}{I_0(\beta\nu+\beta/2)}$$
$$+\frac{1}{\pi}\sum_{n=1}^{\infty}\frac{\cosh k_n z/a}{J_1(k_n)[1+e^{2\pi k_n/\beta}]}. \quad (10)$$

It may be emphasized that our proof of (10) holds for $\beta>0$ and $-\pi a/\beta<z<\pi a/\beta$. The first series on the right of (10) is convergent for all real values of z. It may be considered as an approximation of the integral in (5), obtained when the integration interval is divided into equal parts of length β, and the integrand in each separate interval is replaced by its central value. The second series should then be interpreted as a correction term. The latter, however, only converges for $-2\pi a/\beta<z<2\pi a/\beta$. By analytic continuation, it can be shown that (10) holds for this extended range, twice as large as might be expected from the proof of (10), as given above. Moreover, for the special value $\beta=a\pi/|z|$, the first series vanishes identically, whilst the "correction term" reduces to the series (6). Consequently, Eq. (10) is more basic than (6).

Equation (10) is very suitable for numerical calculations. The constant β is still arbitrary, except for $-2\pi a/\beta<z<2\pi a/\beta$. Let us consider the extreme case $z=0$ in detail. We already saw that in this case (6) cannot be used on behalf of its divergence. Equation (10) can be used with any positive β. We calculated $-2\pi^2a^2\eta(0)$ in seven decimals with $\beta=1$, $\beta=3$, respectively. In the first case we had to take eighteen terms of the first series and only one of the second. The result was found to be

$$2.0832296+0.0000033=2.0832329.$$

With $\beta=3$ we had to consider six terms of the first, and three terms of the second series, obtaining in this case

$$2.0053020+0.0779307=2.0832327,$$

in close agreement with the earlier value. Thus we can state

$$\int_0^{\infty}\frac{dt}{I_0(t)}=2.083232\cdots, \quad \eta(0)=-\frac{0.10554}{a^2}. \quad (11)$$

Numerical computation of the surface charge density is now easily established. When $z \geqslant a$, already the first four terms of (6) are sufficient to guarantee the correctness of the fourth decimal. Inserting known data from existing Bessel-function tables, (6) becomes

$$\begin{aligned}-a^2\eta(z) = {} & 0.30657 \exp(-2.40z/a) \\ & -0.46774 \exp(-5.52z/a) \\ & +0.58636 \exp(-8.65z/a) \\ & -0.68466 \exp(-11.79z/a). \end{aligned} \quad (12)$$

In the remaining range $0 \leqslant z \leqslant a$, Eq. (10) may be used with $\beta = 2$. Then one obtains

$$\begin{aligned}-a^2\eta(z) = {} & 0.08003 \cos(z/a) + 0.02076 \cos(3z/a) \\ & +0.00372 \cos(5z/a) + 0.00060 \cos(7z/a) \\ & +0.00009 \cos(9z/a) + 0.00001_4 \cos(11z/a) \\ & +0.00032 \cosh(2.4z/a). \end{aligned} \quad (13)$$

The data of Fig. 1 were computed by means of Eqs. (12) and (13). The curve shows a rapid decrement of the surface charges with increasing distance from the cut plane.

By expanding both sides of (9) into a power series of λ, and identifying the corresponding coefficients, we obviously obtain

$$\int_0^\infty \frac{t^{2r}}{I_0(t)}dt = \beta \sum_{\nu=0}^{\infty} \frac{(\beta\nu+\beta/2)^{2r}}{I_0(\beta\nu+\beta/2)} + (-1)^r 2\pi \sum_{n=1}^{\infty} \frac{k_n^{2r}}{J_1(k_n)[1+e^{2\pi k_n/\beta}]}.$$

The numerical values of these integrals can be found in the same way as shown above for $r=0$. Then for $\eta(z)$ a power series in z^2/a^2 can be derived, convergent for $|z| < a$. The expression (13), however, is much more useful for numerical purposes in the corresponding range of z-values.

3. FORMULAS FOR THE POTENTIAL AND THE ELECTRIC FIELD

The potential $V(P)$ can be considered as the sum of the potential $1/r$, due to the unit charge in the origin, and the potential $V_0(P)$, due to the induced charges on the surface of the cylinder:

$$V(P) = \frac{1}{r} + V_0(P) = \frac{1}{r} + \int \frac{\eta(\zeta)}{r_1} d\sigma.$$

In this r, r_1, denote the distances from P to the origin, and the surface element, respectively. Again, $V_0(P)$ depends only upon z and ρ.

At first we restrict ourselves to points on the axis of the cylinder. Then we have

$$V_0(z, 0) = 2\pi a \int_{-\infty}^{\infty} \frac{\eta(x+u)}{(u^2+a^2)^{\frac{1}{2}}} du.$$

Using (5), we obtain

$$V_0(z, 0) = -\frac{2}{\pi} \int_0^\infty \frac{\cos\lambda z}{I_0(\lambda a).} d\lambda \int_0^\infty \frac{\cos\lambda u}{(u^2+a^2)^{\frac{1}{2}}} du.$$

On account of a well-known integral for the K-function, namely

$$K_0(\lambda a) = \int_0^\infty \frac{\cos\lambda u}{(u^2+a^2)^{\frac{1}{2}}} du, \quad (14)$$

we obtain for the potential of the induced charges, at points on the axis of the cylinder

$$V_0(z, 0) = -\frac{2}{\pi} \int_0^\infty \frac{K_0(\lambda a)}{I_0(\lambda a)} \cos\lambda z d\lambda. \quad (15)$$

In the rotationally symmetrical problem under consideration, the potential outside the axis is easily obtained, once the potential on the axis of symmetry has been found. We simply have to take the mean value of $V_0(z+i\rho\cos\varphi, 0)$ over a full period of the angle φ. Thus

$$V_0(z, \rho) = \frac{1}{2\pi} \int_0^{2\pi} V_0(z+i\rho\cos\varphi, 0) d\varphi. \quad (16)$$

The integration over φ can be performed, leading to

$$V_0(z, \rho) = -\frac{2}{\pi} \int_0^\infty \frac{K_0(\lambda a)}{I_0(\lambda a)} I_0(\lambda\rho) \cos\lambda z d\lambda, \quad (17)$$

and for the total potential we get

$$V(z, \rho) = \frac{1}{(z^2+\rho^2)^{\frac{1}{2}}} - \frac{2}{\pi a} \int_0^\infty \frac{K_0(t)}{I_0(t)} \times I_0(t\rho/a) \cos(tz/a) dt. \quad (18)$$

The corresponding axial and radial components of the electric force are readily derived from

(18) by differentiation

$$E_z=\frac{z}{(z^2+\rho^2)^{\frac{3}{2}}}-\frac{2}{\pi a^2}\int_0^\infty \frac{K_0(t)}{I_0(t)} \times tI_0(t\rho/a)\sin(tz/a)dt, \tag{19}$$

$$E_\rho=\frac{\rho}{(z^2+\rho^2)^{\frac{3}{2}}}+\frac{2}{\pi a^2}\int_0^\infty \frac{K_0(t)}{I_0(t)} tI_1(t\rho/a)\cos(tz/a)dt.$$

It does not seem possible to transform these integrals explicitly into known functions.

Having thus found expressions for the electric field inside the cylinder, we can easily verify them afterwards. For any real value of λ, the function

$$\cos(\lambda z)\cdot I_0(\lambda\rho)$$

is a regular solution of the potential equation inside the cylinder. Furthermore, the right-hand side of (17), being an absolutely convergent linear combination of those functions, is here a regular potential as well. Therefore, the function V of (18) is also a regular potential, with exception of the origin, where it has just the required singularity. It only remains to be checked that V vanishes on the boundary at $\rho=a$. This, however, is evident from the Fourier inversion of (14):

$$\frac{2}{\pi}\int_0^\infty K_0(\lambda a)\cos\lambda z d\lambda=\frac{1}{(z^2+a^2)^{\frac{1}{2}}}.$$

4. A SECOND METHOD TO SOLVE THE POTENTIAL PROBLEM[6]

The *first* method to obtain expressions for the field inside the cylinder, as given above, started from a certain pre-calculated surface charge distribution on the boundary. This method is a little unconventional. Usually one works in the opposite direction: first the potential is obtained as the solution of a boundary value problem, and then the surface charges are calculated. The results above immediately indicate how this *second* method runs. One should try to find a function $f(\lambda)$ such that the potential of the yet unknown charges be expressible as follows

$$V_0(z,\rho)=\int_0^\infty f(\lambda)I_0(\lambda\rho)\cos\lambda z d\lambda,$$

this being a continuous sum of elementary potential functions. Fortunately, the primary potential of the unit point charge can already be expressed in that way:

$$\frac{1}{r}=\frac{2}{\pi}\int_0^\infty K_0(\lambda\rho)\cos\lambda z d\lambda, \tag{20}$$

and, hence, for the total potential

$$V(z,\rho)=\int_0^\infty \left\{f(\lambda)I_0(\lambda\rho)+\frac{2}{\pi}K_0(\lambda\rho)\right\}\cos\lambda z d\lambda.$$

A sufficient condition that $V(z,\rho)$ be zero on the boundary of the cylinder is that the integrand vanish there; consequently the function $f(\lambda)$ can be determined from

$$f(\lambda)I_0(\lambda a)+\frac{2}{\pi}K_0(\lambda a)=0,$$

and then one obtains (17).

Moreover, in combining Eqs. (17) and (20), we can derive the following expression

$$V(z,\rho)=\frac{2}{\pi}\int_0^\infty \frac{I_0(\lambda a)K_0(\lambda\rho)-K_0(\lambda a)I_0(\lambda\rho)}{I_0(\lambda a)} \times\cos\lambda z d\lambda, \tag{21}$$

which more directly shows the vanishing at $\rho=a$. Equation (21) enables us to come to the integral expression (5) for the charge density. Theretofore, we use (1) and the Wronskian of I_0, K_0:

$$I_0(t)K_0'(t)-I_0'(t)K_0(t)=-\frac{1}{t}, \tag{22}$$

and so we are back at our former starting point.

5. APPROXIMATE EXPRESSIONS FOR THE SURFACE CHARGES

Weber,[6] in his theory of a point charge inside a cylinder, follows the second method apart from slight modifications of minor importance. His Eqs. (13), (17), and (18) are equivalent to ours as shown in Eqs. (18) and (19). Equation (5) for

[6] E. Weber, "The electrostatic field produced by a point charge in the axis of a cylinder," J. App. Phys. **10**, 663 (1939).

the surface charge density, however, was not given by Weber.

As for numerical calculations, Weber writes "the actual evaluation of the field distribution is rather difficult on account of the Fourier integrals which necessitate a point for point numerical integration in infinite limits," and further "the numerical evaluation of the integrals is very laborious." Weber, therefore, does not integrate point for point, but approximates the integrands by more tractable elementary functions, such that the remaining integrals can be computed explicitly.

As a fair approximation, suggested by existing tables of Bessel functions, Weber uses, for instance

$$\frac{K_0(t)}{I_0(t)}tI_1(t)\approx\frac{t}{2}e^{-t},\quad(t>0).\tag{23}$$

From the lower integral in (19), E_ρ can then be evaluated at the surface of the cylinder. Weber's result for the corresponding density of charge, according to $\eta(z)=-E_\rho/4\pi$, may be written

$$-a^2\eta(z)\approx\frac{1}{4\pi}\left\{\frac{1}{(1+\zeta^2)^{\frac{1}{2}}}+\frac{1}{\pi}\frac{1-\zeta^2}{(1+\zeta^2)^2}\right\},\qquad(\zeta=z/a).\tag{23'}$$

Furthermore, Weber derives expressions for the field in the cut plane as well for points at the surface of the cylinder, by another approximation, different from (23). His approximation (21) reads

$$\frac{K_0(t)}{I_0(t)}\approx(2\pi)^{\frac{1}{2}}te^{-2t},\quad(t>0).\tag{24}$$

We need not, however, confine ourselves to the special values $z=0$ or $\rho=a$, as did Weber. When (24) is applied, we obtain

$$\frac{1}{(2\pi)^{\frac{1}{2}}}\int_0^\infty\frac{K_0(t)}{I_0(t)}I_0(t\rho/a)\cos(tz/a)dt\approx Re\int_0^\infty e^{-t(2+i\zeta)}J_0(it\rho/a)tdt\approx Re\frac{2+i\zeta}{[(2+i\zeta)^2-\rho^2/a^2]^{\frac{1}{2}}};$$

TABLE I. Values of surface charge density $|\eta|$ in units $1/a^2$. First column: rigorous values; second: Weber's approximation (23'). Third and fourth columns: approximations (25'), (24'), respectively.

z/a	$-a^2\eta(z)$			
0	0.1055	0.1049	0.1040	0.1285
0.2	0.0980	0.0975	0.0969	0.1144
0.4	0.0795	0.0795	0.0792	0.0827
0.6	0.0581	0.0589	0.0586	0.0510
0.8	0.0396	0.0413	0.0406	0.0280
1.0	0.0259	0.0281	0.0269	0.0147
1.2	0.0165	0.0190	0.0174	0.0076
1.4	0.0104	0.0129	0.0111	0.0041
1.6	0.0065	0.0087	0.0069	0.0025
1.8	0.0040	0.0060	0.0042	0.0018
2.0	0.0025	0.0041	0.0025	0.0016

and then, from (18)

$$V(z,\rho)\approx\frac{1}{(z^2+\rho^2)^{\frac{1}{2}}}-\frac{1}{a}\left(\frac{8}{\pi}\right)^{\frac{1}{2}}Re\frac{2+i\zeta}{[(2+i\zeta)^2-\rho^2/a^2]^{\frac{1}{2}}}.$$

Especially on the cut plane, when differentiated to $(-\rho)$, this formula yields

$$E_\rho\approx\frac{1}{\rho^2}\left\{1+\left(\frac{8}{\pi}\right)^{\frac{1}{2}}\frac{6\rho^3/a^3}{[4-\rho^2/a^2]^{5/2}}\right\},\quad(z=0).$$

This result is apparently in disagreement with that of Weber. His relation reads

$$E_{\rho,\,\text{Weber}}\approx\frac{1}{\rho^2}\left\{1+\left(\frac{8}{\pi}\right)^{\frac{1}{2}}\frac{\rho^3/a^3}{[4-\rho^2/a^2]^{\frac{1}{2}}}\right\},\quad(z=0).$$

The reason for this discrepancy is that Weber dropped one factor γ in the integrand of his integral (22), so that actually he has used the following approximation

$$\frac{K_0(t)}{I_0(t)}\approx(2\pi)^{\frac{1}{2}}e^{-2t}\tag{25}$$

instead of (24).

In the latter case we find for general values of z and ρ

$$V(z,\rho)\approx\frac{1}{(z^2+\rho^2)^{\frac{1}{2}}}-\frac{1}{a}\left(\frac{8}{\pi}\right)^{\frac{1}{2}}Re\{(2+i\zeta)^2-\rho^2/a^2\}^{-\frac{1}{2}}$$

leading exactly to Weber's formula for E_ρ.

In either of the cases Eqs. (24) and (25), the corresponding surface charges, can be calcu-

lated. We obtained, respectively,

$$-a^2\eta(z)\approx\frac{1}{4\pi}\left\{\frac{1}{(1+\zeta^2)^{\frac{1}{2}}}+\left(\frac{8}{\pi}\right)^{\frac{1}{2}}Re\frac{3(2+i\zeta)}{(1+i\zeta)^{5/2}(3+i\zeta)^{5/2}}\right\},\quad(24')$$

$$-a^2\eta(z)\approx\frac{1}{4\pi}\left\{\frac{1}{(1+\zeta^2)^{\frac{1}{2}}}+\left(\frac{8}{\pi}\right)^{\frac{1}{2}}Re\frac{1}{(1+i\zeta)^{\frac{1}{2}}(3+i\zeta)^{\frac{1}{2}}}\right\}.\quad(25')$$

Table I shows the three different approximations (23′), (24′), (25′), in presence of the correct values, as computed from (12), (13). The approximation (24′) is obviously very poor, leading to values which are too large at $z\approx 0$ and too small at $z\approx 2a$. Either of the approximations (23′) and (25′) is excellent. That of Weber (23′) is a better approximation at small values of z than is (25′). On the other hand, for values of z exceeding a, the latter is much better than the former. Moreover, Weber's formula yields negative values for $-a^2\eta(z)$, when $\zeta>3.6$. This is physically impossible, however. The surface charge density must always have the same sign. The right-hand side of (25′), on the contrary, is positive for large values of ζ. Therefore, as a whole, the approximation (25) may be considered as the most useful one, at least as far as we confine ourselves to the surface charges.

The radial field at the surface of the cylinder, just opposite the point charge, is 1.3262 times as large as it would be under influence of the free-point charge, when the cylinder was removed. The corresponding factors in the three approximations (23), (25), and (24), are 1.3071, 1.3183, and 1.6142, respectively.

6. FORMULAS WHICH ADMIT OF NUMERICAL CALCULATIONS INSIDE THE CYLINDER

For exact numerical calculations the integral representation (18) is almost without any value. In Section 2 we derived expressions for the charge density which served its useful purpose. The field can be dealt with in a similar manner. The integral (15), however, is no suitable starting point, because its integrand shows a logarithmic singularity in the lower limit. The difficulties owing to the many-valuedness of the K-function may be conveniently avoided in the following way. By partially integrating (15) and using (22), one readily obtains

$$V_0(z,0)=-\frac{2}{\pi z}\int_0^\infty\frac{\sin(tz/a)}{tI_0^2(t)}dt.\qquad(26)$$

We now proceed in the same manner as we did before with (5). In this case the path of integration in the complex plane has to avoid the origin by a small indentation in the upper-half plane. We then obtain for $z>0$

$$\frac{1}{\pi}\int_0^\infty\frac{\sin(tz/a)}{tI_0^2(t)}dt=\tfrac{1}{2}+\sum_{n=1}^{\infty}\underset{(t=ik_n)}{\text{residue}}\frac{e^{itz/a}}{tI_0^2(t)}.$$

We calculate the residue in $t=ik_n$ by putting $t=x+ik_n$, developing the function into ascending powers of x, and taking the coefficient of $1/x$ in that expansion. The function is of the type $f(x)/g^2(x)$, where $g(x)$ has a simple zero in $x=0$, and $f(0)\neq 0$. The coefficient of $1/x$ turns out to be

$$\frac{f}{g'^2}\left\{\frac{f'}{f}-\frac{g''}{g'}\right\}_{x=0}=-\frac{z}{ak_n}\frac{e^{-k_nz/a}}{J_1^2(k_n)}.$$

Consequently, for $z>0$

$$V_0(z,0)=-\frac{1}{z}+\frac{2}{a}\sum_{n=1}^{\infty}\frac{e^{-k_nz/a}}{k_nJ_1^2(k_n)}.$$

To obtain the total potential on the axis of the cylinder we must add the potential of the unit charge in the origin. For positive values of z the latter is $1/z$. Hence

$$V(z,0)=\frac{2}{a}\sum_{n=1}^{\infty}\frac{e^{-k_nz/a}}{k_nJ_1^2(k_n)}.$$

Applying (16), we finally obtain for $z>0$

$$V(z,\rho)=\frac{2}{a}\sum_{n=1}^{\infty}\frac{J_0(k_n\rho/a)}{k_nJ_1^2(k_n)}e^{-k_nz/a}.\qquad(27)$$

The series (27) converges also for $x=0$ with the only exception of the origin, where it diverges to infinity. In actual numerical work (27) appears to be useful for $z/a\geqslant 0.2$; in the remaining range $0\leqslant z/a\leqslant 0.2$ other methods should be applied.

One naturally asks whether or not it is possible to establish developments for the potential, analogous to that of formula (10) for the surface charge density. Actually, the required transformation is readily performed for points in the axis of the cylinder. We only write down the final result:

$$V_0(z,0)=-\frac{2}{\pi z}\sum_{\nu=0}^{\infty}\frac{\sin(\beta\nu+\beta/2)z/a}{(\nu+\frac{1}{2})I_0^2(\beta\nu+\beta/2)}\cdot$$

$$+\frac{1}{a}\sum_{n=1}^{\infty}\frac{\{1+e^{-2\pi k_n/\beta}\}\cosh(k_nz/a)-(2\pi a/\beta z)\sinh(k_nz/a)}{k_nJ_1^2(k_n)\cosh^2(\pi k_n/\beta)}. \quad (28)$$

The first series converges for all real z, the second for $|z|\leqslant 2\pi a/\beta$; β is an arbitrary positive number. If especially $\beta=2\pi a/z$, the first series vanishes identically, whereas the second one reduces to (27) for $\rho=0$.

For actual numerical evaluation we have chosen $\beta=2$. Then the series (28) becomes

$$-aV_0(z,0)=-\frac{a}{z}\{0.79432\sin(z/a)$$
$$+0.01782\sin(3z/a)+0.00034\sin(5z/a)$$
$$+0.00000_6\sin(7z/a)+0.01014\sinh(2.4z/a)\}$$
$$-0.00323\cosh(2.4z/a). \quad (29)$$

Although convergent for $z/a<\pi$, (29) may be useful for $z/a\leqslant 1$.

Unfortunately, there do not seem to exist simple developments for general non-zero values of ρ, because (16) yields for the continuation of $(\sin z/a)/(z/a)$ outside the axis

$$\frac{a}{\rho}\int_0^{\rho/a}\cos(tz/\rho)I_0(t)dt,$$

which integral cannot be solved explicitly.

For small values of z we can expand the initial integral (26) into powers of z/a. We then obtain

$$V_0(z,0)=-\frac{2}{a}\sum_{\nu=0}^{\infty}\frac{(-1)^\nu\lambda_{2\nu}}{(2\nu)!}\left(\frac{z}{a}\right)^{2\nu}, \quad (30)$$

where

$$\lambda_{2\nu}=\frac{1}{(2\nu+1)\pi}\int_0^{\infty}\frac{t^{2\nu}}{I_0^2(t)}dt, \quad (31)$$

$$\lambda_0=0.4353382,$$
$$\lambda_2=0.2059112,$$
$$\lambda_4=0.6588568.$$

TABLE II. Values of the potential (measured in units $1/a$) inside a grounded cylinder under induction of an axial positive unit-point charge; a = radius of the cylinder, z and ρ the usual cylindrical coordinates. Point charge in the origin.

z/a \ ρ/a	0	0.2	0.4	0.6	0.8
0	∞	4.125	1.612	0.756	0.303
0.1	9.131	3.600	1.539	0.736	0.297
0.2	4.137	2.670	1.357	0.681	0.280
0.3	2.480	1.919	1.131	0.603	0.253
0.4	1.661	1.395	0.916	0.518	0.224
0.5	1.178	1.033	0.729	0.432	0.192
0.6	0.864	0.776	0.575	0.355	0.161
0.7	0.648	0.591	0.410	0.287	0.133
0.8	0.493	0.454	0.355	0.231	0.109
0.9	0.379	0.353	0.281	0.189	0.091
1.0	0.292	0.272	0.219	0.147	0.071
1.2	0.176	0.164	0.135	0.092	0.045
1.4	0.107	0.101	0.083	0.057	0.028
1.6	0.066	0.062	0.051	0.036	0.017
1.8	0.041	0.039	0.032	0.022	0.011
2.0	0.025	0.024	0.019	0.014	0.007

Except λ_0, these numerical values were given by Watson.[5]

We can now apply (16) with greater success than before. In performing the transformation (16) upon (30) we obtain

$$V_0(z,\rho)=-\frac{2}{a}\sum_{\nu=0}^{\infty}\frac{(-1)^\nu\lambda_{2\nu}}{(2\nu)!}F_\nu\left(\frac{z}{a},\frac{\rho}{a}\right), \quad (32)$$

where

$$F_\nu(u,v)=\frac{1}{2\pi}\int_0^{2\pi}(u+iv\cos\varphi)^{2\nu}d\varphi$$
$$=(u^2+v^2)^\nu P_{2\nu}\left\{\frac{u}{(u^2+v^2)^{\frac{1}{2}}}\right\}, \quad (33)$$

and $P_{2\nu}$ is the usual symbol for the Legendre polynomial. For instance

$$F_0=1,$$
$$F_1=u^2-\tfrac{1}{2}v^2,$$
$$F_2=u^4-3u^2v^2+\tfrac{3}{8}v^4.$$

It may be remarked that (32) converges for $z^2+\rho^2<4a^2$.

The development (32) becomes much more familiar when spherical coordinates r, ϑ, are introduced, connected to the cylindrical ones by means of

$$r^2=z^2+\rho^2; \quad \tan\vartheta=\rho/z.$$

Then (32) is transformed into

$$V_0(z, \rho) = -\frac{2}{a}\sum_{\nu=0}^{\infty} \frac{(-1)^\nu \lambda_{2\nu}}{(2\nu)!}\left(\frac{r}{a}\right)^{2\nu} P_{2\nu}(\cos\vartheta). \quad (34)$$

This series is convergent for $r/a<2$; it is nothing else but the development of $V_0(P)$ into spherical potential functions.

Especially in the cut plane $z=0$ we found

$$-aV_0(0, \rho) = 0.8707 + 0.1030(\rho/a)^2 + 0.0206(\rho/a)^4 + 0.0057(\rho/a)^6.$$

The first three coefficients are calculated from the values λ_0, λ_2, and λ_4, as specified above; the last coefficient is taken so that the total is 1.0000, on account of $V_0(0, a)$ being $-1/a$, thus neglecting terms of higher order than $(\rho/a)^6$.

Numerical evaluation of the potential inside the cylinder may be readily accomplished now. The different expressions (27), (28), and (34) have reasonable overlapping regions of useful convergence. Numerical data for the total potential are to be found in Table II.

The electric field itself can also be calculated numerically. From (27) we deduce for $z>0$

$$E^z = \frac{2}{a^2}\sum_{n=1}^{\infty} \frac{J_0(k_n\rho/a)}{J_1^2(k_n)} e^{-k_n z/a}, \qquad E_\rho = \frac{2}{a^2}\sum_{n=1}^{\infty} \frac{J_1(k_n\rho/a)}{J_1^2(k_n)} e^{-k_n z/a}. \quad (35)$$

It may be noted that in Watson's paper[5] two series S_1, S_2 occur which are related to the series (35) by

$$E_z = \frac{2}{a^2} S_1; \quad E_\rho = -\frac{2}{a}\frac{\partial S_2}{\partial z}.$$

Therefore, Watson's series can be obtained from that shown in (27). Whereas Watson has given explicitly only the first four terms of the development corresponding to (32), we found the general term here expressible in spherical potential functions; cf. (34). With exclusion of the immediate neighborhood of the cut plane $z=0$, Eqs. (35) are very useful for numerical purposes. Around the cut plane we better use (34) and compute E_r, E_ϑ instead of the cylindrical components; further details may be omitted, however.

7. A THIRD METHOD OF SOLUTION

Either of the two distinct methods developed previously yields complete information concerning the field of the axial point charge in the cylinder. The mathematics there involved are quite instructive, and can serve successfully as a guide in problems of wave propagation inside the same cylinder.

The reader is aware that even in the simplest potential problem, as was treated above, a considerable amount of analysis was used. In this respect wave guide theory is still less tractable. The question whether this is really necessary, from an engineer's point of view, will be answered in due course.

In practical wave guide applications, one is mainly interested in the fields far from the exciting antenna, where many of the higher modes have already been damped out. With this restriction in mind, and thus ignoring the field in the nearby zone, we have investigated whether it is possible to calculate the field in the far zone more directly, without the usual extensive amount of complex function theory. This new method was found by inspection and generalization of the expansion (27), obtained for the potential in the preceding section. Each separate term of that series, for non-vanishing z, is a solution of the potential equation, fulfilling the required boundary condition at the surface of the cylinder, and showing the suitable behavior at infinity. So we might have expected in advance the possibility of solving our potential problem by means of such a development, in terms of discrete normal solutions of the potential equation:

$$V(z, \rho) = \sum_{n=1}^{\infty} c_n J_0(k_n\rho/a) e^{-k_n|z|/a}. \quad (36)$$

When the proposed method actually works, it must be possible, somehow, to calculate the unknown coefficients c_n in this development from the behavior of $V(z, \rho)$ in the immediate neighborhood of the prescribed singularity at the origin, although just in the point charge, (36) is known to diverge. In the following we will show how this problem can be solved. We consider a more general problem, however, so that the new method is equally well applicable to solutions of

the wave equation. Moreover, we need not restrict ourselves to rotationally symmetrical fields. In many cases the prescribed singularity is of the type

$$\frac{1}{R}=\{z^2+\rho^2-2\rho\rho_0\cos\varphi+\rho_0^2\}^{-\frac{1}{2}},$$

where R denotes the distance between the field point (z, ρ, φ) and the source at $(0, \rho_0, 0)$. Singularities of this character are commonly used, both in electrostatics and in wave guide theory. We may, however, admit still more general types of sources.

Suppose $G(z, \rho)$ is a *given function* with one or more singularities for $z=0$, $0\leqslant\rho\leqslant a$. Let G be even in z, and let it have continuous derivatives of the second order, outside the singularities. In the previous case of an axial point charge, $G=(z^2+\rho^2)^{-\frac{1}{2}}$.

Furthermore, we suppose that $f_n(z)$ is a *given system* $(n=1, 2, \cdots)$ of continuously differentiable functions with the property $f_n'(0)\neq 0$. For instance, $f_n(z)=\exp(-k_n z/a)$.

The problem under consideration can now be stated in the following general form: How to find the coefficients c_n in (37), when the following properties of the function $F(z, \rho)$ are *known*:

(i) F is an even function of z.

(ii) $F-G$ has continuous derivatives of the second order, both outside and inside the singularities of G.

(iii) For $z\neq 0$, F can be expanded into a uniformly (in ρ) convergent series of the form

$$F(z, \rho)=\sum_{n=1}^{\infty} c_n J_m(k_{n,m}\rho/a) f_n(|z|), \tag{37}$$

where $k_{n,m}$ denotes the nth positive zero of the Bessel function $J_m(k)$, and m is a given integer.

The answer to this question is readily given if appropriate use is made of the well-known Fourier-Bessel-Dini series theory, for details of which the reader may be referred to Watson's standard work on Bessel functions.[7]

On account of the conditions stated under (ii) we infer that $(\partial/\partial z)(F-G)$ can be developed into a Fourier-Bessel series. This series is uniformly convergent in any closed interval, contained in $0<\rho<a$, for any value of z, whether outside or on the cut plane $z=0$. Thus we have

$$\frac{\partial}{\partial z}(F-G)=\sum_{n=1}^{\infty} b_n(z) J_m(k_{n,m}\rho/a).$$

The coefficients $b_n(z)$ can be determined in the conventional manner, using the orthogonality of the set of functions $\rho^{\frac{1}{2}}\cdot J_m(k_{n,m}\rho/a)$ upon $0\leqslant\rho\leqslant a$. One finds[7]

$$b_n(z)=\frac{2}{a^2 J_{m+1}^2(k_{n,m})}\int_0^a \rho\frac{\partial}{\partial z}(F-G)J_m(k_{n,m}\rho/a)d\rho.$$

As either of the two functions F, G is even in z, with continuous derivatives, we have $b_n(0)=0$. For points *above* the cut plane $(z>0)$ the integral may be broken up into two other integrals, namely

$$b_n(z)=\frac{2}{a^2 J_{m+1}^2(k_{n,m})}\frac{\partial}{\partial z}\int_0^a \rho F(z, \rho)J_m(k_{n,m}\rho/a)d\rho$$
$$-\frac{2}{a^2 J_{m+1}^2(k_{n,m})}\int_0^a \rho\frac{\partial G}{\partial z}J_m(k_{n,m}\rho/a)d\rho.$$

From (37), which, for fixed $z\neq 0$ is nothing else but the Fourier-Bessel series of the function $F(z, \rho)$, we obtain

$$\int_0^a \rho F(z, \rho)J_m(k_{n,m}\rho/a)d\rho$$
$$=c_n f_n(|z|)\frac{a^2}{2}J_{m+1}^2(k_{n,m})$$

Therefore, if $z>0$

$$b_n(z)=c_n f_n'(z)$$
$$-\frac{2}{a^2 J_{m+1}^2(k_{n,m})}\int_0^a \rho\frac{\partial G}{\partial z}J_m(k_{n,m}\rho/a)d\rho.$$

Now let z tend to zero through positive values; then $b_n(z)\to 0$, and $f_n'(z)\to f_n'(0)\neq 0$. Consequently, the above integral must tend to a limit value also, and the coefficient c_n is equal to

$$c_n=\frac{2}{a^2 f_n'(0)J_{m+1}^2(k_{n,m})}\lim_{z\to 0^+}\int_0^a \rho\frac{\partial G}{\partial z}$$
$$\times J_m(k_{n,m}\rho/a)d\rho. \tag{38}$$

The actual evaluation of the limit in (38) usually does not lead to difficulties. Let us take

[7] G. N. Watson, *A Treatise on the Theory of Bessel Functions* (Cambridge, 1944), Chapter XVIII.

as an example the potential problem in its simplest form, whereby the point charge is situated on the axis. Then (38) may be applied for $m=0$, $G=(z^2+\rho^2)^{-\frac{1}{2}}$. In the limit, the main contribution to the integral (38) is attributed to the values of the integrand in the neighborhood of $\rho=0$. Therefore we may substitute unit value for the Bessel function J_0. Consequently for the limit value

$$\lim \int_0^a \rho \frac{\partial}{\partial z}(z^2+\rho^2)^{-\frac{1}{2}} d\rho = \lim \frac{\partial}{\partial z} \int_0^a \frac{\rho d\rho}{(z^2+\rho^2)^{\frac{1}{2}}}$$

$$= \lim \frac{\partial}{\partial z}\{(z^2+a^2)^{\frac{1}{2}} - z\} = -1.$$

Furthermore, $f_n'(0) = -k_{n,0}/a = -k_n/a$; thus,

$$c_n = \frac{2}{a^2 k_n J_1^2(k_n)},$$

in agreement with (27).

Until now we were only interested in boundary-value problems of the *first* kind, with vanishing V at the surface of the cylinder. In boundary-value problems of the *second* kind, the normal component of grad V vanishes there; this means $\partial V/\partial \rho = 0$ in case of the cylinder. In this second problem the potential can also be developed in terms of Bessel functions. The difference is that the argument $k_{n,m}\rho/a$ is changed into $\kappa_{n,m}\rho/a$, where $\kappa_{n,m}$ means the nth positive zero of $J_m'(\kappa)$. Completely analogous to (37), (38), under similar conditions, we now have the following device:

Given

$$\Phi(z, \rho) = \sum_{n=1}^{\infty} \gamma_n J_m(\kappa_{n,m}\rho/a) f_n(|z|), \quad (37')$$

"behaves like" $G(z, \rho)$ for $z \to 0$, then the coefficients γ_n can be determined from

$$\gamma_n = \frac{2}{a^2 f_n'(0)\{1-m^2/\kappa_{n,m}^2\} J_m^2(\kappa_{n,m})} \times \lim_{z\to 0^+} \int_0^a \rho \frac{\partial G}{\partial z} J_m(\kappa_{n,m}\rho/a) d\rho. \quad (38')$$

We would like to emphasize that in practical applications we may forget all the precise mathematical conditions and restrictions. Then there only remains the very simple procedure to obtain the coefficients in the postulated expansions (37) and (37') from the Eqs. (38) and (38'), respectively. In this connection the actual evaluation of those limits is of secondary importance.

This *third* powerful method is incomplete, in so far that it does not very well provide numerical calculations in the nearby zone, because the convergence of the series (37) and (37') is usually too slow there. This, however, might always be overcome by suitable extrapolation of the data outside the cut plane. On the other hand, it has many advantages. For instance, unlike the other two methods, it is equally well applicable to either the potential or the wave equation; the only difference occurs in the system of functions $f_n(z)$. Nor does it matter whether or not there is symmetry around the axis of the cylinder.

8. FIELD OF AN ECCENTRIC POINT CHARGE

In case of an eccentric point charge, situated at $(0, \rho_0, 0)$, the potential $V(z, \rho, \varphi)$ will be expressible as a Fourier series with respect to φ, containing only cosine terms. Thus*

$$V(z, \rho, \varphi) = \sum_{m=0}^{\infty} \epsilon_m \cos m\varphi \sum_{n=1}^{\infty} c_{n,m} \times J_m(k_{n,m}\rho/a) e^{-k_{n,m}|z|/a}. \quad (39)$$

The coefficients $c_{n,m}$ have to be determined from the knowledge that V behaves like $(z^2+\rho^2-2\rho\rho_0\cos\varphi+\rho_0^2)^{-\frac{1}{2}}$ in the neighborhood of the source at $(0, \rho_0, 0)$. Obviously the method of Section 7 is applicable, if the functions G, F, are defined as follows:

$$G(z, \rho) \equiv \frac{1}{2\pi} \int_{-\pi}^{\pi} \frac{\cos m\varphi d\varphi}{(z^2+\rho^2-2\rho\rho_0\cos\varphi+\rho_0^2)^{\frac{1}{2}}}, \quad (40)$$

$$F(z, \rho) \equiv \frac{1}{2\pi} \int_{-\pi}^{\pi} V(z, \rho, \varphi) \cos m\varphi d\varphi = \sum_{n=1}^{\infty} c_{n,m} J_m(k_{n,m}\rho/a) e^{-k_{n,m}|z|/a}. \quad (40')$$

It remains to show how the limit in (38) can be actually evaluated in case of the special G-function (40). This can be accomplished by

* $\epsilon_0 = 1$; $\epsilon_m = 2$ if $m > 0$.

means of a useful *symbolic* formula, namely

$$\lim_{z\to 0^+}(\partial G/\partial z) = -(1/\rho_0)\delta(\rho-\rho_0), \qquad (41)$$

where δ denotes a delta-function, "vanishing everywhere, except for $\rho=\rho_0$, such that its integral over ρ from $-\infty$ to $+\infty$ has unit value." As G is even in z, one has, outside the singularity, $\partial G/\partial z\to 0$ if $z\to 0$; for $\rho=\rho_0$, this derivative tends to infinity. Therefore, the existence of something like (41) seems reasonable. Our final result is completely rigorous, although (41) has only a symbolic meaning. For further details the reader may be referred to the appendix.

When (41) is applied to (38), we easily obtain

$$c_{n,m} = \frac{2}{a}\frac{J_m(k_{n,m}\rho_0/a)}{k_{n,m}J_{m+1}^2(k_{n,m})},$$

and thus for the potential of the eccentric charge

$$V(z,\rho,\varphi) = \frac{2}{a}\sum_{m=0}^{\infty}\epsilon_m\cos m\varphi \times\sum_{n=1}^{\infty}\frac{J_m(k_{n,m}\rho_0/a)J_m(k_{n,m}\rho/a)}{k_{n,m}Y_{m+1}^2(k_{n,m})}e^{-k_{n,m}|z|/a}. \qquad (42)$$

As it should be, this Green function of the first kind for the potential equation inside the cylinder, is symmetrical in ρ and ρ_0. For $\rho_0=0$, (42) obviously reduces to (27).

The method of the discrete normal solutions has thus proved its value. We could write the proper solution almost at once. Of course, this is not the only way; it is certainly possible to generalize the first or second method, treated in the preceding sections. For instance, one will find for the analog of (5)

$$\eta(z,\varphi) = -\frac{1}{2\pi^2a^2}\sum_{m=0}^{\infty}\epsilon_m\cos m\varphi \times\int_0^{\infty}\frac{I_m(t\rho_0/a)}{I_m(t)}\cos(tz/a)dt,$$

and by contour integration, analogous to (6),

$$\eta(z,\varphi) = -\frac{1}{2\pi a^2}\sum_{m=0}^{\infty}\epsilon_m\cos m\varphi \times\sum_{n=1}^{\infty}\frac{J_m(k_{n,m}\rho_0/a)}{J_{m+1}(k_{n,m})}e^{-k_{n,m}|z|/a}.$$

The same expression for the surface charge density is obtained from (42) if (1) is applied to it.

Similarly, other formulas for the axial point charge can be generalized to an eccentric charge. Further details may be omitted. We better demonstrate the usefulness of the third method by a problem of wave propagation.

9. THE GREEN FUNCTIONS FOR THE WAVE EQUATION INSIDE THE CYLINDER. RADIATION OF ENERGY BY ACOUSTIC POINT SOURCES

We restrict ourselves to harmonic vibrations of frequency $\omega/2\pi$, and time dependence $\exp(-i\omega t)$. The velocity potential of a free-point source is

$$U_0 = e^{ikR}/R; \quad R^2 = z^2+\rho^2-2\rho\rho_0\cos\varphi+\rho_0^2. \qquad (43)$$

Outside the point source, the velocity potential U is a solution of the wave equation

$$\Delta U + k^2U = 0. \qquad (44)$$

There are two different types of wave functions, according to whether U or $\partial U/\partial\rho$ vanishes at the wall of the cylinder. The Green function of the first kind U is that solution of (44) which vanishes at the surface of the cylinder, which has at infinity the character of plane waves, coming from the direction of the origin of coordinates, and finally such that $U-U_0$ remains finite for $R\to 0$. The Green function of the second kind U_2 has a vanishing $\partial/\partial\rho$ at $\rho=a$, the other requirements being the same as those for U_1. Instead of the singularity (43) we may take merely $1/R$.

Discrete normal solutions of the wave equation (44) are

$$\cos m\varphi\cdot J_m(k_{n,m}\rho/a) \times\exp[-(z/a)(k_{n,m}^2-k^2a^2)^{\frac{1}{2}}], \qquad (45)$$

$$\cos m\varphi\cdot J_m(\kappa_{n,m}\rho/a) \times\exp[-(z/a)(\kappa_{n,m}^2-k^2a^2)^{\frac{1}{2}}]. \qquad (45')$$

The functions (45) vanish at $\rho=a$, those of (45′) have a vanishing derivative with respect to ρ. On account of symmetry around the plane $\varphi=0$, the potentials do not contain terms with $\sin(m\varphi)$.

Therefore we may expect for $z \neq 0$

$$u_1 = \sum_{m=0}^{\infty} \epsilon_m \cos m\varphi \sum_{n=1}^{\infty} c_{n,m} J_m(k_{n,m}\rho/a) \times \exp[-(|z|/a)(k_{n,m}^2 - k^2a^2)^{\frac{1}{2}}], \quad (46)$$

$$u_2 = \sum_{m=0}^{\infty} \epsilon_m \cos m\varphi \sum_{n=1}^{\infty} \gamma_{n,m} J_m(\kappa_{n,m}\rho/a) \times \exp[-(|x|/a)(\kappa_{n,m}^2 - k^2a^2)^{\frac{1}{2}}]. \quad (46')$$

In these cases the functions $f_n(z)$ are, respectively,

$$\exp[-(z/a)(k_{n,m}^2 - k^2a^2)^{\frac{1}{2}}],$$

$$\exp[-(z/a)(\kappa_{n,m}^2 - k^2a^2)^{\frac{1}{2}}].$$

It is seen that the only difference between (39) and (46) is in the occurrence of different functions $f_n(z)$. Consequently we can at once write down the result

$$c_{n,m} = \frac{2}{a} \frac{J_m(k_{n,m}\rho_0/a)}{(k_{n,m}^2 - k^2a^2)^{\frac{1}{2}} J_{m+1}^2(k_{n,m})}. \quad (47)$$

Obviously the Green function U_1 for the wave equation reduces to that of the potential equation (cf. (42)) when k tends to zero. Concerning the square root, we must define for $ka > k_{n,m}$

$$(k_{n,m}^2 - k^2a^2)^{\frac{1}{2}} = -i(k^2a^2 - k_{n,m}^2)^{\frac{1}{2}}$$

because of the time factor $\exp(-i\omega t)$.

For the second Green function we obtain by application of (38′)

$$\gamma_{n,m} = \frac{2}{a} \frac{J_m(\kappa_{n,m}\rho_0/a)}{(1 - m^2/\kappa_{n,m}^2)(\kappa_{n,m}^2 - k^2a^2)^{\frac{1}{2}} J_m^2(\kappa_{n,m})}, \quad (47')$$

It is to be noticed that in case of *resonance* the method fails, because then some coefficient c or γ becomes infinitely large. This resonance phenomenon occurs for special values of the applied frequency, namely $ka = k_{n,m}$ or $ka = \kappa_{n,m}$, respectively, for some values of n, m. They correspond to the cut-off frequencies of the circular wave guide. In practice actual infinities do not occur, because of certain corrections which have been neglected in our treatment, and which only play an important part near the cut-off frequencies.

Once the amplitudes of the different modes of propagation are known, it is not difficult to compute the amount of energy, radiated by the point source into the cylinder. At large distances from the cut plane $z=0$, the potential is determined by the undamped waves only. So we have

$$u_1 \approx \sum\sum_{0 < k_{n,m} < ka} \epsilon_m c_{n,m} \cos m\varphi J_m(k_{n,m}\rho/a) \times \exp[-i(\omega t - (|z|/a)(k^2a^2 - k_{n,m}^2)^{\frac{1}{2}})].$$

Because of the fact that the system of functions

$$\cos m\varphi J_m(k_{n,m}\rho/a)$$

is orthogonal over the cross section of the cylinder, one evidently has

$$\frac{1}{2\pi} \int\int |u_1|^2 dS = \sum |c_{n,m}|^2 \int_0^a J_m^2(k_{n,m}\rho/a)\rho d\rho,$$

where the surface integral is extended over the cross section of the cylinder, and the summation extends over n, m such that $k_{n,m} < ka$. The integration over ρ can be performed, and after inserting the values of $c_{n,m}$ from (47), one obtains

$$\frac{1}{2\pi} \int\int |u_1|^2 dS = 2 \sum_{0 < k_{n,m} < ka} \frac{J_m^2(k_{n,m}\rho_0/a)}{(k^2a^2 - k_{n,m}^2) J_{m+1}^2(k_{n,m})}. \quad (48)$$

Similarly, for the other problem

$$\frac{1}{2\pi} \int\int |U_2|^2 dS = 2 \sum_{0 < \kappa_{n,m} < ka} \times \frac{J_m^2(\kappa_{n,m}\rho_0/a)}{(k^2a^2 - \kappa_{n,m}^2)[1 - (m^2/\kappa_{n,m}^2)] J_m^2(\kappa_{n,m})}. \quad (48')$$

The physical meaning of the right-hand side of (48′) is that it provides us with the numeric by which the output energy of a *freely* radiating source should be multiplied in order to obtain the energy output, when the same source is placed inside the cylinder, at a distance ρ_0 from the axis.

By the method of images we can also treat the case of a point source inside a cylinder with one end closed. Let d denote the distance from the source to the closed end. Then, by introducing an unclosed cylinder with two sources, a distance $2d$ apart, and vibrating out or in

phase, we obtain for the potentials

$$u_1 = U_1(z+d,\ \rho,\ \varphi) - U_1(z-d,\ \rho,\ \varphi),$$
$$u_2 = U_2(z+d,\ \rho,\ \varphi) + U_2(z-d,\ \rho,\ \varphi).$$

The far field is a result of two interfering systems of plane waves. It is not difficult to obtain the correspondingly changed energy factors. Before in (48) and (48′) the summation is performed, each separate term must be multiplied by suitable interference factors; these factors are

$$2\sin^2\left[\frac{d}{a}(k^2a^2-k_{n,m}{}^2)^{\frac{1}{2}}\right], \tag{49}$$

$$2\cos^2\left[\frac{d}{a}(k^2a^2-\kappa_{n,m}{}^2)^{\frac{1}{2}}\right], \tag{49′}$$

respectively. The resulting expressions, which we need not write down in detail, will then provide us with the numerical factors, by which the output of the free source should be multiplied to obtain its output, when placed at distances d and ρ_0 from the closed end and the axis, respectively, inside a one-sided cylinder.

Questions of wave propagation in electromagnetic theory can be dealt with in quite the same way, further details of which will not be given at present.

APPENDIX

The validity of the symbolic formula (41) remains to be proved. That means, in rigorous mathematical terms, we have to prove

$$\lim_{z\to 0^+}\int_0^a \rho f(\rho)\frac{\partial G_m}{\partial z}d\rho = -f(\rho_0), \tag{A}$$

where G_m is defined by

$$G_m = \frac{1}{2\pi}\int_{-\pi}^{\pi}\frac{\cos m\varphi\, d\varphi}{(z^2+\rho^2-2\rho\rho_0\cos\varphi+\rho_0{}^2)^{\frac{1}{2}}}. \tag{B}$$

Equation (A) holds true for $0<\rho_0<a$, if $f(\rho)$ is continuous upon the closed interval $(0, a)$, but otherwise arbitrary.

For a complete proof of (A) it is sufficient to know that (A) is valid in the following two special cases:

(1) $f(\rho)=\rho^m$, where m is the same as in G_m;
(2) $f(\rho)$ vanishes at $\rho=\rho_0$.

The most general case is obviously a linear combination of these special cases, because one can always write

$$f(\rho) = \frac{f(\rho_0)}{\rho_0{}^m}\cdot\rho^m + g(\rho),$$

where $g(\rho)$ vanishes at $\rho=\rho_0$.

Case 1

For $z>0$, from well-known formulas in Bessel-function theory, we have

$$(z^2+\rho^2-2\rho\rho_0\cos\varphi+\rho_0{}^2)^{-\frac{1}{2}} = \int_0^\infty e^{-zt}J_0[t(\rho^2-2\rho\rho_0\cos\varphi+\rho_0{}^2)^{\frac{1}{2}}]dt = \sum_0^\infty \epsilon_\nu\cos\nu\varphi\int_0^\infty e^{-zt}J_\nu(\rho_0 t)J_\nu(\rho t)dt.$$

Upon multiplication by $\cos(m\varphi)$, and integration over a full period of φ, we obtain

$$G_m = \int_0^\infty e^{-zt}J_m(\rho_0 t)J_m(\rho t)dt. \tag{C}$$

Consequently

$$\int_0^a \rho\cdot\rho^m(\partial G_m/\partial z)d\rho = \int_0^a \rho^{m+1}d\rho\int_0^\infty -te^{-zt}J_m(\rho_0 t)J_m(\rho t)dt = -\int_0^\infty t^{-m-1}e^{-zt}J_m(\rho_0 t)dt\int_0^{zt}\kappa^{m+1}J_m(x)dx = -a^{m+1}\int_0^\infty e^{-zt}J_m(\rho_0 t)J_{m+1}(at)dt.$$

Let z tend to zero; then the integral above tends to

$$\int_0^\infty J_m(\rho_0 t)J_{m+1}(at)dt = (\rho_0{}^m/a^{m+1}) \quad (0<\rho_0<a).$$

Hence

$$\lim_{z\to 0^+}\int_0^a \rho\cdot\rho^m(\partial G_m/\partial z)d\rho = -\rho_0{}^m \tag{D}$$

which is (A) for the special function $f(\rho)=\rho^m$.

Case 2

It is easy to demonstrate that the contribution of the intervals outside the immediate vicinity of ρ_0 is zero; that means

$$\lim_{z\to 0^+}\left\{\int_0^{\rho_0-\epsilon}\rho f(\rho)\frac{\partial G_m}{\partial z}d\rho + \int_{\rho_0+\epsilon}^a \rho f(\rho)\frac{\partial G_m}{\partial z}d\rho\right\} = 0, \tag{E}$$

where ϵ is any positive constant, such that $0\leqslant\rho_0-\epsilon<\rho_0+\epsilon\leqslant a$. For the proof of (E) we introduce M, the upper bound of $|f(\rho)|$ upon $(0, a)$. Then

$$\left|\int_0^{\rho_0-\epsilon}\rho f(\rho)\frac{\partial G_m}{\partial z}d\rho\right| \leqslant M\int_0^{\rho_0-\epsilon}\rho\left|\frac{\partial G_m}{\partial z}\right|d\rho.$$

Furthermore,

$$\frac{\partial G_m}{\partial z} = -\frac{z}{2\pi}\int_{-\pi}^{\pi}\frac{\cos m\varphi\, d\varphi}{(z^2+\rho^2-2\rho\rho_0\cos\varphi+\rho_0{}^2)^{\frac{1}{2}}};$$

thus

$$\left|\frac{\partial G_m}{\partial z}\right| \leqslant \frac{z}{2\pi}\int_{-\pi}^{\pi}\frac{d\varphi}{(z^2+\rho^2-2\rho\rho_0\cos\varphi+\rho_0{}^2)^{\frac{1}{2}}} \leqslant \frac{z}{[z^2+(\rho-\rho_0)^2]^{\frac{1}{2}}}.$$

Therefore,

$$\left|\frac{\partial G_m}{\partial z}\right| \leqslant \frac{z}{(z^2+\epsilon^2)^{\frac{1}{2}}} \quad \text{if} \quad |\rho-\rho_0|\geqslant\epsilon.$$

Consequently

$$\left|\int_0^{\rho_0-\epsilon}\rho f(\rho)\frac{\partial G_m}{\partial z}d\rho\right| \leqslant \frac{Mz}{(z^2+\epsilon^2)^{\frac{1}{2}}}\int_0^{\rho_0}\rho d\rho.$$

A similar bound is found for the contribution of the interval $(\rho_0+\epsilon, a)$. Upon combining them we obtain

$$\left|\int_0^{\rho_0-\epsilon}\rho f(\rho)\frac{\partial G_m}{\partial z}d\rho+\int_{\rho_0+\epsilon}^{a}\rho f(\rho)\frac{\partial G_m}{\partial z}d\rho\right|\leqslant\frac{Mza^2}{2(z^2+\epsilon^2)^{\frac{1}{2}}}.$$

Let now z tend to zero, ϵ being kept constant. Then (E) follows at once. (It should be noted that (E) holds for general functions $f(\rho)$, not necessarily vanishing at ρ_0.)

For the special function $f(\rho)$, with $f(\rho_0)=0$, the contribution of the remaining interval $\rho_0-\epsilon\leqslant\rho\leqslant\rho_0+\epsilon$ is very small, because $f(\rho)$ is very small there. Let us introduce the upper bound of $|f(\rho)|$ in this interval, thus

$$M(\epsilon)=\operatorname*{Max}_{|\rho-\rho_0|\leqslant\epsilon}|f(\rho)|,$$

then obviously $M(\epsilon)\to 0$ if $\epsilon\to 0$. Furthermore,

$$\left|\frac{\partial G_m}{\partial z}\right|\leqslant\frac{z}{2\pi}\int_{-\pi}^{+\pi}\frac{d\varphi}{(z^2+\rho^2-2\rho\rho_0\cos\varphi+\rho_0^2)^{\frac{1}{2}}}=-\frac{\partial G_0}{\partial z}.$$

Therefore,

$$\left|\int_{\rho_0-\epsilon}^{\rho_0+\epsilon}\rho f(\rho)\frac{\partial G_m}{\partial z}d\rho\right|\leqslant -M(\epsilon)\int_{\rho_0-\epsilon}^{\rho_0+\epsilon}\rho\frac{\partial G_0}{\partial z}d\rho$$

$$\leqslant -M(\epsilon)\int_0^a\rho\frac{\partial G_0}{\partial z}d\rho.$$

Let now z tend to zero; then the right-hand integral tends to -1, as follows from (D) when the latter formula is applied with $m=0$.

Thus we have

$$\left|\lim_{z\to 0+}\int_{\rho_0-\epsilon}^{\rho_0+\epsilon}\rho f(\rho)\frac{\partial G_m}{\partial z}d\rho\right|\leqslant M(\epsilon);$$

that means, on account of (E)

$$-M(\epsilon)\leqslant\lim_{z\to 0+}\int_0^a\rho f(\rho)\frac{\partial G_m}{\partial z}d\rho\leqslant M(\epsilon).$$

This is true for any $\epsilon>0$; as $M(\epsilon)\to 0$ for $\epsilon\to 0$, consequently

$$\lim_{z\to 0+}\int_0^a\rho f(\rho)\frac{\partial G_m}{\partial z}d\rho=0=-f(\rho_0)$$

and this is the required expression in case 2. So we have rigorously proved the validity of the symbolic formula (41). It may be noticed here that according to Watson[8]

[8] G. N. Watson, reference 7, page 389, Eq. (2).

we can deduce from (C) the following interesting formula

$$G_m=\frac{1}{\pi(\rho\rho_0)^{\frac{1}{2}}}Q_{m-\frac{1}{2}}\left(\frac{z^2+\rho^2+\rho_0^2}{2\rho\rho_0}\right),\qquad\text{(F)}$$

where Q denotes the Legendre function of the second kind. The Q-function has a singularity at the point where the argument is equal to 1; this corresponds with $z=0$, $\rho=\rho_0$.

Eindhoven, March, 1946.

The Elastic Constants of Materials Loaded with Non-Rigid Fillers

JANE M. DEWEY
General Laboratories, United States Rubber Company, Passaic, New Jersey
(Received November 14, 1946)

General expressions are given for the modulus of rigidity, $\bar{\lambda}_2$, and compressibility, $\bar{k}$, of a medium of Lame's constants, λ_1 and λ_2, loaded with a volume fraction, ϕ, of a filler of constants λ_1' and λ_2'. To terms in the first power of ϕ

$$\bar{\lambda}_2=\lambda_2\left(1+\frac{15(\lambda_2'-\lambda_2)(\lambda_1+2\lambda_2)}{2\lambda_2'(3\lambda_1+8\lambda_2)+\lambda_2(9\lambda_1+14\lambda_2)}\phi\right)$$

$$\bar{k}=k+\frac{3+4\lambda_2 k'}{3+4\lambda_2 k}(k'-k)\phi.$$

If the "filler" is a gas at a pressure, p, in a nearly incompressible medium, these give

Young's modulus	$\bar{E}=E\left(1-\frac{E}{9p+4E}\phi\right)$.
Modulus of rigidity	$\bar{\lambda}_2=\lambda_2(1-\frac{5}{3}\phi)$.
Compressibility	$\bar{k}=k+\frac{3}{3p+4\lambda_2}\phi$.
Poisson's ratio	$\bar{\sigma}=\sigma\left(1-\frac{3E}{9p+4E}\phi\right)$,

where ϕ is the volume loading, p is the pressure within the spherical cavities in the deformed state. Barred symbols refer to the properties of the loaded material; unbarred, to the medium alone. Expressions for the displacements and stresses within the medium and the particles, neglecting interactions between particles, are also given.

IN a letter to the Editor of this Journal,[1] the writer gave a solution of the linear equations describing small elastic deformations of a medium containing a single spherical inclusion of any elastic constants. This problem had previously been solved for simple tension by J. N. Goodier.[2] The solution can be extended to the determination of the elastic constants of a medium loaded with small spheres by the method applied by A. Einstein[3] to the calculation of the viscosity of a suspension and by H. M. Smallwood[4] to the problem of rigid fillers. This method gives the terms in the first power of the volume loading only, and is valid, with neglect of surface effects, for very dilute suspensions.*,[5]

Consider a single sphere of radius R at the origin of coordinates in an isotropic medium in which the displacement, $\mathbf{s}$, at a large distance from the sphere is given by

$$\mathbf{s}\underset{r\to\infty}{\longrightarrow}Axi+Byj+Czk. \tag{1}$$

Lame's constants of the sphere will be denoted by λ_1' and λ_2', of the medium by λ_1 and λ_2. λ_2 is the modulus of rigidity, λ_1 may be defined by $\lambda_1+\frac{2}{3}\lambda_2=k^{-1}$, where k is the compressibility.

The dilatation, strain, and radial components of the stress tensor, $\mathbf{T}$, in the medium are

$$\nabla\cdot\mathbf{s}=A+B+C-6\lambda_2(3\lambda_1+5\lambda_2)^{-1}c_{-2}r^{-3}M_1(\theta,\phi), \tag{2}$$

$$s_r=\tfrac{1}{3}(r+b_{-2}r^{-2})(A+B+C)+(r+c_{-2}r^{-2}+c_{-4}r^{-4})M_1(\theta,\phi), \tag{3}$$

$$s_\theta=[r+2\lambda_2(3\lambda_1+5\lambda_2)^{-1}c_{-2}r^{-2}-\tfrac{2}{3}c_{-4}r^{-4}]M_2(\theta,\phi), \tag{4}$$

$$s_\phi=s_\theta M_2^{-1}(\theta,\phi)M_3(\theta,\phi), \tag{5}$$

[1] Jane M. Dewey, J. App. Phys. **16**, 55 (1945); Erratum, **18**, 132 (1947).
[2] J. N. Goodier, J. App. Mech. **1**, 39 (1933).
[3] A. Einstein, Ann. d. Physik **19**, 289 (1906) and **34**, 591 (1911).
[4] H. M. Smallwood, J. App. Phys. **15**, 758 (1944).
* The numerical value of the coefficient of the terms in the second power of the volume loading is given by Guth and Gold (reference 5), but no details of their calculation are available.
[5] E. Guth and O. Gold, Phys. Rev. **53**, 322 (1938) (abstract). See also E. Guth, J. App. Phys. **16**, 20 (1945).

$$T_{rr}=(\lambda_1+\tfrac{2}{3}\lambda_2-\tfrac{4}{3}\lambda_2 b_{-2}r^{-3})(A+B+C)$$
$$+2\lambda_2[1-(9\lambda_1+10\lambda_2)(3\lambda_1+5\lambda_2)^{-1}$$
$$\times c_{-2}r^{-3}-4c_{-4}r^{-5}]M_1(\theta,\phi) \quad (6)$$

$$T_{r\theta}=2\lambda_2[1+(3\lambda_1+2\lambda_2)$$
$$\times(3\lambda_1+5\lambda_2)^{-1}c_{-2}r^{-3}$$
$$+\tfrac{8}{3}c_{-4}r^{-5}]M_2(\theta,\phi), \quad (7)$$

$$T_{r\phi}=T_{r\theta}M_2^{-1}(\theta,\phi)M_3(\theta,\phi), \quad (8)$$

$$M_1(\theta,\phi)=A\sin^2\theta\cos^2\phi+B\sin^2\theta\sin^2\phi$$
$$+C\cos^2\theta-\tfrac{1}{3}(A+B+C), \quad (9)$$

$$M_2(\theta,\phi)=\tfrac{1}{2}\frac{\partial M_1}{\partial\theta}=\sin\theta\cos\theta$$
$$\times(A\cos^2\phi+B\sin^2\phi-C), \quad (10)$$

$$M_3(\theta,\phi)=\frac{1}{2\sin\theta}\frac{\partial M_1}{\partial\phi}$$
$$=-(A-B)\sin\theta\sin\phi\cos\phi, \quad (11)$$

$$b_{-2}=(3\lambda_1+2\lambda_2-3\lambda_1'-2\lambda_2')$$
$$\times(4\lambda_2+3\lambda_1'+2\lambda_2')^{-1}R^3, \quad (12)$$

$$c_{-2}=-5(\lambda_2'-\lambda_2)(3\lambda_1+5\lambda_2)$$
$$\times[2\lambda_2'(3\lambda_1+8\lambda_2)$$
$$+\lambda_2(9\lambda_1+14\lambda_2)]^{-1}R^3, \quad (13)$$

$$c_{-4}=9(\lambda_2'-\lambda_2)(\lambda_1+\lambda_2)$$
$$\times[2\lambda_2'(3\lambda_1+8\lambda_2)$$
$$+\lambda_2(9\lambda_1+14\lambda_2)]^{-1}R^5. \quad (14)$$

The energy of deformation is given by

$$2W=\int_S \mathbf{T}_n\cdot\mathbf{s}\,da, \quad (15)$$

where $\mathbf{T}_n$ is the normal component of the stress tensor and the integration is over the outer surface of the medium. To calculate the energy of deformation of an infinite medium containing a single imbedded sphere, it is convenient to take a spherical surface with the particle at the center. Then,

$$W=\tfrac{1}{2}\int_S (T_{rr}s_r+T_{r\theta}s_\theta+T_{r\phi}s_\phi)da,$$
$$=\tfrac{1}{2}V[\lambda_1(A+B+C)^2$$
$$+2\lambda_2(A^2+B^2+C^2)]+\frac{2\pi}{3}(\lambda_1-\tfrac{2}{3}\lambda_2)$$
$$\times\{[b_{-2}-\tfrac{2}{5}\lambda_2(3\lambda_1+5\lambda_2)^{-1}c_{-2}]$$
$$\times(A+B+C)^2-2\lambda_2 c_{-2}(3\lambda_1+5\lambda_2)^{-1}$$
$$\times(A^2+B^2+C^2)\}, \quad (16)$$

for an infinite volume, where V is the total volume of the loaded medium.

Assuming that to the first power of the volume loading the added energy due to N spheres is N times the added energy due to a single sphere

$$W/V=\tfrac{1}{2}\{\lambda_1+(\lambda_1-\tfrac{2}{3}\lambda_2)$$
$$\times[b_{-2}-\tfrac{2}{5}\lambda_2(3\lambda_1+5\lambda_2)^{-1}c_{-2}]R^{-3}\phi\}$$
$$\times(A+B+C)^2+\lambda_2[1-(\lambda_1-\tfrac{2}{3}\lambda_2)$$
$$\times(3\lambda_1+5\lambda_2)^{-1}c_{-2}R^{-3}\phi]$$
$$\times(A^2+B^2+C^2), \quad (17)$$

where $\phi=\frac{4}{3}\pi NR^3/V$, the partial volume of the filler particles.

The strain constants, A, B, and C of this expression are those for the medium, as appears from the derivation. The observed mean strain constants, A_0, B_0, and C_0, can be calculated to the first approximation by the method outlined by Einstein. The displacement in the x direction can be written

$$s_x=Ax+\textstyle\sum_i \Delta s_{xi}=A_0x, \quad (18)$$

where Δs_{xi} is the added displacement due to the ith particle.

If X_i is the x coordinate of the center of the ith particle and x_i is the x coordinate measured from X_i

$$x=x_i+X_i. \quad (19)$$

Differentiating (18)

$$A_0=A+\frac{\partial}{\partial x}\textstyle\sum_i \Delta s_{xi}=A+\sum_i\dfrac{\partial}{\partial x_i}\Delta s_{xi}. \quad (20)$$

Assume that the added displacement is given by Eqs. (3) to (5) less the displacement in the

medium at a distance from a particle

$$\Delta s_{xi}=s_{xi}-Ax=s_{xi}-Ax_i-AX_i. \quad (21)$$

Two assumptions are made here: the first, that at any point the added displacement due to each particle is the same as if the other particles were not present, and second, that the displacement at a distance from a particle is described by the boundary condition of Eq. (1). The first assumption should be correct to the first approximation in the volume loading. The second is approximately correct if each particle is surrounded by a region free of particles of dimensions much greater than the particle radius. This is true of most of the particles if they are randomly distributed and the volume loading is much less than one.

For randomly distributed particles $\sum\Delta X_i=0$ and

$$\sum\Delta s_{xi}=\sum s_{xi}-Ax_i. \quad (22)$$

We replace the summation by N times the mean value of Δs_{xi}

$$\sum_i\frac{\partial}{\partial x_i}\Delta s_{xi}=N/V\int_V\frac{\partial\Delta s_{xi}}{\partial x_i}dV=N/V\int_S\Delta s_{xi}\frac{x_i}{r_i}da, \quad (23)$$

where the first integral is over the volume and the second over the surface. To terms in R^3r^{-2} the integral is independent of r_i and since the limits of angle are independent of i,

$$A_0=A+N/V\int_S\Delta s_x\sin\theta\cos\phi da, \quad (24)$$

where Δs_x may be taken for a particle at the origin. B_0 and C_0 are obtained by interchanging variables.

Carrying out the integration

$$A_0=(1+\tfrac{2}{5}(3\lambda_1+8\lambda_2)(3\lambda_1+5\lambda_2)^{-1}R^{-3}\phi)A+\tfrac{1}{3}[b_{-2}R^{-3}-\tfrac{2}{5}(3\lambda_1+8\lambda_2)\times(3\lambda_1+5\lambda_2)^{-1}c_{-2}R^{-3}](A+B+C)\phi, \quad (25)$$

whence, by combining with corresponding expressions for B_0 and C_0,

$$A_0+B_0+C_0=(1+b_{-2}\phi)(A+B+C), \quad (26)$$

$$A_0^2+B_0^2+C_0^2=[1+\tfrac{4}{5}(3\lambda_1+8\lambda_2)\times(3\lambda_1+5\lambda_2)^{-1}c_{-2}R^{-3}\phi]\times(A^2+B^2+C^2)+\tfrac{2}{3}(b_{-2}-\tfrac{2}{5}c_{-2})R^{-3}\times(A+B+C)^2\phi. \quad (27)$$

The constants $\bar{\lambda}_1$ and $\bar{\lambda}_2$ of the suspension are obtained by equating the expression for the work per unit volume

$$W/V=\tfrac{1}{2}\bar{\lambda}_1(A_0+B_0+C_0)^2+\bar{\lambda}_2(A_0^2+B_0^2+C_0^2) \quad (28)$$

to the expression (17).

Substituting (26) and (27) in (17) and equating coefficients of $(A_0+B_0+C_0)^2$

$$\bar{\lambda}_1=\lambda_1-(\lambda_1+2\lambda_2)\times(b_{-2}-2\lambda_2(3\lambda_1+5\lambda_2)^{-1}c_{-2})R^{-3}\phi. \quad (29)$$

Equating coefficients of $(A_0^2+B_0^2+C_0^2)$,

$$\bar{\lambda}_2=\lambda_2[1-3(\lambda_1+2\lambda_2)(3\lambda_1+5\lambda_2)^{-1}c_{-2}R^{-3}\phi]$$
$$=\lambda_2\{1+15(\lambda_2'-\lambda_2)(\lambda_1+2\lambda_2)\times[2\lambda_2'(3\lambda_1+8\lambda_2)+\lambda_2(9\lambda_1+14\lambda_2)]^{-1}\phi\}. \quad (30)$$

Whence

$$\frac{1}{\bar{k}}=\bar{\lambda}_1+\tfrac{2}{3}\bar{\lambda}_2=\frac{1}{k}[1-(\lambda_1+2\lambda_2)b_{-2}R^{-3}\phi], \quad (31)$$

or

$$k=k+(3+4\lambda_2k)(3+4\lambda_2k')^{-1}(k'-k)\phi. \quad (32)$$

Two special cases are of importance:

(a) The case of a rigid filler,

$$\lambda_2'\gg\lambda_2, \quad \text{and} \quad k'\ll k.$$

Then,

$$k=k[1-(1+\tfrac{4}{3}\lambda_2k)\phi]. \quad (32a)$$

$$\bar{\lambda}_2=\lambda_2[1+\tfrac{5}{2}(\lambda_1+2\lambda_2)(\lambda_1+\tfrac{8}{3}\lambda_2)^{-1}\phi]. \quad (30a)$$

(b) The case of included air or other gas

$$\lambda_2'=0, \quad \lambda_1'\simeq p,$$

where p is the pressure of the included gas

(after the deformation)*

$$k=k+(3+4\lambda_2 k)(3p+4\lambda_2)^{-1}(1-kp)\phi. \quad (32b)$$

The application of this formula to data on elastomers containing small amounts of gas is difficult as p is not known and λ_2 and p are of the same order of magnitude. If aged samples of reasonably permeable elastomers are studied, p can probably be taken as 1 atmosphere. In GR-I or other nearly impermeable materials, p, for very long times after molding, is probably approximately equal to the gas pressure at the time of molding. It may, therefore, differ considerably from 1 atmosphere. For any reasonably low gas pressure $kp \ll 1$ and

$$\bar{k}\simeq k+(3+4\lambda_2 k)(3p+4\lambda_2)^{-1}\phi, \quad (32b')$$

$$\bar{\lambda}_2\simeq\lambda_2[1-\tfrac{5}{3}(\lambda_1+2\lambda_2)(\lambda_1+\tfrac{14}{9}\lambda_2)^{-1}\phi]. \quad (30b)$$

The approximate formulae for Young's modulus, E, and Poisson's ratio, σ, valid for a medium of $\lambda_1 \gg \lambda_2$, containing gas at a low pressure are

$$\bar{E}\simeq E[1-E(9p+4E)^{-1}\phi], \quad (33)$$

$$\bar{\sigma}\simeq\sigma[1-3E(9p+4E)^{-1}\phi]. \quad (34)$$

The percentage changes in the modulus of rigidity and Young's modulus are of the same order of magnitude as the volume percent of gas in the material. The change in compressibility of a gum rubber stock caused by 0.01 percent of gas at atmospheric pressure is of the order of the compressibility, however. At pressures above an atmosphere, the compressibility varies rapidly with the pressure of the included gas.

Within an embedded sphere and at its surface,

$$\nabla\cdot\mathbf{s}=3a_1, \quad (35)$$

$$s_r=(c_1M_1(\theta,\phi)+a_1)r, \quad (36)$$

$$s_\theta=c_1rM_2(\theta,\phi), \quad (37)$$

$$s_\phi=c_1rM_3(\theta,\phi), \quad (38)$$

$$T_{rr}=2\lambda_2'c_1M_1(\theta,\phi)+(3\lambda_1'+2\lambda_2')a_1, \quad (39)$$

$$T_{r\theta}=2\lambda_2'c_1M_2(\theta,\phi), \quad (40)$$

$$T_{r\phi}=2\lambda_2'c_1M_3(\theta,\phi), \quad (41)$$

$$a_1=(\lambda_1+2\lambda_2)(4\lambda_2+3\lambda_1'+2\lambda_2')^{-1}\times(A+B+C), \quad (42)$$

$$c_1=15\lambda_2(\lambda_1+2\lambda_2)[2\lambda_2'(3\lambda_1+8\lambda_2)+\lambda_2(9\lambda_1+14\lambda_2)]^{-1}. \quad (43)$$

As would be expected, the radial components of stress on the surface of a particle have their maximum value when the filler is rigid, the case treated by Smallwood.[4]

Comparison of Eq. (30) for the modulus of rigidity with the calculation made by Taylor[6] of the viscosity of a suspension of fluid spheres of viscosity in a fluid of viscosity

$$\bar{\mu}=\mu\left[1+\frac{5\mu'+2\mu}{2(\mu'+\mu)}\phi\right],$$

shows that the two relations are of the same form only for λ_1, λ_1', μ', and λ_2' infinite. The difference between the two cases lies in the importance of surface tension in the suspension of fluid droplets. Suspension of droplets of any fluid in another increases the viscosity, while blowing, for instance, reduces the rigidity of a solid. Added work on the fluid suspension is done against surface tension, deforming the droplets. Mathematically, the difference appears in the omission of the condition that the normal component of stress on the droplet be single valued. This difference in stress on the two sides of the surface is balanced by surface tension.

* The equations and boundary conditions used in determining the displacements and stresses of Eqs. (2)–(8) are the conditions of equilibrium for a media obeying Hooke's law and a linear relation between volume and pressure. When differential values of the constants are used, these conditions are valid for media of any type, since a linear relation may always be assumed for an infinitesimal deformation. For an ideal fluid $\lambda_2=0$ and $dp=-\lambda_1(dV/V)$, which reduces approximately to $\lambda_1=p$ for a gas.

[6] G. I. Taylor, Proc. Roy. Soc. **A138**, 41 (1932).

Heat Transfer between a Fluid and a Porous Solid Generating Heat[1]

STUART R. BRINKLEY, JR.[2]
Central Experiment Station, U. S. Bureau of Mines, Pittsburgh, Pennsylvania
(Received September 16, 1946)

The theory, due to Anzelius, of the transfer of heat between a fluid flowing with constant velocity through a porous solid is extended to include the case where the solid generates heat. Expressions are obtained for the temperatures of solid and fluid as functions of position and time, it being assumed that the heat source function is a linear function of the temperature of the solid with coefficients independent of position and time. The application of the theory to a description of the temperature in catalytic reactions is indicated.

INTRODUCTION

A THEORY of the transfer of heat between a porous body and a warm fluid has been developed by Anzelius[3] and Schumann.[4] A fluid carrying heat is supposed to flow with constant velocity through a porous substance such as a solid body in a finely divided state which is initially at a different temperature than that of the fluid. The temperatures of solid and fluid are determined for different positions at later times, it being assumed that the volume specific heats of solid and fluid are constant, and that there is no conduction of heat in either the solid or the fluid. The problem is, of course, idealized by these simplifying assumptions. However, in his extensive series of measurements of heat transfer from a gas stream to a bed of broken solids, Furnas[5] obtained excellent experimental confirmation of the simple theory.

In the present communication, this theory is extended to the case where the solid is generating heat. In addition to the assumptions above, it is further assumed that the heat source function is a linear function of the temperature of the porous solid, the parameters of the linear function being independent of position or time.

The theory should be applicable to a calculation of solid and gas temperatures in catalytic reactions if the reaction vessel is so designed that all but a negligible amount of the heat of reaction is transported by the sensible heat of the gas and if either (a) the reaction is of the zeroth other without volume change, or (b) the flux of the gas through the reaction vessel is so large that reaction is limited to a few percent.

THE BASIC EQUATIONS

Consider a semi-infinite ($x \geqslant 0$) porous solid through which a fluid is flowing in the positive x-direction with volume current g. Let the temperatures of solid and fluid at a distance x from the origin and at time t be $U(x, t)$ and $V(x, t)$, respectively. It is assumed that the solid in a particular element of volume loses heat by transfer to the fluid and gains heat by generation at a rate F per unit volume of porous solid, where in general,

$$F = F(x, t; U), \tag{1}$$

and that the fluid in the element of volume gains heat by transfer from the solid and by the flux of heat into the volume which accompanies the flow of the fluid. By considering the rate of increase of heat in the solid and fluid contained between the transverse planes x and $x+dx$, and assuming that the rate of heat transfer is governed by Newton's law of cooling, it is easy to show that the transfer of heat from solid to fluid is governed by the relations,

$$\begin{aligned} c_s\rho_s\frac{\partial U}{\partial t} + h(U-V) - F(x, t; U) &= 0, \\ c_f\rho_f\frac{\partial V}{\partial t} + h(V-U) + c_f\rho_f g\frac{\partial V}{\partial x} &= 0, \end{aligned} \tag{2}$$

where c_s and c_f are the heat capacities per unit

[1] Published by permission of the Director, Bureau of Mines, U. S. Department of the Interior.
[2] Physical chemist, Research and Development Division, Bureau of Mines, Pittsburgh, Pennsylvania.
[3] A. Anzelius, Zeits. f. ang. Math. u. Mech. **6**, 291 (1926).
[4] T. E. W. Schumann, J. Frank. Inst. **208**, 405 (1929).
[5] C. C. Furnas, U. S. Bureau of Mines Bulletin 361 (1932).

mass of solid and fluid, respectively, ρ_s and ρ_f are masses of solid and gas contained in unit volume of porous solid, respectively, h is the coefficient of heat transfer between solid and gas per unit volume of porous solid, and where it has been assumed that the quantities $c_s\rho_s$, $c_f\rho_f$, and g are constants.

In the present communication, the solution of Eqs. (2) is obtained for the case where the heat source function is a linear function of the temperature of the solid,

$$F(x, t; U) = h(\alpha + \beta U), \tag{3}$$

with α and β constant. If the heat is generated by chemical reaction, one will usually have

$$F \sim e^{-\epsilon/RT} = e^{-\epsilon/RT_0}\left[1 + \frac{\epsilon}{RT_0^2}(T - T_0) + \cdots\right],$$

from which the accuracy of the linear approximation, Eq. (3), may be estimated. Here, ϵ is the activation energy of the reaction, R is the gas constant, and T is the absolute temperature.

For convenience, the temperature of the inlet fluid is taken to be zero, and the temperature of the porous solid at the initial instant of time on the same temperature scale is denoted by U_0. The boundary conditions for Eqs. (2) are therefore

$$\begin{aligned} U &= U_0, \quad x \geqslant gt, \\ V &= 0, \quad x = 0. \end{aligned} \tag{4}$$

The first condition is a statement of the fact that the porous solid is at its initial temperature at points which have not yet been reached by the fluid.

With the notation $a = h/c_f\rho_f g$, $b = h/c_s\rho_s g$, and the change of independent variable

$$\xi = ax, \quad \tau = b(gt - x), \tag{5}$$

Eqs. (2) and (3) become

$$\begin{aligned} \partial U/\partial\tau &= V + (\beta - 1)U + \alpha, \\ \partial V/\partial\xi &= U - V, \end{aligned} \tag{6}$$

with the boundary conditions, $U = U(\xi, \tau)$, $V = V(\xi, \tau)$,

$$U(\xi, 0) = U_0, \quad V(0, \tau) = 0. \tag{7}$$

Equations (6) and (7) lead immediately to a pair of ordinary differential equations for $U(0, \tau)$ and $V(\xi, 0)$.

$$\begin{aligned} &\frac{d}{d\tau}U(0, \tau) + (1 - \beta)U(0, \tau) = \alpha, \quad U(0, 0) = U_0, \\ &\frac{d}{d\xi}V(\xi, 0) + V(\xi, 0) = U_0, \quad V(0, 0) = 0. \end{aligned} \tag{8}$$

The subsidiary boundary conditions are obtained by solution of Eq. (8).

$$\begin{aligned} U(0, \tau) &= U_0 e^{(\beta-1)\tau} - \frac{\alpha}{1 - \beta}\left[e^{(\beta-1)\tau} - 1\right], \\ V(\xi, 0) &= U_0(1 - e^{-\xi}). \end{aligned} \tag{9}$$

Equation (6) may be simplified in a manner analogous to that employed by Schumann[4] by introducing new independent variables, Γ and Δ, where

$$\begin{aligned} \Gamma &= (U + V)e^{\xi + (1-\beta)\tau}, \\ \Delta &= (U - V)e^{\xi + (1-\beta)\tau}. \end{aligned} \tag{10}$$

One obtains

$$\begin{aligned} \partial\Gamma/\partial\tau + \partial\Delta/\partial\tau &= \Gamma - \Delta + 2\alpha e^{\xi + (1-\beta)\tau}, \\ \partial\Gamma/\partial\xi - \partial\Delta/\partial\xi &= \Gamma + \Delta, \end{aligned} \tag{11}$$

and by further differentiation

$$\partial^2\Delta/\partial\xi\partial\tau = \Delta. \tag{12}$$

The boundary conditions for Γ and Δ are evidently

$$\begin{aligned} &\Gamma(\xi, 0) = U_0(2e^{\xi} - 1), \quad \Delta(\xi, 0) = U_0, \\ &\Gamma(0, \tau) = \Delta(\xi, 0) = U_0 + \frac{\alpha}{1 - \beta}\left[e^{(1-\beta)\tau} - 1\right]. \end{aligned} \tag{13}$$

The characteristics of Eq. (12) are the straight lines parallel to the axes through the point of interest (ξ, τ), and the boundary values of Δ are specified along a pair of characteristics (the axes). The solution of Eqs. (12) and (13) is thus a characteristic initial value problem and is straightforward by the method of Riemann.[6] The Reimann function is $I_0[2((\xi - \xi')(\tau - \tau'))^{\frac{1}{2}}]$, in which ξ' and τ' are the variables of integration around the boundary of the region determined by the characteristics and the axes, and I_0 is the zeroth-order Bessel function of the first kind for

[6] R. Courant and D. Hilbert, *Methoden der Mathematischen Physik* (Julius Springer, Berlin 1924), Vol. II, pp. 311–317.

imaginary argument. The solution for Δ is

$$\Delta = U_0 I_0[2(\xi\tau)^{\frac{1}{2}}] + \alpha \int_0^\tau e^{(1-\beta)\tau'} I_0[2(\xi(\tau-\tau'))^{\frac{1}{2}}]d\tau'. \quad (14)$$

This result may be rewritten in the convenient form,

$$\Delta = U_0 I_0[2(\xi\tau)^{\frac{1}{2}}] + \frac{\alpha}{1-\beta}\varphi[\tau(1-\beta), \xi/(1-\beta)], \quad (15)$$

in which the function $\varphi(x, y)$, defined by

$$\varphi(x, y) = e^x \int_0^x e^{-x'} I_0[2(x'y)^{\frac{1}{2}}]dx', \quad (16)$$

has been introduced. This function, originated by Laplace,[7] has been discussed by Thomas,[8] who has obtained the following useful properties:

$$\begin{aligned} &\varphi(x, y) + \varphi(y, x) = e^{x+y} - I_0[2(xy)^{\frac{1}{2}}], \\ &(\partial/\partial x)\varphi(x, y) = \varphi(x, y) + I_0[2(xy)^{\frac{1}{2}}], \\ &(\partial/\partial y)\varphi(x, y) = \varphi(x, y) - (\partial/\partial y) I_0[2(xy)^{\frac{1}{2}}], \\ &\varphi(0, y) = 0, \quad \varphi(x, 0) = e^x - 1. \end{aligned} \quad (17)$$

Tables of a related function,

$$g(x, y) = e^{-x^2-y^2}\varphi(x^2, y^2), \quad (18)$$

have been constructed[9] and are to be published. By means of Eqs. (17), Eq. (15) is readily shown to satisfy Eqs. (12) and (13), and this solution is unique.[6]

An expression for the quantity Γ can be obtained by the integration of either of Eqs. (11), employing Eqs. (15) and (17). Expressions for the temperatures of solid and fluid can then be obtained by the combination of this result with the solution for the variable Δ, Eq. (15). However, the temperature of the fluid is obtained more directly from the relation,

$$\partial V/\partial\xi = \Delta e^{-\xi-(1-\beta)\tau}, \quad (19)$$

which results from the substitution of the definition of Δ in the second of Eqs. (6). The temperature of the solid is then obtained at once by the combination of this result with the expression for Δ.

THE TEMPERATURES OF SOLID AND FLUID

If the solution for Δ be combined with Eq. (19), there is obtained

$$\frac{\partial V}{\partial\xi} = \left\{ U_0 I_0[2(\xi\tau)^{\frac{1}{2}}] + \frac{\alpha}{1-\beta}\varphi[\tau(1-\beta), \xi/(1-\beta)] \right\} e^{-\xi-(1-\beta)\tau}. \quad (20)$$

Integrating this expression between limits as an ordinary differential equation, and recalling that $V(0, \tau) = 0$, one obtains

$$V = U_0\varphi(\xi, \tau)e^{-\xi-(1-\beta)\tau} + \frac{\alpha}{1-\beta}e^{(\beta-1)\tau}\int_0^\xi e^{\xi'}\varphi[\tau(1-\beta), \xi'/(1-\beta)]d\xi'. \quad (21)$$

The integral of Eq. (21) can be evaluated by the method of integration by parts, employing the properties of $\varphi(x, y)$ which are summarized by Eqs. (17). The result of this process is

$$\int_0^\xi e^{-\xi'}\varphi[\tau(1-\beta), \xi'/(1-\beta)]d\xi' = \frac{1-\beta}{\beta}\{\varphi(\xi, \tau) - \varphi[\xi/(1-\beta), \tau(1-\beta)] + [e^{\xi/(1-\beta)} - e^\xi]e^{\tau(1-\beta)}\}e^{-\xi}, \quad (22)$$

if $\beta \neq 0$, and

$$\int_0^\xi e^{-\xi'}\varphi[\tau(1-\beta), \xi'/(1-\beta)]d\xi' = \{\xi\varphi(\tau, \xi) + \tau\varphi(\xi, \tau) - (\xi\tau)^{\frac{1}{2}}I_1[2(\xi\tau)^{\frac{1}{2}}]\}e^{-\xi}, \quad (23)$$

[7] H. Bateman, *Partial Differential Equations of Mathematical Physics* (The Cambridge University Press, New York 1932), p. 128.
[8] H. C. Thomas, J. Am. Chem. Soc. 66, 1664 (1944).
[9] S. R. Brinkley, Jr. and R. F. Brinkley, unpublished tables.

if $\beta=0$. I_1 is the first-order Bessel function of the first kind for purely imaginary argument. Therefore, the temperature of the fluid is given by

$$V(\xi,\tau)=\left(U_0+\frac{\alpha}{\beta}\right)\varphi(\xi,\tau)e^{-\xi-(1-\beta)\tau}+\frac{\alpha}{\beta}\{e^{\beta\xi/(1-\beta)}-\varphi[\xi/(1-\beta),\tau(1-\beta)]e^{-\xi-(1-\beta)\tau}-1\},\quad(24)$$

if $\beta\neq0$, and by

$$V(\xi,\tau)=\{(U_0+\alpha\tau)\varphi(\xi,\tau)+\alpha\xi\varphi(\tau,\xi)-\alpha(\xi\tau)^{\frac{1}{2}}I_1[2(\xi\tau)^{\frac{1}{2}}]\}e^{-\xi-\tau},\quad(25)$$

if $\beta=0$. The temperature of the solid is immediately obtained by combination of these results with the expression for Δ. Then,

$$U(\xi,\tau)=\left(U_0+\frac{\alpha}{\beta}\right)\{e^{\beta\tau}-\varphi(\tau,\xi)e^{-\xi-(1-\beta)\tau}\}-\frac{\alpha}{\beta}\left\{\frac{1}{1-\beta}\varphi[\tau(1-\beta),\xi/(1-\beta)]e^{-\xi-(1-\beta)\tau}+1\right\},\quad(26)$$

if $\beta\neq0$, and

$$U(\xi,\tau)-U_0=\{[\alpha(\xi+1)-U_0]\varphi(\tau,\xi)+2\tau\varphi(\xi,\tau)-\alpha(\xi\tau)^{\frac{1}{2}}I_1[2(\xi\tau)^{\frac{1}{2}}]\}e^{-\xi-\tau},\quad(27)$$

if $\beta=0$. The rate of heat transfer from solid to fluid per unit volume of porous solid is equal to $h\Delta(\xi,\tau)c^{-\xi-(1-\beta)\tau}$.

The application of these results to particular systems will be the subject of subsequent reports from this laboratory.

THE STEADY STATE

The steady state values of the temperatures of fluid and solid are obtained from Eqs. (24) to (27) by proceeding to the limit of infinite τ. The function $\varphi(\xi,\infty)$ is finite for finite ξ, and the function $\varphi(\tau,\xi)$ tends to $e^{\xi+\tau}$ as τ tends to infinity. Then, one obtains

$$V(\xi,\infty)=(\alpha/\beta)\{e^{\beta\xi/(1-\beta)}-1\},\quad U(\xi,\infty)=\frac{\alpha}{\beta}\left\{\frac{1}{1-\beta}e^{\beta\xi/(1-\beta)}-1\right\},\quad(28)$$

if $\beta\neq0$, and

$$V(\xi,\infty)=\alpha\xi,\quad U(\xi,\infty)=\alpha(\xi+1),\quad(29)$$

if $\beta=0$. These steady state solutions have been previously obtained and employed for the calculation of catalyst and gas temperatures in a typical operation of the Michael process for the synthesis of hydrocarbons from carbon monoxide and hydrogen.[10]

[10] S. R. Brinkley, Jr., 110th Meeting, American Chemical Society, Chicago, Illinois, Sept. 1946.

Letters to the Editor

Concerning Estimates of the Minimum Sparking Potential Based upon the Cathode Work Function

DONALD H. HALE AND W. S. HUXFORD
Department of Physics, Northwestern University, Evanston, Illinois
April 4, 1947

JACOBS and LaRocque[1] have recently suggested a method for estimating the minimum sparking potential for cold cathode tubes. They measured the minimum sparking potentials for several cathodes in argon and calculated the corresponding value for γ_m. These values for γ_m were then plotted against the corresponding values of the work functions and the minimum sparking potentials. By use of these two curves an attempt is made to estimate γ_m and the minimum sparking potential in argon for any cathode, provided only the work function for the cathode material is known. Applying this method the authors obtain an approximate and reasonable value for the minimum sparking potential of a sodium cathode in argon.

This method of determining γ_m from sparking data is not reliable. It has been pointed out that this procedure cannot be expected to yield good values for γ in all cases.[2] This is shown by the results obtained by these authors since their values of γ vary widely from those found by other workers. Schöfer[3] and Engstrom[4] found that the values of γ for a barium cathode in argon increased with increasing values of E/p starting with an E/p of about 40. The authors found just the opposite. Their values of γ decrease with increasing values of E/p. Further, their value of γ at an E/p of about 40 is three times greater than that measured by Schöfer. Since they worked at higher gas pressures than did earlier workers it may be that in their work the mechanism of electron emission by photons at the cathode was enhanced. However it is difficult to see how this could account entirely for their high values of γ.

The agreement between the calculated and experimental values of the minimum sparking potential for a sodium cathode in argon may be fortuitous. Bowls[5] measured γ for a sodium cathode in nitrogen and Ehrenkrantz[6] measured the sparking potentials. Bowls found that the sodium cathode gave distinctly lower values of γ, for a wide range of values of E/p, than did a platinum cathode. Yet, Ehrenkrantz found that the sodium cathode showed a lower minimum sparking potential than did the platinum. Hale[7] and Ehrenkrantz found a similar situation with regard to sodium cathodes in hydrogen. The authors explain the lower γ for sodium on the grounds that hydrogen or nitrogen combines with sodium to give a surface of high work function. Such an assumption would explain the low values for γ but it cannot explain, on the basis of the author's argument, the observed low value of the minimum sparking potential. Actually it has been pointed out that sodium surfaces in hydrogen or nitrogen show low photoelectric thresholds.[8] Here then is a case of a cathode material which has a low work function, which shows low values of γ, in at least two gases, and yet has a low minimum sparking potential.

There are other interesting examples. The work functions for nickel and platinum are 5.01 and 6.30 volts, respectively.[9] Yet the minimum sparking potential for argon with cathodes of these materials is 195 volts in each case.[10] The work function for iron is 4.72 volts.[9] However, the minimum sparking potential for argon with an iron cathode is 265 volts. This is distinctly higher than the minimum sparking potential for platinum in argon. Yet platinum has the higher work function.

It is probably correct to say that, in a very general way, materials with low work functions will show high values of γ. However, exceptions are known and any prediction of the minimum sparking potential which is based upon the work function of the cathode may be badly in error. Much work remains to be done before this point is clear.

We wish to call attention to what appears to be a misstatement. The authors state that Bowls found a lower γ for platinum in a large region of E/p than he did for sodium. It appears that they intended to refer to a lower γ for sodium which was what Bowls observed.

[1] H. Jacobs and A. P. LaRocque, J. App. Phys. **18**, 199 (1947).
[2] L. B. Loeb, *Fundamental Processes of Electrical Discharge in Gases*, pp. 348 and 416.
[3] R. Schöfer, Zeits. f. Physik **110**, 21 (1938).
[4] R. W. Engstrom, Phys. Rev. **55**, 239 (1939).
[5] W. E. Bowls, Phys. Rev. **55**, 293 (1938).
[6] F. Ehrenkrantz, Phys. Rev. **55**, 219 (1939).
[7] D. H. Hale, Phys. Rev. **55**, 815 (1939).
[8] L. B. Loeb, reference 2, p. 395.
[9] A. L. Hughes and L. A. DuBridge, *Photoelectric Phenomena*, p. 75.
[10] M. J. Druvesteyn and F. M. Penning, Rev. Mod. Phys. **12**, 114 (1940).

Measurement of the Dynamic Stretch-Modulus and Hysteresis of Tire Cords

W. JAMES LYONS AND IRVEN B. PRETTYMAN
The Firestone Tire and Rubber Company, Akron 17, Ohio
April 17, 1947

THE modulus of elasticity (Young's) of synthetic filaments and films has been measured by Meyer and Lotmar[1] and Ballou and Silverman,[2] who employed sound-velocity methods which gave the dynamic value of the modulus at acoustical frequencies. These methods, however, are not applicable to the measurement of concomitant hysteretic losses. Wakeham and Honold[3] studied the elastic modulus and hysteresis effects in cotton, rayon, and Nylon tire cords under dynamic conditions, but at a relatively low frequency: 1 cycle/sec.

The exploratory studies reported herein were undertaken to develop a method for measuring not only the dynamic

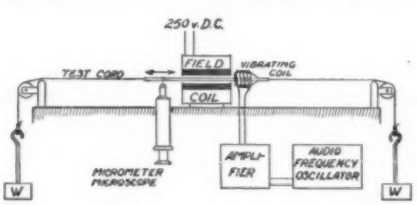

FIG. 1. Schematic diagram of cord stretch-vibrometer.

TABLE I. Representative measurements of dynamic properties of conventional tire cords, obtained on cord vibrometer at constant impressed force-amplitude.

Cord sample		Static properties (conditioned at 65% R.H., 70°F)			Dynamic properties (at approximately 14% R.H., 78°F)		
Fiber	Construction	Breaking load (Kg)	Ultimate elongation (Percent)	Resonant frequency, f_0 (cycles/sec.)	Dynamic modulus, E (10^{10} dynes/cm^2)	Internal friction, η (10^6 poises)	Hysteresis index, $2\pi f\eta$ (10^{10} dynes/cm^2)
Cotton	11/4/2	8.5	14.3	169	7.7	4.0	0.42
Viscose rayon	1100/2	6.8	15.9	148	11.2	5.3	0.49
Nylon	210/3/3	14.6	19.5	116	6.1	2.4	0.17

modulus of filaments, yarns, and cords in the sonic or near-sonic range, but also their internal frictional (hysteretic) properties. Measurements of the modulus and friction have been successfully made on cotton, rayon, and Nylon cords forcibly vibrated longitudinally at frequencies above 100 cycles/sec., by electromagnetic means.

The apparatus is shown schematically in Fig. 1. A small light-weight coil is placed coaxial with the core of a strong electromagnetic field coil, so that the former is in a powerful magnetic field when a direct current passes through the field coil. The small coil is rigidly mounted on a plastic rod which passes through a hole at the axis of the core. The rod is supported by pieces of the test cord attached coaxially at each end. Static loads at the outer ends of the two pieces of cord balance each other and allow the cords to be placed under tension without displacing the rod and small coil. When an oscillating current is sent through this coil, the rod vibrates longitudinally, causing small periodic extensions and contractions in the pieces of test cord. In the initial trials, a small mirror was rotatably connected to the rod at the end opposite the vibrating coil, so that by means of an optical-lever system, amplitude of vibration could be detected and measured on a ground-glass scale. It was subsequently found that a micrometer microscope could be advantageously substituted for the optical-lever system, with improved accuracy; and this method was used to obtain the results reported herein. In the present experiments the vibrating coil was energized by a 50-watt power amplifier which was controlled by a regular commerical calibrated audiofrequency oscillator unit.

The principle underlying the present method is expressed by the equation of motion of the vibrating element under impressed force:

$$m(d^2s/dt^2)+(\eta/q)(ds/dt)+(E/q)s=F\cos\omega t, \qquad (1)$$

where m = vibrating mass, s = displacement from the equilibrium position; η = coefficient of internal friction (hysteresis); E = dynamic stretch modulus; q = shape factor of cord; and F = amplitude of applied force having frequency $\omega/2\pi$. Equation (1) has been applied to forced compressive vibrations in flat cylinders of rubber by Gehman, Woodford, and Stambaugh,[4] and to shear vibrations in similar specimens by Dillon, Prettyman, and Hall.[5] The design of the driving mechanisms used by these groups provided the prototype for the corresponding elements of the present equipment.

It can be shown readily that at resonance, to good approximation:

$$E=mq\omega_0^2=m(L/2A)(2\pi f_0)^2, \qquad (2)$$

where A = cross-sectional area of cord or yarn (exclusive of interstices between fibers); L = free length of each matched piece of cord, and f_0 = resonant frequency.

Equation (2) has been applied to observations of resonant frequencies made with the cord stretch-vibrometer on three kinds of tire cord, with the results summarized in Table I. To identify the cords the conventional static properties have been included in the table. All cord samples were vibrated under a tensional load of 1.2 kg, with L = 25.4 cm (10 in.). The effective mass of the vibrating system, m, was found to be 17.0 g. The cross-sectional area of each sample was determined from the weight of a 200-cm specimen of the cord and the bulk density of the component fiber.

Internal friction, η, may be readily derived from observations on the stretch-vibrometer by means of the equation:

$$\eta=Fq/s_m\omega_0, \qquad (3)$$

s_m being the maximum (resonance) strain-amplitude. Values of this quantity, as well as of an index of hysteresis losses $2\pi f\eta$, are entered in Table I. The latter quantity has been shown, in the case of rubber,[5] to be substantially independent of frequency.

[1] K. H. Meyer and W. Lotmar, Helv. Chim. Acta **19**, 68 (1936).
[2] J. W. Ballou and S. Silverman, Textile Research **14**, 282 (1944), J. Acoust. Soc. Am. **16**, 113 (1944).
[3] H. Wakeham and E. Honold, J. App. Phys. **17**, 698 (1946).
[4] S. D. Gehman, D. E. Woodford, and R. B. Stambaugh, Ind. Eng. Chem. **33**, 1032 (1941).
[5] J. H. Dillon, I. B. Prettyman, and G. L. Hall, J. App. Phys. **15**, 309 (1944).

On the Analysis of Internal Flow Machinery

SABINUS H. CHRISTENSEN
Carrier Corporation, Syracuse, New York
April 11, 1947

THIS is a brief report of a new method of applied research which has opened an area of analysis hitherto inaccessible to internal flow machinery having moving passages (centrifugal and axial-flow compressors, and turbines).

The new technique is based on the rejection of the idealization in the gas-dynamic analysis of internal flow machinery that the fluid may be considered to be a compressible ideal gas, i.e. frictionless. It has been found by exhaustive analytic study of test data that the use of the frictionless gas concept fails to explain performance within very wide limits.

It is well known that the inefficiency of internal flow machinery is caused by the dissipation of available energy

which is reflected in increase of entropy through the machine. The basic domain for research on internal flow machinery is then recognized to be that of making a detailed explanation of entropy increase caused by friction, separation, and turbulence. Taking the detailed change of entropy into full account now explains such hitherto inaccessible phenomena as quantitative values of shock loss at the entrance to rotating grids, and the theory of the maximum flow in a centrifugal compressor (as have been done by the writer in unpublished company reports).

The new method is directed towards the local evaluation of entropy in rapidly moving or rotating passages. The method utilizes the device of speeding up the moving passage (or the equally effective method of using a very heavy gas with slower passage speeds) until somewhere within the passage the relative velocity is locally sonic. The exact equations of state, energy, and continuity are then satisfied by a definite entropy value at the blocking point. If a study is made of the energy *vs.* area gradient along the passage it will be seen that the blocking point is fixed by the passage design, thus providing the fourth simultaneous equation which solves the problem of determining the exact thermodynamic state inside a rapidly moving passage. It is believed that this technique is far superior to the less reliable method of trying to measure the state of the fluid by instruments which are forced to transmit their data through commutator rings and packings.

Instead of working with entropy change, re-arrangement of the gas-dynamic equations shows that the isentropic relations apply if the passage area is modified by the factor $\exp(-J\Delta S/R)$, J being Joule's mechanical equivalent of heat, ΔS the increase in entropy, and R the gas constant.

Objective Aperture System for the Electron Microscope

CECIL E. HALL
Massachusetts Institute of Technology, Cambridge, Massachusetts
April 17, 1947

THE conventional objective aperture used in magnetic electron microscopes consists of a circular diaphragm about 25 microns in diameter, fixed with respect to the lens and coaxial with it. It prevents electrons scattered through angles larger than about 10^{-2} radian from reaching the image plane, thereby reducing background intensity and enhancing contrast in the image. An objective aperture is necessary for the examination of thick objects producing a high scattered intensity, such as replicas, sections, and the like, but it is of lesser value in the examination of specimens of suitable thinness and contrast. Electron microscopists are familiar with the many practical difficulties associated with the use of apertures. They are difficult to make, install, and align, and must be replaced frequently, because they accumulate films of non-conducting material which become charged and produce distortions in the image. It is therefore desirable to have an objective aperture system that can be installed quickly and renewed as occasion demands.

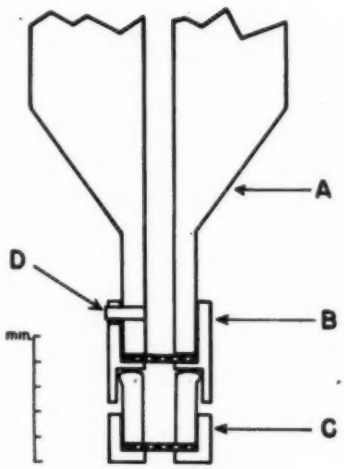

FIG. 1. Objective aperture system.

An objective aperture system having the advantage that it is attached to the specimen cartridge rather than to the lens, is shown in Fig. 1. It has been used successfully in this laboratory with an RCA type B electron microscope. The device consists essentially of a second screen mounted and aligned so that each opening of the specimen screen has below it a corresponding opening serving as an aperture stop. Aperture screens may be detached readily, if they are not required for the specimen under examination, and may be renewed frequently from standard material. A is the lower part of the specimen cartridge to which is fitted the cap, B, containing the specimen. The tip, C, containing the aperture screen is mounted in a friction cup so that it may be turned about the axis and rocked slightly to give small lateral displacements. Aperture screens, which must be non-magnetic since they are in the lens field, are punched from 200-per-inch copper Lektromesh.[1]

The procedure in using the device is as follows: Clip the cartridge to the stage of a 100-power optical microscope with cross-hairs in the eyepiece. Focus on the object screen and rotate the eyepiece until the cross-hairs are aligned with the screen wires. Focus on the aperture screen and rotate the tip C until the screen wires are square with the cross-hairs. Refocus on the object and center an open square on the cross-hairs with the mechanical stage. Focus on the aperture mesh and rock the tip, C, until an open square is centered on the cross-hair intersection. This procedure usually takes one or two minutes. Possibly a smaller object-to-aperture distance than the three milli-

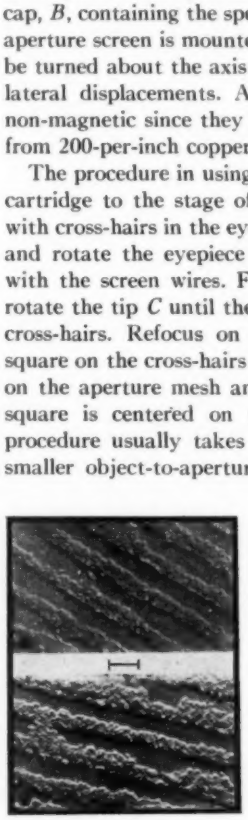

FIG. 2. Collodion-silicon replica of glass grating, shadowed with chromium; (a) without an aperture, (b) with mesh aperture. ×3600.

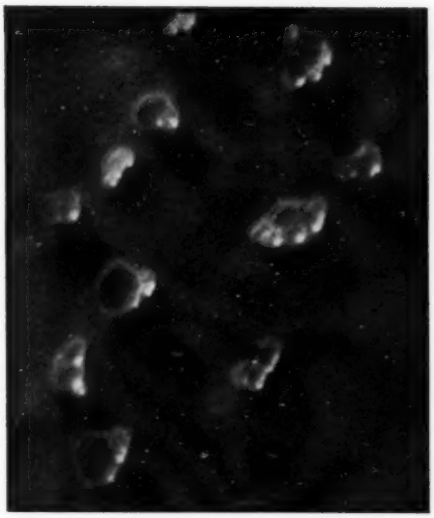

FIG. 3. Dark-field electron micrograph of carbon particles shadowed with uranium. ×11,666.

meters shown in the diagram would provide adequate contrast in the image and at the same time simplify the alignment of the two meshes.

Two micrographs of a collodion-silicon replica of a glass grating are shown in Fig. 2, to demonstrate the difference in contrast with and without the aperture screen; (a) was taken without an aperture, while (b) was taken with one. The replica was shadowed with chromium. Contacts were made from the original micrographs on the same Eastman Medium lantern slide plate and a contact print made from this on F-3 Kodabromide. Contrast, of course, depends on the photographic processing, but an effort was made to have the prints represent a reasonable comparison of the original plates. Although improved contrast in the image is most pronounced with thick specimens, improvement has also been noted in thin specimens containing small particles of low scattering power. Open areas in standard Lektromesh screens are square, but no distortions have been noted in the image which could be attributed to this unusual shape. Also, it is possible that electrons may be so widely scattered that they will reach the image plane through an opening other than the one directly below the point under observation. In the mesh normally employed the solid parts are three times as wide as the open squares, and since scattered intensity falls off rapidly with angle, the proportion of such widely scattered electrons appears to be inappreciable.

The multiple aperture was originally devised to enhance contrast in images of thick specimens, but it has proved to be very useful also for dark-field electron microscopy. If alignment of the two meshes is not perfect, and it very rarely is, a part of each object opening will be seen in dark field. An example of a dark-field micrograph made in this manner is reproduced in Fig. 3. The specimen consisted of carbon particles[2] on a collodion film, shadowed with uranium to a calculated thickness of about 13A. Shadow areas are dark because they contain no uranium, hence scatter least. The uranium film appears as a background of discrete spots ranging in diameter from 50 to 200A. The spots are quite well resolved for dark field, indicating that they are produced by electrons that have been scattered coherently and are therefore confined to a narrow angular aperture and velocity range. The dark-field micrograph thus reveals the presence of small ordered regions in the film that are not perceptible as such in bright field. Similar structure has also been observed with thin films of several other metals and compounds.

Images of the carbon particles shown in Fig. 3 are characterized by bright contours and dark centers, resulting from the fact that at small angles there is a relatively high intensity from electrons scattered close to the surface. Electrons scattered within the particles are spread over a much larger solid angle so that a smaller proportion enter the limiting aperture. An interesting feature, not visible in bright field, is the occurrence of numerous bright spots at the edges of the particles. This appearance is not associated with the uranium since the spots also appear in unshadowed specimens. In the micrograph shown, all such spots appear on edges *away* from the aperture, hence represent pencils that have been deflected *under* the particles. However, the occurrence on one edge only, is dependent on alignment of the electron microscope and on the objective current. They have been observed on edges toward or away from the aperture and on all sides simultaneously. The reason for enhanced scattered intensities is not evident at present. Possibly they are in the nature of crystalline reflections owing to regularities near the surface, although the images are considerably more diffuse than those produced by diffractions from common crystalline substances. Whether the enhanced scattering is to be accounted for on the basis of crystallinity or not, it must be noted that near the edges, electrons are incident and emergent at such small angles that refraction effects may be expected to be of significant magnitude. The observed deflection of electrons under the particles could be accounted for on the basis of refraction resulting from an inner potential of the order of 10 volts.

These observations demonstrate the utility of the multiple aperture which is, to be sure, a compromise for convenience rather than the equivalent of a clean, well-centered aperture of the conventional type. Probably a completely satisfactory solution of the aperture problem will require the redesign of present objectives to allow for insertion and alignment of apertures fixed to the lens, without the difficulties and hazards that presently attend this operation. As an alternative, the multiple aperture has some advantages, and furthermore, the ease with which it may be used for dark-field observations may stimulate this interesting and somewhat neglected aspect of electron microscopy.

[1] C. O. Jelliff Manufacturing Corporation, Southport, Connecticut.
[2] P33, Thermatomic Carbon Company, Inc.

New Books

A Shorter History of Science

By Sir William Cecil Dampier. The Macmillan Company, New York, 1944.

When Sir William Cecil Dampier's larger book, *A History of Science and Its Relations with Philosophy and Religion*, came from the press, we recognized that a great service had been rendered: science had been given its "setting in other modes of thought." Could Dampier streamline the larger book and produce *A Shorter History of Science* without devitalizing the story of the growth of science which made the larger book famous? In the condensation, the story has been more simply told, but even so its vitality has been preserved. The connections of science with other human activities have been reduced to the more direct impacts, but these fewer situations have been used expertly to show the relations of science to philosophy and religion. Undoubtedly the shorter history, like its monumental prototype, will become known, not simply for the facts and dates which it contains, but especially for the story it tells of the expanding mind and spirit of man.

"Science has two streams," we read in the first chapter, "corresponding to two sources, the first a gradual invention of tools and implements whereby men earn their living more safely and easily, and second the beliefs they form to explain the wonderful universe around them. The first may perhaps better be called technology, for its problems are too difficult for early theory, and only in later stages does it become applied science; the second, which in historic times grew into a pure search for knowledge, is the main subject of this book."

As one reads the book's eleven chapters—with titles such as: the origins, Greece and Rome, Galileo and Newton, the eighteenth century, recent biology, the new physics and chemistry, and the stellar universe—one turns back to the Preface for this summary: "The Greek Atomists, besides speculating on the structure of matter, developed therefrom a mechanical theory of life. Conversely, the philosophy of Plato, as modified by Aristotle, laid too much stress on innate ideas and logical deduction to make a favorable background for the beginnings of inductive experimental science. To Newton and his immediate followers the Heavens declared the Glory of God, but Newton's work produced a very different effect on the minds of Voltaire and other eighteenth-century sceptics. Darwin's revival of the old theory of evolution on the new basis of natural selection not only suggested an alternative origin for mankind, but spread evolutionary doctrine far beyond the limits of biology. The recent revolution in physics has shaken the evidence for philosophic determinism which the older synthesis seemed to require. Such broad effects must be noticed, but the more technical aspects of philosophy may be passed by."

Exponents of general education, who insist that all courses should be integrated into the whole life pattern of the learner, will like the spirit of *A Shorter History of Science*. Its author thinks that "early specialization is dangerous," and writes, "Those older schoolboys whose chief subjects are scientific should look at them also from a humanist standpoint, and realize their setting in other modes of thought, while those studying literature need some knowledge of science before they can be said to be well educated. For both groups, I believe that the history of science, the story of man's attempts to understand the mysterious world in which he finds himself, makes the best way of approach to common ground."

Carl F. Eyring
Brigham Young University, Provo, Utah

Applied Atomic Power

By E. Smith, A. Fox, R. Sawyer, and H. Austin. Pp. 227, 6¼×9¼ in. Prentice-Hall, New York, 1946. Price $4.00.

This book with a rather ambitious title is easy and interesting reading uncomplicated by mathematics. Undergraduates will find everything simple except perhaps the descriptions of nuclear physics work at Los Alamos in Appendix I, which had best be read after reading Part III.

Part I contains a description of 32 uranium-bearing minerals and a history of radioactivity. Part II is introductory physics, mostly off-the-slide-rule stuff. Part III is an abstract of the Smyth Report with two noteworthy portraits of Fermi and Dunning, and a description of the three production piles at Hanford. The description of the Clinton Engineer Works is more sketchy because of security reasons.

Part IV, comprising the meat of the book, describes in considerable detail possible methods of using atomic power. The author, Sawyer, projects a 35,000 hp AK gas turbine using a closed cycle with a helium-carbon dioxide mixture. The inert helium makes possible a simple uranium heater. Many arrangements are discussed using fission heat in place of one fuel or another. It is emphasized that atomic energy will never replace other fuels but will supplement them. For some uses it is suggested that water be used as a moderator-coolant which is vaporized and then used to run a turbine. Atomic energy locomotives, ships, and rockets are considered.

Industrial benefits from gaseous-diffusion research are the subject of Part V.

Appendix III lists nuclear and atomic masses of isotopes from hydrogen to gold-197. A seven-page index is provided.

Duane Studley
Colorado Springs, Colorado

Analytical Experimental Physics (Revised Edition)

By Harvey B. Lemon and Michael Ference, Jr., University of Chicago. Pp. 588+XVI, Figs. 584, Plates 66, 24×30 cm. University of Chicago Press, 1946. Price $8.00.

This college textbook first published in 1942 was hailed as the "Colossus of General Physics, one of the seven wonders of the textbook world." Now it has been revised, corrections have been made, rough spots have been

smoothed out, figures, plates, and pages have been added. It is indeed a colossus in quantity and quality.

Little revision has been made in the chapters on mechanics, while in the section on heat qualitative discussions of the quantum theory of specific heats and of the properties of dilute solutions have been added. The chapter on alternating currents now includes a section on parallel circuits containing resistance, inductance, and capacitance. Much has been added to the chapter on conduction through gases so that it now includes a discussion of the motion of charged particles in electric and magnetic fields, of relativistic variation of mass with velocity, of the cyclotron, and of the betatron. As is to be expected the sections on nucleonics and electronics have been greatly expanded. A discussion is given of some nuclear reactions of tracers, nuclear fission, transuranic elements, nuclear chain reactions, and the atomic bomb. The electronic chapter now includes an analysis of the equivalent circuit of a triode, a discussion of gas-filled tubes, pentodes, photoelectric cells, electronic oscillators, radio transmitting and receiving apparatus, microelectric waves with radar transmitting and receiving systems, television, and the electron microscope. An interesting plate is added on radar, showing typical sending and receiving apparatus, a "P.P.I. scope" presentation of a convoy leaving New York harbor, and the trace in an oscilloscope of the reflection of radar waves from the moon. Some additions have been made to the chapter on wave motion and only minor changes in the chapters on sound and light. A useful set of trigonometric and logarithmic tables, together with a table of important physical constants, has been appended.

The book is what its title implies, both analytical and experimental in its approach to physics. Physical concepts are carefully interwoven with experimental data. The mathematics employed in the analysis is largely algebra and trigonometry with calculus used sparingly. The presentation is excellent and of the kind to appeal to the abler students. Though the book is more inclusive and more difficult than almost any other college one-year general text in physics, the authors have starred about one hundred sections which may be omitted so as to bring it within the scope of most college courses. There is, however, a section on the equivalent circuit of a triode which would appear to be beyond even the abler students with their present knowledge of physics. The topics are discussed in such a manner as to leave the student with a clear idea of the fundamental concepts and how these were developed.

Since the book is so large and heavy it might have been more practical to publish it in two smaller volumes. Whether this be good or bad advice the authors are to be congratulated on the challenge which they have given to students. Any student who masters this material can be sure of having a solid foundation in physics.

R. J. STEPHENSON
The College of Wooster

New Booklets

Allied Radio Corporation, 833 West Jackson Boulevard, Chicago 7, Illinois, has announced the publication of a new 164-page catalog for 1947, covering radio and electronic products. Special emphasis is placed on equipment for industrial maintenance, research, and production requirements as well as for the needs of government agencies. 10,000 items. Free on request.

The Superpressure Division of the American Instrument Company, Silver Spring, Maryland, has issued its new 88-page catalog No. 406, entitled *Superpressure Catalytic Hydrogenation Apparatus*. Inquire on company letterhead.

United States Testing Company, Inc., 1415 Park Avenue, Hoboken, New Jersey, has revised its booklet *Testing Terms for Better Understanding*. The book describes some of the important tests of merchandise—tells how tests are made, what the results mean, what are standard and minimum specifications.

The Scientific Personnel Branch of the Navy Department, Washington 25, D. C., issues bi-monthly a *Scientific Personnel Bulletin*, listing employment opportunities in the Navy Department for scientists and technicians. 76 pages in the January-February, 1947, issue.

Eberbach and Son Company, Ann Arbor, Michigan, featured in its March issue of *The Announcer of Scientific Equipment* an article on the background and development of the modern analytical balance. 16 pages. Available on request.

Fischer and Porter Company, Hatboro, Pennsylvania, has released a new bulletin including dimensional and operational details of an improved continuous liquid specific gravity indicator. Address Department 6F-B of the company.

National Carbon Company, Inc., 30 East 42 Street, New York 17, New York, has published a new bulletin, *Catalogue Section M8808*, describing standard, seven-tube heat exchangers of "Karbate" impervious graphite for use under highly corrosive conditions.

The Winter 1946–47 number of *Interchemical Review*, published at 432 West 45th Street, New York 19, New York, has the following table of contents:

Maleic and Fumaric Resins....Charles S. Rowland.
Market Research in Industrial Fields....John P. Duane.
Oilcloth Pioneers in Maine....Charles R. Bragdon.

The Gaertner Scientific Corporation, 1201 Wrightwood Avenue, Chicago 14, Illinois, has recently published a new bulletin, 156–74, describing its optical benches and accessories. 26 pages.

Here and There

New Appointments

Eugene W. Boehne and Lan Jen Chu were recently appointed associate professors in the Department of Electrical Engineering at the Massachusetts Institute of Technology.

Two new appointments to the staff of the National Bureau of Standards were recently announced. Albert S. Cahn, Jr., will assist in the research involved in the design of two high speed electronic computing machines to be built for the Bureau of the Census and the Navy. P. J. Selgin will work on the development of electronic ordnance for the military services in the Ordnance Development Division.

The U. S. Weather Bureau has announced the appointment of Ross Gunn as the director of a newly organized Division of Physical Research, which will undertake studies of the atmosphere and basic physical processes that are related to the weather and the earth.

F. C. Henriques, Jr., has joined the staff of Tracerlab, Inc., at Boston, Massachusetts, as director of the Radiochemical Division.

Awards

Latest Franklin Institute awards for 1947 are as follows:

The Franklin Medal, highest honor of the Institute, to Enrico Fermi, physicist at the Nuclear Research Institute in Chicago, and to Sir Robert Robinson, professor of chemistry at Oxford University, England.

The Newcomen Medal to Everett G. Ackart, recently retired chief engineer of the E. I. du Pont de Nemours and Company.

The Clark Medal to Edward G. Boyer, manager of the Philadelphia Electric Company's gas department.

The Ballantine Medal to George C. Southworth of the Bell Telephone Laboratories.

New Chairman for A. I. P.

George R. Harrison, dean of the School of Science, Massachusetts Institute of Technology, has been elected chairman of the American Institute of Physics, succeeding Paul E. Klopsteg, director of research, Northwestern University Technological Institute, who has served as chairman since 1940.

Western Branch for Airborne Instruments Laboratory

A branch of the Airborne Instruments Laboratory, Inc., Mineola, New York, was recently established at Burbank, California. This will make possible a closer liaison between the main laboratory and west coast aircraft manufacturers in need of a consultation and development service. Airborne Instruments Laboratory is the peacetime outgrowth of the NDRC laboratory of the same name which operated under the direction of Columbia University during the war. Hector R. Skifter is president of the Laboratory and Robert D. Martin is supervising the west coast unit.

Electrochemical Symposium at Pittsburgh

The annual spring symposium of the Pittsburgh section of the Electrochemical Society was held May 23 and 24 at the Mellon Institute. The subject was "High Temperature and Hetrogeneous Reactions."

Electrochemical Congress at Louisville

A congress sponsored by the Electrochemical Society met in Louisville, Kentucky, April 9 to 12. A day's session was devoted to electronics, one to the corrosion of metals at elevated temperatures, and a third to the production of the best steels in the electric furnace. The Young Authors' Prizes were awarded to N. A. Neilsen of Du Pont and to Burke Cartwright of the U. S. Bureau of Mines.

Engineering Foundation Issues Report

The Engineering Foundation, 29 West 39th Street, New York 18, New York, made public in March its 32nd annual report to the board of trustees. The report stated, "It is clear that industry has, in general, become more research minded and large expansions of industrial research are to be expected. In some cases this will be by individual companies, in others, by associations of various types." Sixteen projects were sponsored by the Engineering Foundation during the past year, six of which were carried over from the preceding year. Among the projects were soil mechanics, fluid mechanics, materials of engineering comprising metal researches, welding, lubrication, and rolling friction. In addition to sponsoring engineering research, the Foundation also supports agencies or activities having as their objectives the advancement of the engineering profession.

Changes in Electrical and Photometric Units

In pursuance of decisions of the International Committee on Weights and Measures, the National Bureau of Standards will introduce as of January 1, 1948, revised values of the units of electricity and of light. While the definitions of the units and the methods of fixing their magnitudes will be different from the present practical systems, the changes in magnitude will be so small as to affect appreciably only measurements of high precision. In certificates for standards and instruments issued by the Bureau during 1947, values will be given in both the old and the new units.

A complete description of the new units has appeared in the *Review of Scientific Instruments* for May, 1947.